Mapping Tropical Peatlands Combustion from Satellite Remote Sensing Data

Parwati Sofan

MSc. Space Technology Applications, BSc. Agrometeorology

This thesis is submitted in fulfilment of the requirements for the degree of

Doctor of Philosophy

Science, Technology, Engineering and Mathematics



University of South Australia

April 2021

Table of Contents

Table of Contents ii
List of Tables vi
List of Figures ix
List of Equations xvi
Abbreviations xvii
Abstract xx
Declaration xxiii
Acknowledgements xxiv
Publications xxv

Chapter 1. An Introduction to Tropical Peatlands, Their Combustion and Monitoring from Space 1

1.1. Peatlands: Their Origins and the Process Leading to Peat Combustion 2
1.1.1. Peatlands, Their Origin and Location 2
1.1.2. Importance and Condition of the Peatlands 4
1.1.3. The Process Leading to Peatland Combustion 6
1.2. Peatlands Combustion/Fire Monitoring from Space 10
1.2.1. Principle Physics for Fire Detection from Remote Sensing 11
1.2.2. Space-based Sensor Capability for Fire Detection 12
1.2.3. Space-based Methods for Fire Detection 14
1.2.3.1. Low Spatial, High Temporal Resolution Data 14
1.2.3.2. Medium Spatial, Low Temporal Resolution Data 15
1.2.3.3. Smallsatellite 16
1.3. Summary of the Challenges in Operational Peatland Combustion Monitoring 17
1.4. The Research Gap and Research Questions 19
1.5. Thesis Structure 21
References 24

Chapter 2. Detecting Peatland Combustion using Shortwave and Thermal Infrared Landsat-8 Data 34

Abstract 35
2.1. Introduction 36
2.2. Material and Methods 37
2.3. Results and Discussion 38
2.3.1. Peat Combustion Identification 38
2.3.2. Fire Temperature Estimation 42

2.3.3. Precision and Comparison 43
2.4. Conclusion 47
References 47

Chapter 3. Detection and Validation of Tropical Peatland Flaming and Smouldering using Landsat-8 SWIR and TIRS Bands 50

Abstract 51
3.1. Introduction 52
3.2. Materials and Methods 55
3.2.1. Study Site 55
3.2.2. Data 58
3.2.3. Pre-processing of Landsat-8 Data 59
3.2.4. Separation of Combustion Area and Non-Combustion Area 60
3.2.5. Smoke Haze Distribution 62
3.2.6. Tropical Peatland Combustion Algorithm 63
3.2.7. Comparison with the Previous Landsat-8 Active Fire of Global Operational Land Imager 66
3.2.8. Validation with Ground Truth 66
3.2.9. Comparison with the 375 m Visible Infrared Imaging Radiometer Suite Active Fire Product 68
3.3. Results 70
3.3.1. Implementation of Tropical Peatland Combustion Algorithm 70
3.3.2. Comparison of Tropical Peatland Combustion Algorithm with Global Operational Land Imager Results 71
3.3.3. Validation of Tropical Peatland Combustion Algorithm Mapping 73
3.3.3.1. Internal Validation in Central Kalimantan Province 73
3.3.3.2. External Validation in Riau Province 76
3.3.4. Statistical Assessment of Tropical Peatland Combustion Algorithm Validation 77
3.3.5. Statistical Assessment of the 375 m Visible Infrared Imaging Radiometer Suite Active Fire Validation 79
3.4. Discussion 81
3.5. Conclusions 86
References 86

Chapter 4. Assessment of VIIRS 375 m Active Fire using Tropical Peatland Combustion Algorithm Applied to Landsat-8 over Indonesia's Peatlands 92

Abstract 93
4.1. Introduction 93
4.2. Data 99
4.2.1. Study Areas 99

4.2.2. Satellite Data 100
4.2.3. VNP14IMG Data 100
4.2.4. Tropical Peatland Combustion Algorithm Applied to Landsat-8 (ToPeCAl-L8) 101
4.2.5. Methods for Analysis Comparison of VNP14IMG with ToPeCAl Landsat-8 102
4.3. Results 105
4.3.1. Probability of Detection of VNP14IMG at Single Time of Acquisition 105
4.3.2. Probability of Detection of VNP14IMG at Multi-Times Combinations of Acquisition 108
4.3.3. Commission and Omission Errors 110
4.4. Discussion 116
4.5. Conclusions 120
References 121

Chapter 5. Applying The Tropical Peatland Combustion Algorithm to Landsat-8 Operational Land Imager (OLI) and Sentinel-2 Multi Spectral Instrument (MSI) Imagery 128

Abstract 129
5.1. Introduction 130
5.2. Data 134
5.2.1. Landsat-8 and Sentinel-2A/B 134
5.2.2. Study Area and Data Acquisition Period 135
5.3. Methods 137
5.3.1. Tropical Peatland Combustion Algorithm with ShortWave InfraRed (SWIR) and Thermal InfraRed (TIR) 137
5.3.2. Tropical Peatland Combustion Algorithm without TIR (ToPeCAl-2) 146
5.3.2.1. Water Masking 147
5.3.2.2. Permanent Bright Object Masking 148
5.3.2.3. ToPeCAl-2 with Contextual Test 149
5.3.2.4. ToPeCAl-2 with Cloud Masking 153
5.3.2.5. Pixel-Based Comparison of ToPeCAl-2 Applied to Landsat-8 Operational Land Imager (OLI) with ToPeCAl-1 Applied to Landsat-8 OLI/Thermal InfraRed Sensor (TIRS) 153
5.3.3. Implementation and Comparison of ToPeCAl-2 on Sentinel-2 Multi Spectral Instrument (MSI) 154
5.3.3.1. Sentinel-2 MSI Data Pre-processing 154
5.3.3.2. Sentinel-2A MSI and Landsat-8 OLI Spectral Reflectance Sensor Comparison 154
5.3.3.3. Implementation of ToPeCAl-2 Applied to Sentinel-2 MSI 156
5.3.3.4. Pixel-Based Comparison of ToPeCAl-2 Applied to Sentinel-2 MSI with ToPeCAl-1 Applied to Landsat-8 OLI/TIRS 157

5.4. Results 157
5.4.1. Statistical Comparison of ToPeCAl-2 Applied to Landsat-8 OLI and ToPeCAl-1 Applied to Landsat-8 OLI/TIRS 157
5.4.2. Relationship between Top of Atmosphere (TOA) Reflectance of Landsat-8 and Sentinel-2 for Aerosol and SWIR Bands 161
5.4.3. Implementation and Comparison of ToPeCAl-2 Applied to Sentinel-2 MSI 162
5.5. Discussion 167
5.5.1. Comparison and Adjustment of ToPeCAl-2 to Landsat-8 OLI 167
5.5.2. Relationships between TOA Reflectance of Sentinel-2 and Landsat-8 at Aerosol and SWIR bands 170
5.5.3. The Application of ToPeCAl-2 to Sentinel-2 Data 171
5.6. Conclusion 172
References 173

Chapter 6. Key Outcomes, Discussions and Future Research 181

6.1. Summary of Key Outcomes 182
6.2. Discussions 184
6.2.1. Flaming and Smouldering Peatland Fires Detection 184
6.2.2. Accuracy of ToPeCAl Fires 188
6.2.3. Opportunity for Integration of Multi Fire Information from Different Observations 190
6.3. Future Research Directions 192
References 194

Appendices 199

Statement of Authorship: Chapter 2 200
Statement of Authorship: Chapter 3 201
Statement of Authorship: Chapter 4 202
Statement of Authorship: Chapter 5 203
Chapter 2 Appendix 204
Chapter 3 Appendix 205
Chapter 4 Appendix 207
Chapter 5 Appendix 208
Chapter 6 Appendix 211

List of Tables

Table 1.1. List of current optical remote sensing sensors with infrared properties commonly used for combustion monitoring. 14

Table 2.1. Detection of flaming (F), smouldering (S), and mixture of flaming and smouldering (FS) over 2 Landsat-8 images (03-08-2015 and 19-08-2015). The hit, Commission (C) and Omission (O) Errors were derived from comparison with the 764-RGB of Landsat-8. 44

Table 3.1. List of Landsat-8 data used for algorithm development and validation. The algorithm development area was in Central Kalimantan (CK) using 2015 data, while validation analysis was conducted in Central Kalimantan (2018) and Riau Provinces (2016 and 2018). 58

Table 3.2. Sample areas (in pixel) for peatland combustion algorithm development. 62

Table 3.3. The ToPeCAl for smouldering (S), mixture of flaming and smouldering (FS), and flaming (F) detection over clear sky conditions and smoky conditions. The criterion of $SICI_{\rho}$ must be satisfied together with the threshold values for SWIR-2 reflectance and TIR-1 brightness temperature (BT) of Landsat-8 data. 65

Table 3.4. The design of the Contingency Table comparing ToPeCAl mapping versus ground truth. Four categories ((S, FS and F, and non-combustion area (Non)) were assessed for both ground truth data and ToPeCAl results. 67

Table 3.5. (**A**) The design of the Contingency Table for the VNP14IMG product versus ground truth data, (**B**) the VNP14IMG product versus Tropical Peatland Combustion Algorithm (ToPeCAl) results from Landsat-8 based on two categories (Yes-Fire, No-Fire), and (**C**) the VNP14IMG product versus ToPeCAl applied to Landsat-8 based on four categories (F, S, FS, and Non). 69

Table 3.6. (**A**) The results of Contingency Table of ToPeCAl validation in Central Kalimantan and Riau Province (data in table shows counts), and (**B**) the scores of PC, FAR, POD, and BIAS of ToPeCAl Mapping compared with ground truth data. 78

Table 3.7. (A) The results of the Contingency Table of VNP14IMG versus ground truth in Central Kalimantan and Riau Provinces (data in table show counts), and (**B**) the scores of PC, FAR, POD, and BIAS of VNP14IMG compared with ground truth data. 79

Table 3.8. (**A**) The scores of PC, FAR, POD, and BIAS of VNP14IMG compared with ToPeCAl with a different time of 3 hours in day-time, and (**B**) a combination of 3 hour and 15 hours difference in time. The calculations were generated for buffer zones of 187.5 m to 1250 m. 80

Table 4.1. List of VIIRS channel for active fire detection at 375 m (Schroeder & Giglio 2016). 96

Table 4.2. List of Landsat-8 OLI/TIRS and VNP14IMG data used in the study area of Riau, Central Kalimantan (CK), and South Kalimantan (SK). 101

Table 4.3. List of Landsat-8 OLI and TIRS spectral bands used in ToPeCAl and their primary application (Sofan et al. 2019; Irons, Dwyer & Barsi 2012; USGS 2019). The Thermal InfraRed band (band-10) was resampled from 100 m to 30 m in Landsat-8 Level-1TP by USGS. 102

Table 4.4. Number of VNP14IMG at night$_{-1}$, day$_0$, and night$_0$, and number of ToPeCAl-L8 fire polygons as the fire reference after cloud masking on both of VIIRS and Landsat-8 data. The fire data were counted at buffer distances from VNP14IMG point of 187.5 m, 375 m, and 750 m. The detected fires were analysed with single buffer and cluster buffer techniques. POD equals the number of detected fires divided by the number of ToPeCAl-L8 fires was without classifying the fire sizes. 106

Table 4.5. The classes and sources of FPR in this study. 110

Table 4.6. The result of VNP14IMG and ToPeCAl-L8 comparison at night$_{-1}$, day$_0$, night$_0$, and night$_{-1}$+day$_0$ within 375 m buffer from cluster buffer analysis; com-0 = commission errors before reducing false positives; com-1 = commission error after removing FPR-2 and FPR-3; com-2=commission error after removing FPR-2, FPR3 and FPR-5. 114

Table 5.1. List of peatland fire detection research using medium to low spatial resolution satellite data in Indonesia (OLI is Operational Land Imager; TIRS is Thermal InfraRed Sensor; BIRD is Bi-spectral InfraRed Detection; HSRS is HotSpot Recognition System; TET-1 is Technology Experiment Carrier; Suomi NPP is Suomi National Polar-orbiting Partnership; SWIR is ShortWave InfraRed; TIR is longwave Thermal InfraRed; MWIR is mid-wave infrared; VIIRS is Visible Infrared Imaging Radiometer Suite; UAV is Unpiloted Aerial Vehicle). 132

Table 5.2. Landsat-8 OLI and Sentinel-2 Multi Spectral Instrument (MSI) spectral band information used in Tropical Peatland Combustion Algorithm (ToPeCAl) and background mapping (Barsi et al. 2018; Du et al. 2016; Irons, Dwyer & Barsi 2012; Schroeder et al. 2016; Sofan et al. 2019; Sun et al. 2017). 135

Table 5.3. List of Landsat-8 data for applying and assessing Tropical Peatland Combustion Algorithm (ToPeCAl) without TIR (ToPeCAl-2) in Central Kalimantan, South Kalimantan, West Kalimantan, Riau, Jambi, and South Sumatera. 136

Table 5.4. List of Landsat-8 and Sentinel-2 data for applying and assessing application of ToPeCAl-2 to images over Central Kalimantan, South Kalimantan, West Kalimantan, Riau, Jambi, and South Sumatera. There are four pairs of Landsat-8 and Sentinel-2 images contained fires in the same areas on the day of acquisition. Descending orbit Landsat-8 images were acquired at 2–12 min after Sentinel-2 image acquisition. The state of fire features was identified from the Red-Green-Blue (RGB) image composites of SWIR-2, SWIR-1, and Red bands of Sentinel-2 and Landsat-8 images. 137

Table 5.5. Visual comparison on false positive fire pixels of ToPeCAl with SWIR and TIR (ToPeCAl-1) and ToPeCAl without TIR (ToPeCAl-2) applied to Landsat-8 images. 146

Table 6.1. Potential future sensors for supporting peatland fires monitoring (ESA 2020; Michel et al. 2011; Briottet et al. 2011; Transon et al. 2018; Futureearth 2020; Koetz 2019; NASA 2020)..... 194

Table A2.1. Statistical values of samples of combustion areas, burnt areas, urban and forest from Landsat-8 on August 3rd and August 19th, 2015. B6, B7, B10 represent TOA radiance ($Wm^{-2}sr^{-1}\mu m^{-1}$) of band-6, band-7 and band-10 of Landsat-8, respectively. SICI is ShortWave InfraRed Combustion Index or the ratio of band-6 to band-7. 204

Table A3.1. Spectral properties of Landsat-8 OLI and TIRS (Morfitt et al. 2015; USGS 2018; Irons et al. 2012). The radiance and temperature values are at sensor at the Top of Atmosphere (TOA). The TOA temperature is only measured in TIR bands. 205

Table A3.2. Statistic median values of Top of Atmosphere (TOA) planetary reflectance of Landsat-8 bands (band 1–7), TOA brightness temperature of TIR-1 (band-10) and the ratio of ShortWave InfraRed band-7 (SWIR-2) and band-6 (SWIR-1) reflectance or ShortWave InfraRed Combustion Index ($SICI_{\rho}$). Samples of combustion areas and non-combustion areas were extracted from Landsat-8 path/row 118/062 over Central Kalimantan in the period of August–October 2015. The sample areas were categorized based on atmosphere conditions, i.e. clear and smoky based on aerosol band (band-1)..... 206

Table A4.1. POD (%), commission error (%), and omission error (%) of VNP14IMG assessment based on ToPeCAl-L8 fires using single buffer analysis and cluster buffer analysis for three buffer distances (187.5 m, 375 m, 750 m) and single time acquisition ($night_{-1}$; day_0; $night_0$) and multi-time acquisition of VNP14IMG ($night_{-1}$ + day_0; day_0 + $night_0$; $night_{-1}$ + day_0 + $night_0$, and nighttime data i.e. $night_{-1}$ + $night_0$)..... 207

Table A5.1. Statistical comparison of ToPeCAl-2 to ToPeCAl-1 applied to Landsat-8 image data based on contextual test and cloud masking approach. The comparison was for one class of fire and ToPeCAl-1 was the reference fire data. Columns a to h are the summation values from 15 datasets of Landsat-8. False positive and false negative pixels consisted of fires spatially related to true positive fires – called related false positive/negative (RFP/RFN) and independent false positive/negative (IFP/IFN) pixels. The RFP pixels were the fire pixels that were adjacent to the true positive fire pixels within a one pixel outer buffer; they were considered not to be counted as commission errors and were classified as true positive pixels. Likewise, the RFN pixels for omission error. (TN=True Negative; TP=True Positive; FP=False Positive; RFP=Related False Positive; IFP=Independent False Positive; FN=False Negative; RFN=Related False Negative; IFN=Independent False Negative; POD=Probability of Detection, ICE=Independent Commission Error, IOE=Independent Omission Error)..... 208

Table A5.2. As per Table A5.1 but showing the comparison of fire classes i.e., flaming (F), smouldering (S), and mix of flaming and smouldering (FS). 208

Table A5.3. Landsat-8 OLI TOA reflectance as a function of Sentinel-2 MSI TOA reflectance at aerosol, SWIR-1, and SWIR-2 bands. Intercept and slope values were derived from the ordinary least squares (OLS) regression of total data (n). The coefficients of determination (R^2) were significant at p-values < 0.001. The data sites were Central Kalimantan and South Kalimantan (CK-SK), Jambi and South Sumatera (JSS), and Riau. 209

Table A5.4. Statistical comparison of fires resultant from ToPeCAl-2 with contextual test and ToPeCAl-2 with cloud masking applied to Sentinel-2 MSI compared with fires resultant from ToPeCAl-1 applied to Landsat-8 OLI/TIRS images. The comparison was for one class of fire. The TOA reflectance used in ToPeCAl-2 were with no transformation values and with transformation values from the merged OLS model and local OLS model. (TN=True Negative; TP=True Positive; FP=False Positive; RFP=Related False Positive; IFP=Independent False Positive; FN=False Negative; RFN=Related False Negative; IFN=Independent False Negative; POD=Probability of Detection, ICE=Independent Commission Error, IOE=Independent Omission Error)..... 210

Table A5.5. As per Table A5.4 but showing the comparison of fire classes i.e., flaming (F), smouldering (S), and mix of flaming and smouldering (FS). 210

Table A6.1.Permanent bright object (BO) before and after masking on the independent false positive pixels applied to fifteen scenes of Landsat-8 OLI data..... 211

List of Figures

Figure 1.1. Peatlands distribution in Indonesia. Peatland data (2011) from the Indonesian MoA overlaid on a world map of SE Asia. 4

Figure 1.2. (a) Natural peatland forest in Kalimantan (Sugardiman 2005); (b) peatland drainage canals in plantation areas. Picture (b) was taken during a ground truth collection in Central Kalimantan on 28 September 2018. 6

Figure 1.3. (a) Evidence of smouldering fire on peat soil to about one metre's depth; (b) Smouldering log in slashed and burnt area; the brown, half-dead trees shown at the back of logs are the result of flaming; (c) Ash and smoke in the peat surface with half-dead shrubs; (d) Field observation in smouldering peatland areas with dispersed smoke near the ground; most of the surface is covered by ash and char with some half-dead (brown) and green vegetation shown in the picture; (e) Smouldering peatland covered by dispersed smoke; (f) Flaming peatland (orange features) with darker smoke emanating from flaming areas; the smouldering areas with white smoke are shown to the back of the flaming front. Figure (d), (e) and (f) were taken from a drone. 9

Figure 1.4. Field temperature of the background, smouldering and flaming peatlands in Kalimantan The temperature was measure by a CEM Instrument DT-9862 Professional Infrared Video Thermometer, which has a dynamic range spanning 215–2373 K (Elvidge et al. 2015) CC BY. 10

Figure 1.5. Top of atmosphere (TOA) spectral radiance simulated using MODTRAN with ground object temperatures at 300 K, 360 K, 500 K, 700 K and 1000 K for a ground target with an albedo of 0.1 (for peatland with limited vegetation) under a rural and tropical atmosphere. The atmospheric transmittance is presented in a light blue background, while water vapour and gas absorption are in grey. 12

Figure 1.6. Distribution of hotspots/active fires data (confidence level ≥ 80%) from MODIS/VIIRS (MOD14 collection 6 and VNP14IMG) and ground validations by the local disaster management agency; (a) Riau Province (data periods span April–October 2016, February 2017 and March–June 2018); (b) Central Kalimantan Province (data period spans June–October 2015). 19

Figure 1.7. General thesis structure 22

Figure 2.1. (**a, b**) The 764-RGB image of Landsat-8 on August 3rd and August 19th, 2015 with 9 samples and 21 samples respectively of potential combustion areas shown inside red squares and non-combustion areas inside cyan circles, respectively. An enlargement of one potential combustion sample area is presented on the right side of each Landsat image, (**c**) Box plots of radiance values of SWIR and TIR bands over combustion, burnt, forest, and urban areas, (**d**) SICI's box plots in combustion and non-combustion areas with the blue line indicating a threshold of 3.0 (the 1rd quartile value of burnt area) which was used to separate combustion from other areas. 40

Figure 2.2. Example of peatland combustion identification (**a**) Smoke in pale bluish tones showed in 764-RGB with the potential combustion area in orange to yellow tones, (**b** & **c**) Pseudo colour of the radiance of band-7 and band-10 respectively were just under / at saturation, (**d**) The SICI < 3 in blue as the potential combustion area, (**e**, **f**, **g**) The identified flaming (red) and smouldering (blue) areas, (**h**) Mixture of flaming and smouldering areas shown in cyan over the 764-RGB image, (**i**) Box

plots of SICI over flaming, smouldering, and mixture of flaming and smouldering areas. 41

Figure 2.3. (**a**) Boxplot represents the minimum, quartile 1st, median, quartile 3rd and maximum values of smouldering (S), mixture of flaming and smouldering (FS), and flaming (F), (**b**) The dotplot of estimated peatland combustion temperature on F, FS, and S with two peaks of temperature and left-skewed distribution indicating a higher contribution of flaming than smouldering to FS temperature. 43

Figure 2.4. (**a**) The nine combustion areas shown in red square and MODIS fire-mask (pink) overlaid on the Landsat-8 764-RGB image of August 3rd, 2015. The MODIS fire-mask only appeared in location #2, (**b**) Enlargement of location #2 showing the MODIS fire-mask (pink) transparency overlaid on the Landsat-8 image which is showing a combustion area in red and cyan (centre right). 45

Figure 2.5. (**a)** The 22 combustion areas shown in red squares and MODIS fire-mask (pink and yellow) overlaid on the Landsat-8 764-RGB image of August 19th, 2015, (**b**) Enlargement of locations of #15 and #16 showing the MODIS fire-mask (pink and yellow) transparency overlaid on Landsat-8's combustion area; the blue polygon represents smouldering area generated from Landsat-8, (**c**) Enlargement of commission error of MODIS fire-mask at 01.35 pm over bare plantation area. 46

Figure 3.1. (**A**) The algorithm development site analysed from the Getis–Ord optimised hotspot applied to 1 km grid cell counts of Moderate Resolution Imaging Spectroradiometer (MODIS) active fires (2007–2017) overlaid on peatland map in Central Kalimantan and (**B**) Validation site in Riau Province. The Hot Spots in red tones represent the high density of MODIS active fires with statistically significant confidence levels from 90% to 99%, while the Cold Spots, in blue tones, represent the low distribution of fire hotspots with statistical significance from 90% to 99%. The white colour is not statistically significant. The MODIS active fire source from The National Aeronautics and Space Administration-Fire Information for Resource Management System (NASA-FIRMS). Peatland map sources from the Ministry of Agriculture (MoA). The boundary administration is from Geospatial Information Agency (BIG). 57

Figure 3.2. (**A**) An example of a combustion area on the 764 Red Green Blue (RGB) images of Landsat-8 on September 20, 2015 with combustion area surrounding non-combustion area (forest, plantation, burnt area), (**B**) The Top of Atmosphere (TOA) planetary reflectance values of Landsat-8 bands. The solid line pattern refers to objects in clear sky condition, while the dotted line pattern relates to smoky objects, (**C**) The median values of TOA brightness temperatures of Thermal InfraRed band-10 (TIR-1) plotted in the clustered column, while the median values of the ratio of ShortWave InfraRed band-7 (SWIR-2) and SWIR-1 reflectance, ShortWave InfraRed Combustion Index ($SICI_{\rho}$), are shown in a black line with markers. Smoky conditions are shown in the light blue shading area to the right of clear sky conditions on the left. The red line is $SICI_{\rho}$ threshold used to separate flaming and smouldering from other background objects. 63

Figure 3.3. (**A**) Sample of combustion area in the 764 RGB image of Landsat-8 on 19 August 2015 which had high reflectance of SWIR-1 and SWIR-2, (**B**) the enlargement of combustion areas showing 10 sample pixels, (**C**) the extracted SWIR-1 and SWIR-2 reflectances with $SICI_{\rho}$ values; pixel$\neq$2, $\neq$3, and $\neq$7 had $SICI_{\rho} \leq 1$. 64

Figure 3.4. Flowchart of Landsat-8 image processing for mapping tropical peatland combustion. 66

Figure 3.5. An example of buffering VNP14IMG point data overlaid with ToPeCAl results from Landsat-8. The VNPIMG data and ToPeCAl mapping relates to

September 28, 2018. There is a 3 and 15 hour time difference from Landsat-8 to VNP14IMG acquisition times. The buffer zones are 187.5 m, 375 m, 500 m, 750 m, 1000 m, 1250 m, and 1500 m from both the VNP14IMG points (5:30 UTC and 18:12 UTC). 70

Figure 3.6. (**A, B**) An example of peatland combustion surrounded by cloud cover on a 764 RGB images of Landsat-8 on 4 September 2015 with the classified peatland combustion, (**C, D**) Peatland combustion in heavy smoke conditions and the classified peatland combustion on 20 September 2015. 71

Figure 3.7. Comparison of Global Operational Land Imager (GOLI) and ToPeCAl implementation on peatland combustion using Landsat-8 28 September 2018, in Central Kalimantan. (**A**) The 764 RGB images of Landsat-8 of peatland combustion area, (**B**) The GOLI active fire (magenta) overlaid on the RGB image, (**C**) The ToPeCAl mapping result on RGB image is shown in three classes of peatland combustion (S, FS, F), (**D**). An overlay of GOLI and ToPeCAl showing a larger area of combustion from ToPeCAL, especially for smouldering fire, (**E**, **F**) Drone image and its enlargement showing smouldering peatland but not active/flaming fire. 72

Figure 3.8. The coverage of ground truth collection in Central Kalimantan (27 September–6 October 2018) overlaid on Landsat-8 images of 28 September 2018 (right) and 5 October 2018 (left). 73

Figure 3.9. (**A**) The 764 RGB image of Landsat-8 on 28 September 2018, (**B**) The result of ToPeCAl mapping which consists of smouldering (S), mixture of flaming and smouldering (FS), and flaming (F) with ground truth base station locations marked in magenta triangle, (**C**) The pictures of peatland fires taken from helicopter on 28 September 2018. Field pictures sourced from the local Indonesian Disaster Management Agency (BNPB) of Central Kalimantan Province. 74

Figure 3.10. (**A**) The 764 RGB image of Landsat-8 on 28 September 2018 and (**B**) the result of peatland combustion mapping with ground truth location marked in red square, (**C**) The picture of peatland smouldering fire taken from a drone on 1 October 2018. 75

Figure 3.11. (**A**) The 764 RGB image of Landsat-8 on 5 October 2018, presented a combustion area which was predominantly vegetated, (**B**) The result of peatland combustion mapping, and (**C**) Drone imaging and (**D**) Terrestrial picture of smouldering vegetation area in the area on 6 October 2018. 76

Figure 3.12. (**A, B**) The 764 RGB image of Landsat-8 on 20 August 2016 showing a combustion area with the result of peatland combustion mapping and **(C)** a helicopter oblique picture taken on the same day taken in Riau Province; (**D, E)** The 764 RGB Image of Landsat-8 on 4 April 2018 and the result of peatland combustion mapping with ground truth location marked in red square. The pictures **(F)** of peatland fires from the ground and helicopter; sourced from local BNPB of Riau Province on 4 April 2018. 77

Figure 3.13. POD of peatland combustion (S, FS, and F) detected by VNP14IMG from day-time and night-time data in buffered zones of 187.5 m to 1500 m. 81

Figure 4.1. Peatlands in Indonesia (red polygon) sourced from Indonesian Ministry of Agriculture. The study sites are peatland area in Riau, Central Kalimantan and South Kalimantan Provinces. The study areas are imaged by Landsat-8 data overpass (blue trapezoids) mostly over of peatland areas in Riau and Kalimantan in path/row of 127/059, 126/060, 117/062, and 118/062. 100

Figure 4.2. The illustration of the assessment of (**a**) single buffer and (**b**) cluster buffer of VNP14IMG with ToPeCAl-L8; (**c**) A sample fire area in the 764-RGB image of

Landsat-8 on 30 August 2019 path/row 118/062; (**d**) the daytime VNP14IMG data on 30 August 2019 (blue dots) with the single buffers of VNP14IMG of 187.5 m, 375 m and 750 m (black, orange and aqua circles respectively); (**e**) the daytime VNP14IMG data on 30 August 2019 with the cluster buffer of VNP14IMG of 187.5 m, 375 m and 750 m (black, orange and aqua polygons respectively). 104

Figure 4.3. Number of agreement fires at 0.09 ha, ≤ 14 ha, and >14 ha from (**a**) single buffer analysis and (**b**) cluster buffer analysis at buffer distances of 187.5 m, 375 m, and 750 m for each VNP14IMG acquisition ($night_{-1}$, day_0, and $night_0$). 107

Figure 4.4. Plots of VNP14IMG active fires which agreed with ToPeCAl-L8 fires within 750 m of VNP14IMG from cluster buffer analysis in Riau (top) and part of Central Kalimantan and South Kalimantan Provinces (bottom); (**a**) and (**b**) are enlargements of the north east part (**a**) and south east part (**b**) of Riau Province; (**c**) presents fire data located in the border of Central Kalimantan and South Kalimantan. The data period is the same listed in Table 3. The black, yellow, and red circles represent VNP14IMG at $night_{-1}$, day_0, and $night_0$, respectively. The relative size of the dot is not associated with the fire size. 108

Figure 4.5. (**a**, **b**) POD (%), (**c**, **d**) commission error (%), and (**e**, **f**) omission error (%) of VNP14IMG assessment based on ToPeCAl-L8 fires using single buffer analysis and cluster buffer analysis for three buffer distances (187.5 m, 375 m, 750 m) and single time acquisition ($night_{-1}$; day_0; $night_0$) and multi-time acquisition of VNP14IMG ($night_{-1}$ + day_0; day_0 + $night_0$; $night_{-1}$ + day_0 + $night_0$, and nighttime data i.e. $night_{-1}$ + $night_0$). 109

Figure 4.6. The percentage of false positive rates (FPR) sources from the total of commission error at single time ($night_{-1}$, day_0, and $night_0$) and multi-time combination ($night_{-1}$+day_0) within 375 m from cluster buffer analysis. $\bar{X}$ is the average value. 111

Figure 4.7. An example of FPR-3. (a) There were no fires in Landsat-8 daytime on 12 September 2018; (b) Sentinel-2 image showed fire features on 13 September 2018; (c) no fire detection from VNP14IMG at $night_{-1}$ (11 September 2018); (d) no fire detection from VNP14IMG at day_0 (12 September 2018) due to cloud and sun glint; (e) active fires detected from VNP14IMG at $night_0$ (12 September 2018) with nominal confidence level. This caused commission error on $night_0$ data when compared to ToPeCAl-L8 daytime. However, there were fire features from Sentinel-2 image one day after Landsat-8 data. 112

Figure 4.8. Examples of commission errors of VNP14IMG: (a) bright object in intensive agricultural area using plastic membranes observed at daytime (30 August 2019; 05:30 UTC); (b) over open land and bright object in settlement area at daytime (28 September 2018; 05:30 UTC); (c) over industrial area with gas flare at nighttime (04 April 2018; 06 April 2019; 07 April 2019). VNP14IMG active fires were overlaid on high spatial resolution image data sourced from ESRI. 113

Figure 4.9. An example of omission fires of VNP14IMG data at $night_{-1}$, day_0, and $night_0$. (a) Landsat-8 image showed fires from ToPeCAl result (red polygon) and recent burnt area in dark brown on RGB image on 12 September 2018; (b) Sentinel-2 image showed larger recent burnt area in dark brown underneath smoke and cloud in white tones on RGB image on 13 September 2018; (c, d) ShortWave InfraRed Combustion Index (SICI) pseudo colour images of Landsat-8 and Sentinel-2; the higher SICI values in darker orange tones ( ) referred to combustion as shown in Figure c, while in lower tones ( ) associate with recent burnt area. A larger SICI with similar orange tones ( ) shown in Sentinel-2 (Figure d) which indicated a larger burnt area, however, thin cloud is affecting the imagery; (e) one fire area detected by VNP14IMG at $night_{-1}$ of 12 September 2018, but other two fires not

detected; (f, g) no fire detection from VNP14IMG at day_0 and $night_0$ of 12 September 2018. 115

Figure 5.1. Estimated annual emission of peatland fires in Equatorial Asia in 1997–2019 from Global Fire Emissions Database version 4.1 (http://www.globalfiredata.org/data.html) and the Oceanic Niño Index (ONI) and Dipole Mode Index (DMI) using 3 month running average of sea surface temperature anomalies during November-December-January period. Climate indices data were accessed at https://origin.cpc.ncep.noaa.gov/products/analysis_monitoring/ensostuff/ ONI_v5.php and https://psl.noaa.gov/gcos_wgsp/Timeseries/Data/dmi.had.long.data. 131

Figure 5.2. Study areas (blue trapezoid) coverage of Landsat-8 scene areas (path/row of 118/062, 119/06, 121/061, 124/062, 125/061, 126/060, 127/059) over Kalimantan and Sumatera's peatland (in red). Peatland data sources from the Indonesian Ministry of Agriculture (2011). Administration boundaries are from Geospatial Information Agency of Indonesia. 136

Figure 5.3. Spectral radiance simulated using MODerate resolution atmospheric TRANSmission (MODTRAN) for peatland with limited vegetation. The simulation was made based on albedo of 0.1 with an assumption of emissivity of 0.9 over burning peatland at 300 K, 360 K, 450 K, 500 K, 700 K and 1000 K under a tropical atmosphere and using a rural model. The atmospheric transmittance is presented in light blue background, while water vapour and gas absorption is portrayed in grey. This graph assumes 100% of the pixels corresponding to objects are at the nominated temperature and that might be unrealistic for some flaming at 30 × 30 m pixels, but it may be realistic for smouldering pixels. The graph is not definitive—it gives suggestions as to where to observe peatland fires using remote sensing. 139

Figure 5.4. (**a**) Example of field picture taken from drone over burnt areas. The areas of interest were selected at homogenous pixels (>80–90% of pixel area of Landsat-8 was burnt area and smouldering peatland). Drone imaging was taken using Da-Jiang Innovations (DJI) Phantom Pro-4 on the same day with Landsat-8 acquisition (28 September 2018); (b) Picture of burnt area taken from the surface by digital camera in the burnt areas shown in Figure (a) at different orientation; (c) Example of smouldering peatlands taken by drone on 30 September 2018, two days after Landsat-8 acquisition time; (d) Picture of smouldering peatlands taken from surface in area of the smouldering peatlands in Figure (c) at different orientation; smoke shown from smouldering logs and surface peatlands; (e) Measurement of surface temperature on smouldering peatland using handheld IRtek IR150 dual-beam laser infrared thermometer; smouldering features below the peatland surface (to −20 cm) with smoke at the surface; (f) An example of peatland depth (1 m) consists of decaying roots and organic soil as the fuels for smouldering peatland; (g) Boxplots of smouldering (S) peatland and burnt area temperatures at the surface from 44 smouldering locations and 16 burnt area (BA) locations. 141

Figure 5.5. (**a**) Inset map of burnt area, smouldering and flaming area with area of interest (AOI) over Landsat-8 image; the AOI of burnt area and smouldering were selected based on drone image while flaming area based on obvious fire features on RGB Landsat-8 image (**b**) Profile of Top of Atmospheric (TOA) radiance of Landsat-8 bands for flaming, smouldering peatland, and burnt areas locations collected from ground truth data on 28 September 2018 to 1 October 2018. Smouldering locations were observed two days after Landsat-8 acquisition due to the longer proses of burning in smouldering peatlands. The Landsat-8 imagery was acquired on 28 September 2018 in Central Kalimantan (path/row of 118/62). Boxplots of band 10,

band-7, band-6 and ratio of band-7 to band-6 of Landsat-8 are presented. The ratio of band-7 to band-6 shows a potential index for separating combustion and non-combustion areas. F, S, and BA represent flaming, smouldering and burnt areas respectively. 144

Figure 5.6. Flowchart of general methods used for ToPeCAl-2 compared with ToPeCAl-1. Two methods were assessed, i.e., ToPeCAl-2 with contextual test and ToPeCAl-2 with cloud masking. F is flaming; FS is mix of flaming and smouldering; S is smouldering. TOA is top of atmosphere; ρ is reflectance; BT is brightness temperature; SWIR is ShortWave InfraRed; TIR is Thermal InfraRed..... 147

Figure 5.7. (**a**) Example of 764 Red-Green-Blue (RGB) image of Landsat-8 on 28 September 2018 and a 61 × 61 pixel window size with some fire features (in yellow to oranges tones) and background pixels with dominant objects, e.g., cloud (white), cloud shadow (black), soil/open land (brown), and vegetation (green); (**b**) The same RGB image as (**a**) overlaid with water/cloud shadow mask (blue) and obvious fire pixels (yellow) as per-previous studies (Giglio et al. 2008; Kumar & Roy 2018; Schroeder et al. 2016); saturated flaming pixels and permanent bright objects did not exist in this sample; (**c**) The same with (**b**) but with additional masks for cloud (light green) and candidate fire pixels (pink); (**d**) The histogram and population statistics of the ratio reflectance band-7 ($\rho_{2.2}$) to band-6 ($\rho_{1.6}$) and reflectance of band-7 of background pixels which excluded water/cloud shadow and unambiguous fire pixels as shown spatially in (**b**); (**e**) The histogram and population statistics of the same variable with (**d**) but with additional masks of cloud and candidate fire pixels. The ratio of band-7/band-6 and reflectance of band-7 data (**d**,**e**) do not follow a normal distribution according the Anderson-Darling goodness of fit statistic at confidence level of 99.7% (3σ), corresponding to a heterogeneous background, but data in (**e**) is more normal then (**d**). 152

Figure 5.8. Relative spectral response curve at aerosol-band, SWIR-1 and SWIR-2 bands of Sentinel-2A/2B and Landsat-8 Operational Land Imager (OLI). The data was accessed from https://landsat.gsfc.nasa.gov/preliminary-spectral-response-of-the-operational-land-imager-in-band-band-average-relative-spectral-response/ and https://earth.esa.int/documents/247904/685211/S2-SRF_COPE-GSEG-EOPG-TN-15-0007_3.0.xlsx. 155

Figure 5.12. (**a**) RGB image of Landsat-8 with SWIR-2 band as Red layer, SWIR-1 band as Green layer, and Red band as Blue layer. Landsat-8 was acquired on 28 September 2018 at 2:34 Universal Time Coordinated (UTC) over Central Kalimantan's peatland; the dark straight line below the fires features (light yellow) is a river canal; green is vegetation and reddish purple is burnt area; (**b**) The same RGB composite image with Figure (**a**), but for Sentinel-2, which was acquired nine minutes before Landsat-8; (**c**) Natural RGB composite of Sentinel-2 on the same data with Figure (**b**); (**d**) Peatland fires from ToPeCAl-2 with contextual test applied to Sentinel-2 image compared with ToPeCAl-1 fires from Landsat-8 overlaid on RGB image of Sentinel-2; (**e**) the same with Figure (**d**) but from ToPeCAl-2 with cloud mask; (**f**) Natural composite of PlanetScope image on 28 September 2018 at 2:47 UTC showing smoke emanating from fire areas (white square) in Figure (**e**)..... 166

Figure 5.13. **(a)** Peatland fire areas (±104 ha) presented in false colour composite for Sentinel-2 image on 28 September 2018 in Central Kalimantan. Light pink to yellow represented fire areas with bluish smoke emanating from fire areas; **(b)** ToPeCAl-2 fires with contextual test overlaid on RGB image of Sentinel-2 in the same area with Figure (a). The RFP and RFN pixels are adjacent to TP fires (red colour). In this data pairs of Sentinel-2 and Landsat-8, the RFP and RFN pixels were within geometric error (38 m) and propagation zones (12 m) which about 50

m from TP pixels (magenta square line); **(c)** As per Figure (b) but from ToPeCAl-2 with cloud mask; **(d)** PlanetScope image in natural colour composite showed smoke emanating from fires areas from in the same area and in three minutes after Sentinel-2's acquisition; **(e)** Surface peatland fires propagation in lateral (horizontal) direction according to (Usup et al. 2004) from field experiment in Central Kalimantan's peatland after ignition and during surface burning in the first stage; the propagation were also in depth spread in the next stage..... 167

Figure 6.1. Schemes of flaming and smouldering peatland fires (Hu et al. 2018) CC-BY-NC-ND..... 188

List of Equations

Equation 1.1. Soil/biomass drying, due to heating and evaporating process 7
Equation 1.2. Pyrolysis, for charcoal formation 7
Equation 1.3. Oxidation of char (oxidation of smouldering) 7
Equation 1.4. Oxidation of gas-phase (oxidation of flaming) 7
Equation 3.1. PC 67
Equation 3.2. FAR 67
Equation 3.3. POD 67
Equation 3.4. BIAS 68
Equation 5.1. $SICI_{\rho}$ 145
Equation 5.2. Aerosol band threshold on clear atmospheric conditions 145
Equation 5.3. Smouldering on clear atmospheric conditions 145
Equation 5.4. Mix of flaming and smouldering on clear atmospheric conditions 145
Equation 5.5. Flaming on clear atmospheric conditions 145
Equation 5.6. Flaming for close to saturated pixel of SWIR radiance on clear atmospheric conditions 145
Equation 5.7. $SICI_{\rho}$ 145
Equation 5.8. Aerosol band threshold on smoky/hazy atmosphere conditions 145
Equation 5.9. Smouldering on smoky/hazy atmosphere conditions 145
Equation 5.10. Mix of flaming and smouldering on smoky/hazy atmospheric conditions 145
Equation 5.11. Flaming on smoky/hazy atmospheric conditions 145
Equation 5.12. Flaming for close to saturated pixel of SWIR radiance on smoky/hazy atmospheric conditions 146
Equation 5.13.Water masking 148
Equation 5.14. Permanent bright object masking-1 149
Equation 5.15. Permanent bright object masking-2 149
Equation 5.16. Unambiguous fire pixels on clear sky or smoky/hazy atmosphere 149
Equation 5.17. Fire pixels at close to saturation for flaming pixel on clear sky or smoky/hazy atmosphere 150
Equation 5.18. Candidate fire pixels for FS pixels on clear sky or smoky/hazy atmosphere 150
Equation 5.19. Candidate fire pixels for smouldering pixels on clear sky or smoky/hazy atmosphere 150
Equation 5.20. Cloud masking 151
Equation 5.21. Contextual test for candidate fire pixels 153

Abbreviations

AHI	Advanced Himawari Imager
ALOS	Advanced Land Observing Satellite
ASTER	Advanced Spaceborne Thermal Emission and Reflection Radiometer
AVHRR	Advanced Very High Resolution Radiometer
BIG	Indonesian Geospatial Information Agency
BIRD	Bi spectral Infra-Red Detector
BIROS	Bi-Spectral Infrared Optical System
BNPB	National Indonesian Disaster Management Agency
BPBD	Local Disaster Management Agency for Province/District Level
BPS	Indonesian Bureau of Statistic
BT	Brightness Temperature
CDAG	Cloud Detection Algorithm Generation
CK	Central Kalimantan
CNES	National Centre for Space Studies
CO_2	Carbon dioxide
CO_2e	Carbon dioxide equivalent
CPC	Climate Prediction Center
DAAC	Distributed Active Archive Center
DEM	Digital Elevation Mode
DInSAR	Differential Interferometric Synthetic Aperture Radar
DLR	German Aerospace Center
DMI	Dipole Mode Index
DMSP-OLS	Defense Meteorological Satellite Program – Operational Linescan System
ENSO	El Nino and the Southern Oscillation
ESA	European Space Agency
ESRI	Environmental Systems Research Institute
ESRL	Earth System Research Laboratories
F	Flaming
FAR	False Alarm Ratio
FIREBIRD	Fire Recognition with Bi spectral Infra-Red Detector
FIRMS	Fire Information for Resource Management System
FN	False Negative
FP	False Positive
FPR	False Positive Rates
FS	Mix of flaming and smouldering
GHG	Green House Gasses
GIS	Geographic Information System
GOES	Geostationary Operational Environmental Satellite System
GOLI	Global Operational Land Imager
GPS	Global Positioning System
Gt	Gigaton
H_2O	Chemical formula for water
HFDI	Hyperspectral Fire Detection Index
HSRS	Hot Spot Recognition System
HypXIM	Hyperspectral X Imagery
ICE	Independent Commission Errors

IFN	Independent False Negative
IFP	Independent False Positive
IMCG	International Mire Conservation Group
IOD	Indian Ocean Dipole
IOE	Independent omission errors
IR	Infra Red
ISRO	Indian Space Research Organisation
JSS	Jambi-South Sumatera
LAADS	Level-1 Atmosphere Archive and Distribution System
LAPAN	Indonesian National Institute of Aeronautics and Space
LEO	Low Earth Orbit
LSTM	Land Surface Temperature Mission
LWIR	LongWave InfraRed
MIR	Middle InfraRed
MNDWI	Modified Normalised Difference Water Index
MoA	Indonesia Ministry of Agriculture
MODIS	Moderate Resolution Imaging Spectroradiometer
MODTRAN	MODerate resolution atmospheric TRANSmission
MSG-SEVIRI	Meteosat Second Generation-Spinning Enhanced Visible and InfraRed Imager
MSI	Multi Spectral Instrument
NASA	National Aeronautics and Space Administration
NDVI	Normalised Difference Vegetation Index
NDWI	Normalised Difference Water Index
NIR	Near InfraRed
NISAR	NASA-ISRO SAR Mission
NOAA	National Oceanic and Atmospheric Administration
O_2	Oxigen
OLI	Operational Land Imager
OLS	Ordinary Least Square
ONI	Oceanic Nino Index
PALSAR	Phased Array type L-band Synthetic Aperture Radar
PC	Percent Correct
POD	Probability of Detection
RFN	Related False Negative
RFP	Related False Positive
RGB	Red Green Blue
RPA	Remotely Piloted Aircraft
S	Smouldering
SAR	Synthetic Aperture Radar
SC	Scene Classification
Sen2COR	Sentinel-2 radiative transfer atmospheric correction code
SICI	ShortWave InfraRed Combustion Index
SICIρ	ShortWave InfraRed Combustion Index-reflectance based
SIPS	Science Investigator Processing System
SK	South Kalimantan
SLSTR	Sea and Land Surface Temperature Radiometer
SNPP	Suomi National Polar-orbiting Partnership
SPOT	Satellite Pour l'Observation de la Terre
SWIR	ShortWave InfraRed

SWIR-1	ShortWave InfraRed at 1.6 μm (band-6 of Landsat-8 OLI/TIRS; band-11 of Sentinel-2 MSI)
SWIR-2	ShortWave InfraRed at 2.2 μm (band-7 of Landsat-8 OLI/TIRS; band-12 of Sentinel-2 MSI)
TET-1	Technologie-Erprobungs-Träger-1 (Technology Experiment Carrier-1)
TIR	Thermal InfraRed
TIR-1	Thermal InfraRed at 10.9 μm (band-10 of Landsat-8 OLI/TIRS)
TIRS	Thermal InfraRed Sensor
TN	True Negative
TOA	Top of Atmosphere
ToPeCAl	Tropical Peatland Combustion Algorithm
ToPeCAl-1	ToPeCAl with SWIR and TIR
ToPeCAl-2	ToPeCAl without TIR
TP	True Positive
TROPOMI	Tropospheric Monitoring Instrument
UAV	Unpiloted Aerial Vehicle
USA	United States of America
USD	United States Dollar
USGS	the U.S. Geological Survey
UTC	Universal Time Coordinated
UTM	Universal Transverse Mercator
VIIRS	Visible Infrared Imaging Radiometer Suite
VIS	Visible
VNP03IMG	VIIRS/NPP Imagery Resolution Terrain-Corrected Geolocation 6-Min L1 Swath at 375 m spatial resolution
VNP14IMG	VIIRS (375 m) active fire product
WGS	World Geodetic System

Abstract

Globally, tropical peatlands occupy 441,025 km^2 with 47% existing in Indonesia and storing 57.4 Gt of carbon or 65% of the total global tropical peatlands carbon (Page, Rieley & Banks 2011; Rieley & Page 2016). In Indonesia, vast areas of peatlands have degraded because of changes in land use from peat swamp forest to agricultural/plantation, the drainage of peatlands and fire. The practice of land clearing in peatlands is mostly accomplished through slash-and-burn activities and causes peatland fire problems every year during the dry season. Indonesian government has committed to reduce 29% of carbon emissions by 2030 (Wijaya et al. 2017). To support this commitment, in this thesis, peatland fires detection prototypes based on remote sensing data, were built to enhance the current monitoring system. So far, the detection of fires based on satellite remote sensing mostly missed small and smouldering peatland. In this thesis, the moderate spatial resolution imageries at 20-30 m (Sentinel-2 and Landsat-8), were explored to detect peatland fires especially for small and smouldering fires, while the lower spatial resolution data from VIIRS 375 m, which produces daily global active fire data was optimised to represent peatland fire information.

The first research question raised the possibility of detecting flaming and smouldering peatland fires from moderate spatial resolution with ShortWave InfraRed (SWIR) and Thermal InfraRed (TIR) satellite imaging using daytime data. This question was answered by the development and application of the Tropical Peatland Combustion Algorithm (ToPeCAl). ToPeCAl was developed using the Landsat-8 Operational Land Imager (OLI)–Thermal InfraRed Sensor (TIRS) daytime data, acquired over Central Kalimantan peatland fires and then implemented over Riau (Sumatera) peatlands. Ground truthing was conducted using direct observation and drone imaging, as well as pictures taken from a helicopter by the Indonesian Disaster Management Agency. An overall accuracy of 82% – consisting of 100% accuracy for flaming, 96% for a mix of flaming and smouldering and 73% for smouldering peatlands – resulted from verification using 103 ground observations in the Central Kalimantan and Riau provinces. Some omission errors corresponding to small smouldering features occurred at mixed pixels and commission errors largely corresponded to bright objects.

The second research question was related to additional analysis for optimising the global active fire products from low spatial satellite sensors to support an efficient ground monitoring. This research question was answered by developing a new method to merge daytime and nighttime active fire data of the Visible Infrared Imaging Radiometer Suite (VIIRS) 375 m. Spatial clustering was achieved by applying a dissolved buffer of 375 m to the VIIRS point data. These techniques improved peatland fire detection by up to 90% more than a single instance of active fire data, which can only predict fire up to 70% accuracy.

The third research question raised the possibility of detecting peatland fires using only SWIR without TIR from a higher spatial resolution satellite than Landsat-8. This question was fulfilled by exploring the performance of ToPeCAl while only relying on SWIR – that is, without TIR from the medium spatial resolution image data. ToPeCAl without TIR was adjusted and tested on Landsat-8 OLI, then applied to Sentinel-2 Multi Spectral Instrument (MSI) to provide complementary peatland fire information at higher spatial and temporal resolutions than those observed from Landsat-8. An improved bright object masking was presented to minimise false detection on permanently bright objects. ToPeCAl without TIR was also developed with the improvement of a contextual test and cloud masking for the selection of candidate fire pixels. The results showed that ToPeCAl without TIR applied to Sentinel-2, with the contextual test, provided a probability of detections of 96% for flaming, 76% for the mix of flaming and smouldering and 35% for smouldering.

This thesis is presented as a "thesis by publication" which contains one peer-reviewed paper in an international conference proceeding and three peer-reviewed papers in journal publications. The significant contributions of this thesis within the field of fire detection using satellite remote sensing are the establishment of a new prototype, ToPeCAl, to monitor peatland fires in Indonesia using Landsat-8 and Sentinel-2, and the establishment of a new technique to optimise the global active fire product from VIIRS 375 m by multi-temporal analysis and spatial buffering. The development of the innovative techniques presented in this thesis provides a new contribution to satellite fire detection, particularly for the mapping of peatland fires with substantially more detail than existing satellite fire products. Additionally, where fires propagate at low speeds, which is the case for peatland fires, this thesis has demonstrated an improvement in accuracy for the existing VIIRS (375 m) product through multi-temporal analysis. These products will support an efficient

ground monitoring program for disaster management agencies in the prevention or reduction of peatland fires and their negative impacts on terrestrial and atmospheric environments.

Declaration

This thesis presents work carried out by myself and does not incorporate without acknowledgment any material previously submitted for a degree or diploma in any university; to the best of my knowledge it does not contain any materials previously published or written by another person except where due reference is made in the text; and all substantive contributions by others to the work presented, including jointly authored publications, are clearly acknowledged.



Parwati Sofan

15 April 2021

Acknowledgements

My first and foremost thanks go to my principal supervisor, David. The completion of this PhD would not be possible without your support, guidance and patience over the past three years and ten months. I thank you for all of the effort and time spent to guide me completing this thesis and publishing manuscripts. I have learnt so much from you throughout this PhD and I feel fortunate to have been provided with the opportunity to complete my doctoral degree under your supervision.

I am also thankful to Eriita for your guidance and support. Thank you for excellent supervision and for sharing your skill and knowledge. I won't forget the cards you gave to keep my spirit up. To Jackie from Landgate WA, thank you so much for supporting and sharing your expertise and experience in forest fires monitoring from satellite in Australia.

My PhD experience was enriched by the friendship of Ruchini, Abid, Du, Genine, Dang, Mark and also Alicia – thanks for sharing your experience in thesis submission by publication. To all friends in BJ2-53 office, Monita Wambrauw in MLK campus and admin staffs in the CE office, thank you for all your support and such unforgettable memories.

There are no words to express my gratitude to my husband, my love and life companion. Thanks for always giving your best for us. To my elder son, Satria– thank you and congratulations on completing your high school here, and to my youngest son Tama, it is so precious to see you enjoying your childhood here. Thanks to Indonesian friends especially to Khusaini-Melly's family for our wonderful times. This PhD journey would not be successful without the prayer of our parents and their unconditional support. Thanks to God for blessing our life in this paradise – South Australia for almost four years.

Finally, this thesis would not be possible without the generous funding from Research and Innovation in Science and Technology Project (RISET-Pro) of Ministry of Research and Technology/National Research and Innovation Agency of the Republic of Indonesia and thanks to my office the Remote Sensing Application Center of Indonesian National Institute of Aeronautics and Space (LAPAN), especially to Dr. Orbita Roswintiarti and Dr. Rokhis Khomarudin who encouraged me to study aboard – A choice I'd never regret. Alhamdulillah.

Publications

Sofan, P.; Bruce, D.; Jones, E.; Marsden, J. Detecting peatland combustion using shortwave and thermal infrared Landsat-8 data. In Advance Forest Fire Research; Imprensa da Universidade de Coimbra: Coimbra,Portugal, 2018; pp. 969–979. https://doi.org/10.14195/978-989-26-16-506_106.

Sofan, P.; Bruce, D.; Jones, E.; Marsden, J. Detection and Validation of Tropical Peatland Flaming and Smouldering Using Landsat-8 SWIR and TIRS Bands. Remote Sens. 2019, 11, 465. https://doi.org/10.3390/rs11040465.

Sofan, P.; Bruce, D.; Jones, E.; Schroeder, W; Marsden, J. Assessment of VIIRS 375 m Active Fire using Tropical Peatland Combustion Algorithm Applied to Landsat-8 over Indonesia's Peatlands. Int J Digit Earth. 2020. https://doi.org/10.1080/17538947.2020.1791268.

Sofan, P.; Bruce, D.; Jones, E.; Khomarudin, M.R.; Roswintiarti, O. Applying the Tropical Peatland Combustion Algorithm to Landsat-8 Operational Land Imager (OLI) and Sentinel-2 Multi Spectral Instrument (MSI) Imagery. Remote Sens. 2020, 12, 3958. https://doi.org/10.3390/rs12233958.

Chapter 1

An Introduction to Tropical Peatlands, Their Combustion and Monitoring from Space

An Introduction to Tropical Peatlands, Their Combustion and Monitoring from Space

To date, tropical peatland fires have been recognised as not only occurring in Southeast Asia, particularly in Indonesia–Malaysia, but also in Papua New Guinea, the Amazon River basin and the Congo River basin. In Indonesia, peatland fires occur every year in the dry season as a result of the agricultural practice of land clearing for plantation development, which is mostly accomplished through slash-and-burn activities. In extreme dry conditions, for example, in 1997, 2015 and 2019, peatland fires resulted in public health impacts across neighbouring countries with poor air conditions, affected the Indonesian economy and released huge amounts of carbon into the atmosphere. Peatland fires, together with agriculture, forestry and other land uses, are the main contributors (about 51%) to greenhouse gas emissions in Indonesia (Boer et al. 2018). To support the target of the Indonesian Government to reduce greenhouse gas emissions by 29% by 2030 (Wijaya et al. 2017), current efforts in peatlands combustion monitoring need to be strengthened. These include ground and space monitoring. Ground-based monitoring is not efficient in time or cost and does not provide adequate coverage in many areas. The existing global active fire products from space provide poor spatial resolution, have mainly been developed for global flaming fires and tend to omit smouldering combustion (e.g. peatlands) in their detection. Thus, this thesis presents new techniques using satellite imagery at moderate spatial resolution (20–30 m) for detecting peatland fires and enhances the lower spatial resolution global active fires product (375 m) by adding analysis of multi-time combinations of global active fire and spatial cluster buffer analysis. This will assist disaster management agencies in the suppression of peatland fires in a more efficient way and provide input for peatlands rehabilitation.

1.1. Peatlands: Their Origins and the Process Leading to Peat Combustion

1.1.1. Peatlands, Their Origin and Location

Peat is formed by the accumulation of organic materials over thousands of years, mostly from plants, that are deposited at higher rates than decomposition occurs, because of the lack of oxygen in water-saturated environments (Charman 2009; Holden 2006;

Page & Braid 2016; Rydin & Jeglum 2006; Vitt 2008). Rydin and Jeglum (2006) proposed that there are many thresholds used to define the minimum organic matter constituting peat, which vary from 20%–80% of dry weight. The minimum organic content has been defined as 30% (Vitt 2008), 50% (Charman 2009; Gumbricht et al. 2017) or 65% (Osaki et al. 2016a; Page, Rieley & Banks 2011). In general, peat-dominated landscapes are described as *peatlands*; these vary in depth, but most have a minimum depth of 30 cm (Charman 2009; Gumbricht et al. 2017; Page, Rieley & Banks 2011; Rydin & Jeglum 2006; Vitt 2008); peatlands can run as deep as 30–60 m in the Democratic Republic of Congo (Page, Rieley & Banks 2011).

Because of the requirement for water saturation, peatland location is strongly influenced by climate conditions (i.e. in a temperate, cold, wet climate and in humid tropical climates) but also by topographical conditions, especially on flat land areas (Joosten & Clarke 2002; Schumann & Joosten 2008). In reference to the Global Peatland Database of the International Mire Conservation Group, Rydin and Jeglum (2006) and Joosten (2004) stated that peatlands occupy 3% (≈ 4 million km^2) of the global land area. Most peatland areas of at least 30 cm peat thickness are in the north at mid to high latitudes (~85%), while the remainder are in the southern temperate or cold climates (less than 1%), and in the intertropical regions (~15–20%) (Rydin & Jeglum 2006). In the northern hemisphere, most peatlands are located in Russia, North America and Europe, in areas with low relief, poor drainage, high precipitation and low temperatures, and are mostly formed from the remains of mosses, grasses, sedges, shrubs and even trees (Page & Baird 2016). Many peatlands in the southern temperate or cold climates are in the Falklands Islands, Chile, Argentina, New Zealand, Australia and Antarctica (Rydin & Jeglum 2006).

The tropical peatland areas (≈ 441,025 km^2) are mainly located in the coastal lowlands of Southeast Asia – especially in Indonesia, Malaysia and Papua New Guinea – and in the Amazon basin of South America, the Congo River basin of Africa, mainland East Asia, the Caribbean and Central America, other Asian countries, Australia and the Pacific regions – regions that experience high precipitation and high temperatures (Rieley & Page 2016). Forty-seven per cent (≈ 206,950 km^2) of tropical peatlands exist in Indonesia. These were formed as spacious domes that are the remains of rainforest trees (branches, leaves, roots and trunks), sustaining the peat swamp forest that encompasses large areas of lowland landscape between major rivers (Page, Rieley & Banks 2011;

Rieley & Page 2016). Under the definition of a minimum soil organic matter of 65%, the Indonesian Ministry of Agriculture (MoA) estimated the peatlands distribution in Indonesia as follows: Sumatera (43% ≈ 6.4 million ha), Kalimantan (32% ≈ 4.7 million ha) and Papua (25% ≈ 3.7 ha) (Ritung, Wahyunto & Nugroho 2012). The peatlands distribution in Indonesia is shown in Figure1.1.

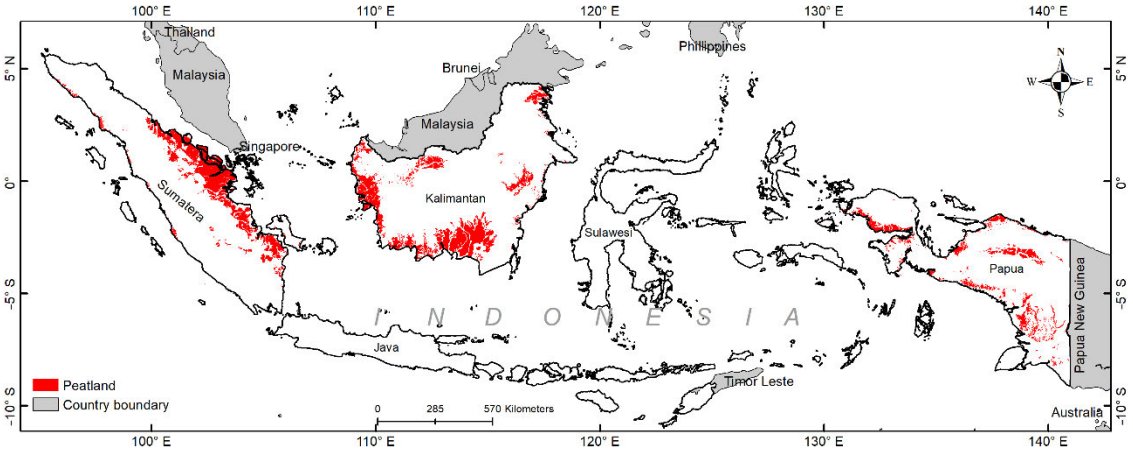


Figure 1.1. Peatlands distribution in Indonesia. Peatland data (2011) from the Indonesian MoA overlaid on a world map of SE Asia.

1.1.2. Importance and Condition of the Peatlands

As one of the Earth's ecosystems, peatlands are important for biodiversity, water control and carbon storage (Joosten, Tapio-Biström & Tol 2012). Peatlands enable biodiversity conservation for both plants and animals. In Indonesia, Widjaja et al. (2011) found at least 5,575 high tree species, 71 lichen species, 376 species of moss, 235 species of fungi among others in Kalimantan alone. Peatland habitats attract fauna (terrestrial and aquatic) that gravitate to the resources they offer. Peatlands act as water control mechanisms, for example, for reducing storm flow and maintaining river flow and water reservoirs under natural conditions at about 95% high groundwater levels, which could decrease to 25% under degraded conditions (Wösten et al. 2008; Osaki et al. 2016b). Although peatlands occupy only 3% of the world's land area, they store around 33% of the world's soil carbon and more than half of the carbon of the Earth's atmosphere. In other words, peatlands are an essential component for global carbon storage and circulation. The undisturbed tropical peatland forests make a significant contribution to terrestrial carbon storage and, therefore, their sustainability has important implications for climate change (Rydin & Jeglum 2006; Page et al. 2002). Page, Rieley and Banks

(2011) estimated the carbon storage in the tropical peatlands of Indonesia to be about 57.4 Gt (65% of the total global tropical peatlands carbon).

To date, 20–25% of the peatlands on Earth have been damaged through the anthropogenic activities of agriculture, forestry and peat extraction (Joosten & Clarke 2002; Rydin & Jeglum 2006). About 50% of damaged peatland areas have been used for agriculture with the main examples occurring in Russia, Germany, Belarus, Poland, Ukraine, Indonesia, the US, Malaysia, China and Canada. Drainage for forestry in peatlands (~30% of damaged peatlands) also happens predominantly in Finland, Russia, Sweden, Latvia, Estonia, the UK, North America and Southeast Asia. Peat extraction mainly exists in non-tropical areas (~10% of damaged peatlands); this extraction is used for horticulture, agriculture, domestic heating and energy generation (Joosten & Clarke 2002; Rydin & Jeglum 2006). Peatland fires, resulting from slash-and-burn activities, have been recorded in tropical areas, such as Indonesia (Osaki et al. 2016a; Tacconi 2003), Malaysia (Smith et al. 2018; Cole et al. 2019), Papua New Guinea (Jenner 2018), the Amazon River basin (van Marle et al. 2017; Read 2019; Bowman 2020) and the Congo River basin (Nasi 2019; Hird 2019).

In Indonesia, agricultural expansion was initially triggered under the Indonesian Government's policy of transmigrating people from the more densely populated islands of Java, Bali and Madura to Sumatera and Kalimantan in the 1980s and significantly increased when plantation companies used peatland areas for expansion purposes (Miettinen & Liew 2010; Page et al. 2002; Suyanto et al. 2004; Tacconi 2003). Fires have been utilised for land clearance and farming preparation by smallholder farmers and by plantation companies for many years (Usup et al. 2004; Dennis et al. 2005; Miettinen, Shi & Liew 2011; Osaki et al. 2016b; Purnomo et al. 2017). In general, peatland combustions in Indonesia have anthropogenic origins (Bowen et al. 2000; Usup et al. 2004; Dennis et al. 2005; Purnomo et al. 2017). However, extreme drought, arising from warm episodes of El Niño Southern Oscillation and positive modes of Indian Ocean Dipole, also contributed to the large peatland fires in Indonesia in 1997, 2009, 2015 and 2019 (Page et al. 2009; Pan et al. 2018; Alsepan & Minobe 2020). Indonesian megafires, consisting of many smouldering peatland episodes, released around 2.57 Gt of CO_2e in 1997 (Page et al. 2002), 1.75 Gt of CO_2e in 2015 (World-Bank 2016) and 0.72 Gt of CO_2e in 2019 (Reuters 2019). In the 2015 Paris agreement, Indonesia committed to reducing 29% of its greenhouse gases (GHG) emissions by 2030 (Wijaya et al. 2017). Peatland fires, together

with agriculture, forestry and other land use, contribute to 51% of GHG emissions in Indonesia (Boer et al. 2018).

The degraded peatlands in Indonesia have resulted from a series of landscape changes, including tree clearing, through slashing and moisture reduction from canal construction, which leads to the draining and desiccation of the peatlands. These processes, particularly the latter, are accentuated during the dry season (Cochrane 2003; Field, Van Der Werf & Shen 2009; Miettinen et al. 2012; Miettinen, Shi & Liew 2011; Rieley & Page 2016; Siegert et al. 2001). Dry peatland is very prone to fire and the drying process leads to the frequent and repeated application of fire to further reduce the biomass for land clearing (Osaki et al. 2016b; Hoscilo et al. 2011). Figure 1.2 shows examples of the natural ecosystems of peat swamp forest in Indonesia and a degraded peatland with canals in plantation areas.



Figure 1.2. (a) Natural peatland forest in Kalimantan (Sugardiman 2005); (b) peatland drainage canals in plantation areas. Picture (b) was taken during a ground truth collection in Central Kalimantan on 28 September 2018.

1.1.3. The Process Leading to Peatland Combustion

Most peatland fires in Indonesia start in slashed areas as land-clearing activities; then, the fire spreads out of control into secondary forest (Bowen et al. 2000; Usup et al. 2004; Dennis et al. 2005; Miettinen & Liew 2009; Miettinen, Shi & Liew 2011). Peatland is the most significant fire-affected soil/organic matter ecosystem and it is easier to ignite in dry conditions than wet ones (Rein 2016; Rein et al. 2008; Rein 2013; Zaccone et al. 2014). According to Rein (2013; 2016) and Santoso et al. (2019), the peatland combustion process, in general, consists of two important chemical pathways: pyrolysis and oxidation. The combustion process is given in by Equations (1.1–1.4). At first,

soil/biomass drying is performed by heating and evaporation (Equation (1.1)); it then continues to pyrolysis, producing char, gas and ash (Equation (1.2)). After that, oxidation occurs, either in char (the solid phase) as smouldering (Equation (1.3)) or in the gas phase as flaming (Equation (1.4)).

- Soil/biomass drying, as a consequence of the heating and evaporating process:

$$Organic\ Soil/Biomass + Water \xrightarrow{heat} Organic\ Soil/Biomass + Water\ vapour \quad \textbf{(1.1)}$$

- Pyrolysis for charcoal formation:

$$Organic\ Soil/Biomass \xrightarrow{heat} Char + pyrolysate\ (gas) + Ash \quad \textbf{(1.2)}$$

- Oxidation of char (oxidation of smouldering):

$$Char + O_2 \rightarrow Heat + CO_2 + H_2O + other\ gases + Particulate\ Matter + Ash \quad \textbf{(1.3)}$$

- Oxidation of gas phase (oxidation of flaming):

$$Pyrolysate\ (gas) + O_2 \rightarrow Heat + CO_2 + H_2O + other\ gases + Particulate\ Matter \quad \textbf{(1.4)}$$

Once the peat has ignited, smouldering combustion dominates the flaming combustion (Rein 2013; 2016); however, when the oxygen supply increases, as occurs with an increase in wind velocity, combustion becomes faster, temperature increases and a flaming state may eventuate (Rein 2013; 2016). This process entails a transition from smouldering to flaming. Flaming and smouldering combustion can each lead to the other (Rein 2016). Smouldering combustion spreads horizontally in surface peat (0–20 cm) and vertically to deeper peat (20–50 cm). Horizontal combustion propagation in surface peatland is potentially supported by the oxygen supply from increased wind, while vertical spread depends on moisture content and ground water level (Usup et al. 2004; Takahashi 2002; Santoso et al. 2019; Rein 2013; Huang & Rein 2017). These typical propagations are volumetric and transfer limited energy with a low speed potentially for long periods of up to weeks. Smouldering can consume two orders of magnitude (100 times) more of the total biomass than flaming (Rein 2013). Bertschi et al. (2003) and Davies et al. (2013) found that about 50% of burnt biomass during wildfires is related to smouldering fires. In general, smouldering occurs with lower temperatures, spread rates and combustion power than flaming (Rein 2016). A low radiant heat can lead to

smouldering ignition for many fuel types, but smouldering ignition is harder to achieve for trees and twigs (Lin, Sun & Huang 2019).

Meanwhile, flaming only occurs at the surface with higher radiant energy and usually over short time periods (± 15 minutes) and it depends on an oxygen supply for oxidation (Rein 2013). At the surface, flaming combustion spreads vertically and relatively rapidly, covering surface fuels and forest crowns. Over relatively short periods, flaming may not harm soil and flora/fauna, but smouldering, which occurs for much longer periods. may cause harm to soil properties and biological systems (Doerr & Cerda' 2005; Rein et al. 2013, Hu et al. 2018). The transition from flaming to smouldering can occur and become the persistent smouldering of biomass, which is found in thick fuel (trees, branches/logs) and organic soil matter after flaming wildfire has passed – this is termed residual smouldering combustion (Rein 2016; Rabelo et al. 2004; Bertschi et al. 2003; Urbanski 2014). As given in Equations (1.1–1.3), smouldering transforms organic soil/biomass into char then releases heat and produces ash with other gases and particulate matter. The state of the ash can be observed from its visual properties, but heat released from the smouldering can be measured by temperature. Gases and particulate matter are characterised by smoke as a result of incomplete combustion (Hu et al. 2018). Flaming also produces smoke; however, gas emissions from smouldering are six times higher than those from flaming (Koppmann et al. 2005; Rein et al. 2009; Wiggins et al. 2018) and the smoke particle size from smouldering is also greater (> 3 times) than that from flaming (Reid et al. 2005).

Some visual evidence from the real situation in Central Kalimantan's peatland fires during a field survey from 28 September to 5 October 2018 is given in Figure 1.3. Figure 1.3a shows evidence of smouldering consuming peat soil. Little smoke is evident from the peatland surface as the extinguishment had successfully been undertaken by firefighters. Figure 1.3b shows residual smouldering combustion in logs with smoke and ash in slashed and burnt areas. Figure 1.3c shows smouldering in half-dead shrub areas with ash and smoke. Dispersed white smoke from smouldering peatland covers the area in Figure 1.3d and 1.3e, which were taken near the surface and above the surface, respectively. Flaming and smouldering peatlands were imaged from a drone in Figure 1.3f. White smoke is evident over the burn area behind the flaming front areas, while

darker smoke emanates from the flaming area. These signatures of smouldering and flaming smoke are like the smoke scheme illustrated by Hu et al. (2018).



Figure 1.3. (a) Evidence of smouldering fire on peat soil to about one metre's depth; (b) Smouldering log in slashed and burnt area; the brown, half-dead trees shown at the back of logs are the result of flaming; (c) Ash and smoke in the peat surface with half-dead shrubs; (d) Field observation in smouldering peatland areas with dispersed smoke near the ground; most of the surface is covered by ash and char with some half-dead (brown) and green vegetation shown in the picture; (e) Smouldering peatland covered by dispersed smoke; (f) Flaming peatland (orange features) with darker smoke emanating from flaming areas; the smouldering areas with white smoke are shown to the back of the flaming front. Figure (d), (e) and (f) were taken from a drone.

In relation to heat measurement from peatland combustion, previous studies have collected field measurements on smouldering temperatures from peatland surfaces in Central Kalimantan. Usup et al. (2004) observed smouldering ignition temperatures of 548–573 K, while Hayasaka et al. (2016) found the average smouldering surface temperature to be 400 K. Elvidge et al. (2015) collected background temperatures (in non-combustion peat soil) from 290–360 K, in smouldering peat soil from 360–500 K, in smouldering wood close to flaming from 500–700 K and in open flames and glowing embers from 700–1,000 K. Figure 1.4 (Elvidge et al. 2015) illustrates that the field temperatures in Kalimantan exhibited a marked separation between flaming and smouldering peatlands. However, background and smouldering temperatures showed less separability, especially in the initial phases of smouldering. Warmer background temperatures can be caused from solar heating in peatlands, particularly in the summer season and during daytime (Elvidge et al. 2015).

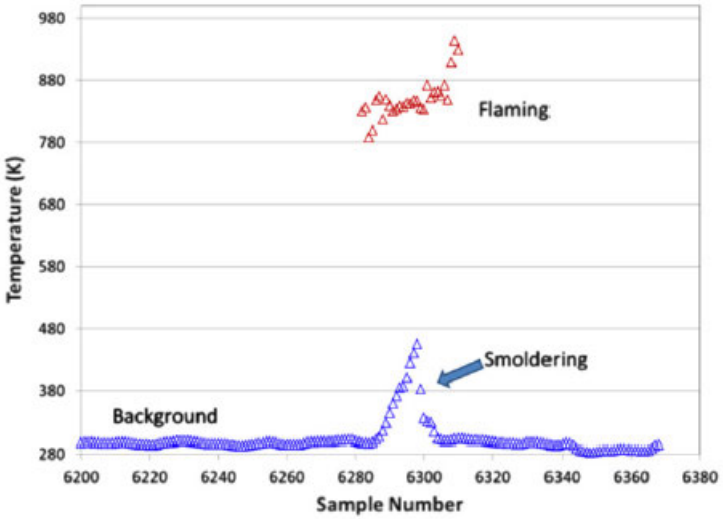


Figure 1.4. Field temperature of the background, smouldering and flaming peatlands in Kalimantan. The temperature was measure by a CEM Instrument DT-9862 Professional Infrared Video Thermometer, which has a dynamic range spanning 215–2373 K (Elvidge et al. 2015) CC BY.

1.2. Peatlands Combustion/Fire Monitoring from Space

In this thesis, another term used for combustion is *fire*. The terms *peatland combustion* and *peatland fire* are synonymous in this thesis.

1.2.1. Principle Physics for Fire Detection from Remote Sensing

Planck's Law is the principle that describes the emission of spectral radiance that leaves a black body at a given temperature. As the temperature of an object increases, there is a shift of the wavelength of peak radiant emission to shorter wavelengths; this feature, explained in Wien's Displacement Law, is derived from Planck's Law. Figure 1.5 demonstrates this principle further by combining the spectral radiance simulation of ground targets with atmospheric scattering and absorption using the MODerate resolution atmospheric TRANSmission (MODTRAN-5) model under a tropical atmosphere and a rural model. The ground albedo of 0.1 for peatland rainforest with limited vegetation (Caiazzo et al. 2014) at different temperatures ranging from background temperature (300 K) to flaming biomass temperature (1000 K) were set with a visibility of 3 km for hazy conditions; visibilities in the range of 2–10 km are classified as hazy conditions in MODTRAN. In Figure 1.5, the atmospheric water vapour and gas absorption are shown in grey, while the light blue areas show a transparent atmosphere for biosphere remote sensing operations.

In the ShortWave InfraRed (SWIR) at 1.5–1.7 µm, flaming objects from 700–1000 K exhibited a high radiance, while smouldering objects in the range of 360–500 K tended to have the same pattern as the background temperature (300 K). The spectral radiance showed a peak in the SWIR region (2.1–2.3 µm) for flaming combustion. Smouldering with temperatures of greater than 360 K to 500 K resulted in a higher radiance than background objects at 2.1–2.3 µm, which clearly rose when temperatures increased to 500 K and from 500–700 K for smouldering close to flaming. In the Middle InfraRed (MIR), at about 3.5–4.0 µm, the presence of flaming (700–1000 K), smouldering close to flaming (500–700 K) and smouldering (360–500 K) was significantly higher than in SWIR and showed good separation from the background temperature (300 K). The presence of cool fires can also be observed in LongWave InfraRed or Thermal InfraRed (TIR), which shows higher radiance than in SWIR. There is a potential for the detection of peatland fires using SWIR, MIR and TIR. However, reflected solar energy in SWIR may infer the detection of flaming at daytime, while the background temperature may affect the detection of cool fire in TIR (Wooster et al. 2013).

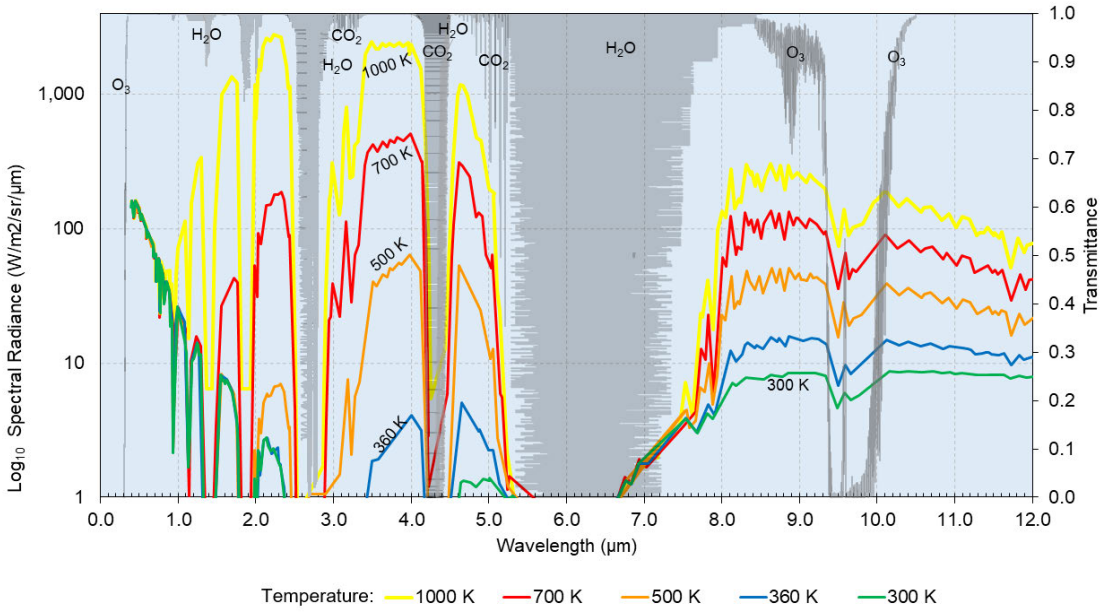


Figure 1.5. Top of atmosphere (TOA) spectral radiance simulated using MODTRAN with ground object temperatures at 300 K, 360 K, 500 K, 700 K and 1000 K for a ground target with an albedo of 0.1 (for peatland with limited vegetation) under a rural and tropical atmosphere. The atmospheric transmittance is presented in a light blue background, while water vapour and gas absorption are in grey.

1.2.2. Space-based Sensor Capability for Fire Detection

Satellite remote sensing technology has provided global combustion monitoring since the 1990s (Arino, Melinotte & Calabresi 1993; Justice at al. 1996; Giglio, Kendall & Justice 1999; Kaufman et al. 1998; Baum & Trepte 1999; Justice & Korontzi 2001). The technology has some advantages especially for spatial and temporal capabilities in contrast to terrestrial, aerial and sea observation. It is potentially more efficient to monitor large areas at a single time of observation; thus, it is likely more effective in time and cost. Thermal sensors on satellite platforms can be used to detect combustion and are able to provide forest/land combustion information on a regular basis, from ten minutes, to half a day and up to every 16 days (Wickramasinghe et al. 2016; Elvidge et al. 2001; Giglio, Schroeder & Justice 2016; Schroeder et al. 2016).

Besides these advantages, remote sensing satellite data have some disadvantages for forest/land combustion monitoring. These include the following:

- Each satellite sensor has a thermal saturation point where increases in object temperature are no longer detected. In some sensors, this affects the differentiation of hot temperature sources. For example, a sensor which has high temperature saturation

at 900 K can detect hotter fires (flaming) than others sensor which only have saturation temperatures around 360 K.

- Even though some sensors on board satellites provide a high temporal resolution, their spatial resolution is extremely coarse. High temporal resolution used in peatland fire monitoring is at least once daily.
- In tropical areas, cloud cover is the main problem that can obscure the detection of fire. The use of multi-temporal imagery may improve the likelihood of cloud-free observation.
- Some optical sensors with thermal infrared which only acquire data in the daytime can monitor fire, but sensors with thermal capability of nighttime observations are generally better because of the higher contrast between non-combusting and combusting materials.

Table 1.1 shows a list of the remote sensing sensors with infrared (IR) detectors that are potentially suitable for combustion monitoring at low spatial (> 100 m) and medium spatial (20–100 m) resolutions. A sensor that has a minimum revisit time of twice daily will be under strong consideration for daily peatland fires monitoring; thus, sensors, such as the Geostationary Operational Environmental Satellite System (GOES), the Meteosat Second Generation-Spinning Enhanced Visible and InfraRed Imager (MSG-SEVIRI), the Defense Meteorological Satellite Program–Operational Linescan System (DMSP–OLS), the Himawari-8/Advanced Himawari Imager (AHI), the Advanced Very High Resolution Radiometer (AVHRR), the Moderate Resolution Imaging Spectroradiometer (MODIS), the Sentinel3-Sea and Land Surface Temperature Radiometer (SLSTR) and the VIIRS, are within scope. Meanwhile, the experimental satellites, the Hot Spot Recognition System–Bi-spectral Infrared Detector (HSRS-BIRD) and the Technology Experiment Carrier-1 (TET-1), have high temperature saturations with temporal resolutions of two to three days. Medium spatial resolution data—for example, the Landsat-8 OLI/TIRS and the Advanced Spaceborne Thermal Emission and Reflection Radiometer (ASTER)—also have the capability to detect combustion at a better spatial resolution at 16 days temporal resolution.

Table 1.1. List of current optical remote sensing sensors with infrared properties commonly used for combustion monitoring.

Sensor	Spatial resolution (m)	Revisit time	IR band width (μm)	Day/Night time acquisition	Temperature saturation (K)	Reference
GOES	4,000	30 minutes	3.80–4.00 10.2–11.2 11.5–12.5	Day–Night	335 342	Xu et al. 2010
MSG-SEVIRI	3,000–4,000	15 minutes	3.48–4.36 11.00–13.00	Day–Night	335 335	Sifakis et al. 2011
DMSP-OLS	2,700	2/day	10.5–12.5	Day–Night	310	Fuller and Fulk 2000; Fuller 2000
AHI	2,000	10 minutes	3.74–3.96 10.3–10.6 11.1–11.3 12.2–12.5 13.2–13.4	Day–Night	400 330 330 330 300	Hally 2016; Wickramasinghe et al. 2016
AVHRR	1,100	2/day	3.55–3.93 10.3–11.3 11.5–12.5	Day–Night	325	Fuller and Fulk 2000; Fuller 2000
MODIS	1,000	4/day (Terra & Aqua)	3.929–3.989 10.780–11.280	Day–Night	500, 400	Giglio et al. 2003; Giglio, Schroeder and Justice 2016
Sentinel3-SLSTR	1,000	1–2 days	3.74 10.85 (central wavelength)	Day–Night	500 400	Calle and Salvador 2013; Wooster, Xu and Nightingale 2012
VIIRS	375 (I-band) 750 (M-band)	2/day	3.55–3.93 10.5–12.4 3.97–4.13 10.26–11.26	Day–Night	367 380 634 363	Csiszar et al. 2014; Elvidge et al. 2013; Schroeder et al. 2014
HSRS-BIRD	370	2–3 days	3.4–4.2 8.5–9.3	Day	650	Siegert et al. 2004
TET-1	160	2–3 days	3.4–4.2 8.5–9.3	Day	900	Atwood et al. 2014
Landsat-8-OLI and TIRS	30 100	16 days	2.11–2.29 10.60–11.19 11.50–12.51	Day, Nighttime on demand	 360 360	Elvidge et al. 2015; Irons, Dwyer and Barsi 2012
ASTER	30 90	16 days, on demand	1.60–2.43 8.12–11.65	Day, Nighttime on demand	739–599 370	Eckmann, Robert and Still 2009; Giglio et al. 2008

1.2.3. Space-based Methods for Fire Detection

1.2.3.1. Low Spatial, High Temporal Resolution Data

In this thesis, the term “low spatial and high temporal resolution” is associated with data from optical sensors that have a pixel size at equal or greater than 375 m and a revisit times of at least two times per-day.

The first combustion detection algorithm for measuring the spectral radiant temperature and sub-pixel hotspots was developed by Dozier (1981), utilising the 3.7 μm (MIR) and 11 μm (TIR) spectral bands of AVHRR. This method was only suitable for stable conditions with homogeneous temperatures and was difficult to implement over time with varying atmospheric conditions and local geographical characteristics (Arino, Melinotte & Calabresi 1993; Baum & Trepte 1999; Wooster et al. 2013). However, using AVHRR data, a contextual approach was developed to overcome this fixed threshold limitation. The contextual approach consisted of pathways—that is, the detection of potential fire pixels, the detection of the pixel containing the fire and the testing of the fire pixel against the background pixels (Justice at al. 1996; Giglio, Kendall & Justice 1999; Kaufman et al. 1998). The fixed threshold and contextual methods were integrated and implemented in the MODIS fire product with some improvements related to sensor specifications (Justice et al. 2002; Giglio, Schroeder & Justice 2016).

The fire algorithms that combine fixed threshold and contextual methods have been adopted and modified in the analysis of other sensor data as a consequence of the specific spectral channel, the temperature saturation and the spatial resolution of each sensor—that is, GOES (Xu et al. 2010), Meteosat-SEVIRI (Robert & Wooster 2008), Sentinel-3-SLSTR (Wooster, Xu & Nightingale 2012), VIIRS (Schroeder et al. 2014) and AHI (Wickramasinghe et al. 2016). The implementation of contextual methods in detecting fire by thermal remote sensing depends on the temperature at which saturation occurs on the sensor and the image quality following cloud cover and sun glint. Some products apply masks, including land/sea, cloud cover and sun glint, before processing for fire detection (Wooster et al. 2013).

1.2.3.2. Medium Spatial, Low Temporal Resolution Data

The term “medium spatial and low temporal resolution”, in this thesis, is associated with optical sensors that have a pixel sizes equal or smaller than 100 m for the spatial resolution and a revisit times smaller than 16 days.

ASTER and Landsat-8 OLI-TIRS have 30 m and 90–100 m resolutions when detecting fire from SWIR and TIR channels, respectively. Giglio et al. (2008) used the contextual fire detection method in ASTER and selected the 2.33 μm (SWIR) for fire detection and the 0.82 μm (NIR) for non-fire pixel detection. Fire pixels from ASTER can be detected for a minimum 4 m^2 at a 900 K temperature (Giglio et al. 2008).

Further, Schroeder et al. (2016) and Kumar and Roy (2018) implemented the contextual methods by using SWIR and NIR reflectance for global fire detection, while Murphy et al. (2016) used the fixed threshold of SWIR reflectance for a global hot target from Landsat-8 data. Kumar and Roy (2018) compared their algorithm with those of Schroeder et al. (2016) and Murphy et al. (2016) and found a low detection of Indonesian peatland fires for all three algorithms.

Meanwhile, Elvidge et al. (2015) found that it was possible to use TIR as well as SWIR for the nighttime data of Landsat-8 to distinguish smouldering from flaming combustion in the tropical peatland. However, the nighttime data from Landsat-8 is not available on a regular basis. Other than Landsat-8, there is Sentinel-2, which is available at no cost every five days in tropical regions. Sentinel-2 has similar spectral capabilities in a higher spatial resolution (20 m) than Landsat-8 but without TIR. Most fire-related Sentinel-2 applications were developed for burnt-area mapping (Roy et al. 2019; Quintano et al. 2018; Fiona et al. 2020).

1.2.3.3. Smallsatellite

The German Aerospace Center (DLR) developed BIRD, TET-1 and the bi-spectral infrared optical system (BIROS) sensors especially for fire detection in low Earth orbit (LEO) at approximately 500–572 km. BIRD was terminated in 2008. Following the BIRD mission, DLR launched a small constellation of satellites known as Fire Recognition with bi-spectral infrared detectors (FireBIRD), namely, the TET-1 and BIROS, in 2012 and 2015, respectively (Hellmann & Rathgeber 2015; Lorenz 2013). The contextual method for fire detection was also implemented in the BIRD-HSRS with some modifications because of its fine spatial resolution (370 m), specific spectral channels, temperature saturation (up to 500 K) and co-registration (Zhukov et al. 2006). Siegert et al. (2004) explored the use of BIRD to detect tropical peatland fires in Central Kalimantan and found that the MIR and TIR channels were able to determine smouldering and flaming combustions. Meanwhile, TET-1 with MIR was able to detect fire through smoke/haze as a result of its temperature saturation at 900 K and demonstrated fire dynamic propagation at a 160 m spatial resolution (Atwood et al. 2016). The contextual algorithm using TET-1 implemented by Mitchell et al. (2016) was used for the detection of fire areas and temperature estimation. Although this small satellite family presents a detailed view of fires with fine resolution and high temperature saturation, the swath width of

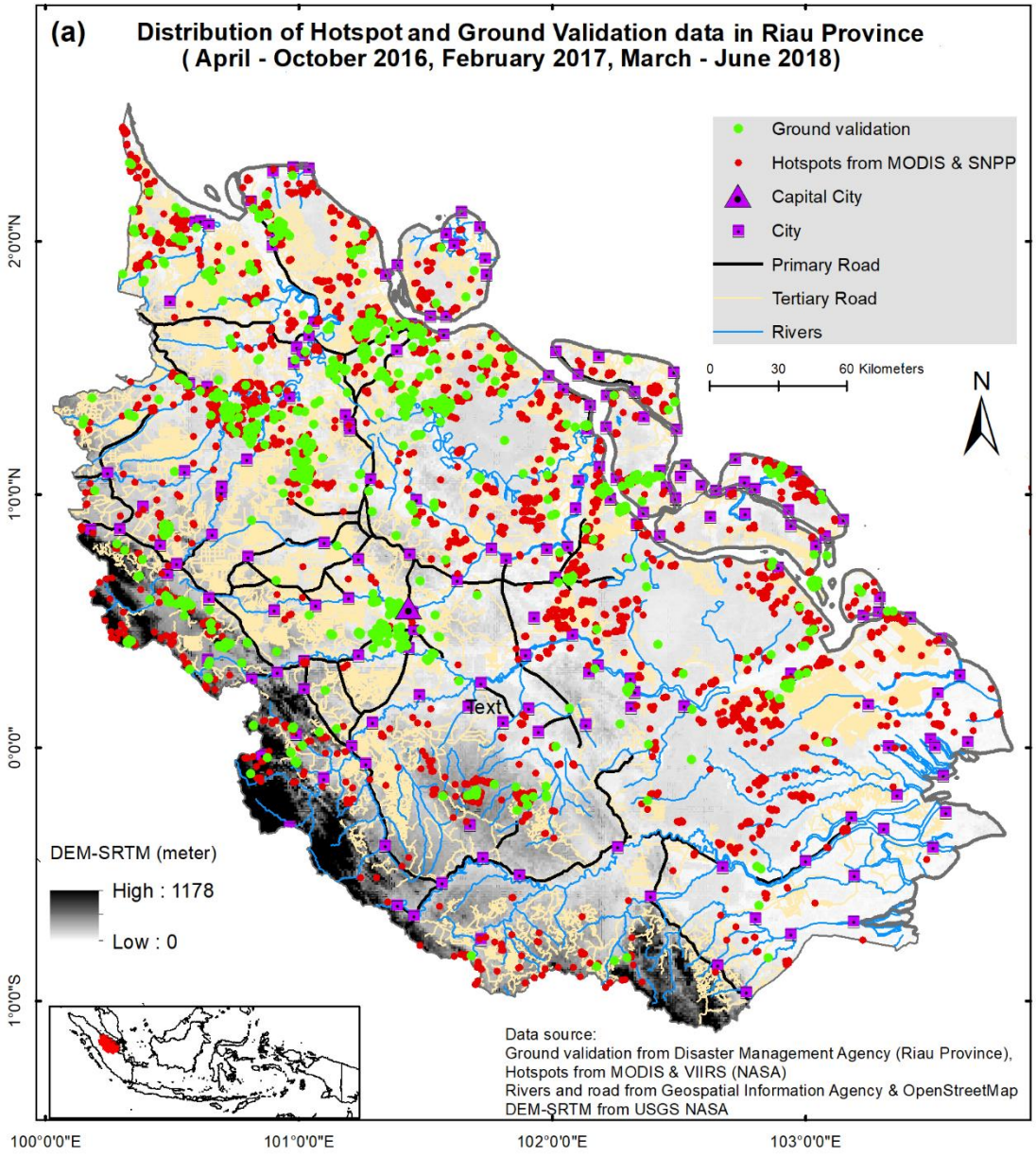
these sensors is so small that only a limited area may be captured and acquisitions need to be requested from the data provider.

1.3. Summary of the Challenges in Operational Peatland Combustion Monitoring

The daily monitoring of Indonesian peatland combustion is undertaken by the local Disaster Mitigation Agency (BPBD) and other related institutions with observations from the air (usually helicopter), the ground (by car and motorcycle) and the rivers and canals (by motor boat) to inspect combustion occurrences in remote areas. To date, the BPBD guidance for active fires data is only from MODIS Terra/Aqua satellites, VIIRS from the Suomi National Polar-orbiting Partnership (S-NPP) and the National Oceanic and Atmospheric Administration/NOAA-20 satellites. Figure 1.6 shows ground validation distribution conducted by BPBD over certain periods of active fires/hotspots (confidence level ≥ 80%); the data are from MODIS and VIIRS in the Central Kalimantan and Riau provinces. Hotspot distribution from satellite-located fires was not only close to settlement areas (cities) or roads, but also in remote areas, surrounding river canals. Meanwhile, the ground validation distribution was not aligned with the hotspot distribution, especially for some of the hotspots located in remote areas; this pattern may be attributed to limited resources and inaccessible locations. The level of risk to humans from fires could also be a factor influencing this pattern, for example, during the mega peatfires in Central Kalimantan in 2015, many hotspots were recorded with limited ground validations, as shown in Figure 1.6b.

Moreover, there are time gaps between satellite data acquisition, data processing, information delivery and action in the field. BPBD performs routine monitoring starting in the morning and uses active fire information that was recorded at night as its first reference. These time gaps may affect the ability of fire suppression tactics in the field to predict fire behaviour. BPBD reported that most fire locations were in remote areas. They also found some false detections of active fires, for which bright rooftops, open/bare land, burnt areas and gas flares in the oil–gas industry were mistaken for each other. In addition, BPBD requires information on small fires, either flaming or smouldering, which may remain undetected with lower spatial resolution sensors. Small fire information is needed to suppress the fire before it extends to a large area and becomes uncontrollable. Detailed spatial information related to flaming and smouldering areas is also required for

establishing a strategy and priorities for extinguishment (Personal communication with BPBD of Central Kalimantan staffs on 27 September 2018). A strategy for understanding and utilising space-based fire information is needed to better manage the ground monitoring of peatland fires with the optimal utilisation of resources (time and cost) in the surveillance of large areas of peatlands.



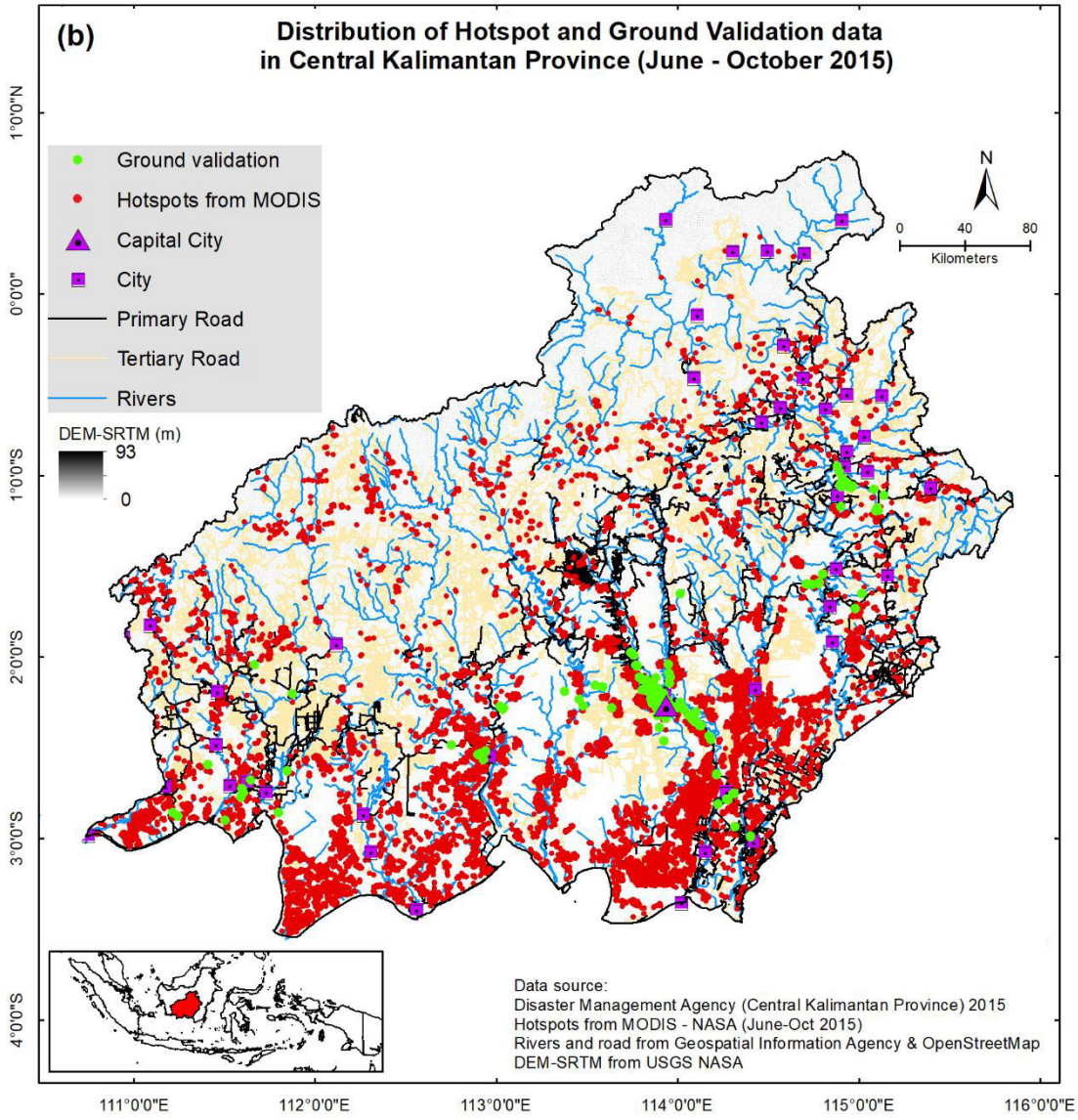


Figure 1.6. Distribution of hotspots/active fires data (confidence level ≥ 80%) from MODIS/VIIRS (MOD14 collection 6 and VNP14IMG) and ground validations by the local disaster management agency; (a) Riau Province (data periods span April–October 2016, February 2017 and March–June 2018); (b) Central Kalimantan Province (data period spans June–October 2015).

1.4. The Research Gap and Research Questions

The monitoring of peatland fires is an action to support Indonesia's commitment to reducing 29% of its GHG emissions by 2030 (Wijaya et al. 2017). So far, the disaster management agency has utilised daily space-based fire information in low spatial resolutions (375 m, 750 m and 1 km) from VIIRS and MODIS to guide ground monitoring. Most of the space-based, available and cost-free fire products are aimed at global wildfire monitoring and are not specifically developed for peatland fires in tropical

environments. The benefits of smouldering fire mapping not only include guiding fire suppression to minimise smoke haze distribution, but also maintaining peat conditions and preventing soil and biological system degradation. Additional sources of information and analysis of space-based fire products are still required to develop an efficient peatland fires monitoring process applicable to time and place as a consequence of limited resources for monitoring large peatland areas.

The spectral specifications of MODIS and VIIRS with MIR and TIR are capable of detecting smouldering and flaming combustion; however, the information they provide is still weak for providing information on smouldering fires in peatland due to the low radiant energy and their occurrence which happens as a result of burning activities on small areas for planting preparation. The information of active fire location produced by global active fire data lacks detailed spatial information because it refers to the coordinate location at the pixel centre, not the actual fire location and cannot present the characterisation or the shape of the fire. Better precision for the location and the shape of the fire can be provided from a finer spatial resolution. So far, the highest spatial resolution freely available fire product is 375 m spatial resolution from VIIRS.

On a more detailed spatial scale, fire algorithms from moderate spatial resolution (30 m), such as Landsat-8, have been developed using SWIR for global fire detection (Schroeder et al. 2016; Murphy et al. 2016; Kumar & Roy 2018). However, the application of these algorithms mostly misses peatland cool fires (Kumar & Roy 2018). A study to explore smouldering peatland detection was conducted using nighttime data from SWIR and the TIR of Landsat-8 (Elvidge et al. 2015). Unfortunately, the nighttime data of Landsat-8 can only be obtained under special request to the data provider; thus, it does not meet the needs for regular monitoring. However, there is an opportunity to explore Landsat-8 using SWIR and TIR to enhance peatland fires information from the daytime data, which is cost-free and available every 16 days. In addition, there is a potential to enhance the spatial resolution of peatland fires information by exploring Sentinel-2 data, which has similar spectral properties to Landsat-8, without TIR. Sentinel-2 has a 20 m spatial resolution and can give more frequent information every five days, cloud permitting.

Based on the gaps mentioned above, the research questions addressed in this thesis are as follows:

(1) Is it possible to map flaming and smouldering peatland fires from moderate spatial resolution (Landsat-8) data with SWIR and TIR using daytime data?

This question is explored and addressed in Chapters 2 and 3.

(2) How can optimise the use of global active fires products from low spatial resolution satellite sensors be optimised to guide disaster management agencies to efficiently conduct ground validation and subsequent suppression?

This question is initially addressed and discussed in Chapter 3, then explored more specifically in Chapter 4, as related to the use of VIIRS active fire data for monitoring peatland fires together with Landsat-8.

(3) To obtain peatlands fire information at higher spatial and temporal resolutions than Landsat-8, is it possible to detect and map peatland fires from higher spatial resolution satellite data without TIR information (e.g. Sentinel-2 MSI)?

This question is explored and addressed in Chapter 5.

1.5. Thesis Structure

After an introduction to peatland fire in Chapter 1, this thesis presents four chapters of papers published in peer-reviewed editions (one e-book chapter and three journal papers). This thesis structure is not intended as a detailed thesis outline, but rather as an overview of how the chapters address the research questions and contribute to the overall structure of the thesis.

This thesis explores how medium (20–30 m) and low (375 m) spatial resolution satellite imagery can be used to map tropical peatland fires, particularly in Indonesia (Figure 1.7). This concept was developed using SWIR and TIR parts of the electromagnetic spectrum to detect flaming and smouldering fires from medium spatial resolution satellite data. The twice-daily global active fire information from low spatial resolution (375 m) satellite sensor was assessed so that it could be utilised together with the peatland fires information, resulting from medium spatial resolution sensors; thus, peatland fires information was established in tropical environments at a higher spatial resolution and a higher temporal resolution than previously available.

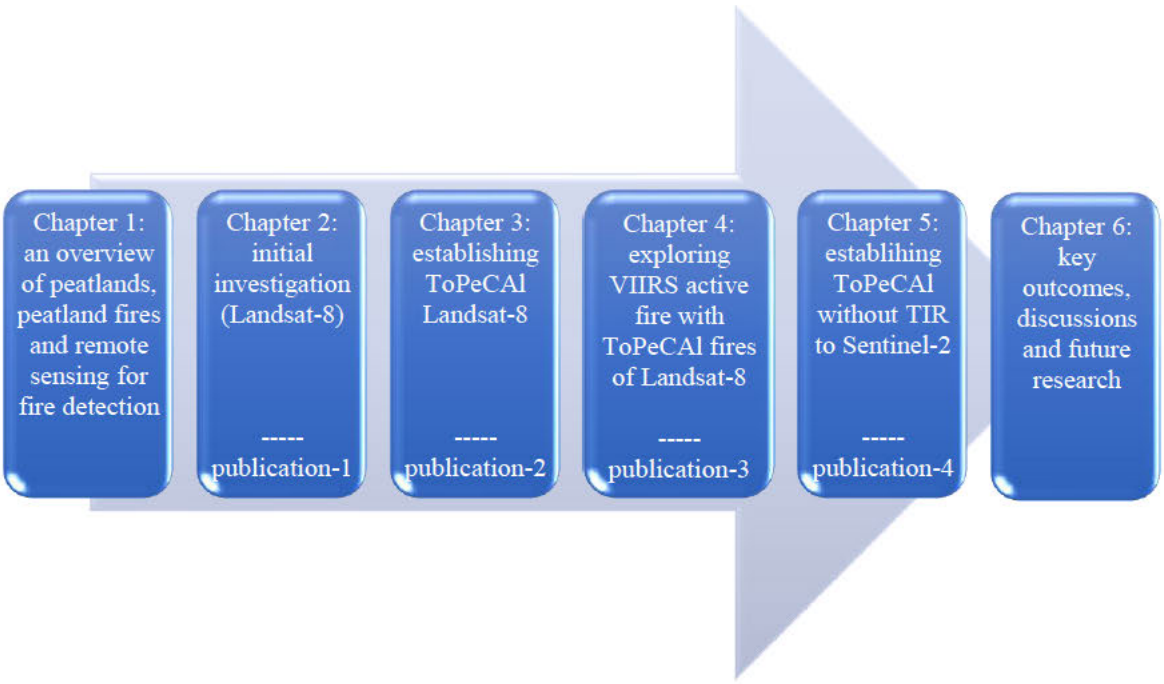


Figure 1.7. General thesis structure

Chapter 1 presents information on global peatlands and their significance for the environment. The chapter explains how peatlands are damaged by fire that is usually used for agricultural land clearing in Indonesia. Then an overview of peatland fire characteristics based on field and laboratory experiments is provided. This chapter also presents the principles of remote sensing for fire detection with a review of current sensor capabilities and available space-based fire algorithms and products. The existing practice of ground-based peatland fires monitoring in Indonesia is also presented and, finally, the chapter presents how this thesis addresses current oversights in remote sensing for fires detection, particularly in tropical peatland environments.

Chapter 2 presents work published in referred conference proceedings as an initial investigation of flaming and smouldering from the SWIR and TIR radiance of medium spatial resolution imagery from Landsat-8 data taken from Central Kalimantan's peatland. The assessment of the mapping results was compared with the RGB images by visual analysis and with a low spatial resolution active fire product; no ground truth data were analysed in the paper. However, the paper shows the possibility of mapping peatland fires using SWIR and TIR from Landsat-8 data. This work was published in a peer-reviewed e-book entitled *Advances in Forest Fire Research 2018,* which compiled the

contributions to the XIII International Conference on Forest Fire Research, organised by the University of Coimbra, Portugal (https://doi.org/10.14195/978-989-26-16-506_106).

Chapter 3 applies a revision of the peatland combustion algorithm, described in Chapter 2, by using additional Landsat-8 data with the combination of top of atmosphere (TOA) reflectance of SWIR, the TOA brightness temperature of TIR and the TOA reflectance of the aerosol band to detect peatland fires under smoky/hazy to relatively clear atmospheric conditions; these are integrated into the tropical peatland combustion algorithm (ToPeCAl). This journal published work, in *Remote Sensing* (https://doi.org/10.3390/rs11040465), also presents the implementation of ToPeCAl using different times, applied outside the development algorithm area and with ground truth validation. A comparison with other Landsat-8 fire algorithms was conducted and with the low spatial resolution active fire product of VIIRS (375 m). This initial comparison introduces a potential merger of peatland fires information generated from Landsat-8 and VIIRS active fire information to address the temporal gaps in information when using Landsat.

Chapter 4 compares VIIRS (375 m) active fire data with the results from ToPeCAl-Landsat-8 fires. It advances the initial work on the relationship between VIIRS active fires and Landsat-8 fires presented Chapter 3. The slow propagation of peat fires permits the validation of VIIRS (375 m) active fire product with ToPeCAl-Landsat-8 fires with a time difference in acquisitions of between three and 15 hours. This shows that both fire products can complement each other in the detection and monitoring of peatland fires. This work is published in the *International Journal of Digital Earth* (https://doi.org/10.1080/17538947.2020.1791268).

Chapter 5 develops a new technique for the implementation of active fires detection in tropical peatland environments using the tropical peatland combustion algorithm (ToPeCAl) applied to Sentinel-2. ToPeCAl without TIR was tested on Landsat-8 OLI and then applied to near simultaneous Sentinel-2 acquisitions to establish a method for the more frequent monitoring of peatland fires at up to five days (cloud permitting) and with greater spatial resolution (20 m) than for Landsat. The adjustment of ToPeCAl was presented by performing permanent bright object masking, cloud masking and contextual tests to select the candidate fire pixels from their background. This work is published in *Remote Sensing* (https://doi.org/10.3390/rs12233958).

Chapter 6 concludes this thesis with a general discussion about flaming and smouldering peatland fires detection, the accuracy of ToPeCAl fires, opportunities for the integration of multi-fire information from different observations and directions for future research.

References

Allison, RS, Johnston, JM, Craig, G & Jennings, S 2016, 'Airborne Optical and Thermal Remote Sensing for Wildfire Detection and Monitoring', *Sensors (Basel, Switzerland)*, vol. 16, no. 8, p. 1310.

Alsepan, G & Minobe, S 2020, 'Relations between Interannual Variability of Regional-Scale Indonesian Precipitation and Large-Scale Climate Modes during 1960–2007', *Journal of Climate*, vol. 33, no. 12, pp. 5271–5291.

Arino, O, Melinotte, J & Calabresi, G 1993, 'Fire, cloud, land, water: The Ionia AVHRR CD-browser of ESRIN', *Earth Observation Quarterly*, vol. 41, pp. 6–7.

Atwood, E, Englhart, S, Lorenz, E, Halle, W, Wiedemann, W & Siegert, F 2016, 'Detection and characterization of low temperature peat fires during the 2015 fire catastrophe in Indonesia using a new high-sensitivity fire monitoring satellite sensor (FireBird)', *PLoS ONE*, vol. 11, no. 8, pp. 1–24.

Baum, BA & Trepte, Q 1999, 'A grouped threshold approach for scene identification in AVHRR imagery', *Journal of Atmospheric and Oceanic Technology*, vol. 16, no. 6, pp. 793–800.

Bertschi, I, Yokelson, RJ, Ward, DE, Babbitt, RE, Susott, RA, Goode, JG & Hao, WM 2003, 'Trace gas and particle emissions from fires in large diameter and belowground biomass fuels', *J. Geophys. Res*, vol. 108, no. D13.

Boer, R, Dewi, RG, Ardiansyah, M & Siagian, UW 2018, *Indonesia Second Biennial Update Report, Under the United Nations Framework Convention on Climate Change*, Directorate General of Climate Change, Ministry of Environment and Forestry, Jakarta, Indonesia. <http://ditjenppi.menlhk.go.id/reddplus/images/adminppi/dokumen/Indonesia-2nd_BUR_web.pdf>.

Bowen, MR, Bompard, JM, Anderson, IP, Guizol, P & Gouyon, A 2000, 'Anthropogenic fires in Indonesia: a view from Sumatra', Anthropogenic fires in Indonesia: a view from Sumatra.

Bowman, KW 2020, *Historic Amazon rainforest fires threaten climate and raise risk of new diseases*, Australia edn, The Conversation, viewed 07 October 2020, <https://theconversation.com/historic-amazon-rainforest-fires-threaten-climate-and-raise-risk-of-new-diseases-146720>.

Burke, C, Wich, S, Kusin, K, McAree, O, Harrison, ME, Ripoll, B, Ermiasi, Y, Mulero-Pázmány, M & Longmore, S 2019, 'Thermal-Drones as a Safe and Reliable Method for Detecting Subterranean Peat Fires', vol. 3, no. 1, p. 23.

Caiazzo, F, Malina, R, Staples, MD, Wolfe, PJ, Yim, SHL & Barrett, SRH 2014, 'Quantifying the climate impacts of albedo changes due to biofuel production: a comparison with biogeochemical effects', *Environmental Research Letters*, vol. 9, no. 2, p. 024015.

Calle, A & Salvador, P 2013, 'The Active Fire FRP Estimation: Study on Sentinel-3/SLSTR', *IEEE Geoscience and Remote Sensing Letters*, vol. 10, no. 5, pp. 1046–1049.

Charman, DJ 2009, 'Peat and Peatlands A2 - Likens, Gene E', Encyclopedia of Inland Waters, Academic Press, Oxford, pp. 541–548.
Cochrane, M 2003, 'Fire science for rainforests', *Nature*, vol. 421, no. 6926, p. 913.

Cole, LES, Bhagwat, SA & Willis, KJ 2019, 'Fire in the Swamp Forest: Palaeoecological Insights Into Natural and Human-Induced Burning in Intact Tropical Peatlands', *Front. For. Glob. Change*, vol. 2, no. 48.

Csiszar, I, Schroeder, W, Giglio, L, Ellicott, E, Vadrevu, KP, Justice, CO & Wind, B 2014, 'Active fires from the Suomi NPP Visible Infrared Imaging Radiometer Suite: Product status and first evaluation results', *Journal of Geophysical Research: Atmospheres*, vol. 119, no. 2, pp. 803–816.

Davies, GM, Gray, A, Rein, G & Legg, CJ 2013, 'Peat consumption and carbon loss due to smouldering wildfire in a temperate peatland', *Forest Ecology and Management*, vol. 308, 2013/11/15/, pp. 169–177.

Dennis, RA, Mayer, J, Applegate, G, Chokkalingam, U, Colfer, CJP, Kurniawan, I, Lachowski, H, Maus, P, Permana, RP, Ruchiat, Y, Stolle, F, Suyanto & Tomich, TP 2005, 'Fire, People and Pixels: Linking Social Science and Remote Sensing to Understand Underlying Causes and Impacts of Fires in Indonesia', *Human Ecology*, vol. 33, no. 4, pp. 465–504.

Dennison, PE, Charoensiri, K, Roberts, DA, Peterson, SH & Green, RO 2006, 'Wildfire temperature and land cover modeling using hyperspectral data', *Remote Sensing of Environment*, vol. 100, no. 2, 2006/01/30/, pp. 212–222.

Dennison, PE & Matheson, DS 2011, 'Comparison of fire temperature and fractional area modeled from SWIR, MIR, and TIR multispectral and SWIR hyperspectral airborne data', *Remote Sensing of Environment*, vol. 115, no. 3, 2011/03/15/, pp. 876–886.

Doerr, SH & Cerdá, A 2005, 'Fire effects on soil system functioning: new insights and future challenges', *J International Journal of Wildland Fire*, vol. 14, no. 4, pp. 339–342.

Dozier, J 1981, 'A method for satellite identification of surface temperature fields of subpixel resolution', *Remote Sensing of Environment*, vol. 11, no. 1, pp. 221–229.

Eckmann, T, Roberts, D & Still, C 2009, 'Estimating subpixel fire sizes and temperatures from ASTER using multiple endmember spectral mixture analysis', *International Journal of Remote Sensing*, vol. 30, no. 22, pp. 5851–5864.

Elvidge, CD, Nelson, I, Hobson, V, Safren, J & Baugh, K 2001, *Detection of Forest at Night Using DMSP-OLS Data*, SPB Academic Publishing BV, The Hague.

Elvidge, CD, Zhizhin, M, Hsu, F, Baugh, K, Khomarudin, M, Vetrita, Y, Sofan, P, Suwarsono & Hilman, D 2015, 'Long-wave infrared identification of smouldering peat fires in indonesia with nighttime landsat data', *Environmental Research Letters*, vol. 10, no. 6, p. 065002.

Elvidge, CD, Zhizhin, M, Hsu, F-C & Baugh, K 2013, 'VIIRS Nightfire: Satellite Pyrometry at Night', *Remote Sensing*, vol. 5, no. 9, p. 4423.

Field, RD, Van Der Werf, GR & Shen, SSP 2009, 'Human amplification of drought-induced biomass burning in Indonesia since 1960', *Nature Geoscience*, vol. 2, no. 3, p. 185.

Fiona, N, Kudzai Shaun, M, Blessing, K, Henry, N & Monalisa Shingirayi, M 2020, 'Exploring the utility of Sentinel-2 MSI and Landsat 8 OLI in burned area mapping for a heterogenous savannah landscape', *PLoS ONE*, vol. 15, no. 5, p. e0232962.

Fuller, DO & Fulk, M 2000, 'Comparison of NOAA-AVHRR and DMSP-OLS for operational fire monitoring in Kalimantan, Indonesia', *International Journal of Remote Sensing*, vol. 21, no. 1, pp. 181–187.

Fuller, DO 2000, 'Satellite remote sensing of biomass burning with optical and thermal sensors', *Progress in Physical Geography*, vol. 24, no. 4, pp. 543–561.

Giglio, L, Csiszar, I, Restás, Á, Morisette, JT, Schroeder, W, Morton, D & Justice, CO 2008, 'Active fire detection and characterization with the advanced spaceborne thermal emission and reflection radiometer (ASTER)', *Remote Sensing of Environment*, vol. 112, no. 6, pp. 3055–3063.

Giglio, L, Descloitres, J, Justice, CO & Kaufman, YJ 2003, 'An Enhanced Contextual Fire Detection Algorithm for MODIS', Remote Sensing of Environment, vol. 87, no. 2, pp. 273–282.

Giglio, L, Kendall, JD & Justice, C 1999, 'Evaluation of global fire detection algorithms using simulated AVHRR infrared data', *International Journal of Remote Sensing*, vol. 20, no. 10, pp. 1947–1985.

Giglio, L, Schroeder, W & Justice, C 2016, 'The collection 6 MODIS active fire detection algorithm and fire products', *Remote Sensing of Environment*, vol. 178, pp. 31–41.

Gumbricht, T, Roman-Cuesta, RM, Verchot, L, Herold, M, Wittmann, F, Householder, E, Herold, N & Murdiyarso, D 2017, 'An expert system model for mapping tropical wetlands and peatlands reveals South America as the largest contributor', *Global Change Biology*.

Hally, B, Wallace, L, Reinke, K & Jones, S 2016, 'Assessment of the utility of the Advanced Himawari Imager to detect active fire over Australia', *International Archives of the Photogrammetry, Remote Sensing and Spatial Information Sciences - ISPRS Archives*, vol. 41, pp. 65–71.

Hayasaka, H, Takahashi, H, Limin, SH, Yulianti, N & Usup, A 2016, 'Peat Fire Occurrence', in M Osaki & N Tsuji (eds), *Tropical Peatland Ecosystems*, Springer Japan, Tokyo, pp. 377–395.

Hird, A 2019, *Congo Basin vs the Amazon: a tale of two forest fires*, RFI, viewed 07 October 2020, <https://www.rfi.fr/en/africa/20190827-africa-forest-fire-amazon-deforestation>.

Hellmann, M & Rathgeber, W 2015, 'European Member States Satellite Programs', in K-U Schrogl et al (eds), *Handbook of Space Security: Policies, Applications and Programs*, Springer New York, New York, NY, pp. 831–842.

Holden, J 2006, 'Chapter 14 Peatland hydrology', in AMC I.P. Martini & W Chesworth (eds), *Developments in Earth Surface Processes*, vol. Volume 9, Elsevier, pp. 319–346.

Hoscilo, A, Page, SE, Tansey, KJ & Rieley, JO 2011, 'Effect of repeated fires on land-cover change on peatland in southern Central Kalimantan, Indonesia, from 1973 to 2005', *International Journal of Wildland Fire*, vol. 20, no. 4, pp. 578–588.

Hu, Y, Fernandez-Anez, N, Smith, TEL & Rein, G 2018, 'Review of emissions from smouldering peat fires and their contribution to regional haze episodes', *J International Journal of Wildland Fire*, vol. 27, no. 5, pp. 293–312.

Huang, X & Rein, G 2017, 'Downward spread of smouldering peat fire: the role of moisture, density and oxygen supply', *International Journal of Wildland Fire*, vol. 26, no. 11, p. 907.

Irons, JR, Dwyer, JL & Barsi, JA 2012, 'The next Landsat satellite: The Landsat Data Continuity Mission', *Remote Sensing of Environment*, vol. 122, pp. 11–21.

Jenner, L 2018, *Papua and Papua New Guinea Experience High Numbers of Wildfires*, NASA/Goddard, viewed 10 October 2020, <https://www.nasa.gov/image-feature/goddard/2018/papua-and-papua-new-guinea-experience-high-numbers-of-wildfires>.

Joosten, H & Clarke, D 2002, Wise use of mires and peatlands, International Mire Conservation Group and International Peat Society, Finland.

Joosten, H 2004, 'The IMCG global peatland database', Hans Joosten (Greifswald University, Germany).

Joosten, H, Tapio-Biström, M-L & Tol, S 2012, Peatlands: guidance for climate change mitigation through conservation, rehabilitation and sustainable use, Food and Agriculture Organization of the United Nations.

Justice, C & Korontzi, S 2001, *A Review of The Status of Satellite Fire Monitoring and the Requirements for Global Environmental Change Research*, SPB Academic Publishing BV, The Hague.

Justice, C, Giglio, L, Korontzi, S, Owens, J, Morisette, J, Roy, D, Descloitres, J, Alleaume, S, Petitcolin, F & Kaufman, Y 2002, 'The MODIS fire products', *Remote Sensing of Environment*, vol. 83, no. 1, pp. 244–262.

Justice, C, Kendall, J, Dowty, P & Scholes, R 1996, 'Satellite remote sensing of fires during the SAFARI campaign using NOAA advanced very high resolution radiometer data', *Journal of Geophysical Research: Atmospheres*, vol. 101, no. D19, pp. 23851–23863.

Kaufman, Y, Justice, C, Flynn, LP & Kendall, JD 1998, 'Potential global fire monitoring from EOS-MODIS', *Journal of Geophysical Research: Atmospheres*, vol. 103, no. D24, pp. 32215–32238.

Koppmann, R, von Czapiewski, K & Reid, JS 2005, 'A review of biomass burning emissions, part I: gaseous emissions of carbon monoxide, methane, volatile organic compounds, and nitrogen containing compounds', *Atmos. Chem. Phys. Discuss.*, vol. 2005, pp. 10455–10516.

Kumar, SS & Roy, DP 2018, 'Global operational land imager Landsat-8 reflectance-based active fire detection algorithm', *International Journal of Digital Earth*, vol. 11, no. 2, pp. 154–178.

Lin, S, Sun, P & Huang, X 2019, 'Can peat soil support a flaming wildfire?', *J International Journal of Wildland Fire*, vol. 28, no. 8, pp. 601–613.

Lorenz, E 2013, 'Thermal Remote Sensing with Small Satellites: BIRD, TET and the Next Generation BIROS', in C Kuenzer & S Dech (eds), *Thermal Infrared Remote Sensing: Sensors, Methods, Applications*, Springer Netherlands, Dordrecht, pp. 149–176.

Miettinen, J & Liew, S 2009, 'Burn-scar patterns and their effect on regional burnt-area mapping in insular South-East Asia', *International Journal of Wildland Fire*, vol. 18, no. 7, pp. 837–847.

Miettinen, J & Liew, S 2010, 'Degradation and development of peatlands in Peninsular Malaysia and in the islands of Sumatra and Borneo since 1990', *Land Degradation and Development*, vol. 21, no. 3, pp. 285–296.

Miettinen, J, Hooijer, A, Wang, J, Shi, C & Liew, SC 2012, 'Peatland degradation and conversion sequences and interrelations in Sumatra', *Regional Environmental Change*, vol. 12, no. 4, pp. 729–737.

Miettinen, J, Shi, C & Liew, S 2011, 'Influence of peatland and land cover distribution on fire regimes in insular Southeast Asia', *Regional Environmental Change*, vol. 11, no. 1, pp. 191–201.

Mitchell, S, Jones, S, Reinke, K, Lorenz, E & Reulke, R 2016, 'Assessing the utility of the TET-1 hotspot detection and characterization algorithm for determining wildfire size and temperature', *International Journal of Remote Sensing*, vol. 37, no. 20, pp. 4731–4747.

Murphy, SW, de Souza Filho, CR, Wright, R, Sabatino, G & Correa Pabon, R 2016, 'HOTMAP: Global hot target detection at moderate spatial resolution', *Remote Sensing of Environment*, vol. 177, pp. 78–88.

Nasi, R 2019, *It's Not Just the Amazon: We Must Also Protect Congo Basin Peatlands From Fire*, Truthout, viewed 7 October 2020, <https://truthout.org/articles/its-not-just-the-amazon-we-must-also-protect-congo-basin-peatlands-from-fire/>.

Osaki, M, Nursyamsi, D, Noor, M, Wahyunto, W & Segah, H 2016a, 'Peatland in Indonesia', in M Osaki & N Tsuji, N (eds), Tropical peatland ecosystems, Springer, Tokyo, Japan, pp. 49–58, ISBN 978-4-431-55680-0, doi: 10.1007/978-4-431-55681-7.

Osaki, M, Setiadi, B, Takahashi, H & Evri, M 2016b, 'Peatland in Kalimantan', in M Osaki & N Tsuji, N (eds), Tropical peatland ecosystems, Springer, Tokyo, Japan, pp. 91–112, ISBN 978-4-431-55680-0, doi: 10.1007/978-4-431-55681-7.

Page, S, Hoscilo, A, Langner, A, Tansey, K, Siegert, F, Limin, S & Rieley, J 2009, 'Tropical peatland fires in Southeast Asia', in MA Cochrane (ed), *Tropical Fire Ecology: Climate Change, Land Use, and Ecosystem Dynamics*, Springer Berlin Heidelberg, Berlin, Heidelberg, pp. 263–287.

Page, SE & Baird, AJ 2016, 'Peatlands and Global Change: Response and Resilience', *Annual Review of Environment and Resources*, vol. 41, pp. 35–57.

Page, SE, Rieley, J & Banks, C 2011, 'Global and regional importance of the tropical peatland carbon pool', *Global Change Biology*, vol. 17, no. 2, pp. 798–818.

Page, SE, Siegert, F, Rieley, J, Boehm, H, Jaya, A & Limin, S 2002, 'The amount of carbon released from peat and forest fires in Indonesia during 1997', *Nature*, vol. 420, no. 6911, p. 61.

Pan, X, Chin, M, Ichoku, CM & Field, RD 2018, 'Connecting Indonesian Fires and Drought With the Type of El Niño and Phase of the Indian Ocean Dipole During 1979–2016', *Journal of Geophysical Research: Atmospheres*, vol. 123, no. 15, pp. 7974–7988, https://doi.org/10.1029/2018JD028402.

Purnomo, H, Shantiko, B, Sitorus, S, Gunawan, H, Achdiawan, R, Kartodihardjo, H & Dewayani, AA 2017, 'Fire economy and actor network of forest and land fires in Indonesia', *Forest Policy and Economics*, vol. 78, pp. 21–31.

Quintano, C, Fernández-Manso, A & Fernández-Manso, O 2018, 'Combination of Landsat and Sentinel-2 MSI data for initial assessing of burn severity', *International Journal of Applied Earth Observation and Geoinformation*, vol. 64, 2018/02/01/, pp. 221–225.

Rabelo, ERC, Veras, CAG, Carvalho, JA, Alvarado, EC, Sandberg, DV & Santos, JC 2004, 'Log smoldering after an amazonian deforestation fire', *Atmospheric Environment*, vol. 38, no. 2, 2004/01/01/, pp. 203–211.

Reid, JS, Koppmann, R, Eck, TF & Eleuterio, DP 2005, 'A review of biomass burning emissions part II: intensive physical properties of biomass burning particles', *Atmos. Chem. Phys.*, vol. 5, no. 3, pp. 799–825.

Read, P 2019, *Amazon fires: Could we reach the tipping point for runaway climate change?*, LENS Monash university, Australia, viewed 07 October 2020, <https://lens.monash.edu/@environment/2019/08/26/1376257/have-we-reached-the-first-tipping-point-for-runaway-climate-change>.

Rein, G 2009, *Smouldering Combustion Phenomena in Science and Technology*, International Review of Chemical Engineering IRECHE, Vol 1, pp 3–18.

Rein, G 2013, 'Smouldering fires and natural fuels', *Fire Phenomena and the Earth System: An Interdisciplinary Guide to Fire Science*, vol. Chapter 2, pp. 13–22.

Rein, G 2016, 'Smouldering Combustion', in MJ Hurley et al (eds), *SFPE Handbook of Fire Protection Engineering*, Springer New York, New York, NY, pp. 581–603.

Rein, G, Cleaver, N, Ashton, C, Pironi, P & Torero, JL 2008, 'The severity of smouldering peat fires and damage to the forest soil', *CATENA*, vol. 74, no. 3, 2008/08/15/, pp. 304–309.

Reuters 2019, World-Bank says Indonesia forest fires cost $5.2 billion in economic losses, viewed 20/09/2020. <https://www.reuters.com/article/us-indonesia-environment-idUSKBN1YF0FJ>.

Rieley, J & Page, S 2016, 'Tropical peatland of the world', in M Osaki & N Tsuji, N (eds), Tropical peatland ecosystems, Springer, Tokyo, Japan, pp. 3–32, ISBN 978-4-431-55680-0, doi: 10.1007/978-4-431-55681-7.

Ritung, S, Wahyunto, W, Nugroho, K 2012, 'Karakteristik dan Sebaran Lahan Gambut di Sumatera, Kalimantan dan Papua', Pengelolaan Lahan Gambut Berkelanjutan. Balai Besar Litbang SDLP, Bogor. (*in Bahasa*).

Roy, DP, Huang, H, Boschetti, L, Giglio, L, Yan, L, Zhang, HH & Li, Z 2019, 'Landsat-8 and Sentinel-2 burned area mapping - A combined sensor multi-temporal change detection approach', *Remote Sensing of Environment*, vol. 231, 2019/09/15/, p. 111254.

Roberts, GJ & Wooster, MJ 2008, 'Fire Detection and Fire Characterization Over Africa Using Meteosat SEVIRI', *Geoscience and Remote Sensing, IEEE Transactions on*, vol. 46, no. 4, pp. 1200–1218.

Rydin, H & Jeglum, JK 2006, *The Biology of Peatlands*, Oxford University Press, UK, Oxford.

Santoso, MA, Huang, X, Prat-Guitart, N, Christensen, E, Hu, Y & Rein, G 2019, 'Smouldering fires and soils', in P Pereira et al (eds), *Fire Effects on Soil Properties*, CSIRO Publishing, Victoria, Australia, p. 382.

Schroeder, W, Oliva, P, Giglio, L & Csiszar, I 2014, 'The New VIIRS 375 m active fire detection data product: Algorithm description and initial assessment', *Remote Sensing of Environment*, vol. 143, pp. 85–96.

Schroeder, W, Oliva, P, Giglio, L, Quayle, B, Lorenz, E & Morelli, F 2016, 'Active fire detection using Landsat-8/OLI data', *Remote Sensing of Environment*, vol. 185, pp. 210–220.

Schroeder, W, Prins, E, Giglio, L, Csiszar, I, Schmidt, C, Morisette, J & Morton, D 2008, 'Validation of GOES and MODIS active fire detection products using ASTER and ETM+ data', *Remote Sensing of Environment*, vol. 112, no. 5, pp. 2711–2726.

Schumann, M & Joosten, H 2008, 'Global peatland restoration manual', Institute of Botany and Landscape Ecology, Greifswald University, Germany.

Siegert, F, Ruecker, G, Hinrichs, A & Hoffmann, AA 2001, 'Increased damage from fires in logged forests during droughts caused by El Niño', *Nature*, vol. 414, no. 6862, p. 437.

Siegert, F, Zhukov, B, Oertel, D, Limin, S, Page, SE & Rieley, JO 2004, 'Peat fires detected by the BIRD satellite', *International Journal of Remote Sensing*, vol. 25, no. 16, pp. 3221–3230.

Sifakis, NI, Iossifidis, C, Kontoes, C & Keramitsoglou, I 2011, 'Wildfire Detection and Tracking over Greece Using MSGSEVIRI Satellite Data', *Remote Sensing*, vol. 3, no. 3, pp. 524–538.

Smith, TEL, Evers, S, Yule, CM & Gan, JY 2018, 'In Situ Tropical Peatland Fire Emission Factors and Their Variability, as Determined by Field Measurements in Peninsula Malaysia', vol. 32, no. 1, pp. 18–31.

Sugardiman, RA 2005, *Natural ecosystems provide essential ecological services including clean air, water and biodiversity. Peat swamp forest, Kalimantan, Indonesia.*, 14 January 2005, viewed 20 September 2020, Ruanda AgungSugardiman/AusAID/CC BY(https://creativecommons.org/licenses/by/2.0),

https://commons.wikimedia.org/wiki/File:Peat_Forest_Swamp_(10712654875).jpg.

Suyanto, S, Applegate, G, Permana, R, Khususiyah, N & Kurniawan, I 2004, 'The Role of Fire in Changing Land Use and Livelihoods in Riau-Sumatra', *Ecology and Society*, vol. 9, no. 1, pp. 15–15.

Tacconi, L 2003, Fires in Indonesia: causes, costs and policy implications, CIFOR, Bogor, Indonesia.

Takahashi, H, Ibie, BF, Usup, A, Shimada, S & Limin, SH 2002, 'Annual changes of water balance and a drought index in a tropical peat swamp forest of Central Kalimantan, Indonesia', *International Symposium on Tropical Peatlands, Jakarta (Indonesia), 22–23 Aug 2002*.

Urbanski, S 2014, 'Wildland fire emissions, carbon, and climate: Emission factors', *Forest Ecology and Management*, vol. 317, pp. 51–60.

Usup, A, Hashimoto, Y, Takashi, H & Hayasaka, H 2004, 'Combustion and thermal characteristics of peat fire in tropical peatland in Central Kalimantan, Indonesia', *Tropics*, vol. 14, no. 1, pp. 1–19.

van Marle, MJE, Field, RD, van der Werf, GR, Estrada de Wagt, IA, Houghton, RA, Rizzo, LV, Artaxo, P & Tsigaridis, K 2017, 'Fire and deforestation dynamics in Amazonia (1973-2014)', *Global Biogeochem. Cycles*, vol. 31, no. 1, pp. 24–38.

Vasterling, M & Meyer, U 2013, 'Challenges and Opportunities for UAV-Borne Thermal Imaging', in C Kuenzer & S Dech (eds), *Thermal Infrared Remote Sensing: Sensors, Methods, Applications*, Springer Netherlands, Dordrecht, pp. 69–92.

Vitt, DH 2008, 'Peatlands A2 - Jørgensen, Sven Erik', in BD Fath (ed), *Encyclopedia of Ecology*, Academic Press, Oxford, pp. 2656–2664.

Wickramasinghe, C, Jones, S, Reinke, K & Wallace, L 2016, 'Development of a Multi-Spatial Resolution Approach to the Surveillance of Active Fire Lines Using Himawari-8', *Remote Sensing*, vol. 8, no. 11, p. 932.

Widjaja, E, Maryanto, I, Wowor, D & Prijono, S 2011, 'Status keanekaragaman hayati Indonesia', Pusat Penelitian Biologi. LIPI. (in Bahasa).

Wiggins, EB, Czimczik, CI, Santos, GM, Chen, Y, Xu, X, Holden, SR, Randerson, JT, Harvey, CF, Kai, FM & Yu, LE 2018, 'Smoke radiocarbon measurements from Indonesian fires provide evidence for burning of millennia-aged peat', *Proceedings of the National Academy of Sciences*, vol. 115, no. 49, p. 12419.

Wijaya, A, Chrysolite, H, Ge, M, Wibowo, CK, Pradana, A, Utami, AF & Austin, K 2017, How can indonesia achieve its climate change mitigation goal? An analysis of potential emissions reductions from energy and land-use policies, World Resources Institute, Jakarta, Indonesia. <https://files.wri.org/s3fs-public/how-can-indonesia-achieve-its-climate-change-mitigation-goal-analysis-potential-emissions-reductions-from-energy-land-use-policies_0.pdf>.

Wooster, MJ, Roberts, G, Smith, AMS, Johnston, J, Freeborn, P, Amici, S & Hudak, AT 2013, 'Thermal Remote Sensing of Active Vegetation Fires and Biomass Burning Events', in C Kuenzer & S Dech (eds), *Thermal Infrared Remote Sensing: Sensors, Methods, Applications*, Springer Netherlands, Dordrecht, pp. 347–390.

Wooster, MJ, Xu, W & Nightingale, T 2012, 'Sentinel-3 SLSTR active fire detection and FRP product: Pre-launch algorithm development and performance evaluation using MODIS and ASTER datasets', *Remote Sensing of Environment*, vol. 120, 5/15/, pp. 236–254.

World-Bank 2016, *The Cost of Fire: An Economic Analysis of Indonesia's 2015 Fire Crisis*, World-Bank Group, Jakarta, Indonesia.

Wösten, JHM, Clymans, E, Page, SE, Rieley, JO & Limin, SH 2008, 'Peat–water interrelationships in a tropical peatland ecosystem in Southeast Asia', *Catena (Giessen)*, vol. 73, no. 2, pp. 212–224.

Xu, W, Wooster, MJ, Roberts, G & Freeborn, P 2010, 'New GOES imager algorithms for cloud and active fire detection and fire radiative power assessment across North, South and Central America', *Remote Sensing of Environment*, vol. 114, no. 9, 9/15/, pp. 1876–1895.

Zaccone, C, Rein, G, D'Orazio, V, Hadden, RM, Belcher, CM & Miano, TM 2014, 'Smouldering fire signatures in peat and their implications for palaeoenvironmental reconstructions', *Geochimica et Cosmochimica Acta*, vol. 137, 7/15/, pp. 134–146.

Zhang, X, Zhang, J, Kuenzer, C, Voigt, S & Wagner, W 2004, 'Capability evaluation of 3–5 μ m and 8–12.5 μ m airborne thermal data for underground coal fire detection', *International Journal of Remote Sensing*, vol. 25, no. 12, pp. 2245–2258.

Zhukov, B, Lorenz, E, Oertel, D, Wooster, M & Roberts, G 2006, 'Spaceborne detection and characterization of fires during the bi-spectral infrared detection (BIRD) experimental small satellite mission (2001–2004)', *Remote Sensing of Environment*, vol. 100, no. 1, pp. 29–51.

Chapter 2

Detecting Peatland Combustion using Shortwave and Thermal Infrared Landsat-8 Data

This chapter is published as:

Sofan, P.; Bruce, D.; Jones, E.; Marsden, J. Detecting peatland combustion using shortwave and thermal infrared Landsat-8 data. In Advance Forest Fire Research; Imprensa da Universidade de Coimbra: Coimbra, Portugal, 2018; pp. 969–979.

(https://doi.org/10.14195/978-989-26-16-506_106)

Note: Minor additional information is inserted in [squared brackets]

Detecting Peatland Combustion using Shortwave and Thermal Infrared Landsat-8 Data

Abstract

Peatland fires occur every year in Indonesia. These fires usually occur in the dry season due to agricultural and plantation expansion practices, which include slash and burn activities. Peatland combustion fires can be classified into smouldering and flaming. Smouldering is described by lower temperatures, spread rates and combustion power compared with flaming. Most of the standard fire products from remote sensing satellites use an apparent fire temperature at 4 μm in the Middle InfraRed (MIR) and background temperature at 11 μm in Thermal InfraRed (TIR). These products only report combustion in a single term as an "active fire" or "fire hotspot", and do not discriminate between smouldering and flaming states. In this research, the ShortWave InfraRed (SWIR) and TIR bands of daytime Landsat-8 were explored to discriminate smouldering and flaming states of peatland combustion. Initial identification of possible combustion areas was from visual observation of false colour composite images (bands 764 to RGB) of Landsat-8, which presented smoke plumes in pale bluish tones emanating from a defined ground location. The potential combustion areas were further investigated using an implementation of the Hyperspectral Fire Detection Index based on SWIR of Landsat-8 and named here as the ShortWave InfraRed Combustion Index (SICI). Potential combustion areas were also analysed using radiances of the SWIR (band 7) and TIR (band 10), which exhibited values close to their saturation. From these radiances, a radiative transfer model using MODTRAN4 and Planck's law, the fire temperatures were estimated. Preliminary results showed that the flaming states, with higher temperatures than smouldering states, are coincident with SWIR radiances near saturation (24–29 $Wm^{-2}sr^{-1}\mu m^{-1}$ for band 7) and TIR (band 10) > 12 $Wm^{-2}sr^{-1}\mu m^{-1}$, while smouldering states, with lower temperatures, occur near flaming areas with lower SWIR radiance and TIR radiance above 11 $Wm^{-2}sr^{-1}\mu m^{-1}$. Based on Landsat-8 imagery on 3rd and 19th August 2015, fire temperatures of flaming areas were estimated at 700–758 K, mixtures of flaming and smouldering at 500–665 K, and smouldering at 320–499 K. This result aligned with prior research that sampled in situ smouldering, smouldering close to flaming, and flaming temperatures taken from Indonesian peatland. The algorithm

developed in the research reported here was able to map some combustion areas that could not be mapped using lower spatial resolution imagery from MODIS. However, the results will undergo further investigation for atmospheric influence such as haze and thin cloud. Results also will be validated with other data such as field measurements. The algorithm developed in this research has potential to be used on a routine basis due to the availability of daytime Landsat-8 data which, at best, has a temporal resolution of 16 days. It can also be implemented for forest fire detection at a detailed scale to complement other fire information, but again temporal resolution is an issue. This research is part of a larger project which is utilising automated smoke detection and soil moisture measurement in the mapping of peatland combustion from space imagery.

Keywords: flaming, smouldering, peatland fires, Landsat-8, remote sensing, SWIR, TIR

2.1. Introduction

In Indonesia, peatland combustion usually has an anthropogenic origin due to agricultural and plantation expansions, which are mostly accomplished through slash and burn activities (Miettinen et al. 2012; Rieley and Page 2016). Most peatland fires occur during the dry season (July–September) when the peatland is drier than in other times of the year and more susceptible to combustion (Usup et al. 2014, Hayasaka et al. 2016). The devastating forest and peatland fires in Indonesia in 2015 caused a total economic loss of about USD 16 billion (World-Bank 2016), released approximately 1.75 gt of atmospheric CO_2 (World-Bank 2016) and contributed to 100,000 premature deaths (Burrows 2016).

In general, peatland combustion consists of flaming and smouldering. Smouldering occurs with lower temperatures, spread rates and combustion power compared with flaming. Once ignition has occurred, smouldering can exist for long periods and extinguishment is dependent on heavy rainfall or fire-fighting attempts (Rein 2013; 2016; Zaccone et al. 2014). Determination of flaming and smouldering phases of peatland combustion from remote sensing data is important for peat fire management before the fire extends into a large area. However, routine satellite-based monitoring to supply smouldering and flaming information has not yet been effectively established. MODIS and VIIRS sensors, generate routine global active fire monitoring products with a low spatial resolution of 1000 m (MODIS), 375 m and 750 m (VIIRS). These sensors utilise

the Middle InfraRed (MIR) and Thermal InfraRed (TIR) to detect active fires with algorithms utilising at a contextual approach, aimed at identifying a combustion pixel relative to a local background and consist of pathways to establish potential fire pixels (Giglio, Kendall & Justice 1999; Justice et al. 1996; Kaufman et al. 1998).

Research on detection of peatland combustion has been conducted with medium spatial resolution at 30-100 m, Landsat-8 nighttime data, using an implementation of Planck's Law on radiant emission and temperature from ShortWave InfraRed (SWIR) and TIR in Indonesia's Kalimantan peatland (Elvidge et al. 2015). At night, no sunlight interferes with the SWIR and TIR radiances over fire areas with sensors only recording emitted radiation. However, the availability of Landsat-8 night-time data is limited with provision only for special requests. There is a possibility to utilise daytime Landsat-8 data, which is freely available every 16 days (atmosphere permitting) to produce flaming and smouldering information. Flaming detection has been explored by Schroeder et al. (2016) who measured SWIR radiance (band 7) of Landsat-8, which reached saturation from 30 m^2 areas of woody burning material in Germany and Brazil, where ground fire temperatures were measured between 870 and 970 K as obtained from a thermal handheld sensor. Dennison and Roberts (2009) found that SWIR bands at 2.061 and 2.429 μm could be utilised in the Hyperspectral Fire Detection Index (HFDI) for flaming detection. Meanwhile, the detection of peatland smouldering based on satellite remote sensing in daytime data remains a challenge, due to its lower radiant emission than that from flaming. The lower temperature of smouldering combustion may be more accurately captured through the use of the longer wavelength infrared or TIR.

In this research, investigation of daytime Landsat-8 data was conducted to distinguish peatland flaming and smouldering states. Landsat-8 has the spectral capability to detect combustion from SWIR and TIR, and also with its medium spatial resolution of 30 m and 100 m, potentially able to detect small burning areas that are often found in the field especially in the initial stages of combustion. This information will be useful for early fire suppression before it extends into a larger area.

2.2. **Material and Methods**

The study area for this research is located in Central Kalimantan, one of the severe peat fire areas in Indonesia. Level 1T (Terrain Corrected) Landsat 8 data (path/row

118/062; August 3rd and 19th, 2015) of the study area were accessed through the U.S. Geological Survey (USGS) Earth Explorer website. The MODIS fire-mask product-collection 6 for both days 3rd and 19th August 2015 were used in order to compare with the Landsat-8's results.

The first identification of possible combustion was from visual inspection of the false colour image composite: bands 764 to Red Green Blue (RGB). Potential combustion areas were further investigated using a SWIR index which is here named as the ShortWave InfraRed Combustion Index (SICI), the ratio of radiance of bands 6 and 7 of Landsat-8, combined with the SWIR and TIR radiances. Based on Planck's Law (relating temperature and wavelength), smouldering fire states will have lower SWIR radiance than flaming, and higher TIR radiance. Subsequently the combustion temperature was estimated using a radiative transfer model (MODTRAN4) combined with Planck's equation for SWIR and TIR (Barduci et al. 2004; Qian and Kong 2012). To evaluate the precision of the combustion detection, the results were overlaid with the same data of RGB images of Landsat-8. In addition, the results were also compared with the MODIS fire-mask product.

2.3. **Results and Discussion**

2.3.1. Peat Combustion Identification

Since the ground validation of peatland combustion was not available at the date of Landsat-8 observations of the study area, the potential combustion areas were visually interpreted from the RGB-764 of Landsat-8. There were nine and 22 samples of potential combustion areas visible in these images in August 3rd and 19th, 2015 respectively in Central Kalimantan's peatland, as shown in Figure 2.1a and 2.1b. The enlarged picture of sample number 9 in Figure 2.1a shows bluish smoke emanating from combustion areas surrounding the burnt area in magenta tones. Sixteen days after that, Figure 2.1b showed an extended burnt area in and around and south-west of sample number nine with some active combustion areas showing bluish smoke in the lower-left part of burnt area. The combustion pixels exhibit in light yellow tones surrounded with orange and pink tones. All the potential combustion areas and non-combustion areas were then analysed statistically to obtain the radiance value of each SWIR and TIR band of Landsat-8. The potential combustion areas and non-combustion areas were chosen by selecting the area which has SWIR and TIR radiances less than and equal to 33% of coefficient of variation

(the ratio of the standard deviation to the mean) from each landcover. In the study area, the landcover types which represented the non-combustion areas were burnt area, forest, and urban. Most combustion areas were located around burnt areas or vegetated areas (forest) as extensions of plantation areas. Urban/city areas are typically bright (high radiance) and therefore could be a potential source of commission errors in the calculation of combustion area. The selected areas are shown in Figure 2.1a. There were 563 potential combustion pixels. Non-combustion areas consisted of 1,594 pixels of burnt area, 84,049 pixels of forest, and 8,424 pixels of urban that were visually interpreted from the RGB images of Landsat-8. In Figure 2.1c box plots contain the minimum, quartile-1, median, quartile-3, and maximum values for combustion and non-combustion areas for every SWIR's radiance (band 6 and 7) and TIR's radiance (band 10). These show, not unsurprisingly, that combustion areas had highest radiance in bands 6 and 7 compared with other objects, while in band 10 the radiances of combustion areas were close to those of burnt areas. Some of the pixels in the combustion areas were close to saturation at radiances of 89.8, 28.5, and 20.9 $Wm^{-2}sr^{-1}\mu m^{-1}$ at band 6, band 7, and band 10, respectively. Even though the median values of combustion and burnt areas were about 11 $Wm^{-2}sr^{-1}\mu m^{-1}$, none of the burnt area radiances were close to saturation in band 10. In Figure 2.1d, the SICI box plot of combustion areas shows about 75 % of SICI were different to burnt area SICI values. About 25 % of the SICI values in combustion areas exhibited the same values as that of burnt and urban areas. In order to have the maximum identification of potential combustion areas, and minimum mixture with burnt and urban areas, SICI values less than the 1st quartile of burnt areas (3.0) were adopted. The SICI value at 3.0 is shown with a blue line in Figure 2.1d. The potential combustion areas were then investigated further using radiance values of bands 7 and 10 as presented in Figure 2.1c to separate the combustion areas from non-combustion areas (burnt area, urban, and forest).

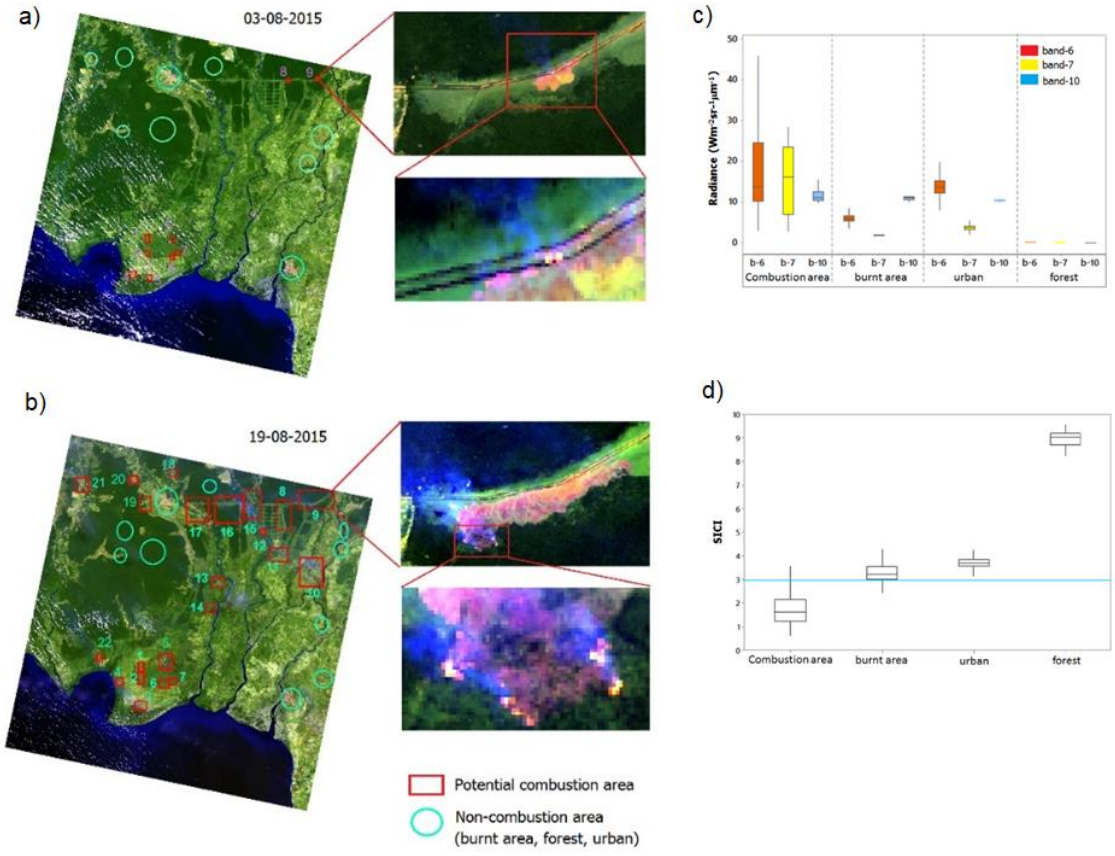


Figure 2.1. (**a, b**) The 764-RGB image of Landsat-8 on August 3rd and August 19th, 2015 with 9 samples and 21 samples respectively of potential combustion areas shown inside red squares and non-combustion areas inside cyan circles, respectively. An enlargement of one potential combustion sample area is presented on the right side of each Landsat image, (**c**) Box plots of radiance values of SWIR and TIR bands over combustion, burnt, forest, and urban areas, (**d**) SICI's box plots in combustion and non-combustion areas with the blue line indicating a threshold of 3.0 (the 1rd quartile value of burnt area) which was used to separate combustion from other areas [numerical data corresponding to this figure is available in Appendix - Table A2.1].

An example of identification of peatland combustion using the SICI, SWIR radiance, and TIR radiance is shown in Figure 2.2. The combustion area in the 764-RGB image, shown in orange to yellow tones (Figure 2.2a), had radiance values that were close to SWIR (band 7) saturation at 24–29 $Wm^{-2}sr^{-1}\mu m^{-1}$ (Figure 2.2b). This agreed with findings by Schroeder et al. (2016). These areas are observed with TIR radiance greater than 12 $Wm^{-2}sr^{-1}\mu m^{-1}$ (saturation occurs at 20.9 $Wm^{-2}sr^{-1}\mu m^{-1}$ for band 10) (Figure 2.2c). SICI values less than 3.0 represented the potential combustion area shown in Figure 2.2d. Pixels with SWIR and TIR's radiance close to saturation were assumed in a flaming stage (Figure 2.2e), while the other neighbouring pixels located inside the SICI < 3.0 area with lower radiance values than flaming pixel, i.e. 11–20 $Wm^{-2}sr^{-1}\mu m^{-1}$ for band 7 and 11–20.9

$Wm^{-2}sr^{-1}\mu m^{-1}$for band 10, were assumed to be in a smouldering stage (Figure 2.2f); these corresponded to the orange tones in the 764-RGB image (Figure 2.2a). The classified flaming and smouldering areas were merged in Figure 2.2g. However, some of combustion pixels were not identified as flaming or smouldering pixels in Figure 2.2g. These were then classified as mixed pixels, exhibiting both flaming and smouldering states. The mixed pixels had lower TIR (band 10) radiances compared with flaming and smouldering pixels. In Figure 2.2h, the mixed flaming and smouldering pixels are mapped in a cyan tone. The median values of SICI of flaming, smouldering, and mixture of flaming and smouldering pixels were 1.4, 2.2, and 2.6, respectively (Figure 2.2i).

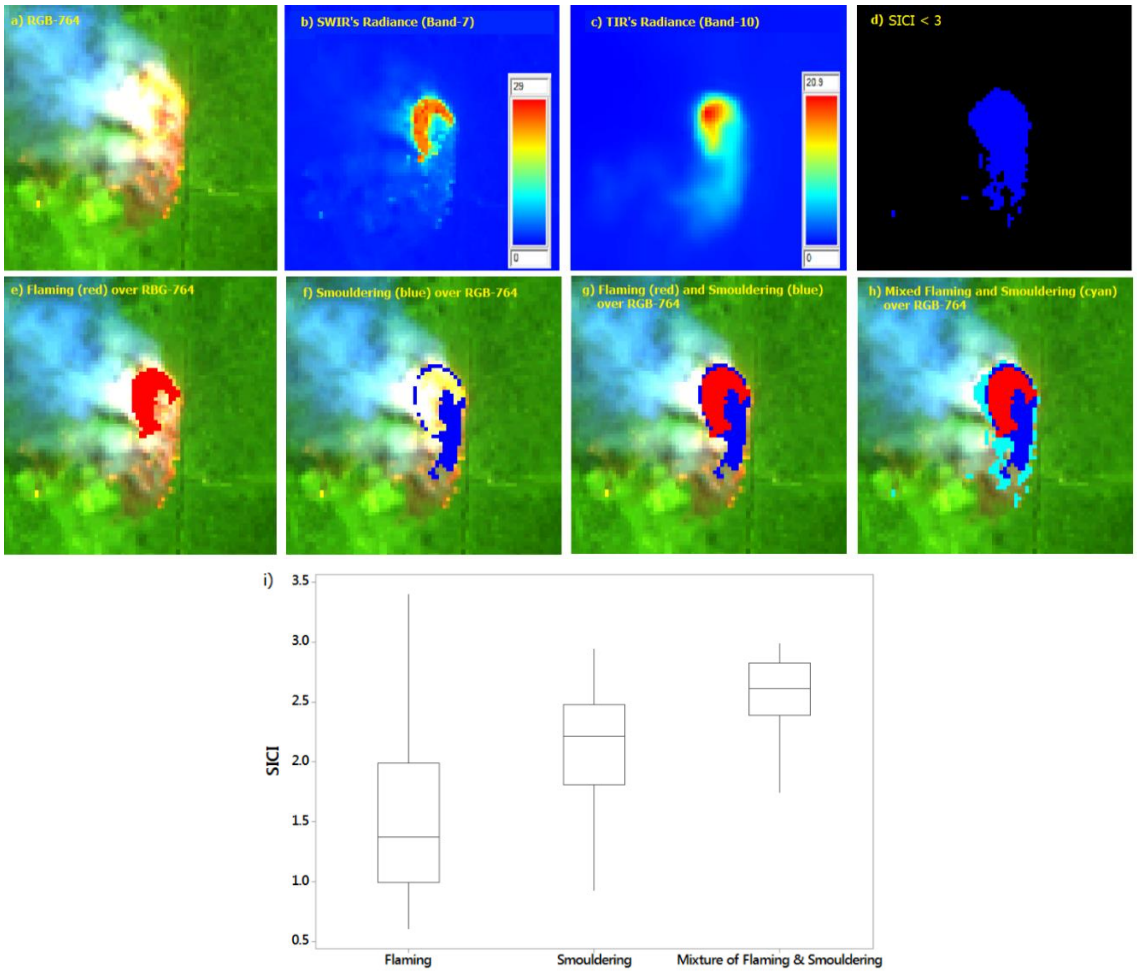


Figure 2.2. Example of peatland combustion identification (**a**) Smoke in pale bluish tones showed in 764-RGB with the potential combustion area in orange to yellow tones, (**b** & **c**) Pseudo colour of the radiance of band-7 and band-10 respectively were just under / at saturation, (**d**) The SICI < 3 in blue as the potential combustion area, (**e**, **f**, **g**) The identified flaming (red) and smouldering (blue) areas, (**h**) Mixture of flaming and smouldering areas shown in cyan over the 764-RGB image, (**i**) Box plots of SICI over flaming, smouldering, and mixture of flaming and smouldering areas.

2.3.2. Fire Temperature Estimation

The estimated fire temperature based on SWIR (bands 6-7) and TIR (band 10) over identified combustion pixels in Landsat-8 images on 3rd and 19th August 2015 is plotted in Figure 2.3. Figure 2.3a shows a boxplot representing the minimum, quartile 1st, median, quartile 3rd and maximum values of smouldering (S), mixture of flaming and smouldering (FS), and flaming (F). There were 402 S pixels in range of 320 K to 499 K, 8,587 FS pixels in range of 500 K to 665 K, and 103 F pixels with temperature of 700 K to 758 K. The median values of S, FS, and F temperatures were about 476 K, 585 K, and 722 K, respectively. According to Usup et al. (2014), smouldering temperatures observed from ground measurements were about 320–500 K, and Elvidge et al. (2015) found smouldering close to flaming at about 500–700 K, and flaming at about 700–1000 K. Thus, the estimated peatland fire temperatures from Landsat-8 in all the peatland combustion stages were in the range of those provided by Usup et al. (2014) and Elvidge et al. (2015) but estimated flaming temperatures could not be higher than 758 K due to the saturation of band-6 in Landsat-8. Figure 2.3b shows a dotplot of S, FS, and F temperatures with each dot representing the average of up to 32 observations. The dotplot shows the distribution of the estimated fire temperature from SWIR and TIR bands. Figure 2.3b also shows the distribution of FS temperature with two peaks of temperature of 505 K and 595 K which represented the most common temperatures in FS. However, the dotplot of FS shows a left skewed distribution which possibly means a higher contribution of flaming than smouldering temperatures.

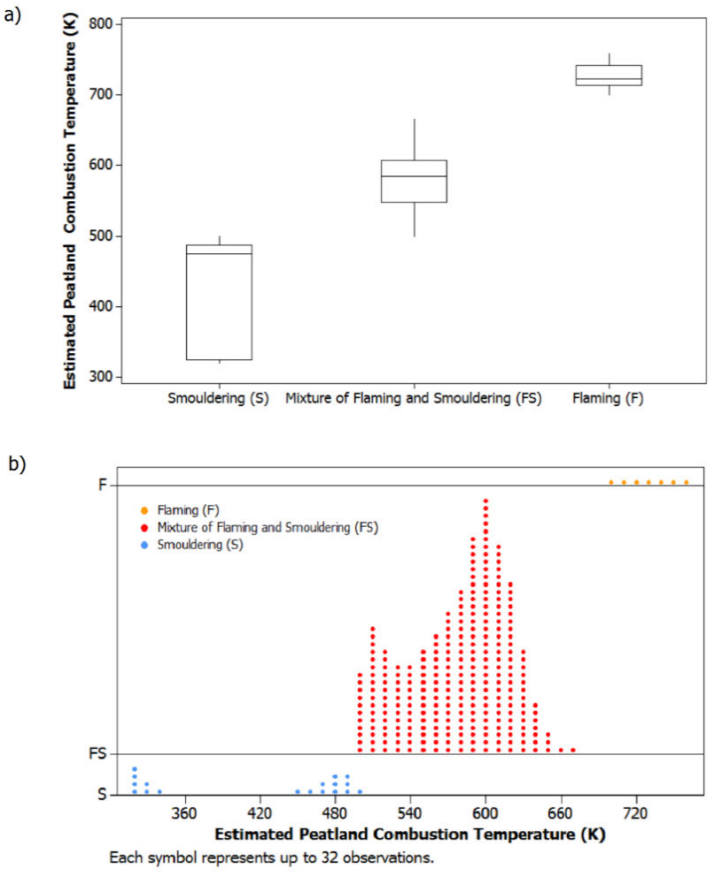


Figure 2.3. (**a**) Boxplot represents the minimum, quartile 1st, median, quartile 3rd and maximum values of smouldering (S), mixture of flaming and smouldering (FS), and flaming (F), (**b**) The dotplot of estimated peatland combustion temperature on F, FS, and S with two peaks of temperature and left-skewed distribution indicating a higher contribution of flaming than smouldering to FS temperature.

2.3.3. Precision and Comparison

The methodology outlined in section 3.1 was implemented over two images including all 31 of potential combustion areas and non-combustion areas. Table 2.1 shows the 31 of potential combustion areas identified as flaming (F), smouldering (S) or mixture of flaming and smouldering (FS). Overall, the result of combustion identification over all the 31 samples shows good mapping precision (Table 2.1). The mixture of flaming and smouldering pixels was identified in all the samples, while flaming or smouldering did not exist in every sample. The spatial resolution (100 m) of TIR may lead to the apparent mixture of flaming and smouldering stages. In one case, the mixture of flaming and smouldering was also found in a commission error in a burnt area separate from a combustion area. In one combustion area experiencing smoky conditions, the flaming and smouldering detection had an omission error leading to less combustion pixels being detected. The mixed flaming and smouldering pixels were also over mapped, producing commission errors over urban areas. The total hit detection was 31 samples with one sample of omission error and six samples of commission error. Overall, the precision of

combustion detection was about 77 % compared to the visual interpretation of 764-RGB image. This is an early estimation of mapping precision and is not an estimate of accuracy which can only be achieved with independent data such as ground data. To reduce omission and commission errors issues associated with smoke, cloud, urban land cover, and bright objects will be dealt with in the next step in the research.

Table 2.1. Detection of flaming (F), smouldering (S), and mixture of flaming and smouldering (FS) over 2 Landsat-8 images (03-08-2015 and 19-08-2015). The hit, Commission (C) and Omission (O) Errors were derived from comparison with the 764-RGB of Landsat-8.

Landsat-8 (03-08-2015)							Landsat-8 (19-08-2015)						
No	Hit			O	C	Note	No	Hit			O	C	Note
	F	S	FS					F	S	FS			
1	√	-	√	-	-	with smoke	1	√	-	√	-	-	with smoke
2	√	-	√	-	-	with smoke	2	√	-	√	-	-	with smoke; Extended burning area from 03-08-2018
3	√	-	√	-	√	Commission on FS over burnt area	3	√	√	√	-	-	with smoke
4	-	-	√	-	√	No smoke	4	√	-	√	-	√	No smoke
5	√	-	√	-	-	with smoke	5	√	-	√	-	-	Extended burning area from 03-08-2018 with smoke
6	√	-	√	-	-	with smoke	6	√	√	√	-	-	Extended burning area from 03-08-2018 with smoke
7	-	-	√	-	-	No smoke	7	√	-	√	-	-	No smoke
8	-	-	√	-	-	with smoke	8	√	-	√	-	-	with smoke
9	√	-	√	-	-	with smoke	9	√	√	√	-	-	with smoke
							10	√	√	√	-	√	with smoke; commission of FS over burnt area
							11	√	-	√	-	-	with smoke
							12	-	-	√	-	-	with smoke
							13	√	√	√	√	-	less detection over smoky condition
							14	-	√	√	-	-	with smoke
							15	√	√	√	-	-	with smoke
							16	√	√	√	-	-	with smoke
*	-	-	-	-	√	Non-combustion area, commission error of FS over urban and cloud	17	√	-	√	-	-	with smoke
							18	-	-	√	-	-	with smoke
							19	√	√	√	-	-	with smoke
							20	√	-	√	-	-	with smoke
							21	-	√	√	-	-	with smoke
							22	√	√	√	-	-	with smoke
							*	-	-	-	-	√	Non-combustion area, commission error of FS over urban

In addition to precision analysis, the results were also compared with the MODIS fire-mask product at the same date and the same location, but slightly different in time. In the first image acquired on August 3rd, 2015, there was only one MODIS acquisition

at the location with a time about four hours later than Landsat-8 (Landsat-8 acquired at 09.34 am while MODIS at 01.35 pm). According to Usup et al. (2004) the maximum spreading time of peatland fire is 6.5 cm/hour at the peat surface (0–20 cm); thus within four hours of the Landsat-8 observation the MODIS observations of the peatland fires potentially corresponded to combustion 26 cm different in position to that observed by Landsat-8. However, of all nine samples of combustion areas found in Landsat-8, the MODIS fire-mask only detected one at location number two (Figure 2.4). The MODIS fire mask did not detect the other eight combustion areas. Of the eight combustion areas not detected by the MODIS fire-mask product, two combustion areas were cloud covered, which possibly caused the non-detection of fire, while six combustion areas with clear sky were undetected by MODIS.

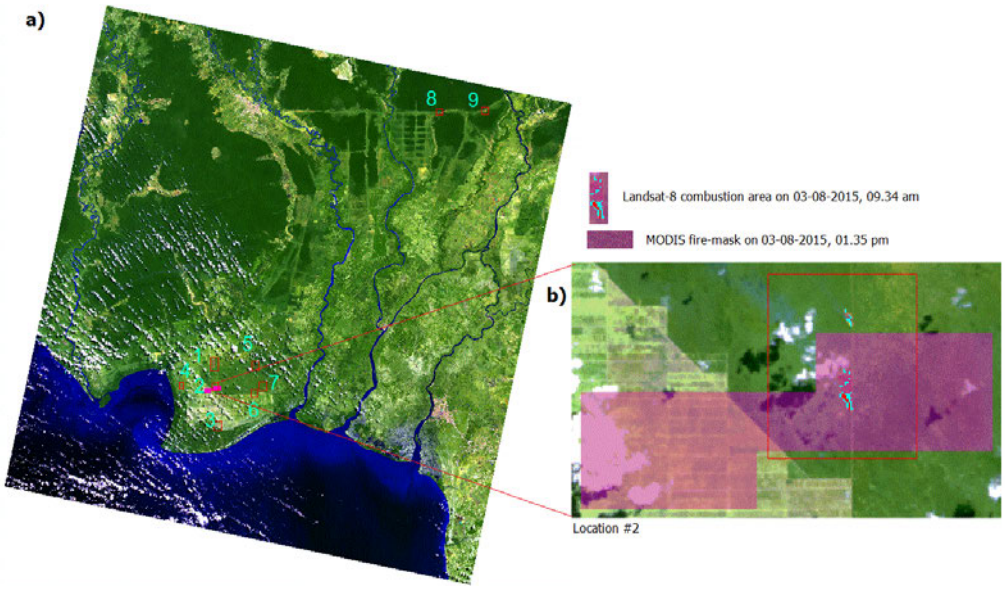


Figure 2.4. (**a**) The nine combustion areas shown in red square and MODIS fire-mask (pink) overlaid on the Landsat-8 764-RGB image of August 3rd, 2015. The MODIS fire-mask only appeared in location #2, (**b**) Enlargement of location #2 showing the MODIS fire-mask (pink) transparency overlaid on the Landsat-8 image which is showing a combustion area in red and cyan (centre right).

The second Landsat-8 image in study area was acquired on 19th August 2015 at 09.35 am, while on the same date and location MODIS fire-masks were available at 01.35 pm and 10.20 pm, thus generating a difference in time with the Landsat acquisition of about four hours and 12 hours respectively. These time differences translate to maximum peat fire spread of about 26 cm and 78 cm (Usup et al. 2004), respectively. Figure 2.5a shows the 22 combustion areas (red squares) on the 764-RGB image of Landsat-8 overlaid with MODIS fire-mask data at 01.35 pm (magenta) and 10.20 pm (yellow). There were only

six combustion areas detected by the MODIS fire-mask at 01.35 pm, with only two of them remaining detected at 10.20 pm, and two other combustion areas additionally detected at 10.20 pm; thus, a total of eight combustion areas detected by MODIS fire-mask. Of the other 14 combustion areas not detected by MODIS fire-mask, five of them were due to cloud cover, while the nine remaining combustion areas were undetected even with a clear sky condition. Figure 2.5b is the enlargement of combustion areas 15 and 16, which matched with the MODIS fire-mask, while in Figure 2.5c there was one commission error of MODIS fire-mask at 01.35 pm over a bare plantation area.

Overall, the comparison of data from the MODIS fire-mask for peat combustion areas with combustion identified from Landsat-8 resulted in nine agreements (29 %) out of 31 for combustion, while 22 areas were undetected (71 %). The undetected combustion areas in the MODIS fire-mask were due to cloud cover (seven areas), low fire temperature and MODIS pixel size, which at one km would reduce detectability of small fires. One commission error in the MODIS fire mask was also found over a bare plantation area.

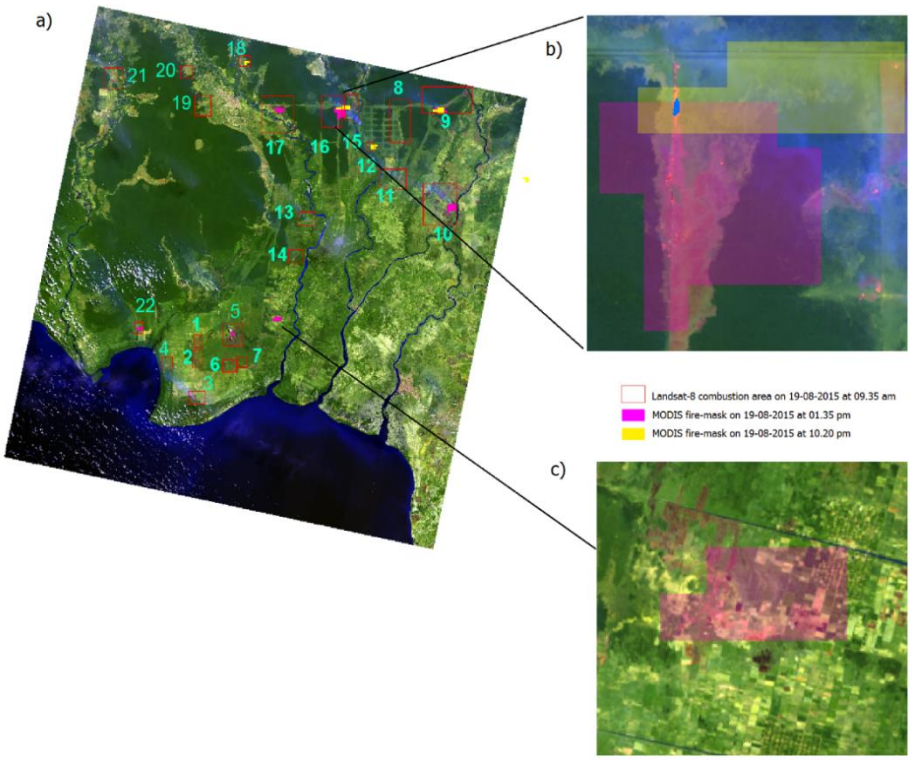


Figure 2.5. (**a)** The 22 combustion areas shown in red squares and MODIS fire-mask (pink and yellow) overlaid on the Landsat-8 764-RGB image of August 19th, 2015, (**b**) Enlargement of locations of #15 and #16 showing the MODIS fire-mask (pink and yellow) transparency overlaid on Landsat-8's combustion area; the blue polygon represents smouldering area generated from Landsat-8, (**c**) Enlargement of commission error of MODIS fire-mask at 01.35 pm over bare plantation area.

2.4. **Conclusion**

Analysis of the SWIR and TIR bands of daytime Landsat-8 data indicates that it is potentially possible to discriminate flaming and smouldering stages in peatland combustion. The SICI integrated with the radiances of band-7 and band-10 of Landsat-8 can be used for separating combustion and non-combustion areas. The detected peatland combustion showed about 77 % precision compared with visual observations of the 764-RGB images of Landsat-8. Whilst there is room for further improvement, this is significantly better than the 71 % of MODIS fire-mask which is widely used for global fire monitoring. The algorithm when applied to Landsat 8 imagery was able to detect combustion areas that could not be mapped using the lower spatial resolution MODIS fire-mask, especially in small burning areas as usually occur in peatland fires. The estimated peat fire temperatures from Landsat-8 aligned with prior research, but the estimated flaming temperatures cannot be higher than 758 K due to the saturation temperature of Landsat-8. However, further analysis is required for verification with a simultaneous field measurements. This algorithm has the potential to be used on a routine basis due to the availability of Landsat-8 data during daytime every 16 days, provided cloud cover permits. It is possible that some merging of information from Landsat and higher temporal but lower spatial resolution satellites (e.g. Sentinel-2 and Sentinel-3, and maybe Himawari) can assist in interpolating the temporal gaps in Landsat data and when cloud cover inhibits use of Landsat. The algorithm presented in this research can also be implemented for forest fire mapping at a detailed scale, as its spatial resolution (30 m) is higher than the standard fire products (1 km). We are currently trialling and validating other algorithms with further research ongoing, as this work is part of a larger project, which is investigating automated smoke detection and soil moisture measurements in the mapping of peatland combustion.

References

Barducci, A, Guzzi, D, Marcoionni, P & Pippi, I 2004, 'Comparison of fire temperature retrieved from SWIR and TIR hyperspectral data', Infrared Physics & Technology, vol. 46, no. 1-2, pp. 1–9.

Burrows, L 2016, *Smoke from 2015 Indonesian fires may have caused 100,000 premature deaths. Research quantifies effects of fires in Equatorial Asia, offers new approach to inform fire management efforts*, Harvard John A. Paulson School of Engineering and Applied Sciences, 19 September, viewed 10 February 2018, <https://www.seas.harvard.edu/news/2016/09/smoke-2015-indonesian-fires-may-have-caused-100000-premature-deaths>.

Csiszar, I, Schroeder, W, Giglio, L, Ellicott, E, Vadrevu, KP, Justice, CO & Wind, B 2014, 'Active fires from the Suomi NPP Visible Infrared Imaging Radiometer Suite: Product status and first evaluation results', *Journal of Geophysical Research: Atmospheres*, vol. 119, no. 2, pp. 803–816.

Dennison, PE & Roberts, DA 2009, 'Daytime fire detection using airborne hyperspectral data', *Remote Sensing of Environment*, vol. 113, no. 8, pp. 1646–1657.

Elvidge, CD, Zhizhin, M, Hsu, F, Baugh, K, Khomarudin, M, Vetrita, Y, Sofan, P, Suwarsono & Hilman, D 2015, 'Long-wave infrared identification of smoldering peat fires in indonesia with nighttime landsat data', *Environmental Research Letters*, vol. 10, no. 6, p. 065002.

Giglio, L, Kendall, JD & Justice, C 1999, 'Evaluation of global fire detection algorithms using simulated AVHRR infrared data', *International Journal of Remote Sensing*, vol. 20, no. 10, pp. 1947–1985.

Giglio, L, Schroeder, W & Justice, C 2016, 'The collection 6 MODIS active fire detection algorithm and fire products', *Remote Sensing of Environment*, vol. 178, pp. 31–41.

Hayasaka, H, Takahashi, H, Limin, SH, Yulianti, N & Usup, A 2016, 'Peat Fire Occurrence', in M Osaki & N Tsuji (eds), *Tropical Peatland Ecosystems*, Springer Japan, Tokyo, pp. 377–395.

Justice, C, Giglio, L, Korontzi, S, Owens, J, Morisette, J, Roy, D, Descloitres, J, Alleaume, S, Petitcolin, F & Kaufman, Y 2002, 'The MODIS fire products', *Remote Sensing of Environment*, vol. 83, no. 1, pp. 244–262.

Justice, C, Kendall, J, Dowty, P & Scholes, R 1996, 'Satellite remote sensing of fires during the SAFARI campaign using NOAA advanced very high resolution radiometer data', *Journal of Geophysical Research: Atmospheres*, vol. 101, no. D19, pp. 23851–23863.

Kaufman, Y, Justice, C, Flynn, LP & Kendall, JD 1998, 'Potential global fire monitoring from EOS-MODIS', *Journal of Geophysical Research: Atmospheres*, vol. 103, no. D24, pp. 32215–32238.

Miettinen, J, Hooijer, A, Wang, J, Shi, C & Liew, SC 2012, 'Peatland degradation and conversion sequences and interrelations in Sumatra', *Regional Environmental Change*, vol. 12, no. 4, pp. 729–737.

Qian, YG & Kong, XS 2012, 'A method to retrieve subpixel fire temperature and fire area using MODIS data', International Journal of Remote Sensing, vol. 33, no. 16, pp. 5009–5025.

Rein, G 2013, 'Smouldering fires and natural fuels', *Fire Phenomena and the Earth System: An Interdisciplinary Guide to Fire Science*, vol. Chapter 2, pp. 13–22.

Rein, G 2016, 'Smouldering Combustion', in MJ Hurley et al (eds), *SFPE Handbook of Fire Protection Engineering*, Springer New York, New York, NY, pp. 581–603.

Rieley, J & Page, S 2016, 'Tropical peatland of the world', in M Osaki & N Tsuji, N (eds), Tropical peatland ecosystems, Springer, Tokyo, Japan, pp. 3–32, ISBN 978-4-431-55680-0, doi: 10.1007/978-4-431-55681-7.

Schroeder, W, Oliva, P, Giglio, L & Csiszar, I 2014, 'The New VIIRS 375 m active fire detection data product: Algorithm description and initial assessment', *Remote Sensing of Environment*, vol. 143, pp. 85–96.

Schroeder, W, Oliva, P, Giglio, L, Quayle, B, Lorenz, E & Morelli, F 2016, 'Active fire detection using Landsat-8/OLI data', *Remote Sensing of Environment*, vol. 185, pp. 210–220.

Usup, A, Hashimoto, Y, Takashi, H & Hayasaka, H 2004, 'Combustion and thermal characteristics of peat fire in tropical peatland in Central Kalimantan, Indonesia', *Tropics*, vol. 14, no. 1, pp. 1–19.

World-Bank 2016, *The Cost of Fire: An Economic Analysis of Indonesia's 2015 Fire Crisis*, Indonesia Sustainable Landscape Knowledge Note: 1 (World Bank Group).

Zaccone, C, Rein, G, D'Orazio, V, Hadden, RM, Belcher, CM & Miano, TM 2014, 'Smouldering fire signatures in peat and their implications for palaeoenvironmental reconstructions', *Geochimica et Cosmochimica Acta*, vol. 137, 7/15/, pp. 134–146.

Chapter 3

Detection and Validation of Tropical Peatland Flaming and Smouldering using Landsat-8 SWIR and TIRS Bands

This chapter is published as:

Sofan, P.; Bruce, D.; Jones, E.; Marsden, J. Detection and Validation of Tropical Peatland Flaming and Smouldering Using Landsat-8 SWIR and TIRS Bands. *Remote Sens.* 2019, *11*, 465.

(https://doi.org/10.3390/rs11040465)

Note: Minor additional information is inserted in [squared brackets]

Detection and Validation of Tropical Peatland Flaming and Smouldering using Landsat-8 SWIR and TIRS Bands

Abstract

A Tropical Peatland Combustion Algorithm (ToPeCAl) was first established from Landsat-8 images acquired in 2015, which were used to detect peatland combustion in flaming and smouldering stages. Detection of smouldering combustion from space remains a challenge due to its low temperature and generally small spatial extent. The ToPeCAl consists of the ShortWave InfraRed Combustion Index based on reflectance ($SICI_{\rho}$), and Top of Atmosphere (TOA) reflectance in ShortWave InfraRed band-7 (SWIR-2), TOA brightness temperature of Thermal InfraRed band-10 (TIR-1), and TOA reflectance of band-1, the Landsat-8 aerosol band. The implementation of ToPeCAl was then validated using terrestrial and aerial images (helicopter and drone) collected during fieldwork in Central Kalimantan, Indonesia in the 2018 fire season, on the same day as Landsat-8 overpasses. The overall accuracy of ToPeCAl was found to be 82% with omission errors in a small area (less than 30 m × 30 m) from mixtures of smouldering and vegetation pixels, and commission errors (with minimum area of 30 m × 30 m) on high reflective building rooftops in urban areas. These errors were further reduced by masking and removing urban areas prior to analysis using landuse Geographic Information System (GIS) data; improving the overall mapping accuracy to 93%. For comparison, the day and night-time VIIRS (375 m) active fire product (VNP14IMG) was utilised, obtaining a lower probability of fire detection of 71% compared to ground truth, and 57–72% agreement in a buffer distance of 375 m to 1500 m when compared to the Landsat-8 ToPeCAl results. The night-time data of VNP14IMG was found to have a better correspondence with ToPeCAl results from Landsat 8 than day-time data. This finding could lead to a potential merger of ToPeCAl with VNP14IMG to fill the temporal gaps of peatland fire information when using Landsat. However, the VNP14IMG product exhibited overestimation compared with the results of ToPeCAl applied to Landsat-8.

Keywords: smouldering; flaming; peatland; tropical; Landsat-8; SWIR; TIR; ToPeCAl; VIIRS; VNP14IMG; validation; ground truth.

3.1. Introduction

Wildfire is a global issue which threatens every year during dry seasons. For almost two decades, forest/land fires have attracted both interest and challenge for research to provide a useful monitoring system from satellite remote sensing data (Csiszar et al. 2014; Giglio, Schroeder & Justice 2016; Justice et al. 2002). Tropical peatland fire is one type of forest/land fire which remains a challenge in providing a fire detection algorithm, due to the characteristics of tropical peat, its terrestrial environment and tropical atmospheres.

Approximately 47% of global tropical peatlands exist in Indonesia. These peatlands were formed as spacious domes that consist of the woody and partly decomposed remains of rainforest trees (branches, leaves, roots and trunks). These domes sustain a peat swamp forest that encompass large areas of lowland landscape between major rivers (Page, Rieley & Banks 2011; Rieley & Page 2016). Under undisturbed conditions, the Indonesian peatland store about 57.4 Gt of Carbon, or 65% of the total global tropical peatland Carbon (Page, Rieley & Banks 2011; Rieley & Page 2016). However, large areas of tropical peatlands in Indonesia have been degraded due to slash and burn activities for development of plantations such as oil palms, rubber, and pulp trees, and for food production (Osaki et al. 2016; Tacconi 2003). In 2015, the forest and peatland fires in Indonesia caused a total economic loss of about USD 16 billion and emitted 1.75 Gt of Carbon into the atmosphere (World-Bank 2016). Although the Indonesian government has declared a zero burning law for land clearance (Law No.32/2009), the Peatland Conversion Moratorium (23 October 2015) and the Peatland Restoration Agency establishment (January 2016), slash and burn activity is still regularly used for land preparation, as it has an economic benefit to farmer groups, given the continuing market demand for illegal land for plantations (Purnomo et al. 2017).

A large coverage in near real-time observation of forest/land fire can be obtained freely from the coarse spatial resolution of satellite sensors such as Geostationary Operational Environmental Satellite System, Meteosat Second Generation-Spinning Enhanced Visible and Infrared Imager, Advanced Very High Resolution Radiometer, Moderate Resolution Imaging Spectroradiometer (MODIS), Visible Infrared Imaging Radiometer Suite (VIIRS), and Advance Himawari Imager (Caúla et al. 2015; Csiszar et al. 2014; Filizzola et al. 2016; Fuller 2000; Giglio, Schroeder & Justice 2016; Hally et al. 2016; Langner & Siegert 2009; Schroeder et al. 2014; Xu et al. 2010). Among them, the

MODIS and VIIRS active fire products have been used by the Indonesian Disaster Management Agency (BNPB) for guidance in monitoring forest/land fires in the field. According to the local BNPB in Central Kalimantan, Indonesia, most of the peatland fires found in the field were in flaming stages (BNPB 2018). The properties of smouldering peat fire, which generates a lower radiance intensity and a lower temperature than flaming (Rein 2016), as well as the coarse spatial resolution likely explain why smouldering fires are often not detected by the above-mentioned satellite fire detection products (Hantson et al. 2013; Hawbaker et al. 2008). Significant smoke generated during fire events and cloud cover can also obscure fire detection (Jones et al. 2018; Loboda & Csiszar 2007). Other than that, smouldering peat fire often occurs in small areas with low spread rates which, if left unattended, can extend into large areas (Rein 2013; 2016; Zaccone et al. 2014). However, smouldering peat fire releases higher concentrations and particulate carbon emissions, such as carbon monoxide and methane, than peat in a flaming state (Koppmann, von Czapiewski & Reid 2005) and also produces larger particles than other fuels (Reid et al. 2005). Thus, it is important to know the location of the smouldering peat fires so that suppression occurs before extension into a larger area and to minimise damaging emissions.

Most of the global operational fire products from low spatial resolution satellite data (~1 km pixel size) use the 3-4 μm (Middle InfraRed (MIR)) and the 10–11 μm (Thermal InfraRed (TIR)) components of the electromagnetic spectrum to detect smouldering and flaming fires, which operate at temperatures from 400 to 1200 K (Giglio & Kendall 2001; Kelhä et al. 2003). However, small and smouldering fires are often undetectable in low spatial resolution data such as MODIS (Hantson et al. 2013; Hawbaker et al. 2008). The higher the spatial resolution of the satellite sensor the greater the portion of fire area that can be detected (Murphy et al. 2016). Research in the United States of America showed the minimum fire area detectable by MODIS was 105 ha (Hawbaker et al. 2008). The small satellite Hot Spot Recognition System-Bi spectral Infra-Red Detector, with its 370 m pixel size, successfully detects smouldering and flaming by estimating fire temperature in Central Kalimantan's peatland with a minimum fire area of 0.15 ha (Siegert et al. 2004). The other small satellite, which is a product of German Aerospace Center (DLR) FireBird Mission, is the Technology Experiment Carrier-1 (TET-1), with a 160 m spatial resolution; detects a minimum fire area of 0.01 ha at temperatures at 500 K or 1 ha at 450 K (smouldering), with a repeated observation of 2–3 days (Mitchell et al. 2016). The MIR

sensor of TET-1 has a high-temperature saturation up to 900 K, which is able to detect peat fire through smoke and haze (Atwood et al. 2016). However, TET-1 data capture on a regular basis is not operational and a specific request to DLR needs to be made for data over a certain region is required. Therefore, there is a need for accurate low-temperature smouldering fire detection in low cost or open-access high temporal frequency imagery with sufficiently small spatial resolution. In the moderate spatial resolution area (30 and 100 m pixels) and repeated observation of 16 days, sensors such us Advanced Space-borne Thermal Emission and Reflection Radiometer (ASTER) and Landsat-8 possibly could be used to detect flaming and smouldering peatland. ASTER has a higher temperature saturation than Landsat-8; however, ASTER is an on-demand instrument which means that data capture over a specific region on a regular basis is difficult to achieve. This is unlike Landsat-8 (Eckmann, Roberts & Still 2009; Giglio et al. 2008) which provides regular coverage (cloud permitting). Fire detection with ASTER data mainly employs the ShortWave InfraRed (SWIR) band and Near InfraRed band for eliminating bright objects (Giglio et al. 2008) and is utilised mainly for validation of the lower spatial resolution products from other sensors, due to its high-temperature saturation and finer spatial resolution (Csiszar et al. 2014; Giglio et al. 2008; Morisette et al. 2005; Polivka et al. 2016; Schroeder et al. 2008; Wooster, Xu & Nightingale 2012).

Instead of MIR data that are available in a lower spatial resolution sensor, the current Landsat-8 moderate spatial resolution sensor, Operational Land Imager (OLI) and Thermal InfraRed Sensor (TIRS) provide hot target detection (flaming fires) using SWIR at 1.6 and 2.2 μm (Murphy et al. 2016; Schroeder et al. 2016). Moreover, from hyperspectral data, the SWIR spectra at 2.061 and 2.429 μm were able to be used to detect flaming fire (Dennison & Roberts 2009). Meanwhile, (Elvidge et al. 2015) detected smouldering fires detection via the use of longwave Thermal InfraRed spectra and the implementation of Planck's radiation law, enabling estimation of fire temperature within a minimum area range of 40–90 m^2 using Landsat-8 night-time data with limited atmospheric disturbance and no sun radiation effects on fire temperature estimation; however Landsat-8 night-time data is also not operationally available like day-time data. Thus, smouldering peat fire detection during day-time needs to be explored. A recent active fire detection algorithm for global application of Landsat-8 day-time data was developed by Kumar and Roy (2018) using the SWIR and red reflectance bands and compared with other fire algorithms developed from Landsat-8 data (Murphy et al. 2016;

Schroeder et al. 2016). They revealed that the most significant underestimation of all three algorithms were found to be in Indonesian peat fires. Additionally, atmospheric issues may interfere with peat fire detection; in the dry season, most peat fires occur with very smoky conditions, thereby increasing the difficulty of satellite image interpretation, which has not been considered in previous research.

This study explores how flaming and smouldering of tropical peat fires, with a variety of atmospheric states (clear and smoke conditions) can be detected from the SWIR and TIR of Landsat-8 day-time data. Although the Landsat-8 day-time data is only available every 16 days, it still is very useful considering the fact that smouldering peat fire can occur from days to months depending on natural extinguishment from rainfall, or firefighting efforts. In 2015, smouldering fires lasted about six months in Central Kalimantan and South Sumatera. Additionally, a peatland combustion algorithm detection based on Landsat-8 data may be able to be applied to other satellite sensors such VIIRS with a lower spatial resolution (375 m), but higher temporal resolution (1–2 times per-day). Thus, the temporal gaps of peatland fire monitoring from a medium spatial resolution (20–30 m) sensor may be filled leading to much needed regular monitoring of peatland fires.

3.2. Materials and Methods

3.2.1. Study Site

Central Kalimantan is located at coordinates of 0°45'N–3°30'S and 110°45'E–115°51'E (BPS 2018a). It was selected as the study area due to the concentration of peatland of about 2.6 million ha, or 52% of the total peatland in Kalimantan. According to the Indonesian Bureau of Statistics (BPS 2018a), palm oil plantations occupy about 1.1 million ha in Central Kalimantan and most plantations exist in the peatland area. The algorithm development site inside the Central Kalimantan province was chosen based on analysis of optimised 'Hot Spot' of MODIS active fire product using the Getis–Ord method, which identifies a statistically significant spatial cluster of high values or 'Hot Spots' and low values or 'Cold Spots' (Getis & Ord 1992; Mitchell 1999). The Getis–Ord analysis of daily MODIS active fires from 2007–2017, as presented in Figure 3.1A, shows a high density of active fires or areas which can be regarded as fire prone in red polygons located in southern part of Central Kalimantan Province. The high density of fire-prone areas was overlaid with the peatland zones in green polylines from The

Ministry of Agriculture (MoA). This shows that the fires in Central Kalimantan predominantly occur in peatland. The Landsat-8 coverage of path/row 118/062 (magenta rectangle) in Figure 3.1A matched the location of this fire-prone area in the peatland of Central Kalimantan. Thus, this area was chosen as the algorithm development site (Figure 3.1A).

For validation purposes, an area outside of Central Kalimantan was selected in Riau Province. This is located in Sumatera Island with bounding coordinates of 2°25'N–1°05'S and 100°00'E–105°05'E (BPS 2018b). Riau Province has a larger peatland and plantation area than Central Kalimantan, with the largest peatland area in Indonesia (3.8 million ha) (Ritung, Wahyunto & Nugroho 2012). The mapping clusters of MODIS active fires in Riau Province are shown in Figure 3.1B with a dominant high 'Hot Spot' in the northern part of Riau Province (red polygons).

Based on the monthly pattern of rainfall versus the monthly count of MODIS active fires from January 2014–August 2018, the fire season in Central Kalimantan is generally associated with low rainfall levels in the dry season and with high counts of MODIS active fires, which mostly occur from July–October, while in Riau Province the fire-prone time generally occurs in two dry periods of February–March and June–August.

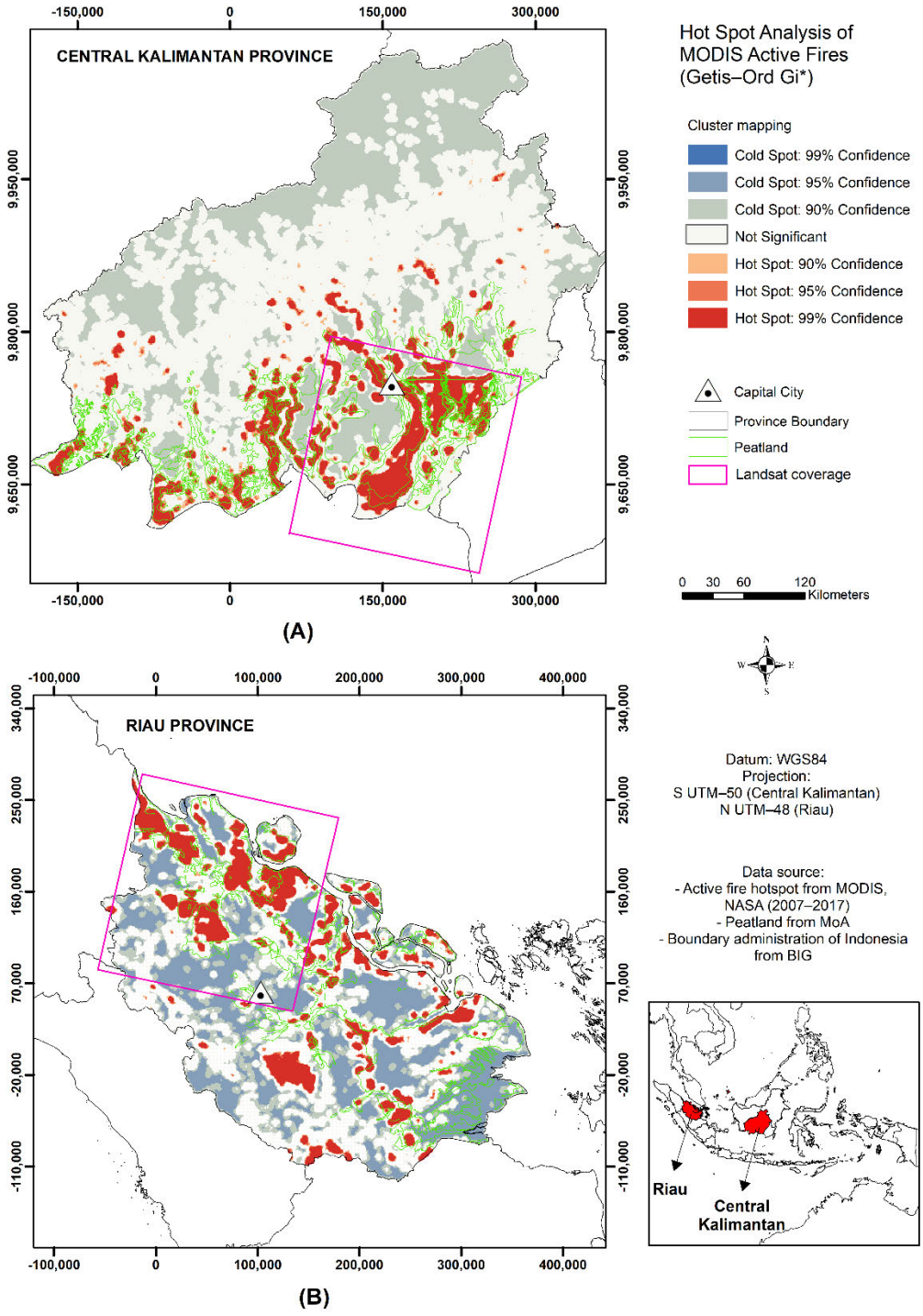


Figure 3. 1. (**A**) The algorithm development site analysed from the Getis–Ord optimised hotspot applied to 1 km grid cell counts of Moderate Resolution Imaging Spectroradiometer (MODIS) active fires (2007–2017) overlaid on peatland map in Central Kalimantan and (**B**) Validation site in Riau Province. The Hot Spots in red tones represent the high density of MODIS active fires with statistically significant confidence levels from 90% to 99%, while the Cold Spots, in blue tones, represent the low distribution of fire hotspots with statistical significance from 90% to 99%. The white colour is not statistically significant. The MODIS active fire source from The National Aeronautics and Space Administration-Fire Information for Resource Management System (NASA-FIRMS). Peatland map sources from the Ministry of Agriculture (MoA). The boundary administration is from Geospatial Information Agency (BIG).

3.2.2. Data

The satellite data used in this study were day-time Landsat-8 acquisitions, which are captured at ~9:34 am (local time) for path/row 118/062 in Central Kalimantan Province, Indonesia. Eleven Landsat-8 scenes with a cloud cover percentage taken from the metadata and haze condition analysed visually from the RGB images, are listed in Table 3.1. Five 2015 scenes were used for algorithm development in Central Kalimantan, while the other six scenes were used for implementation and validation purposes in Central Kalimantan and Riau province, Indonesia. The Landsat-8 OLI and TIRS data were obtained from the Earth Explorer Data Archive Centre of the United States Geological Survey (USGS) at Level 1T, with standard instrumental radiometric and geometric corrections based on Digital Elevation Model (DEM). The Level 1T product provides a resampling of TIRS thermal bands at 30 m from 100 m spatial resolution.

Table 3.1. List of Landsat-8 data used for algorithm development and validation. The algorithm development area was in Central Kalimantan (CK) using 2015 data, while validation analysis was conducted in Central Kalimantan (2018) and Riau Provinces (2016 and 2018).

Acquisition date	Path-row	Study site	Utilised for	Cloud cover (land)	Haze condition
3 August 2015	118-062	CK	development	1.48%	no haze
19 August 2015	118-062	CK	development	1.96%	thin smoke haze
4 September 2015	118-062	CK	development	47.2%	medium smoke haze
20 September 2015	118-062	CK	development	96.07%	thick smoke haze
22 October 2015	118-062	CK	development	99.69%	thick smoke haze
28 September 2018	118-062	CK	internal validation	3.96%	thin smoke haze
5 October 2018	119-062	CK	internal validation	40.50%	thin smoke haze
20 August 2016	127-059	Riau	external validation	29.08%	thin smoke haze
4 April 2018	127-059	Riau	external validation	38.67%	thin smoke haze
7 July 2018	126-059	Riau	external validation	77.55%	medium smoke haze
7 July 2018	126-060	Riau	external validation	43.29%	medium smoke haze

Moreover, pan-sharpened of Satellite Pour l'Observation de la Terre (SPOT)-6 and SPOT-7 images were used as a reference for fire locations with their high spatial

resolution of 1.5 m. The SPOT-6/7 data is available via on demand tasking through the Indonesian National Institute of Aeronautics and Space (LAPAN). During the fire period of 2015, due to the emergency situation of forest/peat fires in Kalimantan, LAPAN was tasked to acquire daily SPOT-6/7 images from LAPAN's ground station. In concordance with the Landsat-8 data period for developing the peatland combustion detection algorithm, the SPOT-6/7 data were acquired on 15–16 August, 18–22 September and 18 October 2015.

For comparison with an operational active fire data product the NASA Land-SIPS VIIRS 375 m active fire product (VNP14IMG) were compiled. To validate the peatland fire map results, ground truth was also collected from two sources: historical fire occurrence data from BNPB and direct ground truth in the field. The historical fire data from BNPB in 2015 were collected mainly using a terrestrial camera and GPS locations of the camera. However, in 2018, BNPB had the added capacity to monitor fires using aerial imaging from a drone and helicopters. Direct ground observation in Central Kalimantan was conducted on 28 September–5 October 2018. The data collection taken on direct ground survey were the position of peat fires using a GPS Montana 680, surface temperature using an IRtek IR150 dual beam laser infrared thermometer, with a specified temperature range of -60–1500 °C and accuracy ±2 °C, terrestrial peat fires pictures taken with a digital camera and aerial images from DJI Phantom Pro 4 drone. In addition weather conditions of air temperature, relative humidity and wind velocity were collected using a handheld anemometer amf-006.

3.2.3. Pre-processing of Landsat-8 Data

The multispectral bands of OLI and the thermal bands of TIRS were radiometrically corrected by converting pixel digital numbers to Top of Atmosphere (TOA) spectral radiance (W m^{-2} sr^{-1} μm^{-1}) using the radiance rescaling factors in the metadata of Landsat-8. Previous research (Schroeder et al. 2016) noted that the SWIR radiance of Landsat-8 at 2.2 µm (SWIR-2) over a woody burning area was at or above 24.3 $Wm^{-2}sr^{-1}\mu m^{-1}$ and corresponded to 870–970 K fire temperature. A similar range of SWIR-2 radiance was also found by Sofan et al. (2018) of about 24–29 $Wm^{-2}sr^{-1}\mu m^{-1}$ from the flaming features identified in the 764 RGB images of Landsat-8. To provide a standardised measure, which is directly comparable between images which are acquired in any season, the TOA radiances of SWIR and other multispectral bands of OLI were

converted to TOA planetary reflectance. The TIR-1 band (band-10) TOA radiance values were converted to TOA brightness temperatures. These values are predominately influenced by the emitted radiance of the surfaces (Nikam et al. 2016; Petitcolin & Vermote 2002; Pierre Guillevic 2018; Sobrino et al. 2008). The atmospheric correction for both OLI and TIRS bands was not applied, as the effect of dynamic smoke haze during fire events was deliberately included for analysis. The spectral properties of Landsat-8 used in this study can be found in Appendix-Table A3.1.

3.2.4. Separation of Combustion Area and Non-Combustion Area

Initially, the 2015 historical firefighting location data obtained from BNPB were mainly aimed to guide the location of peatland combustion on a satellite image. However, in the development site (Central Kalimantan) it was discovered that the firefighting locations in 2015 (July–October) predominantly were distributed close to urban areas and there were limited ground validation sites collected for large peatland fires far from urban areas. This geographical bias could be caused by the priority for human safety reasons and/or due to the difficulties in access to peatland fire areas which were largely burning at that time. Thus, the reference of fire locations for development algorithm in 2015 was based on the Red Green Blue (RGB) pan-sharpened images of SPOT-6/7 or the 764 RGB images of Landsat-8 with smoke as an indicator of fire presence and in some cases its origin.

The tropical peatland combustion algorithm was developed in the area covered by Landsat-8 path/row 118/062 over Central Kalimantan in the period of August–October 2015. Data for the sample areas of combustion and non-combustion areas were collected on five Landsat-8 scenes. The types of landcover of the non-combustion area were plantation, forest, burnt area, urban (mixture of buildings, roads, vegetation, etc.), mining, and cloud as the brightest object. Predominantly peat fire locations, based on the historical MODIS active fire product and maps of peatland and landuse, were in or around plantation areas close to forest and burnt areas. Urban, building, mining areas and cloud features are typically bright during day-time with high reflectance, and thus could influence the identification of combustion areas. Thus, these bright objects are the potential sources of commission error for fire detection. We eliminated this source of error by masking out bright non-fire objects from the analysis (including

settlement/urban) using the Indonesian national landuse map previously mentioned (Kumar & Roy 2018; Murphy et al. 2016; Schroeder et al. 2016).

The OLI false colour image composite: bands-764 to RGB was chosen to visually enhance the burning areas from the background objects as SWIR bands (6–7) are sensitive to fire detection (Dennison & Roberts 2009; Kumar & Roy 2018; Murphy et al. 2016; Schroeder et al. 2016), while band-4 (visible, red spectrum) highlights smoke. In the 764 RGB image composite of Landsat-8, the combustion area exhibits in light yellow tones surrounded with orange and pink tones, with bluish smoke emanating from combustion areas. Flaming shows in bright yellow tones indicating a high reflectance value in SWIR-2; smouldering shows in reddish to orange tones, surrounding flaming with smoke from the surface (Figure 3.2A).

The sample areas of combustion and non-combustion area were delineated separately under clear sky and smoky conditions. There were a total of 238,772 clear sky pixels and 26,237 smoky pixels used as the samples with the type of objects as shown in Table 3.2. Each pixel is 30 m × 30 m in size, so in total there was approximately 23,851 ha used for peatland combustion algorithm development. The coefficient of variation within each sample area was less than 30%. The statistics of minimum, maximum, first quartile, median, third quartile and median of each sample area were calculated. Figure 3.2B shows the median values for TOA planetary reflectance of Landsat-8 from visible to SWIR bands of each sample area in clear sky and smoky conditions. In SWIR-2 the highest reflectance was for flaming pixels (clear sky), then decreasing to smoky flaming, cloud, smouldering, smoky building, smoky smouldering, urban and burnt area, while plantation and forest areas had the least reflectance. The reflectance of all sample areas was higher in smoky conditions than clear sky conditions (Figure 3.2B), which is caused by high scattering from aerosols in a smoky atmosphere.

The TOA brightness temperature of TIR-1 and the ratio of reflectance SWIR-1 to SWIR-2 of Landsat-8 for each object of combustion and non-combustion indicate that the flaming combustion had the highest median temperature in TIR-1 (Figure 3.2C). In smoky conditions, the brightness temperature of flaming and smouldering were lower than in clear sky conditions, as well as the other sample areas. To separate flaming and smouldering pixels from the other background objects, the ratio of SWIR-2 and SWIR-1, based on TOA planetary reflectance values, was calculated and termed the ShortWave InfraRed

Combustion Index or $SICI_{\rho}$. The median values of $SICI_{\rho}$ were plotted in Figure 3.2C showing the flaming and smouldering threshold for both clear sky and smoky conditions in the scale of $SICI_{\rho}$ to be above 1.0. This value was adopted to separate combustion and non-combustion objects. Even though, the $SICI_{\rho}$ threshold was close to that of burnt area objects, this threshold was used to deliberately over classify potential combustion areas. This over estimation was subsequently eliminated using TOA reflectance of SWIR-2 and TOA brightness temperature of TIR-1.

Table 3.2. Sample areas (in pixel) for peatland combustion algorithm development.

Object	Clear sky (pixel)	Smoky (pixel)
Flaming	584	1,143
Smouldering	515	1,347
Burnt area	9,068	5,107
Forest	211,501	9,160
Plantation	6,076	3,779
Urban	4,212	5,303
Building	1,640	398
Cloud	5,176	
Total	238,772	26,237

3.2.5. Smoke Haze Distribution

One of the designations for the coastal aerosol band (band-1) in the OLI sensor of Landsat-8 is to sense aerosol particles such as smoke and haze in the atmosphere (USGS, 2018). However, the detection of aerosol properties of smoke using band-1 of Landsat-8 still lacks research. Heavy smoke may obscure the detection of forest/land fire using optical satellite data during fire season, but it also has a cooling effect on the atmospheric temperature (Marchetti 2015). Here the coastal aerosol band-1 of Landsat-8 is used to generally classify clear sky and smoky conditions, using the median value in band-1 reflectance (shown in Figure 3.2B), corresponding to a TOA reflectance threshold of 0.27.

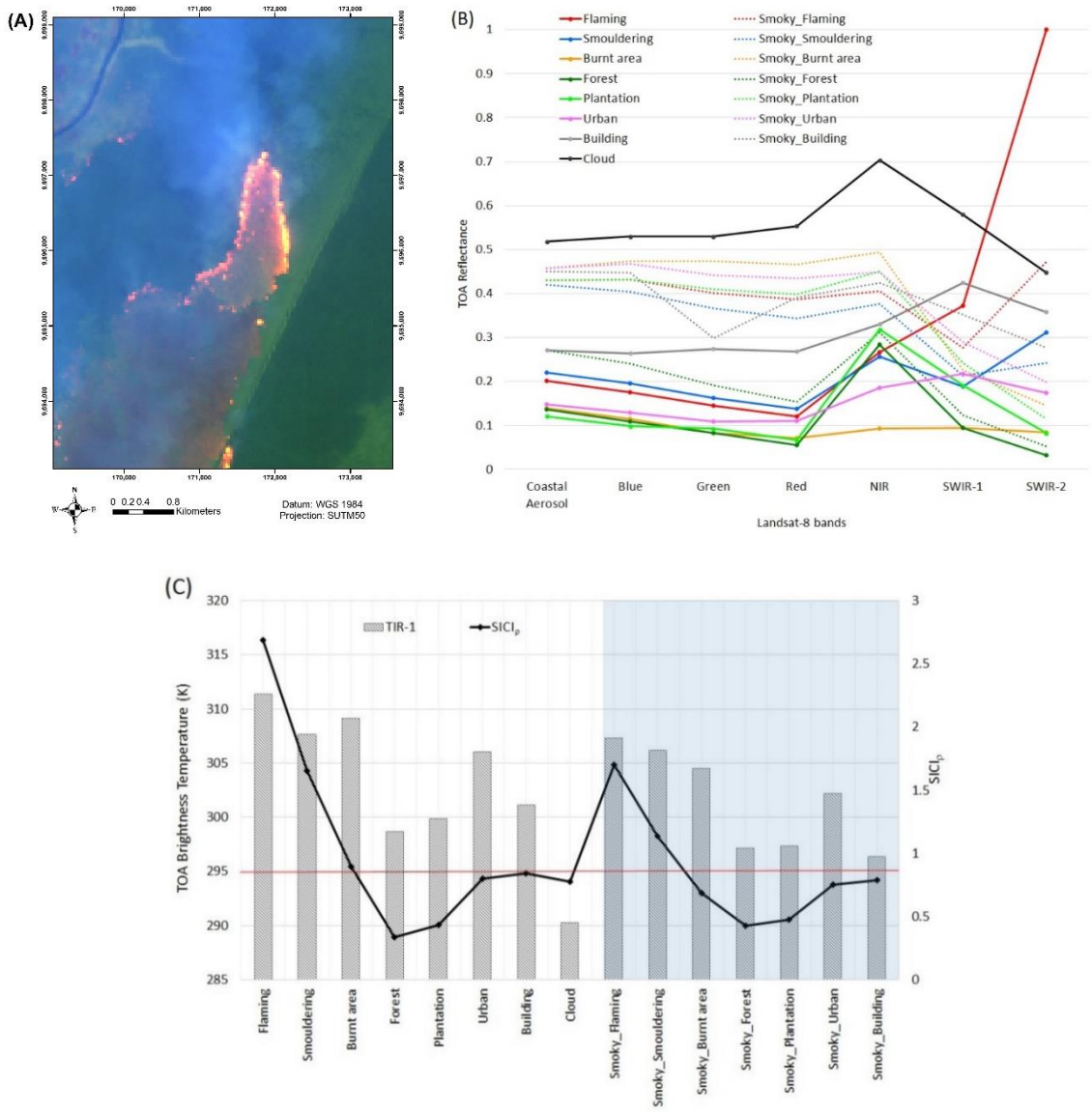


Figure 3. 2. (**A**) An example of a combustion area on the 764 Red Green Blue (RGB) images of Landsat-8 on September 20, 2015 with combustion area surrounding non-combustion area (forest, plantation, burnt area), (**B**) The Top of Atmosphere (TOA) planetary reflectance values of Landsat-8 bands. The solid line pattern refers to objects in clear sky condition, while the dotted line pattern relates to smoky objects, (**C**) The median values of TOA brightness temperatures of Thermal InfraRed band-10 (TIR-1) plotted in the clustered column, while the median values of the ratio of ShortWave InfraRed band-7 (SWIR-2) and SWIR-1 reflectance, ShortWave InfraRed Combustion Index ($SICI_{\rho}$), are shown in a black line with markers. Smoky conditions are shown in the light blue shading area to the right of clear sky conditions on the left. The red line is $SICI_{\rho}$ threshold used to separate flaming and smouldering from other background objects. [numerical data corresponding to Figure B and C is available in Appendix – Table A3.2]

3.2.6. Tropical Peatland Combustion Algorithm

The Tropical Peatland Combustion Algorithm (ToPeCAl) algorithm developed here consists of three criteria, i.e. (i) a threshold for $SICI_{\rho}$ of 1 to separate the potential combustion areas (including bright objects) from non-combustion areas, (ii) a threshold

of reflectance in band-1 of 0.27 for smoke haze distribution mapping, and (iii) identification and separation of flaming and smouldering peat combustion. The identification of flaming and smouldering peat was based on the SWIR-2 reflectance and TIR-1 brightness temperature, which were divided into two general atmosphere conditions, i.e. clear sky condition and smoky condition.

As mentioned in Section 2.4 and in Figure 3.2C, the flaming and smouldering combustion states occurred when values of $SICI_{\rho}$ were greater than 1.0. However, in the case of pixels in between radiance maximum to saturated levels of radiance in SWIR-1 and SWIR-2, the $SICI_{\rho}$ value will be less than 1.0. For example, in Figure 3.3, the combustion areas with high reflective pixels were extracted; there were three of 10 pixels which had $SICI_{\rho}$ values less than 1.0 (pixel#2, pixel#3, and pixel#7). Here, both SWIR-1 and SWIR-2 of those three pixels had TOA reflectance greater than 1.0 and $SICI_{\rho} \leq 1$— these were classified as flaming pixels. The condition of pixels in $SICI_{\rho} \leq 1$ should be in line with the conditions in SWIR-2 reflectance and the brightness temperature of TIR-1. For flaming pixels in clear sky conditions, the first quartile value of SWIR-2 reflectance (0.68) and TIR-1 brightness temperature (307 K) were adopted as thresholds, while in smoky conditions, 0.47 for SWIR-2 reflectance and 303 K for TIR-1 brightness temperature were adopted. According to Morfit et al (2015), the maximum radiance for saturated levels of SWIR-1 and SWIR-2 are 71.3–96 Wm-2sr-1µm-1 and 24.3–29 $Wm^{-2}sr^{-1}\mu m^{-1}$, respectively. The saturation in SWIR-1 and SWIR-2 can be caused by fires (Schroeder et al. 2016) and lava (Aufaristama et al. 2018).

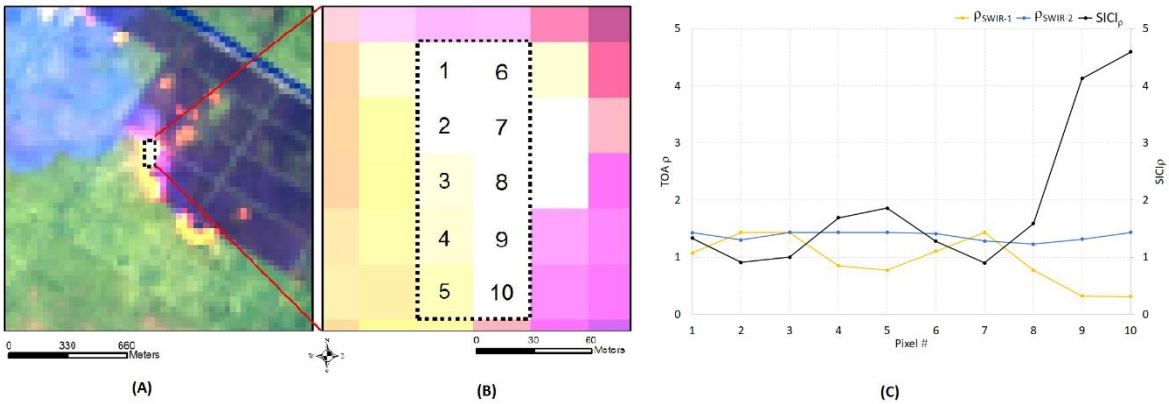


Figure 3. 3. (**A**) Sample of combustion area in the 764 RGB image of Landsat-8 on 19 August 2015 which had high reflectance of SWIR-1 and SWIR-2, (**B**) the enlargement of combustion areas showing 10 sample pixels, (**C**) the extracted SWIR-1 and SWIR-2 reflectances with $SICI_{\rho}$ values; pixel#2, #3, and #7 had $SICI_{\rho} \leq 1$.

For smouldering pixels, the $SICI_{\rho}$ is greater than 1, with the condition that SWIR-2 reflectance ranges from minimum to median value 0.09–0.31 (clear sky conditions) and 0.11–0.32 (smoky conditions). In addition, the minimum value of brightness temperature of TIR-1 was set at 297 K in clear sky and smoky conditions. Moreover, when pixels consist of a mix of flaming and smouldering, which may occur around combustion areas, an adjustment of thresholds for SWIR-2 reflectance and TIR-1 brightness temperature values between flaming and smouldering were used. Based on the statistical results of $SICI_{\rho}$, SWIR-2 reflectance and TIR-1 brightness temperature, the ToPeCAl can be formulated as in Table 3.3.

Table 3.3. The ToPeCAl for smouldering (S), mixture of flaming and smouldering (FS), and flaming (F) detection over clear sky conditions and smoky conditions. The criterion of $SICI_{\rho}$ must be satisfied together with the threshold values for SWIR-2 reflectance and TIR-1 brightness temperature (BT) of Landsat-8 data.

Combustion types	**Criterion 1** $\mathbf{SICI_{\rho}}$	**AND**	**Criterion 2** $\boldsymbol{\rho_{band\text{-}1}}$	**AND**	**Criterion 3** $\boldsymbol{\rho_{SWIR\text{-}2}}$	**AND**	**Criterion 4** $\mathbf{BT_{TIR\text{-}1}}$ **(K)**
S	>1				≥0.09 and ≤0.31		≥297
FS	>1		Clear sky ($\rho_{band\text{-}1}$ < 0.27)		> 0.31		>300
F	>1				≥0.68		≥307
F (for close to saturated pixel)	≤1		Clear sky ($\rho_{band\text{-}1}$ < 0.27)		≥0.68		≥307
S	>1				≥0.11 and ≤0.32		≥297
FS	>1		Smoky ($\rho_{band\text{-}1}$ ≥ 0.27)		≥0.32 and ≤0.47		>297
F	>1				≥0.47		≥303
F (for close to saturated pixel)	≤1		Smoky ($\rho_{band\text{-}1}$ ≥ 0.27)		≥0.47		≥303

In summary, the processing steps of peatland combustion mapping using Landsat-8 data are outlined in Figure 3.4.

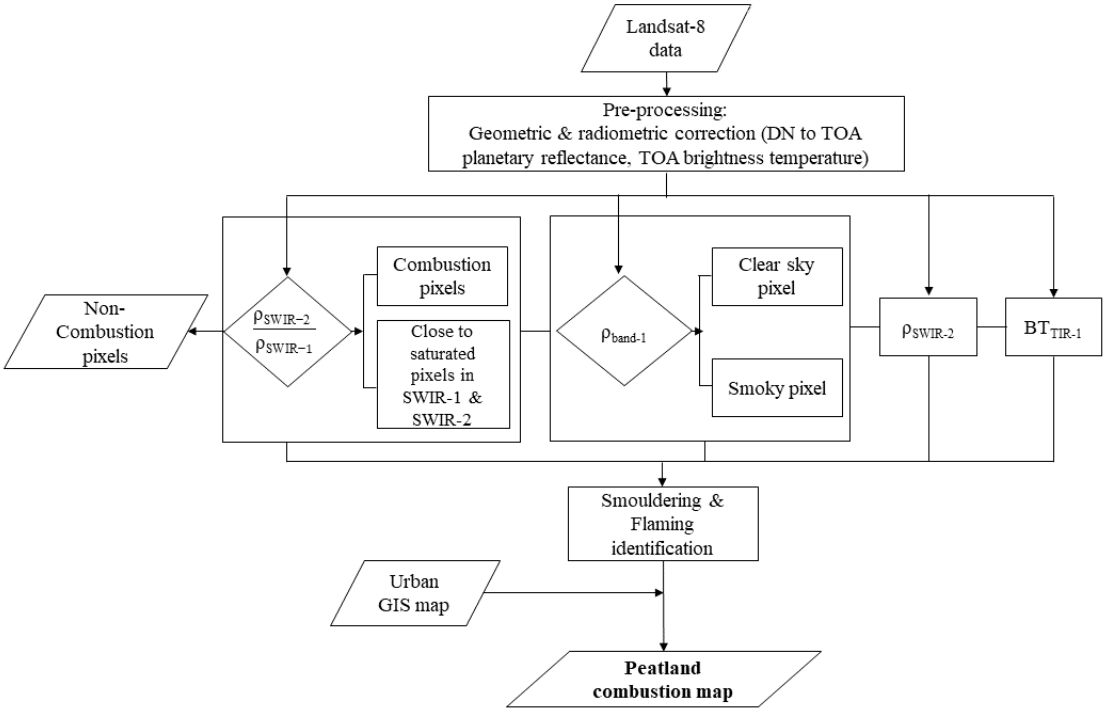


Figure 3.4. Flowchart of Landsat-8 image processing for mapping tropical peatland combustion.

3.2.7. Comparison with the Previous Landsat-8 Active Fire of Global Operational Land Imager

The Global Operational Land Imager (GOLI) active fire algorithm (Kumar & Roy 2018) uses Landsat 8 daytime TOA planetary reflectance in SWIR-1, SWIR-2, and visible red band, with bright object subtraction using either SWIR-2 reflectance or Normalised Difference Vegetation Index (NDVI). In contrast, ToPeCAl uses TOA planetary reflectance of SWIR-2 and TOA brightness temperature of TIR-1, with elimination of non-combustion areas using a $SICI_{\rho}$ threshold and masking for building rooftops using a Landuse GIS dataset. According to Kumar and Roy (2018), GOLI had omission errors in the tropical peatland fire environment in Indonesia (49 of 77 fires) and is compared here to the ToPeCAl results on 28 September 2018, in Central Kalimantan, Indonesia.

3.2.8. Validation with Ground Truth

Not all of the peatland combustion mapping results were validated directly on the ground due to accessibility difficulties from the road and the large size of some fires. Most of the ground truth data locations were collected about 0–2 km away from the fire area. Thus point to point checking was used to validate the ToPeCAl results with the ground truth data with Yes and No scores. The Yes and No scores of ground truth data

versus ToPeCAl results mapping were summarised in a contingency table as shown in generic form in Table 3.4. In the contingency table a count of each peatland combustion category (smouldering (S), flaming and smouldering (FS), and flaming (F)) and also the non-combustion area (Non) from the field was compared to the mapping results entries from ToPeCAl.

Table 3.4. The design of the Contingency Table comparing ToPeCAl mapping versus ground truth. Four categories ((S, FS and F, and non-combustion area (Non)) were assessed for both ground truth data and ToPeCAl results.

		ToPeCAl results mapping				
	Categories	**S**	**FS**	**F**	**Non**	**Total**
Ground truth	S	a_1	a_2	a_3	a_4	$G\,\Sigma_S$
	FS	b_1	b_2	b_3	b_4	$G\Sigma_{FS}$
	F	c_1	c_2	c_3	c_4	$G\Sigma_F$
	Non	d_1	d_2	d_3	d_4	$G\Sigma_{Non}$
	Total	$T\Sigma_S$	$T\Sigma_{FS}$	$T\Sigma_F$	$T\Sigma_{Non}$	Σ

The scores computed from the counts in the contingency table (Table 3.4) are Percent Correct (PC), False Alarm Ratio (FAR), Probability of Detection (POD), and bias (BIAS). PC is the total percent of correct mapping (the diagonal elements), including hits (a_1, b_2, c_3) and correct rejections (d_4) divided by the total number of data (Σ). FAR is the proportion of positive mapping results which did not occur in ground truth. POD refers to the portion of the mapping category that was correctly classified as the same category in ground truth. BIAS measures the mapping ability which demonstrates either over (BIAS > 1) or under estimation (BIAS < 1). It is calculated by dividing the sum of the counts of mapping results ($T\Sigma_S, T\Sigma_{FS}, T\Sigma_F, T\Sigma_{Non}$) by the sum of the counts of ground truth in each category ($G\Sigma_S, G\Sigma_{FS}, G\Sigma_F, G\Sigma_{Non}$). Referring to the generic variables in Table 3.4, the mapping scores can be formulated as (Stanski, Wilson & Burrows 1989; Stefano Mariani 2008):

$$PC(\%) = \frac{a_1 + b_2 + c_3 + d_4}{\Sigma} x\ 100 \quad \textbf{(3.1)}$$

$$FAR\ (\%) = \frac{d_1}{T\Sigma_S}, \frac{d_2}{T\Sigma_{FS}}, \frac{d_3}{T\Sigma_F}, \frac{d_4}{T\Sigma_{Non}} x\ 100 \quad \textbf{(3.2)}$$

$$POD(\%) = \frac{a_1}{G\Sigma_S}, \frac{b_2}{G\Sigma_{FS}}, \frac{c_3}{G\Sigma_F}, \frac{d_4}{G\Sigma_{Non}} x\ 100 \quad \textbf{(3.3)}$$

$$\text{BIAS (\%)} = \frac{T\Sigma_S}{G\Sigma_S}, \frac{T\Sigma_{FS}}{G\Sigma_{FS}}, \frac{T\Sigma_F}{G\Sigma_F}, \frac{T\Sigma_{Non}}{G\Sigma_{Non}} \quad \textbf{(3.4)}$$

For perfect mapping, the value of Percent Correct (PC) = 100%, False Alarm Ratio (FAR) = 0%, Probability of Detection (POD) = 100%, and bias (BIAS) = 1.

3.2.9. Comparison with the 375 m Visible Infrared Imaging Radiometer Suite Active Fire Product

The VNP14IMG fire pixels consist of three classes of fire pixel detection, i.e. low confidence, nominal confidence, and high confidence. The low confidence fire pixels have an effect of water sun glint during day-time and a weak temperature anomaly less than 15 K, while the nominal confidence level of fire pixel has no contamination due to sun glint and a strong temperature anomaly greater than 15 K. The high confidence level of fire pixels refers to saturated pixels (Schroeder 2017)

Here a preliminary analysis was conducted to explore the possibility of merging VNP14IMG with ToPeCAl results from Landsat-8 by firstly, comparing VNP14IMG to the same ground truth used to validate the ToPeCAl results, and secondly comparing VNP14IMG directly to the Landsat -8 ToPeCAl results.

In comparison with ground truth data, all the fire level confidences of VNP14IMG were classified into a single fire class as was the ground truth data. The same method of point to point checking validation described in the Section of 2.8 was used in the validation of VIIRS active fire versus ground truth data, with one class of fire (Table 3.5A). Meanwhile, in comparison with the ToPeCAl result from Landsat-8, there were two techniques for comparison used, i.e. (i) single fire class comparison for both ToPeCAl and VNP14IMG (Table 3.5B), and (ii) multiple fire class comparison with three combustion classes of ToPeCAl versus one fire class of VNP14IMG (Table 3.5C). For the single fire class comparison, the ToPeCAl combustion classes (S, FS, and F) were converted to a single fire class to compare with VNP14IMG data. In addition no comparisons were made with low, nominal, and high confidence levels.

Table 3.5. (**A**) The design of the Contingency Table for the VNP14IMG product versus ground truth data, (**B**) the VNP14IMG product versus Tropical Peatland Combustion Algorithm (ToPeCAl) results from Landsat-8 based on two categories (Yes-Fire, No-Fire), and (**C**) the VNP14IMG product versus ToPeCAl applied to Landsat-8 based on four categories (F, S, FS, and Non).

(A)

		VNP14IMG		
	Categories	**Yes-Fire**	**No-Fire**	**Total**
Ground truth	Yes-Fire	a_1	a_2	$G\Sigma_{Yes\text{-}Fire}$
	Yes-Fire	b_1	b_2	$G\Sigma_{No\text{-}Fire}$
	Total	$V\Sigma_{Yes\text{-}Fire}$	$V\Sigma_{No\text{-}Fire}$	Σ

(B)

		VNP14IMG		
	Categories	**Yes-Fire**	**No-Fire**	**Total**
ToPeCAl	Yes-Fire	a_1	a_2	$T\Sigma_{Yes\text{-}Fire}$
	No-Fire	b_1	b_2	$T\Sigma_{No\text{-}Fire}$
Total	$V\Sigma_{Yes\text{-}Fire}$	$V\Sigma_{No\text{-}Fire}$	Σ	Σ

(**C**)

		VNP14IMG		
	Categories	**Yes-Fire**	**No-Fire**	**Total**
ToPeCAl	S	a_1	a_2	$T\Sigma_S$
	FS	b_1	b_2	$T\Sigma_{FS}$
	F	c_1	c_2	$T\Sigma_F$
	Non	d_1	d_2	$T\Sigma_{Non}$
Total		$V\Sigma_{Yes\text{-}Fire}$	$V\Sigma_{No\text{-}Fire}$	Σ

Before conducting the comparisons, the raster cells of ToPeCAl were converted to polygons, while the VNP14IMG data were converted from point to polygon format using spatial buffering of 187.5 m (half a VIIRS pixel), 375 m (one VIIRS pixel), 500 m, 750 m, 1000 m, 1250 m, and 1500 m (Figure 3.5). Spatial buffering at increasing distances was applied to VNP14IMG points so that the spatial relationship and corresponding accuracy assessment metrics could be analysed. The data used for both VNP141IMG and Landsat-8 was from 28 September 2018. The Landsat-8 image was acquired at 2:34 UTC, while VNP141IMG data was acquired at 5:30 UTC and 18:12 UTC; thus, there was

approximately 3 hours and 15 hours of time difference, respectively. Firstly, the comparison of ToPeCAl was conducted using the 3 hours time lag of VNP14IMG data, and secondly the combined VNP14IMG data (5:30 and 18:12 UTC) was used for comparison with ToPeCAl.

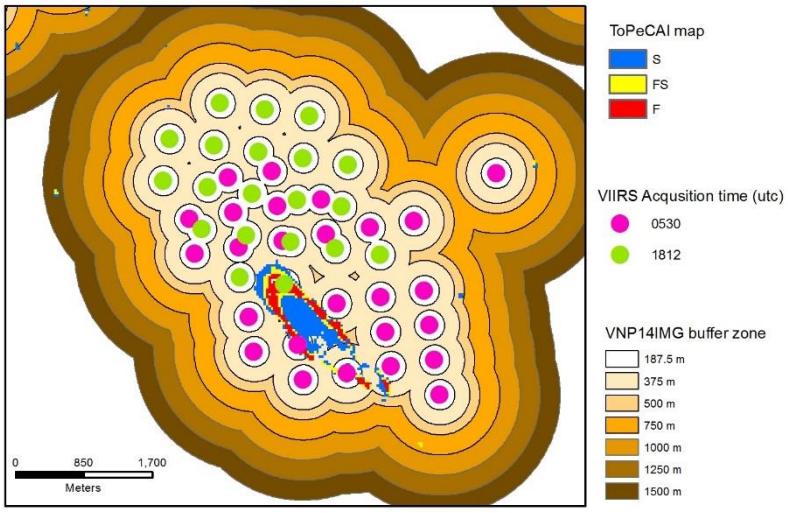


Figure 3.5. An example of buffering VNP14IMG point data overlaid with ToPeCAl results from Landsat-8. The VNPIMG data and ToPeCAl mapping relates to September 28, 2018. There is a 3 and 15 hour time difference from Landsat-8 to VNP14IMG acquisition times. The buffer zones are 187.5 m, 375 m, 500 m, 750 m, 1000 m, 1250 m, and 1500 m from both the VNP14IMG points (5:30 UTC and 18:12 UTC).

3.3. Results

3.3.1. Implementation of Tropical Peatland Combustion Algorithm

The algorithm was applied to the five scenes of Landsat-8 on the 2015 fire period in Central Kalimantan (8 August, 19 August, 4 September, 20 September, and 22 October). There were 1,727 flaming pixels and 1,862 smouldering pixels used to develop the algorithm, but then after the implementation of ToPeCAl, there were a total of 35,892 flaming pixels, 10,411 smouldering pixels and 3379 flaming and smouldering mixed pixels. Examples of implementation of the peatland combustion algorithm on Landsat-8 images (4 and 20 September 2015) under different atmospheric conditions, i.e. cloudy and thick smoke, are shown in Figure 3.6. Figure 3.6A,B shows the burning areas surrounded by clouds were well mapped using visual inspection from the 764 RGB image, where combustion was classified into smouldering (S), mixture of flaming and smouldering (FS), and flaming (F) stages. Under heavy smoke conditions, the combustion area shows in light pink tones on the 764 RGB images of Landsat-8 (Figure 3.6C), and the mapping performed quite well, even though not all the pink tones in the RGB image

were identified by ToPeCAl (Figure 3.6D). The lack of detection of combustion pixels under the thick smoke could be caused by the simplicity of the smoke classification algorithm.

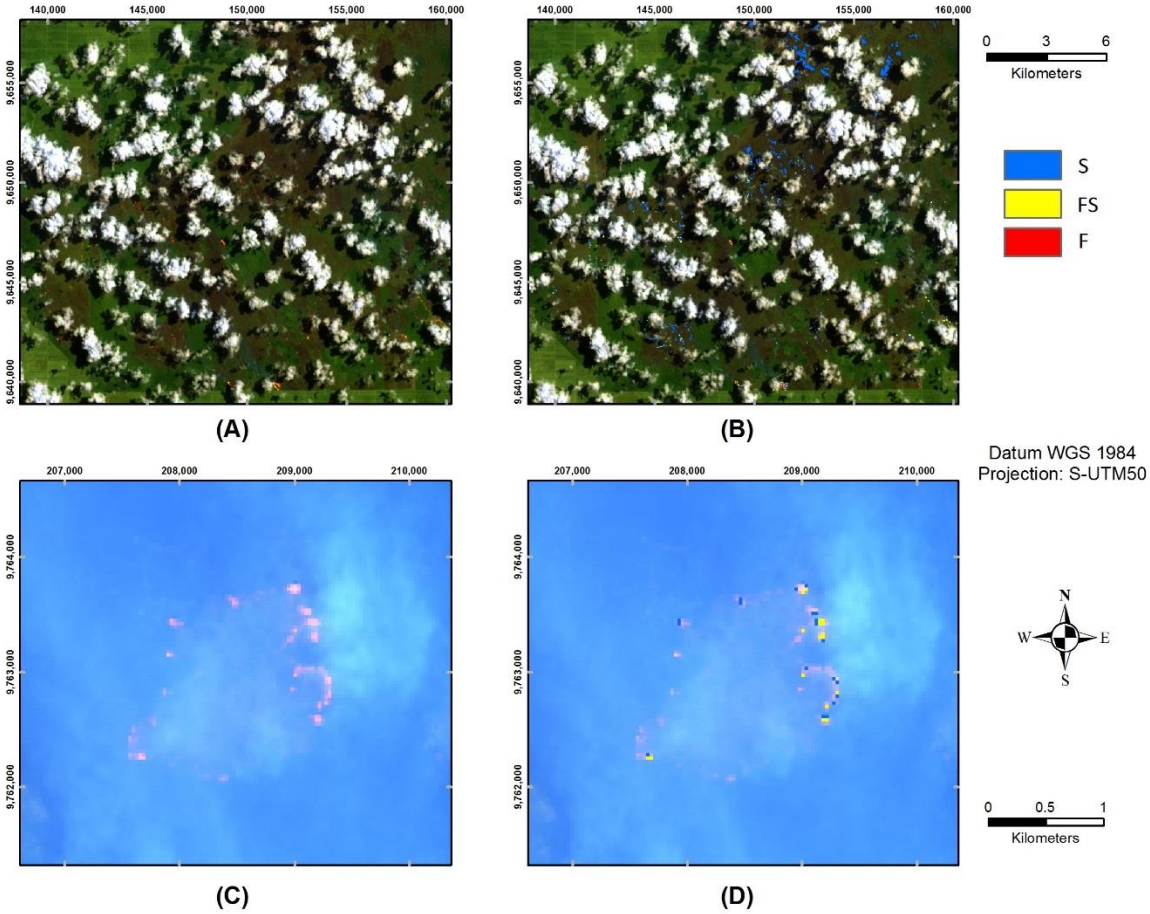


Figure 3.6. (**A, B**) An example of peatland combustion surrounded by cloud cover on a 764 RGB images of Landsat-8 on 4 September 2015 with the classified peatland combustion, (**C, D**) Peatland combustion in heavy smoke conditions and the classified peatland combustion on 20 September 2015.

3.3.2. Comparison of Tropical Peatland Combustion Algorithm with Global Operational Land Imager Results

Figure 3.7 shows the combustion area in the 764 RGB images of Landsat-8 with bluish smoke emanating from the ground (purple tones) and active fire features in yellow and red tones (Figure 3.7A). GOLI was implemented over the area and mapped active fire in magenta pixels (Figure 3.7B), while the ToPeCAl map in Figure 3.7C shows that most of the purple area (ground and smoke) was identified as smouldering fire. In Figure 3.7D, an overlay of ToPeCAl and GOLI maps show that ToPeCAl detected a larger peatland combustion area which consisted of smouldering (light blue), mixture of

smouldering and flaming (yellow), and flaming (red) pixels. Drone imaging was acquired over a part of the smouldering area two days after the Landsat-8 acquisition, then overlaid on the ToPeCAl, GOLI, and RGB images (Figure 3.7E), with an enlargement in Figure 3.7F that shows a large smouldering area in the field, but no active/flaming fire.

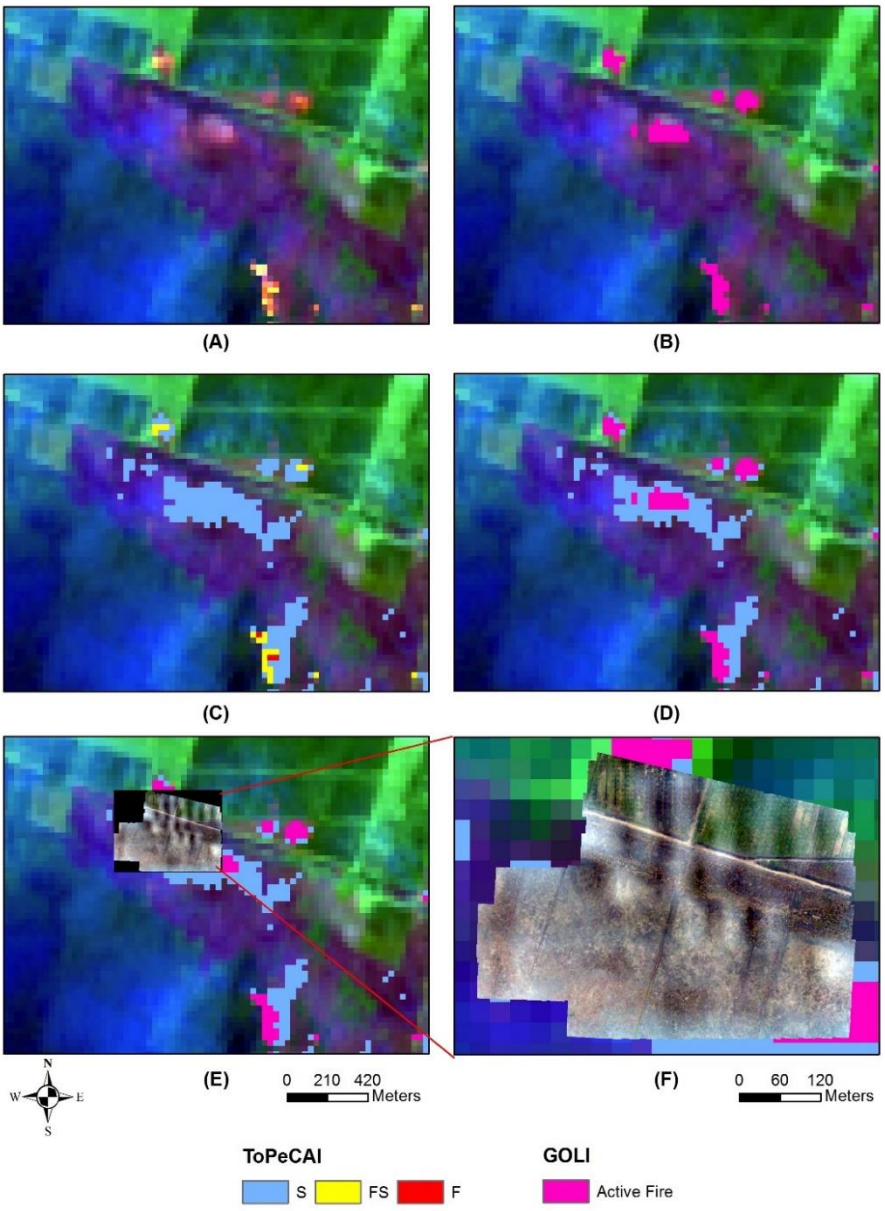


Figure 3.7. Comparison of Global Operational Land Imager (GOLI) and ToPeCAl implementation on peatland combustion using Landsat-8 28 September 2018, in Central Kalimantan. (**A**) The 764 RGB images of Landsat-8 of peatland combustion area, (**B**) The GOLI active fire (magenta) overlaid on the RGB image, (**C**) The ToPeCAl mapping result on RGB image is shown in three classes of peatland combustion (S, FS, F), (**D**). An overlay of GOLI and ToPeCAl showing a larger area of combustion from ToPeCAL, especially for smouldering fire, (**E**, **F**) Drone image and its enlargement showing smouldering peatland but not active/flaming fire.

There is no significant computational time different between GOLI and ToPeCAl methods. Both algorithms are semi-automatic running in remote sensing image processing software. However, additional data, from existing GIS urban/settlement mapping, is needed to minimise the commission errors in ToPeCAl mapping in the finishing stages.

3.3.3. Validation of Tropical Peatland Combustion Algorithm Mapping

3.3.3.1. Internal Validation in Central Kalimantan Province

There were 101 point locations collected during the ground survey in Central Kalimantan on 27 September–6 October 2018. The points included 82 peat combustion locations and 19 non-combustion areas (burnt area, urban area, reeds, and bright objects). Two scenes of Landsat-8 data were acquired on 28 September and 5 October 2018. The 28 September 2018 image observed the area of path/row 118/062 which was predominantly in clear sky conditions with thin smoke observed from the ground. According to local BNPB, there were peatland fires in that area since August 2018. Most of the ground locations were collected on path/row 118/062. Meanwhile, the Landsat-8 image acquired on October 5 (path/row of 119/062) was mostly in cloudy conditions (40.5% cloud cover over land) and fewer ground truth data were collected for this image (Figure 3.8). The average land surface temperature in smouldering peat was measured at 364 °C.

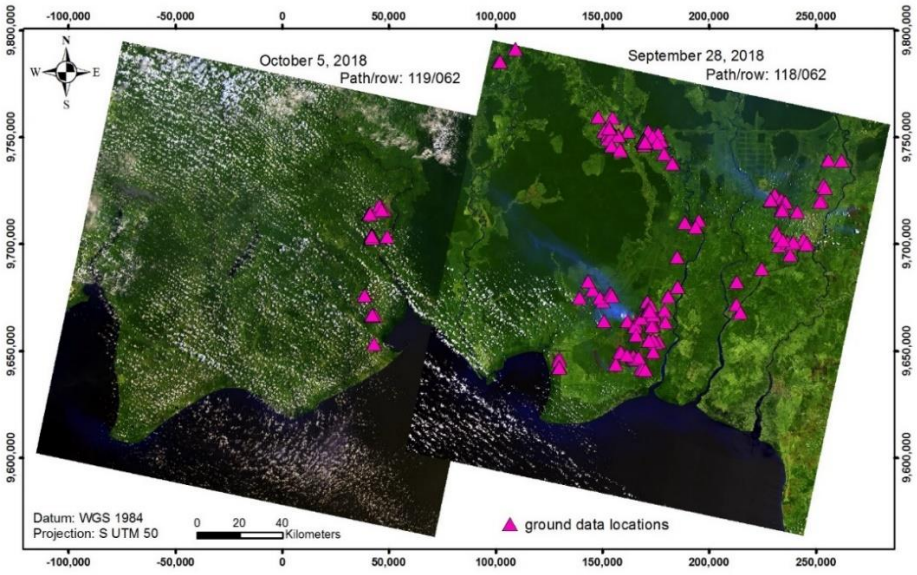


Figure 3.8. The coverage of ground truth collection in Central Kalimantan (27 September–6 October 2018) overlaid on Landsat-8 images of 28 September 2018 (right) and 5 October 2018 (left).

Figure 3.9 shows a large peatland fire on 28 September 2018, displaying a large group of flaming pixels in yellow tones in the 764 RGB image of Landsat-8 (Figure 3.9A). Flaming occurs at the fire-front with smouldering and mixture of flaming and smouldering pixels in orange to reddish tones inside the boundary of fire. The result of peatland combustion mapping corresponds to the 764 RGB images of Landsat-8 which were classified into three classes; red for flaming, blue for smouldering, and yellow for the mixture of flaming and smouldering pixels (Figure 3.9B). Ground truth were collected by local BNPB on the same day (28 September 2018) from a helicopter, because of both the large size of the peat fires and their inaccessibility from the land. The location of ground truth base stations is shown by the magenta triangles. The picture taken from the helicopter in Figure 3.9C shows the large area of peat fires on the ground. The upper picture was taken from a water bombing helicopter (its shadow is visible in the picture), while the lower picture shows the peatland fires with significant smoke emanating from the ground; this oblique picture was captured from about 2 km distance from the fire.

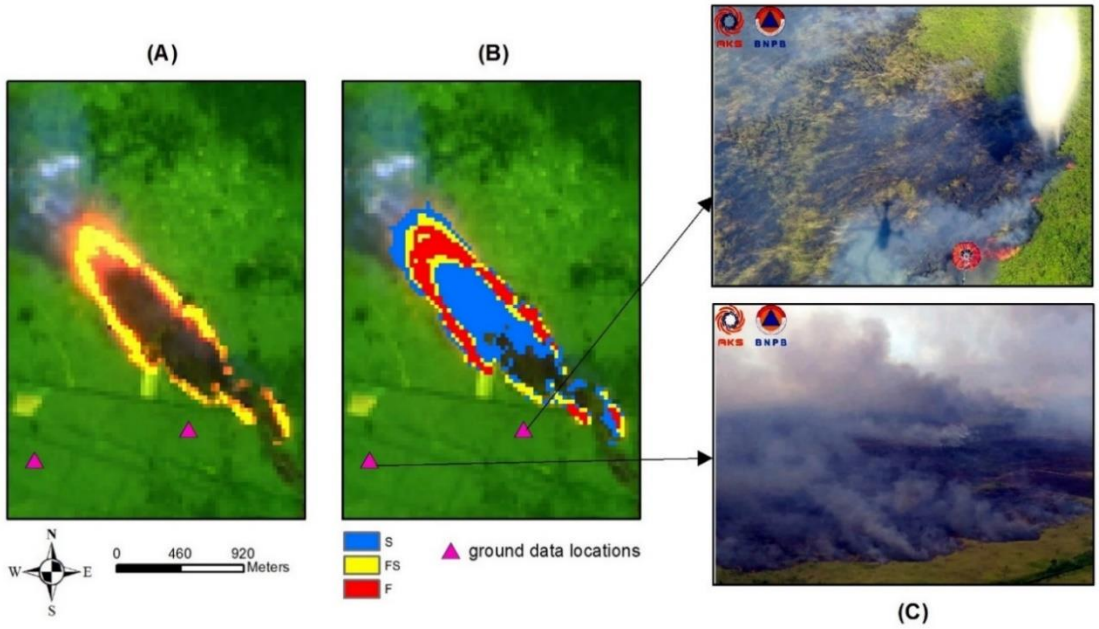


Figure 3.9. (**A**) The 764 RGB image of Landsat-8 on 28 September 2018, (**B**) The result of ToPeCAl mapping which consists of smouldering (S), mixture of flaming and smouldering (FS), and flaming (F) with ground truth base station locations marked in magenta triangle, (**C**) The pictures of peatland fires taken from helicopter on 28 September 2018. Field pictures sourced from the local Indonesian Disaster Management Agency (BNPB) of Central Kalimantan Province.

The second example of peatland fires validation was dominated by smouldering fire (Figure 3.10). The combustion area in the 764 RGB image of Landsat-8 on 28 September

2015 (Figure 3.10A) presented in dark red tones with flaming features in orange tones and yellow tones. The resulting mapping from ToPeCAl detected the smouldering fire (blue tone) and a small area of flaming (in red) and a mixture of smouldering and flaming (in yellow). A drone was flown on 1 October 2015 over some parts of smouldering area (Figure 3.10C). The drone image shows a smouldering area with smoke and indicated that the smouldering still existed three days after the Landsat-8 pass over the area.

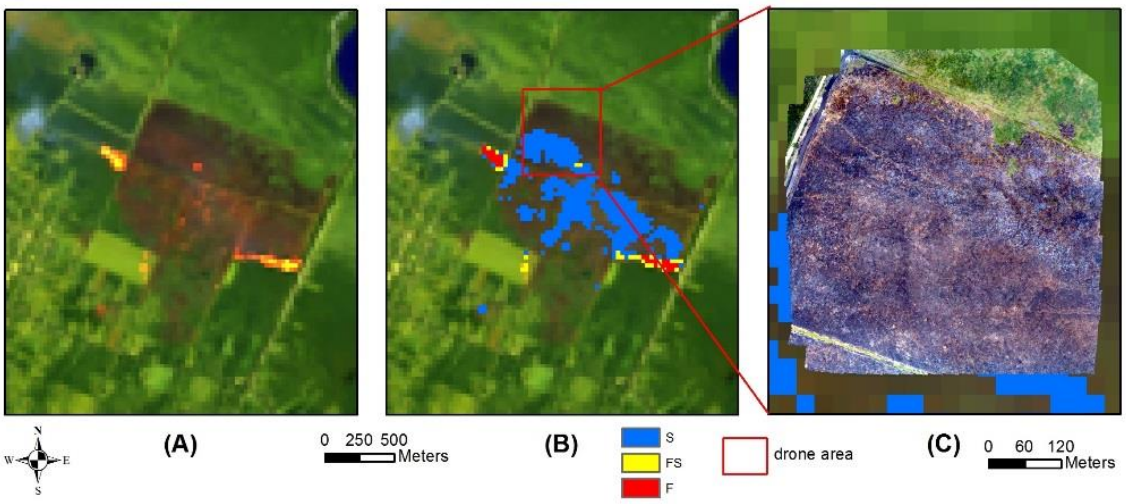


Figure 3.10. (**A**) The 764 RGB image of Landsat-8 on 28 September 2018 and (**B**) the result of peatland combustion mapping with ground truth location marked in red square, (**C**) The picture of peatland smouldering fire taken from a drone on 1 October 2018.

The third example of the application of ToPeCAl is shown in Figure 3.11 where combustion occurred predominantly in a healthy vegetation area. In Figure 3.11A, the 764 RGB image of Landsat-8 shows a potential combustion area in orange tones around green tones of vegetation. ToPeCAl appeared to perform quite well, indicating there was smouldering and a mixture of flaming and smouldering pixels in that particular area on 5 October 2018 (Figure 3.11B). One day after that, drone imaging was acquired for the area and it showed (Figure 3.11C) that the area has been burnt and still had smoke emanating from the ground. Parts of the area included a mixture of green vegetation with smouldering components, as is indicted in Figure 3.11D. This evidence shows that a mixture of smouldering and green vegetation in a heterogeneous environment might be a possible cause for the lack of detection when ToPeCAl was applied to the Landsat-8 image.

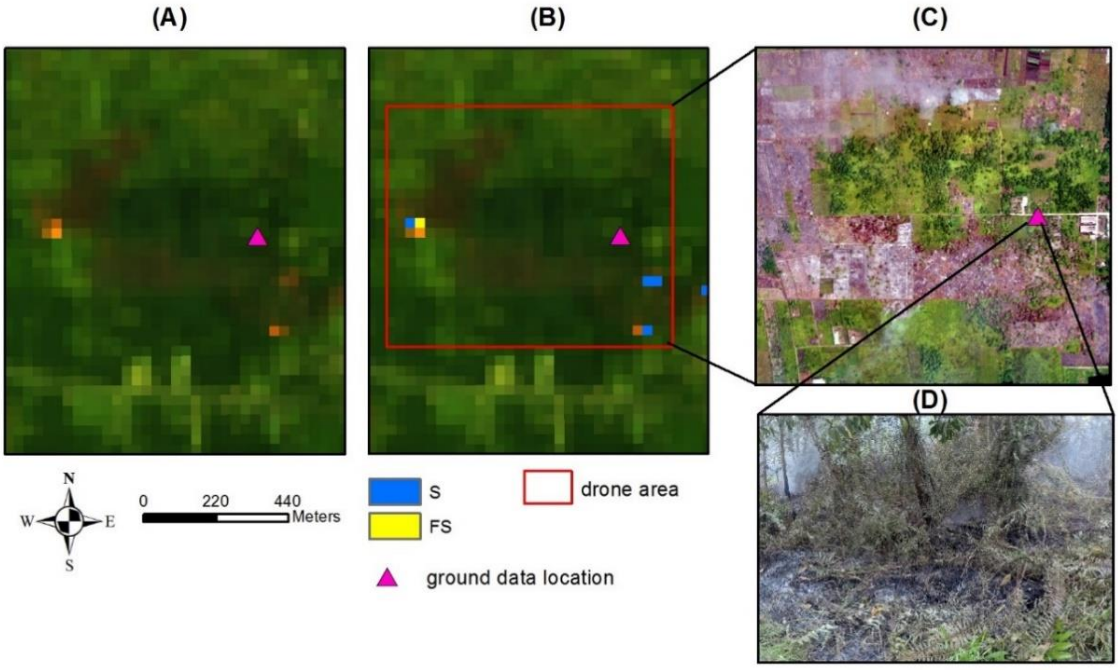


Figure 3.11. (**A**) The 764 RGB image of Landsat-8 on 5 October 2018, presented a combustion area which was predominantly vegetated, (**B**) The result of peatland combustion mapping, and (**C**) Drone imaging and (**D**) Terrestrial picture of smouldering vegetation area in the area on 6 October 2018.

3.3.3.2. External Validation in Riau Province

The external validation of peatland combustion algorithm was conducted using one scene of Landsat-8 in 2016 and three scenes in 2018 in Riau Province. There were 21 ground points of fire locations which mapped well in Riau by using ToPeCAl developed in Central Kalimantan. Two examples of peatland fire with the ground truth are shown in Figure 3.12. One large peatland fire, which contained three classes of peat fires (S, F, FS), is shown in Figure 3.12A–C, with a helicopter picture (Figure 3.12C) taken on the same day as the Landsat-8 acquisition (20 August 2016). The second example, which is classified as smouldering fire, shows peat fire surrounded by cloud cover captured by Landsat-8 on 4 April 2018, (Figure 3.12D and 3.12E). Figure 3.12F shows smoky conditions taken from terrestrial and helicopter cameras.

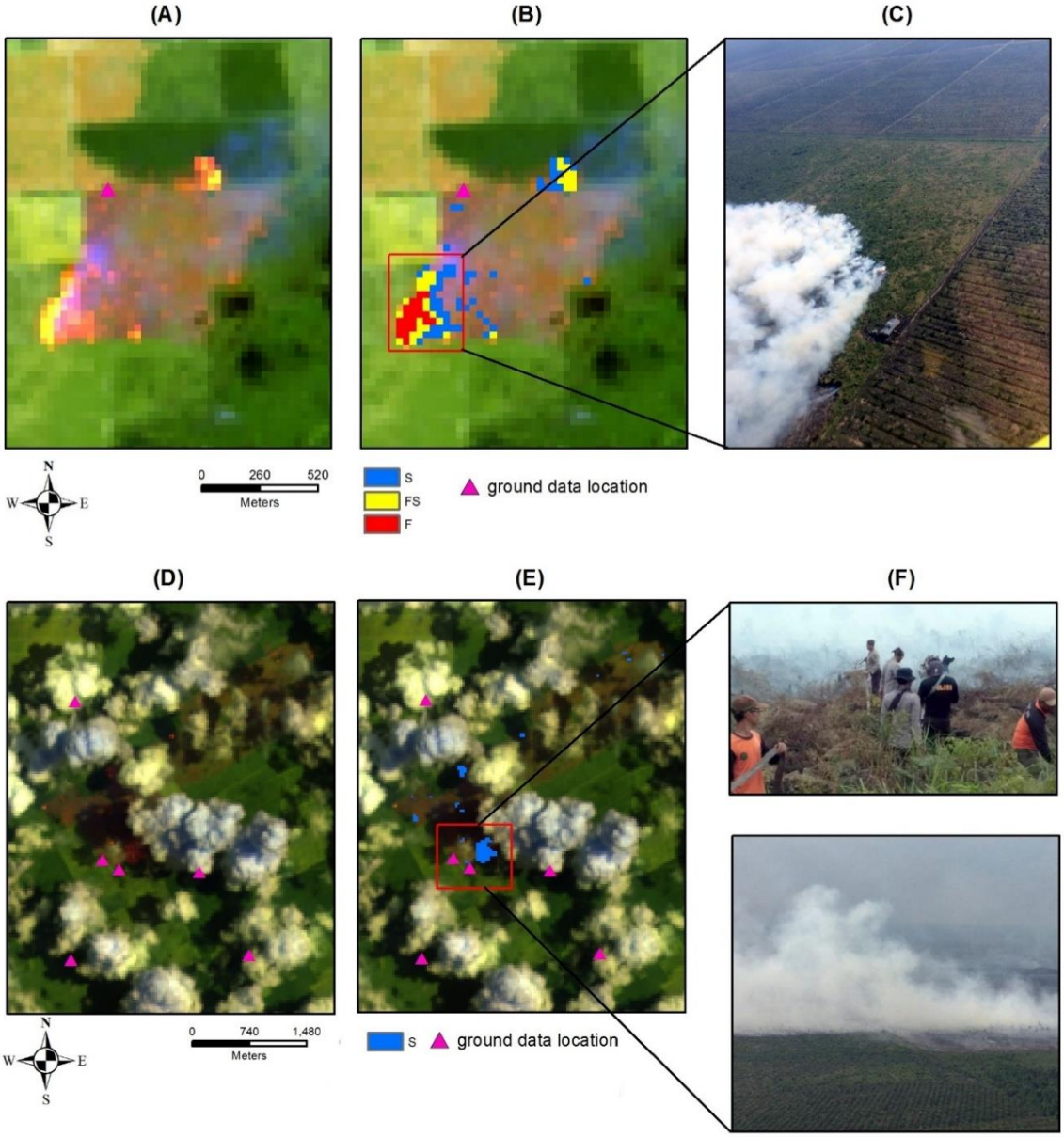


Figure 3.12. (**A, B**) The 764 RGB image of Landsat-8 on 20 August 2016 showing a combustion area with the result of peatland combustion mapping and **(C)** a helicopter oblique picture taken on the same day taken in Riau Province; (**D, E)** The 764 RGB Image of Landsat-8 on 4 April 2018 and the result of peatland combustion mapping with ground truth location marked in red square. The pictures **(F)** of peatland fires from the ground and helicopter; sourced from local BNPB of Riau Province on 4 April 2018.

3.3.4. Statistical Assessment of Tropical Peatland Combustion Algorithm Validation

There was a total of 122 areas of observation collected from the ground for validation in Central Kalimantan and Riau Provinces; these consisted of 103 areas of peatland combustion and 19 areas of non-combustion. The 103 combustion areas from the application of ToPeCAl comprised 44 areas of smouldering (S), 26 areas of a mixture of flaming and smouldering (FS) and 16 areas of flaming (F) stages. Additionally, two

combustion areas were mixed, classified as flaming and mixture of smouldering and flaming areas and 15 smouldering areas were not identified by the ToPeCAl algorithm in the non-combustion area. The 19 non-combustion areas (Non) consisted of reeds, urban/settlement, bright objects and burnt areas. Five of the 19 non-combustion areas, which were bright roofs tops, were falsely classified as a mixture of smouldering and flaming, but 14 of them were well classified as non-combustion areas. The summary of the field observation versus ToPeCAl is shown in the Contingency Table (Table 3.6A). Meanwhile, the score results based on Contingency Table of ground truth versus ToPeCAl are presented in Table 3.6B. This shows the overall PC of ToPeCAl mapping is 82% for three categories (S, FS, and F). For smouldering mapping, the FAR is low with a POD of 73% and underestimated detection shown by the low BIAS. The mixture of flaming and smouldering mapping had a FAR of 16% and high POD with a low overestimated detection. Flaming mapping was quite good, with low FAR, high POD and low overestimated detection. The non-combustion areas (Non) mapping had a 48% FAR and 74% POD with a low overestimated detection. The underestimated detection, or omission error, of smouldering mostly occurred in the urban areas and in forest areas where there was a mixture (over a 30 m pixel) with vegetation and half dead vegetation. The overestimated detection of FS occurred in the non-combustion areas on bright building rooftops. Masking the urban area upgraded the percentage of correct mapping from 82% up to 93%.

Table 3.6. (**A**) The results of Contingency Table of ToPeCAl validation in Central Kalimantan and Riau Province (data in table shows counts), and (**B**) the scores of PC, FAR, POD, and BIAS of ToPeCAl Mapping compared with ground truth data.

(**A**)

		ToPeCAl Mapping Counts				
	Categories	S	FS	F	Non	Total
Ground truth	S	44	1	0	15	60
	FS	0	26	1	0	27
	F	0	0	16	0	16
	Non	0	5	0	14	19
	Total	44	32	17	29	122

(**B**)

ToPeCAl Mapping	SCORES			
	PC	FAR	POD	BIAS
S	82%	0%	73%	0.73
FS		16%	96%	1.19
F		0%	100%	1.06
Non		48%	74%	1.53

3.3.5. Statistical Assessment of the 375 m Visible Infrared Imaging Radiometer Suite Active Fire Validation

From the total of 122 ground truth data collected in Central Kalimantan and Riau Province, there were 73 hits, 15 misses, 20 false alarms and 14 correct negatives (Table 3.7A). The calculation of PC resulted in 71 % with a FAR of 22%. The POD of fire was 83%, and the BIAS was 1.05 which refers to overestimated mapping (Table 3.7B).

Table 3.7. (A) The results of the Contingency Table of VNP14IMG versus ground truth in Central Kalimantan and Riau Provinces (data in table show counts), and (**B**) the scores of PC, FAR, POD, and BIAS of VNP14IMG compared with ground truth data.

(**A**)

		VNP14IMG		
	Categories	Yes-Fire	No-Fire	Total
Ground truth	Yes-Fire	73	15	88
	No-Fire	20	14	34
	Total	93	29	122

(**B**)

VNP14IMG	**SCORES**			
	PC	**FAR**	**POD**	**BIAS**
Yes-Fire	71%	22%	83%	1.05
No-Fire		48%	41%	0.85

In comparison with ToPeCAl results, the PC scores were high which derived more from the higher correct negative hits than the correct positive hits. The FAR scores were also high because many of VNP14IMG existed while ToPeCAl did not exist. Table 3.8

shows the POD of VNP14IMG compared with ToPeCAl tends to rise with the increasing of buffer zone which could be caused by the geometric error of the VNP14IMG point location, which is automatically assigned to the center of a pixel, even if the true fire is located in the edge of pixel, for example. Using VNP14IMG data during only day-time (5:30 UTC) resulted in a lower value of POD than the combined day-time (5:30 UTC) and nighttime (18:12 UTC). About 72% of ToPeCAl can be detected by VNP14IMG using combination of day-time (+ 3 hours) and night-time data (+16 hours) within a 1.5 km distance from the VNP14IMG points. The BIAS of VNP14IMG compared with ToPeCAl results shows significant overestimation in mapping. The greater the distance from original point of VNP14IMG, the greater the BIAS.

Table 3.8. (**A**) The scores of PC, FAR, POD, and BIAS of VNP14IMG compared with ToPeCAl with a different time of 3 hours in day-time, and (**B**) a combination of 3 hour and 15 hours difference in time. The calculations were generated for buffer zones of 187.5 m to 1250 m.

(**A**)

Buffer zone (m)	PC	FAR	POD	BIAS
187.5	99.9%	94.3%	6%	1.1
375	99.8%	95.9%	19%	4.7
500	99.8%	96.2%	21%	5.3
750	97.7%	97.7%	29%	12.8
1000	99.2%	98.3%	33%	19.6
1250	98.9%	98.7%	37%	27.5
1500	98.5%	98.8%	42%	35.7

(**B**)

Buffer zone (m)	PC	FAR	POD	BIAS
187.5	99.9%	91.7%	23%	2.8
375	99.7%	92.8%	57%	8.0
500	99.6%	94.4%	62%	11.0
750	99.4%	96.3%	66%	17.8
1000	99.1%	97.3%	69%	25.4
1250	98.8%	97.9%	70%	33.9
1500	98.5%	98.3%	72%	43.0

In order to know which parts of peatland combustion were dominantly detected by VNP14IMG, the comparison was conducted for all combustion stages of ToPeCAl, which

consisted of 14,157 pixels of S, 3173 pixels of FS, and 3815 pixels of F with the combination of VNP14IMG at 5:30 UTC and 18:12 UTC. The results of POD of S, FS, and F were plotted against the buffer zone distances as shown in Figure 3.13. There were a significant increase in POD rising from a distance of 187.5 m to 375 m of VNP14IMG points. The highest portion of ToPeCAl detected by VNP14IMG shown by POD scores corresponded to flaming combustion, starting from the zone of 375 m, at about 80% to 83% in the zone of 1500 m. Meanwhile, the portion of smouldering detected was about 50% at 375 m then rising to 70% at 1500 m. The POD for a mixture of flaming and smouldering was about 60% from 375–1500 m.

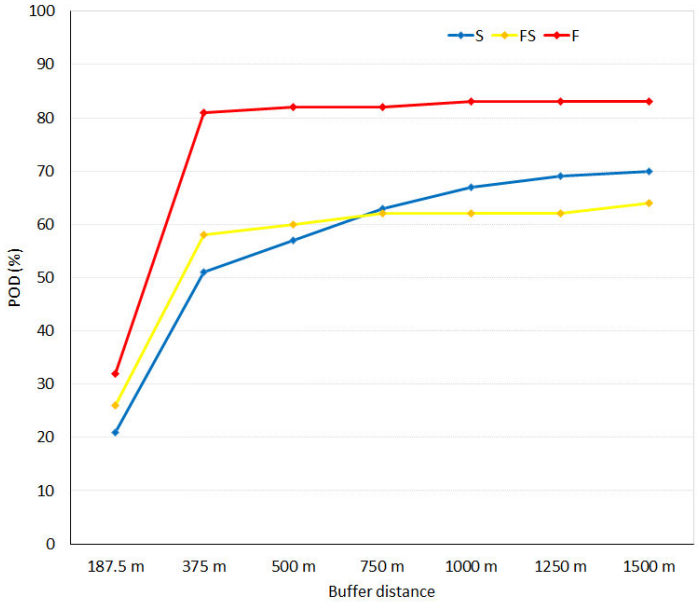


Figure 3.13. POD of peatland combustion (S, FS, and F) detected by VNP14IMG from day-time and night-time data in buffered zones of 187.5 m to 1500 m.

3.4. Discussion

ToPeCAl was developed to detect flaming and smouldering peat fire in clear sky and smoky atmospheric conditions using day-time images of Landsat-8. The TIR-1 band was used along with SWIR-2 band to strengthen the detection of smouldering peat fire. ToPeCAl was developed in Central Kalimantan peatland from the Landsat-8 data acquired during the 2015 fire period, was tested on different acquisition days and also outside the development area in Riau, Sumatera Island. The recent fire algorithm, GOLI, takes advantage of the reflectance of SWIR (SWIR-1 and SWIR-2) and the visible red bands of Landsat-8. However, GOLI did not perform well on smouldering peatland fire (Kumar & Roy 2018). Here, ToPeCAl was compared with GOLI in one peatland

combustion area in Central Kalimantan on September 28, 2018, and it was found that ToPeCAl generated a better detection on smouldering fire than GOLI. The fire product in GOLI is termed “active fire” (Kumar & Roy 2018). The consideration of using a suitable and consistent term to determine which part of a fire stage (smouldering, flaming, etc.) which is dominantly detected by a specific algorithm applied to a satellite sensor needs greater attention. Many previous researchers (Giglio, Schroeder & Justice 2016; Kumar & Roy 2018; Schroeder et al. 2014; Schroeder et al. 2016) use the “active fire” term derived from different sensors with different spectra. For example, in low spatial resolution data, MODIS and VIIRS, the fire product is based on Middle InfraRed/MIR (3–4 µm) and TIR (10-12 µm), and the product is termed “active fire’’ (Giglio, Schroeder & Justice 2016; Schroeder et al. 2014). Meanwhile for medium spatial resolution such as Landsat-8, in which MIR does not exist, the fire detection is generated from SWIR, and some researchers label the fire product as “active fire’’ (Kumar & Roy 2018; Schroeder et al. 2016) or “hot target for fire” or “lava flow” (Murphy et al. 2016). In the Middle InfraRed, fire objects, even with low temperatures (e.g. smouldering) can emit radiance at two orders (100 times) of magnitude greater than background, while in Thermal InfraRed radiance can be one order (10 times) of magnitude higher than non-burning surfaces(Giglio et al. 2008). Meanwhile, according to the Wien displacement law, higher temperatures, such as flaming fire, are better observed at the shorter wavelengths, while the lower temperature fire, such as smouldering, is better observed at longer spectral wavelengths. This supports the logic that the SWIR is advantageous in detecting flaming rather than smouldering, while the MIR is better for flaming and smouldering detection than TIR. In case the MIR does not exist in a sensor then TIR is better to detect smouldering than SWIR.

During day-time, atmospheric disturbances in the tropics, as well as smoky condition from smouldering fires, can affect the detection of smouldering peatland. Thus, ToPeCAl introduces an adjustment of SWIR-2 and TIR-1 thresholds for flaming and smouldering detection based on atmospheric conditions. The effect of smoke on the detectability of objects was described in section 2.4, which shows lower brightness temperatures of TIR-1 over various non combustion and combustion areas, compared to those in clear sky conditions; this concurs with (Marchetti 2015) who write that smoke has a cooling effect on the atmosphere. In some pixels around the flaming or smouldering pixels, we found that not all combustion pixels were mapped due to heavy smoke obscuration. This

suggests that further smoke detection and analysis research is required to enhance ToPeCAl. The use of aerosol band of Landsat-8 for smoke property detection still lacks research; perhaps multiband techniques can be utilised to better characterise smoke in more quantitative ways or perhaps other satellites, which focus on atmospheric properties, can be combined with Landsat to improve this aspect of ToPeCAl?.

Previous research on fire detection from medium spatial resolution satellite data reports that bright objects, especially high reflective rooftops, have been a consistent source of commission errors due to high day-time radiance in SWIR wavelengths (Kumar & Roy 2018; Murphy et al. 2016; Schroeder et al. 2016). Thresholds in SWIR spectrum at 2.2 µm were used to eliminate the bright rooftops, and even with the use of NDVI from the period immediately prior to the fire detection, the bright rooftops still existed (Kumar & Roy 2018; Murphy et al. 2016; Schroeder et al. 2016). In this study, the advantages of SWIR were also used for non-combustion masking, but we also generated the ratio of SWIR-2 and SWIR-1 reflectance, $SICI_{\rho}$, with a threshold from its median value to separate combustion areas from non-combustion areas (burnt area, urban, plantation, forest, urban, mining, water, and cloud). However, over very high reflective building rooftops, we still experienced the same problem as other previous researches. Thus, to finalise the ToPeCAl, a GIS was used to mask urban areas, as recommended by previous researches (Kumar & Roy 2018; Schroeder et al. 2016). In Indonesia, the landuse map is updated yearly by the Ministry of Forestry using multi-temporal images of Landsat-8 data, with a reference to high spatial resolution such as SPOT-6/7 provided by LAPAN. The scale of the landuse map is 1:50.000 with the smallest pixel size of 6.25 ha or similar to 250 m pixel resolution. In this case, the masking of settlements or urban areas, which have a dominance of high reflective rooftops, will potentially introduce omission errors of peatland combustion detection in the urban area. However, the local disaster management agency has a good social network in the community and if a fire occurs in the urban area, it will be first solved by the authority due to the fast information given from residents, as the people's safety is the priority for the firefighters. Another problem of using the urban GIS, especially at 1:50,000 scale, is the limitation of mapping a small individual building or small groups of buildings with bright rooftops. These will potentially still be detected as false positives.

The ground validation of forest/peatland fire is relatively difficult, compared with other ground surveys for remote sensing applications. Ideally, the ground truth is

collected at the same time of satellite overpass of the fire area. However, the optical satellite image of fire occurrence in tropical areas can be interrupted by cloud cover and smoke. Thus, if a perfect time for observation of both ground truth and satellite image is not available, then ground truth often may not temporally coincide with satellite observations. However, because peatland fire spread rates are slow, ground truth collected one week before or after the satellite image acquisition still can be used for validation, particularly with significant support information from local histories of a particular fire occurrence in a certain area. Other than that, there is a problem in obtaining precise ground fire locations in tropical peatland environment if the accessibility is limited. For example, there were some significant large peatland fires on the day of ground survey on 28 September 2018, which coincided with a Landsat-8 pass over the area. However, the locations of peat fires were in deeply forested peatland, which could not be reached by road transportation, and forced ground crews to use small boats on rivers and canals and then continue walking for about 1–4 km. To compensate for this limited accessibility, the ground truth in some locations was collected by drone or helicopter imaging, often using oblique image orientations to avoid direct flight over fire. These conditions lead to manual choice of points for validation of ToPeCAl.

The performance of ToPeCAl to ground truth was statistically analysed with the Yes and No scores presented in the contingency table (Table 3.6). Over internal (Central Kalimantan) and external (Riau) validation areas, ToPeCAl had a correct mapping of 82%, with omission an error of 27% for small smouldering fires. About 15 locations of the 103 combustion areas were not classified as smouldering fires. The 15 smouldering fires found in the field were mostly small in size (far less than one Landsat pixel) and located in areas immediately adjacent to healthy vegetation or half dead vegetation. According to (Elvidge et al. 2015), the detection of smouldering fires using night-time data also was limited to 40-90 m^2, corresponding to some of the small smouldering peat fires found in urban areas. The limitation in detecting small smouldering fires can also be partially attributed to the fact that the original spatial resolution of TIR is 100 m while the SWIR is 30 m.

A preliminary analysis for comparing the 375 m VIIRS active fire product (VNP14IMG) with ToPeCAl was conducted in this study. This analysis was done based on the idea of introducing image/data fusion to obtain high spatial and high temporal resolution for peatland combustion monitoring. The VNP14IMG was quite good when

compared with ground truth with 71% PC and a BIAS score of 1.05, which represents a slight overestimation. Compared with ToPeCAl results from Landsat-8, the VNP14IMG gave a high (>90%) PC when utilising a buffer zone for the comparison. However, the FAR was quite high (>90%) which infers over detection of fire by the VIIRS product compared with ToPeCAl. A low POD (<30%) existed when using day-time data alone, even though it was close in time (+3 hours) to the Landsat-8 acquisition. By combining the day-time data (+3 hours from Landsat-8) and the night-time data (+16 hours from Landsat-8), a higher POD was obtained of about 57% (375 m buffer zone) and up to 72% (1.5 km buffer zone). This due to a higher correct positive and lower false positive fire pixels detected with night-time data, with POD about of 49% (375 m buffer zone) to 69% (1.5 km buffer zone).The highest portion of POD when using the combined VNP14IMG (+3 and +16 hours) in detecting peatland combustion stages from ToPeCAl applied to Landsat-8 was on the flaming stage (~80%), while the smouldering stage was about 60%. Overall, the BIAS showed that the VNP14IMG product overestimated detection of fire and that this increased with buffer zone size compared with ToPeCAl results. A further investigation needs to be conducted to check the problem of omission and commission error of VNP14IMG product over peatland area before fusion of fire information with Landsat-8 is instituted. A better POD might be achieved by combining the day-time (+3 hours), night-time (+16 hours), and the previous data of VNP14IMG at night-time which at about –8 hours different from Landsat-8.

The tropical peatland combustion algorithm from day-time Landsat-8 data can be potentially operationalised in Indonesia by LAPAN as mandated by the government as the national satellite data provider of mapping of forest fires including peatland fire. This fire information is delivered to the BNPB as the agency who use the fire information for extinguishment support. In order to fill the temporal gaps between Landsat- overpasses, further research into the VNP14IMG product is needed. As peatland fire detection requires a high spatial resolution, the use of Sentinel-2 sensors with a higher temporal resolution (5 days) than Landsat, a 20 m spatial resolution and the same SWIR spectra in 2.2 µm, but without TIR spectra, could be explored, but with an adjustment for lack of a TIR spectra.

3.5. Conclusions

The discrimination of flaming and smouldering combustion of peatland fires over tropical areas can be mapped through the use of day-time images from Landsat-8. ToPeCAl consists of the $SICI_{\rho}$ for separating combustion from the non-combustion areas, TOA planetary reflectance of SWIR-2 (2.2 µm), and TOA brightness temperature of TIR-1 (10.9 µm) for classifying the peatland combustion into flaming and smouldering stages. The overall accuracy of peatland combustion mapping is 82%, with omission errors in small areas corresponding to smouldering mixed with green vegetation. Commission errors relate to bright building rooftops, which can be eliminated by urban area masking with landuse data and leads to a higher accuracy up to 93%.

The operationalisation of the peatland combustion algorithm for providing peatland fire information is possible for the whole Indonesian archipelago, including other tropical peatland area such as Malaysia, though clearly the issue of cloud obscuration needs overcoming. There is a possibility to merge the Landsat-8 results on peatland combustion mapping with other satellite sensors such as the 375 m VIIRS active fire product (VNP14IMG) for the supply of daily information. The preliminary assessment of the VNP14IMG (+3 and +16 hours from Landsat-8) data provided a 57–72% probability of detection of fire compared with ToPeCAl results of Landsat-8 in 375–1500 m zones. The VNP14IMG product at night-time provides a better probability of detection compared with ToPeCAl results than day-time data. These need further investigation. Other than VNP14IMG, Sentinel-2 images with higher spatial resolution (20 m) and a repeat cycle (5 days) could also be explored for enhancing peatland fire detection for small smouldering fires.

References

Atwood, E, Englhart, S, Lorenz, E, Halle, W, Wiedemann, W & Siegert, F 2016, 'Detection and characterization of low temperature peat fires during the 2015 fire catastrophe in Indonesia using a new high-sensitivity fire monitoring satellite sensor (FireBird)', *PLoS ONE*, vol. 11, no. 8, pp. 1–24.

Aufaristama, M, Hoskuldsson, A, Jonsdottir, I, Ulfarsson, MO & Thordarson, T 2018, 'New Insights for Detecting and Deriving Thermal Properties of Lava Flow Using Infrared Satellite during 2014–2015 Effusive Eruption at Holuhraun, Iceland', *Remote Sensing*, vol. 10, no. 1, p. 151.

BNPB 2018, Central Kalimantan Province, Indonesia, Personal Communication.

BPS-Statistic Central Kalimantan Province 2018a, 'Kalimantan Tengah in Figures 2018'.

BPS-Statistic Riau Province 2018b, 'Riau Province in Figures 2018'.

Caúla, RH, Oliveira-Júnior, JF, Lyra, GB, Delgado, RC & Heilbron Filho, PFL 2015, 'Overview of fire foci causes and locations in Brazil based on meteorological satellite data from 1998 to 2011', *Environmental Earth Sciences*, vol. 74, no. 2, July 01, pp. 1497–1508.

Csiszar, I, Schroeder, W, Giglio, L, Ellicott, E, Vadrevu, KP, Justice, CO & Wind, B 2014, 'Active fires from the Suomi NPP Visible Infrared Imaging Radiometer Suite: Product status and first evaluation results', *Journal of Geophysical Research: Atmospheres*, vol. 119, no. 2, pp. 803–816.

Dennison, PE & Roberts, DA 2009, 'Daytime fire detection using airborne hyperspectral data', *Remote Sensing of Environment*, vol. 113, no. 8, pp. 1646–1657.

Eckmann, T, Roberts, D & Still, C 2009, 'Estimating subpixel fire sizes and temperatures from ASTER using multiple endmember spectral mixture analysis', *International Journal of Remote Sensing*, vol. 30, no. 22, pp. 5851–5864.

Elvidge, CD, Zhizhin, M, Hsu, F, Baugh, K, Khomarudin, M, Vetrita, Y, Sofan, P, Suwarsono & Hilman, D 2015, 'Long-wave infrared identification of smoldering peat fires in indonesia with nighttime landsat data', *Environmental Research Letters*, vol. 10, no. 6, p. 065002.

Filizzola, C, Corrado, R, Marchese, F, Mazzeo, G, Paciello, R, Pergola, N & Tramutoli, V 2016, 'RST-FIRES, an exportable algorithm for early-fire detection and monitoring: description, implementation, and field validation in the case of the MSG-SEVIRI sensor', *Remote Sensing of Environment*, vol. 186, pp. 196–216.

Fuller, DO 2000, 'Satellite remote sensing of biomass burning with optical and thermal sensors', *Progress in Physical Geography*, vol. 24, no. 4, pp. 543–561.

Getis, A & Ord, JK 1992, 'The Analysis of Spatial Association by Use of Distance Statistics', vol. 24, no. 3, pp. 189–206.

Giglio, L & Kendall, JD 2001, 'Application of the Dozier retrieval to wildfire characterization: a sensitivity analysis', *Remote Sensing of Environment*, vol. 77, no. 1, pp. 34–49.

Giglio, L, Csiszar, I, Restás, Á, Morisette, JT, Schroeder, W, Morton, D & Justice, CO 2008, 'Active fire detection and characterization with the advanced spaceborne thermal emission and reflection radiometer (ASTER)', *Remote Sensing of Environment*, vol. 112, no. 6, pp. 3055–3063.

Giglio, L, Schroeder, W & Justice, C 2016, 'The collection 6 MODIS active fire detection algorithm and fire products', *Remote Sensing of Environment*, vol. 178, pp. 31–41.

Hally, B, Wallace, L, Reinke, K & Jones, S 2016, 'Assessment of the utility of the Advanced Himawari Imager to detect active fire over Australia', *International Archives of the Photogrammetry, Remote Sensing and Spatial Information Sciences - ISPRS Archives*, vol. 41, pp. 65–71.

Hantson, S, Padilla, M, Corti, D & Chuvieco, E 2013, 'Strengths and weaknesses of MODIS hotspots to characterize global fire occurrence', *Remote Sensing of Environment*, vol. 131, no. C, pp. 152–159.

Hawbaker, TJ, Radeloff, VC, Syphard, AD, Zhu, Z & Stewart, SI 2008, 'Detection rates of the MODIS active fire product in the United States', *Remote Sensing of Environment*, vol. 112, no. 5, pp. 2656–2664.

Irons, JR, Dwyer, JL & Barsi, JA 2012, 'The next Landsat satellite: The Landsat Data Continuity Mission', *Remote Sensing of Environment*, vol. 122, pp. 11–21.

Jones, S, Hally, B, Reinke, K, Wickramasinghe, C, Wallace, L, Engel, C, 2018, 'Next Generation Fire Detection from Geostationary Satellites', *IGARSS 2018 - 2018 IEEE International Geoscience and Remote Sensing Symposium*, 22–27 July 2018.

Justice, C, Giglio, L, Korontzi, S, Owens, J, Morisette, J, Roy, D, Descloitres, J, Alleaume, S, Petitcolin, F & Kaufman, Y 2002, 'The MODIS fire products', *Remote Sensing of Environment*, vol. 83, no. 1, pp. 244–262.

Kelhä, V, Rauste, Y, Häme, T, Sephton, T, Buongiorno, A, Frauenberger, O, Soini, K, Venäläinen, A, Miguel-Ayanz, JS & Vainio, T 2003, 'Combining AVHRR and ATSR satellite sensor data for operational boreal forest fire detection', *International Journal of Remote Sensing*, vol. 24, no. 8, pp. 1691–1708.

Koppmann, R, von Czapiewski, K & Reid, JS 2005, 'A review of biomass burning emissions, part I: gaseous emissions of carbon monoxide, methane, volatile organic compounds, and nitrogen containing compounds', *Atmos. Chem. Phys. Discuss.*, vol. 2005, pp. 10455–10516.

Kumar, SS & Roy, DP 2018, 'Global operational land imager Landsat-8 reflectance-based active fire detection algorithm', *International Journal of Digital Earth*, vol. 11, no. 2, pp. 154–178.

Langner, A & Siegert, F 2009, 'Spatiotemporal fire occurrence in Borneo over a period of 10 years', *Global Change Biology*, vol. 15, no. 1, pp. 48–62.

Loboda, TV & Csiszar, IA 2007, 'Reconstruction of fire spread within wildland fire events in Northern Eurasia from the MODIS active fire product', *Global and Planetary Change*, vol. 56, no. 3, 2007/04/01/, pp. 258–273.

Marchetti, D 2015, 'A Physics Exhibit to Show the Effect of the Aerosol in the Atmosphere on Electromagnetic Wave Propagation', *Procedia - Social and Behavioral Sciences*, vol. 174, 2015/02/12/, pp. 2975–2982.

Mitchell, A 1999, *The ESRI guide to GIS analysis*, 1st ed. edn, Redlands, Calif. : ESRI, Redlands, Calif.

Mitchell, S, Jones, S, Reinke, K, Lorenz, E & Reulke, R 2016, 'Assessing the utility of the TET-1 hotspot detection and characterization algorithm for determining wildfire size and temperature', *International Journal of Remote Sensing*, vol. 37, no. 20, pp. 4731–4747.

Morfitt, R, Barsi, J, Levy, R, Markham, B, Micijevic, E, Ong, L, Scaramuzza, P & Vanderwerff, K 2015, 'Landsat-8 Operational Land Imager (OLI) Radiometric Performance On-Orbit', *Remote Sens.*, vol. 7, no. 2, pp. 2208–2237.

Morisette, J, Giglio, L, Csiszar, I & Justice, C 2005, 'Validation of the MODIS active fire product over Southern Africa with ASTER data', *International Journal of Remote Sensing*, vol. 26, no. 19, pp. 4239–4264.

Murphy, SW, de Souza Filho, CR, Wright, R, Sabatino, G & Correa Pabon, R 2016, 'HOTMAP: Global hot target detection at moderate spatial resolution', *Remote Sensing of Environment*, vol. 177, pp. 78–88.

Nikam, BR, Ibragimov, F, Chouksey, A, Garg, V & Aggarwal, SP 2016, 'Retrieval of land surface temperature from Landsat 8 TIRS for the command area of Mula irrigation project', *Environmental Earth Sciences*, vol. 75, no. 16, August 12, p. 1169.

Osaki, M, Nursyamsi, D, Noor, M, Wahyunto, W & Segah, H 2016, 'Peatland in Indonesia', in M Osaki & N Tsuji (eds), *Tropical peatland ecosystems*, Springer, Tokyo, pp. 49–58.

Page, SE, Rieley, J & Banks, C 2011, 'Global and regional importance of the tropical peatland carbon pool', *Global Change Biology*, vol. 17, no. 2, pp. 798–818.

Petitcolin, F & Vermote, E 2002, 'Land surface reflectance, emissivity and temperature from MODIS middle and thermal infrared data', *Remote Sensing of Environment*, vol. 83, no. 1, 2002/11/01/, pp. 112–134.

Pierre Guillevic, FG, Jaime Nickeson, Glynn Hulley, Darren Ghent, Yunyue Yu, Isabel Trigo, Simon Hook, José A. Sobrino, John Remedios, Miguel Román and Fernando Camacho 2018, *Land Surface Temperature Product Validation Best Practice Protocol*, Land Product Validation Subgroup (WGCV/CEOS).

Polivka, TN, Jun Wang, LT, Ellison, EJ, Hyer, CM & Ichoku, CM 2016, 'Improving Nocturnal Fire Detection With the VIIRS Day–Night Band', *Geoscience and Remote Sensing, IEEE Transactions on*, vol. 54, no. 9, pp. 5503–5519.

Purnomo, H, Shantiko, B, Sitorus, S, Gunawan, H, Achdiawan, R, Kartodihardjo, H & Dewayani, AA 2017, 'Fire economy and actor network of forest and land fires in Indonesia', *Forest Policy and Economics*, vol. 78, pp. 21–31.

Reid, JS, Koppmann, R, Eck, TF & Eleuterio, DP 2005, 'A review of biomass burning emissions part II: intensive physical properties of biomass burning particles', *Atmos. Chem. Phys.*, vol. 5, no. 3, pp. 799–825.

Rein, G 2013, 'Smouldering fires and natural fuels', *Fire Phenomena and the Earth System: An Interdisciplinary Guide to Fire Science*, vol. Chapter 2, pp. 13–22.

Rein, G 2016, 'Smoldering Combustion', in MJ Hurley et al (eds), *SFPE Handbook of Fire Protection Engineering*, Springer New York, New York, NY, pp. 581–603.

Rieley, J & Page, S 2016, 'Tropical Peatland of the World', in M Osaki & N Tsuji (eds), *Tropical peatland ecosystems*, Springer, Tokyo, pp. 3–32.

Ritung, S, Wahyunto, W & Nugroho, K 2012, 'Karakteristik dan Sebaran Lahan Gambut di Sumatera, Kalimantan dan Papua', *Pengelolaan Lahan Gambut Berkelanjutan. Balai Besar Litbang SDLP, Bogor*, In Bahasa.

Schroeder, W, Prins, E, Giglio, L, Csiszar, I, Schmidt, C, Morisette, J & Morton, D 2008, 'Validation of GOES and MODIS active fire detection products using ASTER and ETM+ data', *Remote Sensing of Environment*, vol. 112, no. 5, pp. 2711–2726.

Schroeder, W, Oliva, P, Giglio, L & Csiszar, I 2014, 'The New VIIRS 375 m active fire detection data product: Algorithm description and initial assessment', *Remote Sensing of Environment*, vol. 143, pp. 85–96.

Schroeder, W, Oliva, P, Giglio, L, Quayle, B, Lorenz, E & Morelli, F 2016, 'Active fire detection using Landsat-8/OLI data', *Remote Sensing of Environment*, vol. 185, pp. 210–220.

Schroeder, W 2017, Visible Infrared Imaging Radiometer Suite (VIIRS) 375 m & 750 m Active Fire Detection Data Sets Based on NASA VIIRS Land Science Investigator Processing System (SIPS) Reprocessed Data-Version 1, NASA. <https://lpdaac.usgs.gov/sites/default/files/public/product_documentation/vnp14_user_guide_v1.3.pdf>.

Siegert, F, Zhukov, B, Oertel, D, Limin, S, Page, SE & Rieley, JO 2004, 'Peat fires detected by the BIRD satellite', *International Journal of Remote Sensing*, vol. 25, no. 16, pp. 3221–3230.

Sobrino, JA, Jimenez-Munoz, JC, Soria, G, Romaguera, M, Guanter, L, Moreno, J, Plaza, A & Martinez, P 2008, 'Land Surface Emissivity Retrieval From Different VNIR and TIR Sensors', *IEEE Transactions on Geoscience and Remote Sensing*, vol. 46, no. 2, pp. 316–327.

Sofan, P, Bruce, D, Jones, E & Marsden, J 2018, 'Detecting peatland combustion using shortwave and thermal infrared landsat-8 data', in DX Viegas (ed), *Advance Forest Fire Research;*, Imprensa da Universidade de Coimbra, Coimbra, pp. 969–979.

Stanski, HR, Wilson, LJ & Burrows, WR 1989, *Survey of Common Verification Methods in Meteorology*, World Meteorological Organization,

Stefano Mariani, MC 2008, *Forecast verification: A summary of common approaches, and examples of application*, University of Trento, Trento, Italy.

Tacconi, L 2003, *Fires in Indonesia: causes, costs and policy implications*, CIFOR, Bogor, Indonesia.

USGS 2018, *Landsat 8 (L8) Data Users Handbook*, LSDS-1574 Version 3.0 edn, South Dakota, U.S.

Wooster, MJ, Xu, W & Nightingale, T 2012, 'Sentinel-3 SLSTR active fire detection and FRP product: Pre-launch algorithm development and performance evaluation using MODIS and ASTER datasets', *Remote Sensing of Environment*, vol. 120, 5/15/, pp. 236–254.

World-Bank 2016, *The Cost of Fire: An Economic Analysis of Indonesia's 2015 Fire Crisis*, World Bank Group, Jakarta, Indonesia.

Xu, W, Wooster, MJ, Roberts, G & Freeborn, P 2010, 'New GOES imager algorithms for cloud and active fire detection and fire radiative power assessment across North, South and Central America', *Remote Sensing of Environment*, vol. 114, no. 9, 9/15/, pp. 1876–1895.

Zaccone, C, Rein, G, D'Orazio, V, Hadden, RM, Belcher, CM & Miano, TM 2014, 'Smouldering fire signatures in peat and their implications for palaeoenvironmental reconstructions', *Geochimica et Cosmochimica Acta*, vol. 137, 7/15/, pp. 134–146.

Chapter 4

Assessment of VIIRS 375 m Active Fire using Tropical Peatland Combustion Algorithm Applied to Landsat-8 over Indonesia's Peatlands

This chapter is published as:

Sofan, P.; Bruce, D.; Schroeder, W.; Jones, E.; Marsden, J. Assessment of VIIRS 375 m Active Fire using Tropical Peatland Combustion Algorithm Applied to Landsat-8 over Indonesia's Peatlands. *Int J Digit Earth.* 2020.

(https://doi.org/10.1080/17538947.2020.1791268)

Note: Minor additional information is inserted in [squared brackets]

Assessment of VIIRS 375 m Active Fire using Tropical Peatland Combustion Algorithm applied to Landsat-8 over Indonesia's Peatlands

Abstract

VIIRS 375 m active fire data (VNP14IMG), the highest spatial resolution available cost-free fire product, were assessed for representing fire in typical degraded tropical peatlands in Indonesia. The results of applying the Tropical Peatland Combustion Algorithm to Landsat-8 (ToPeCAl-L8) daytime imagery were utilised as the fire references. To permit the comparison of non-simultaneous VNP14IMG and ToPeCAl-L8, peatland fire propagation speeds resulting from previous study using TET-1 data in Central Kalimantan's peatlands were utilised. Most peatland fires were still within 750 m from their source over 15 h under uniform conditions, except for very large fires. The detection rates of nighttime VNP14IMG compared with ToPeCAl-L8 showed about 80% agreement for small fire areas (< 14 ha). For fires larger than 14 ha, a dissolved 375 m buffer (cluster buffer) of VNP14IMG active fires with an integration of nighttime and daytime acquisitions, produced a probability of detection up to 90%. These results generated a recommendation for implementing cluster buffer analysis and integration of nighttime and daytime analysis of VNP14IMG data for better accuracy in fire detection for ground fire management. They also demonstrate the utility of the ToPeCAl-L8 algorithm with VIIRS 375 m active fire data.

Keywords: assessment; VIIRS 375 m active fire (VNP14IMG); ToPeCAl-Landsat-8; peatland fires.

4.1. Introduction

In Indonesia vast areas of peatlands have degraded due to agricultural and plantation expansions, logging, and forest/land fires. The practice of agricultural and plantation expansion in peatlands are mostly undertaken through slash and burn activities (Bowen et al. 2000; Cochrane 2003; Dennis et al. 2005; Field, Van Der Werf & Shen 2009; Miettinen et al. 2012; Miettinen, Shi & Liew 2011; Rieley & Page 2016; Siegert et al. 2001). Fires have been used for land clearance and farming preparation by smallholder farmers for many years and have resulted in small area burn scars. Plantation companies

have also used fire for larger-scale land clearance (Dennis et al. 2005; Miettinen, Shi & Liew 2011). Wildfires occur during dry conditions when the ground water level and vegetation moisture content have decreased in summer (July-September), but are in general rare (Takahashi et al. 2002). They can be accidently started when the fires from slash and burn activities have spread out of control and result in irregular burnt area shapes in the peatlands (Bowen et al. 2000; Dennis et al. 2005; Miettinen, J & Liew 2009; Miettinen, Shi & Liew 2011). The 2015 forest and peatland fires resulted in public health impacts with unhealthy air quality conditions which led to mortalities in Indonesia, Singapore, and Malaysia (Koplitz et al. 2016; Crippa et al. 2016). The economic cost of these fires in Indonesia was at least USD 16.1 billion and fires released 1.75 Gt of Carbon into the atmosphere (World-Bank 2016); for comparison, this is approximately 5 times the amount of CO_2 released from Australia's devastating 2019-2020 bushfires (Foley 2020 and Freedman 2020). In 2019, the economic loss from forest and peatland fires in Indonesia was USD 5.0 billion (World-Bank 2019). Although the land burning activities have been banned by the Indonesian government (law No.32/2009), fire is, and still will be, used for land clearance and farming preparation, due to the economic profit for farmers driven by the continuing market demand for the goods produced from plantations (Purnomo et al. 2017).

Satellite remote sensing technology has provided global combustion monitoring since the 1990's (Justice & Korontzi 2001). The current technology has some advantages with its spatial coverage and temporal capability compared with terrestrial, aerial, and sea observations. Satellite observations can monitor large areas and generally more frequently than those from airborne systems, thus leading to potential effectiveness in time and cost. Thermal sensors on satellite platforms can be used to detect fire and are able to provide forest/land fire information on a standard regular basis from 10 minutes, half day, and up to every 16 days (Elvidge et al. 2001; Giglio, Schroeder & Justice 2016; Huang & Rein 2015; Koltunov et al. 2016; Roberts & Wooster 2008; Schroeder et al. 2014; Stolle et al. 2004; Wickramasinghe et al. 2016). Referring to the revisit time issue, a sensor that has a minimum revisit time of twice daily will be high in consideration; thus sensors such us Geostationary Operational Environmental Satellite System (GOES), Meteosat Second Generation-Spinning Enhanced Visible and InfraRed Imager (MSG-SEVIRI), Defense Meteorological Satellite Program-Operational Linescan System (DMSP-OLS), Himawari-8-Advanced Himawari Imager (AHI), National Oceanic and

Atmospheric Administration-Advanced Very High Resolution Radiometer (NOAA-AVHRR), Terra/Aqua-Moderate Resolution Imaging Spectroradiometer (MODIS), Sentinel3-Sea and Land Surface Temperature Radiometer (SLSTR), and Suomi National Polar-orbiting Partnership-Visible Infrared Imaging Radiometer Suite (SNPP-VIIRS) are within scope. Among these high temporal and low spatial resolution satellite sensors, the Visible Infrared Imaging Radiometer Suite (VIIRS) on-board the SNPP and NOAA-20 satellites, provides the highest spatial resolution for global forest fire monitoring, at 375 m at daytime and nighttime (Schroeder et al. 2014). VIIRS 375 m active fire product, termed as VNP14IMG (Schroeder & Giglio 2018) can be accessed from the Level-1 and Atmosphere Archive and Distribution System (LAADS), Distributed Active Archive Center (DAAC). The temporal revisit times of VNP14IMG data are daily at about 1:30 pm (ascending node) and 1:30 am (descending node) equatorial crossing time with an approximate ground swath of 3060 km (Schroeder & Giglio 2018).

Observations twice per 24 hours might not be sufficient from the point of view of having high temporal frequency in subtropical forest fire situations, where fires move very fast due to the specific weather conditions, e.g. strong winds, low precipitation, high temperature, and dry fuel (van der Werf et al. 2008). However, twice daily observation might be sufficient in the tropical peatland environment where the fires move slowly due to the bulk density of the soil, low wind speed, and relatively low drought index/ higher moisture content compared with fast moving fires e.g. in Australia (Ishii et al. 2016; Kumar & Dharssi 2015; Novitasari et al. 2019; Prat-Guitart et al. 2016).Tropical peatland fires, e.g. those in Indonesia, which are mostly triggered by humans for agricultural purposes (Osaki & Tsuji 2016a; Purnomo et al. 2017), are mainly ignited in small areas surrounded by healthy and half-dead vegetation, and exhibit relatively low fire temperatures (Sofan et al. 2019; Elvidge et al. 2015; Usup et al. 2004). These fires slowly extend into a larger area over a number of days if there is no significant rainfall nor attempts to extinguish the fire (Miettinen, Shi & Liew 2011; Rein 2013). In these conditions, it becomes imperative to be able to detect small fires in order to prevent them from growing into larger areas. However, higher spatial resolution (20–30 m) satellite data on a daily basis, with sufficient spectral resolution for fire detection, is still unavailable, at least at low cost. To obtain appropriate peatland fire information, there is an opportunity to merge the fire products obtained from the high temporal and low spatial resolution satellite such as VIIRS with a higher spatial (20–30 m) and a lower temporal

resolution fire-based information from satellites such as Landsat-8 or possibly Sentinel-2. However, the validation of the fire products needs to be conducted before merging information from different sensors.

An assessment of VNP14IMG has been undertaken by Oliva and Schroeder (2015) and Schroeder et al. (2014) in some globally distributed regions, but not including degraded tropical peatlands in Indonesia. The algorithm in the VNP14IMG product is conceptually similar to the heritage Moderate Resolution Imaging Spectroradiometer (MODIS) 1 km active fire algorithm (Giglio et al. 2003; Giglio, Schroeder & Justice 2016; Schroeder et al 2014). The spectral channels utilised in the VNP14IMG algorithm are specified in Table 4.1.

Table 4.1. List of VIIRS channel for active fire detection at 375 m (Schroeder & Giglio 2016).

Channel	Spectral range (µm)	Spatial resolution (m)	Utilities
I1	0.60–0.68	375	Cloud and water classification
I2	0.85–0.88	375	Cloud and water classification
I3	1.58–1.64	375	Water classification
I4	3.55–3.93	375	Fire detection
I5	10.5–12.4	375	Fire detection and cloud classification
M13	3.97–4.13	750	Fire radiative power retrieval and fire detection

The VNP14IMG data is available cost-free on a daily basis. The theoretical 50% probability of detection of fire by VNP14IMG is for a minimum area of 10 m^2 with fire temperature at ≥ 850 K at nighttime (Schroeder et al. 2014). Elvidge et al. (2015) and Usup et al. (2004) observed typical smouldering peat fire in Central Kalimantan at 360–500 K and 320–550 K, respectively. Given those smouldering temperature ranges, the theoretical 50% probability of fire detection by VIIRS 375 m applies to a homogeneous area of approximately 150 m^2 at an average temperature of 550 K at nighttime (Schroeder et al. 2014).

The assessment of active fire information from satellites in real time at ground level is problematic due to factors such as poor accessibility, high cost and high risk for safety reasons (Sofan et al. 2019; Tanpipat, Honda & Nuchaiya 2009). One of the techniques for conducting a satellite product validation is by intercomparison with another satellite product (Hall et al. 2019; Wickramasinghe et al. 2018; Schroeder et al. 2008). Previous studies concerning the comparison of VNP14IMG product with other high temporal and

low spatial data, e.g. MODIS, have shown that the VNP14IMG performed better (10–35%) than MODIS for fire areas less than 50 ha (Hantson et al. 2013; Oliva & Schroeder 2015). In the Brazilian forest, Schroeder et al. (2014) found that VNP14IMG product provided an improvement in spatial agreement with the burnt area from Landsat-7 imagery when compared with MODIS.

Oliva and Schroeder (2015) proposed that ecosystem characteristics and fire behaviour influenced the VNP14IMG performance. The comparison of VNP14IMG with direct burnt area estimation from VIIRS for fires larger than 10 ha resulted a detection rates of fires about 80%–85% in boreal forest, Mediterranean forest, and North Australian savannas, and varies from 25% to 65% in tropical grasslands of Brazil, Colombia and South Africa, agricultural areas of North India, temperate forests in Australia, and tropical dry forest in Cambodia (Oliva and Schroeder 2015). However, thus far, there are limited validations of VNP14IMG in tropical peatlands environments, particularly in Indonesia.

Meanwhile, there is a potential to utilise the result from the application of fire-based products from higher spatial resolution imagery as the fire reference for VNP14IMG assessment. Cost-free higher spatial resolution (20–30 m) data, which is possible for fire monitoring is available from Landsat-8 every 16 days and the Sentinel-2 constellation every five days at equatorial latitudes (ESA 2015). Landsat-8 has an equatorial crossing at 10:11 am (± 15 minutes). The Level-1TP (precision and terrain corrected) product of Landsat-8 data can be obtained from the United States Geological Survey (USGS) Earth Explorer.

In terms of spectral capability for fire detection, the Middle InfraRed (MIR) does not exist in both Landsat-8 Operational Land Imager (OLI)/Thermal InfraRed Sensor (TIRS) and Sentinel-2 Multispectral Instrument (MSI), as they only have ShortWave InfraRed (SWIR) bands at central wavelength of 1.609 µm and 2.201 µm at 30 m spatial resolution for Landsat-8 (Morfitt et al. 2015) and 1.610 µm and 2.190 µm at 20 m spatial resolution for Sentinel-2 (ESA 2015; Drusch et al. 2012). In addition, Landsat-8 has Thermal InfraRed (TIR) bands at central wavelengths of 10.9 µm and 12.0 µm with 100 m spatial resolution (Irons, Dwyer & Barsi 2012), while Sentinel-2 does not have thermal bands. The active fire algorithm of Landsat-8 had been researched using SWIR bands (Kumar & Roy 2018; Murphy et al. 2016; Schroeder et al. 2016) and together with the TIR band over tropical peatland environments, particularly in Indonesia (Elvidge et al.

2015; Sofan et al. 2019). Sofan et al. (2019) established an algorithm for detecting peatland combustion termed Tropical Peatland Combustion Algorithm (ToPeCAl) using daytime observations of Landsat-8 OLI and TIRS for application over Indonesia. An assessment of ToPeCAl Landsat-8 (ToPeCAl-L8) using ground truth data in Kalimantan provided 82% accuracy with commission errors from rooftops building and reached 93% if these errors were eliminated using Geographic Information System (GIS) urban data.

The higher spatial resolution of fire-based satellite information from algorithm's such as ToPeCAl-L8 can act as potential reference data. However, there is about a three and 15 hours time difference in acquisition of Landsat-8 compared with VIIRS daytime and nighttime acquisitions, respectively. To allow the comparison of fire information over these periods of time, the propagation speed of peatland fires needs to be considered. Fires spread rate estimations from satellite data have mostly utilised active fire products to show the spatial dynamics of large fires from the lower spatial resolution e.g. MODIS and AHI-8 (Liu et al. 2018; Loboda & Csiszar 2007; Sá et al. 2017), and from the moderate spatial resolution (30 m) e.g. Landsat and ASTER (Csiszar & Schroeder 2008). Atwood et al. (2016) utilised the Technology Experiment Carrier (TET-1), an experimental small satellite, to estimate peatland fire propagation speeds in Central Kalimantan, Indonesia using the fire front lines detected by MIR with a high sensor saturation temperature of 900 K, which enabled fire detection through smoke and haze with 160 m spatial resolution. The peatland fires propagation speeds estimated from TET-1 ranged between a minimum value of 4.0 m/day and a maximum value of 1,903 m/day in secondary swamp forest of Central Kalimantan (Atwood et al. 2016). At a lower spatial resolution, the Global Fire Atlas estimated fire duration and speed using burnt area mapping from MODIS at 500 m spatial resolution during 2003–2016 in Equatorial Asian regions, including Indonesia, over about 5.5 days of fire duration and resulted in fire speeds of 0.7–1.3 km/day (Andela et al. 2019). Sentinel-2 and Landsat-8 may improve the spatial information of peatland fire spread rate estimation with pixel sizes up to 20 m; however, this comes with limitations on sensor spectral properties and on temperature saturation of some sensors. In addition, the detection of tropical peatland fires in Indonesia from optical sensor are often obscured by cloud, and for some optical sensors which have low temperature saturation the existence of peat fires, particularly smouldering fires, can be inferred by thick smoke (Atwood et al. 2016).

The objective of this study was to assess VNP14IMG using fire information from ToPeCAl-L8 over the tropical peatlands environment of Indonesia. The assessment was conducted using 3, 9, and 15 hours time differences between the acquisitions of Landsat-8 daytime and VIIRS daytime/nighttime. The comparison of fire products from different acquisition times took into account the peatland fire propagation speeds results from previous studies, particularly from Atwood et al. (2016). By considering peatland fire behaviour from fire propagation, comparison between fire products from different sensors and acquisitions times can be entertained to support the temporal gaps in fire monitoring.

4.2. Data

4.2.1. Study Areas

In Indonesia, there are two main sites of peatland fires which occur in most years i.e. Sumatera and Kalimantan islands (Figure 4.1). Riau Province in Sumatera Island, and Central Kalimantan/South Kalimantan Provinces were selected as the study areas for VNP14IMG assessment in tropical peatlands environment. The largest peatland area in Indonesia is located in Riau with about 3.8 million ha, 2.2 million ha, which support palm oil plantations (Ritung, Wahyunto & Nugroho 2012). This is followed by Central Kalimantan with 1.7 million ha of peatland and 1.1 million ha of these devoted to palm oil plantations, which mostly are geographically close to the location of 500 thousand ha of palm oil plantations in South Kalimantan (BPS 2015). Most of these plantation areas are subject to high fire risk, as fires have been used for land clearance and farming preparation for many years by smallholder farmers and plantation companies (Dennis et al. 2005; Miettinen, Shi & Liew 2011).

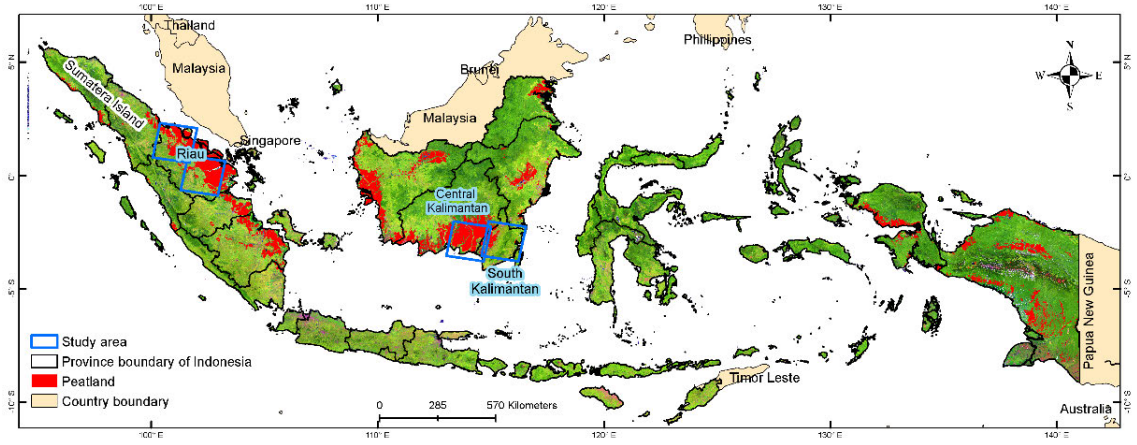


Figure 4.1. Peatlands in Indonesia (red polygon) sourced from Indonesian Ministry of Agriculture. The study sites are peatland area in Riau, Central Kalimantan and South Kalimantan Provinces. The study areas are imaged by Landsat-8 data overpass (blue trapezoids) mostly over of peatland areas in Riau and Kalimantan in path/row of 127/059, 126/060, 117/062, and 118/062.

4.2.2. Satellite Data

For the comparison of VNP14IMG with ToPeCAl-L8, Table 4.2 shows the three generic times of VNP14IMG acquisition assessed in this research, (1) nighttime on the night before Landsat-8 or about nine hours before ($night_{-1}$), (2) daytime on the same day with Landsat-8 about three hours after (day_0), and (3) nighttime on the same day (in UTC) with Landsat-8 about 15 hours after ($night_0$). Nine scenes of daytime Landsat-8 images and 27 VNP14IMG data ($night_{-1}$, day_0, and $night_0$) were utilised in this study with a total of 2,719 active fires as detected by VNP14IMG (Table 4.2).

4.2.3. VNP14IMG Data

The flag fire pixels of VNP14IMG are signed from their confidence level, i.e. low confidence level which relates to the fire pixels affected by sun glint or water during daytime, and lower relative temperature anomaly (< 15 K) in I4 band; nominal confidence level for fire pixels free from sun glint and with a high temperature anomaly during day or nighttime; high confidence level for saturated fire pixels during day or nighttime (Schroeder & Giglio 2018). For this research in order to detect smouldering peatland fires, which exhibit a low relative temperature, all of the confidence levels of VNP14IMG were utilised and merged in one fire class.

The other VIIRS data utilised in this study was the VIIRS/NPP Imagery Resolution Terrain-Corrected Geolocation 6-Min L1 Swath at 375 m spatial resolution (VNP03IMG) used for reprojecting the VNP14IMG, particularly for extracting fire-mask classification.

These VIIRS data were obtained from the LAADS DAAC's website at https://ladsweb.modaps.eosdis.nasa.gov/search/.

Table 4.2. List of Landsat-8 OLI/TIRS and VNP14IMG data used in the study area of Riau, Central Kalimantan (CK), and South Kalimantan (SK).

Landsat-8			Site	VNP14IMG			
Scene	**Date**	**Time (UTC)**		**Date**	**Time (UTC)**	**Time code**	**# Active fire**
127/059	20/08/2016	03:29	Riau	19/08/2016	18:48	$night_{-1}$	265
				20/08/2016	05:54	day_0	86
				20/08/2016	18:30	$night_0$	493
127/059	04/04/2018	03:28	Riau	03/04/2018	18:48	$night_{-1}$	16
				04/04/2018	05:48	day_0	5
				04/04/2018	18:30	$night_0$	27
127/059	07/04/2019	03:28	Riau	06/04/2019	18:48	$night_{-1}$	7
				07/04/2019	05:48	day_0	4
				07/04/2019	18:30	$night_0$	26
127/059	22/03/2019	03:28	Riau	20/03/2019	18:48	$night_{-1}$	52
				21/03/2019	05:48	day_0	0
				22/03/2019	18:30	$night_0$	105
126/060	07/09/2019	03:28	Riau	06/09/2019	17:42; 19:42	$night_{-1}$	158
				07/09/2019	06:24	day_0	77
				07/09/2019	19:00; 19:06	$night_0$	177
117/062	07/10/2018	02:28	CK/ SK	06/10/2018	17:24	$night_{-1}$	41
				07/10/2018	06:00	day_0	15
				07/10/2018	17:06	$night_0$	26
118/062	28/09/2018	02:34	CK	27/09/2018	18:30	$night_{-1}$	144
				28/09/2018	05:30	day_0	386
				28/09/2018	18:12	$night_0$	296
118/062	12/09/2018	02:34	CK	11/09/2018	16:54	$night_{-1}$	11
				12/09/2018	05:30	day_0	37
				12/09/2018	18:12	$night_0$	8
118/062	30/08/2019	02:34	CK	29/08/2019	18:30	$night_{-1}$	55
				30/08/2019	05:30	day_0	90
				30/08/2019	18:12	$night_0$	112

4.2.4. Tropical Peatland Combustion Algorithm Applied to Landsat-8 (ToPeCAl-L8)

ToPeCAl was developed by Sofan et al. (2019) using the daytime observation of Landsat-8 OLI and TIRS to enhance the peatland combustion (smouldering and flaming) mapping, using top of atmosphere (TOA) reflectances of aerosol band (band 1) and SWIR bands (band 6 and 7), and TOA brightness temperature of TIR band (band-10). TOA

reflectances were also utilised in previous studies for fire detection using ASTER and Landsat-8 (Giglio et al. 2008; Kumar & Roy 2018; Murphy et al. 2016; Schroeder et al. 2016). In ToPeCAl, the aim of using TOA reflectance was to enhance the detection of peatland fires under hazy conditions thus atmospheric effects were not corrected (Sofan et al. 2019). Table 4.3 shows the spectral bands and their uses in ToPeCAl.

Readers are referred to Sofan et al. (2019) for a complete description of ToPeCAl. The ToPeCAl was finalised by masking urban areas with a landuse Geographic Information System map, to eliminate commission errors from bright rooftops in urban areas. The landuse information was from Indonesian Ministry of Environment and Forestry and was generated from the annual mosaic of Landsat-8 data of 2018. The result of ToPeCAl applied to Landsat-8 is fire pixels with combustion classes of flaming, smouldering, or mixture of flaming and smouldering. However, in this study, all of peatland fire combustion classes were merged into one fire class to be compared with VNP14IMG data.

Table 4.3. List of Landsat-8 OLI and TIRS spectral bands used in ToPeCAl and their primary application (Sofan et al. 2019; Irons, Dwyer & Barsi 2012; USGS 2019). The Thermal InfraRed band (band-10) was resampled from 100 m to 30 m in Landsat-8 Level-1TP by USGS.

Band#	Spectral range (µm)	Spatial resolution (m)	Primary application
1	0.433–0.453	30	Hazy and relative-clear atmosphere classification
6	1.560–1.660	30	Separating combustion area from non-combustion areas
7	2.100–2.300	30	Separating combustion area from non-combustion areas; fire detection
10	10.60–11.19	30	Fire detection

4.2.5. Methods for Analysis Comparison of VNP14IMG with ToPeCAl Landsat-8

The inherent assumption in this study is that the fire spread over the time period between VNP14IMG and Landsat-8 daytime acquisitions is less than a pre-defined buffer of fire pixel point (pixel centroid) derived from VNP14IMG Level-2 product. In this study, the values of fires spread were utilised from a previous study conducted by Atwood et al. (2016). in Central Kalimantan's peatlands. They estimated fire propagation speeds from the movement of fire front lines derived from the MIR band of TET-1 images, which

resulted in average and maximum of fire propagation speed at about 343 m/day and 1903.5 m/day, respectively. Atwood et al. (2016) fire propagation speeds were assumpted to be in linear direction and at a constant speed and used to estimate the fire spreads over 3, 9, and 15 hours for supporting the comparison of ToPeCAl-L8 daytime and VNP14IMG data from different time acquisitions. Thus, the average and maximum peatland fires propagation speeds in this study were adopted at 14 m/hours and 79 m/hours, respectively.

The comparison between VNP14IMG and ToPeCAl-L8 only occurred over valid areas with no cloud, no cloud-shadow and non-water areas. Cloud and water masks of VNP14IMG were obtained from the fire mask classes. These were combined with the mask of cloud, cloud-shadow and water of Level-2 of Landsat-8.

A buffer analysis from the points of VNP14IMG was used for fire pixels comparison with ToPeCAl-L8. A buffer technique was also implemented for the comparison of hotspot among different sensors, e.g. GOES, MODIS, AHI-8, and burnt area of Landsat-8 (Hantson et al. 2013; Koltunov et al. 2016; Koltunov, Ustin & Prins 2012; Wickramasinghe et al. 2018). Each VNP14IMG active fire coordinate is located at the centre of corresponding pixel, which may not represent the actual fire location on the ground (Giglio, Schroeder & Justice 2016); thus, in this study we utilised buffer zones of 187.5 m, 375 m and 750 m (half, one, and two VIIRS pixel size respectively) from the active fire coordinate.

The buffers were analysed into two ways, i.e. single buffer and group/cluster buffer (Figure 4.2). In a single buffer, each VNP14IMG point was individually compared with ToPeCAl-L8 fire polygons only in its buffer zone. Meanwhile for the cluster buffer, the buffer of the neighbourhood of VNP14IMG points were dissolved into one buffer according their buffer distances (187.5 m, 375 m, and 750 m) and termed “cluster buffer”. The assessment was undertaken by if there were any ToPeCAl fire polygons inside one VNP14IMG buffer, either single or cluster buffer, then the VNP14IMG point was counted as the true positive (agreement) of active fire. The probability of detection (POD) was calculated by dividing the agreement fires with the total of ToPeCAl fire polygons (i.e. the reference). Alternatively, if the ToPeCAl fire polygons occurred outside the buffer area then they were counted as missed fires (i.e. omission). Thus, the omission error was 1 - POD. Otherwise, if there were no ToPeCAl identified fires inside the VNP14IMG

buffer, then the VNP14IMG identification was counted as a false positive. The commission error was counted by dividing the sum of false positive by the total of VNP14IMG data.

The percentage of agreement of fires based on the fire area detected by ToPeCAl Landsat-8 were classified into three fire area size classes, i.e. (1) 0.09 ha as the minimum area of one pixel of Landsat-8 (30 x 30 m); (2) less one pixel of VNP14IMG (375× 375 m or about ≤ 14 ha); and (3) fire areas larger than one pixel of VNP14IMG at 375 x 375 m or about more than 14 ha.

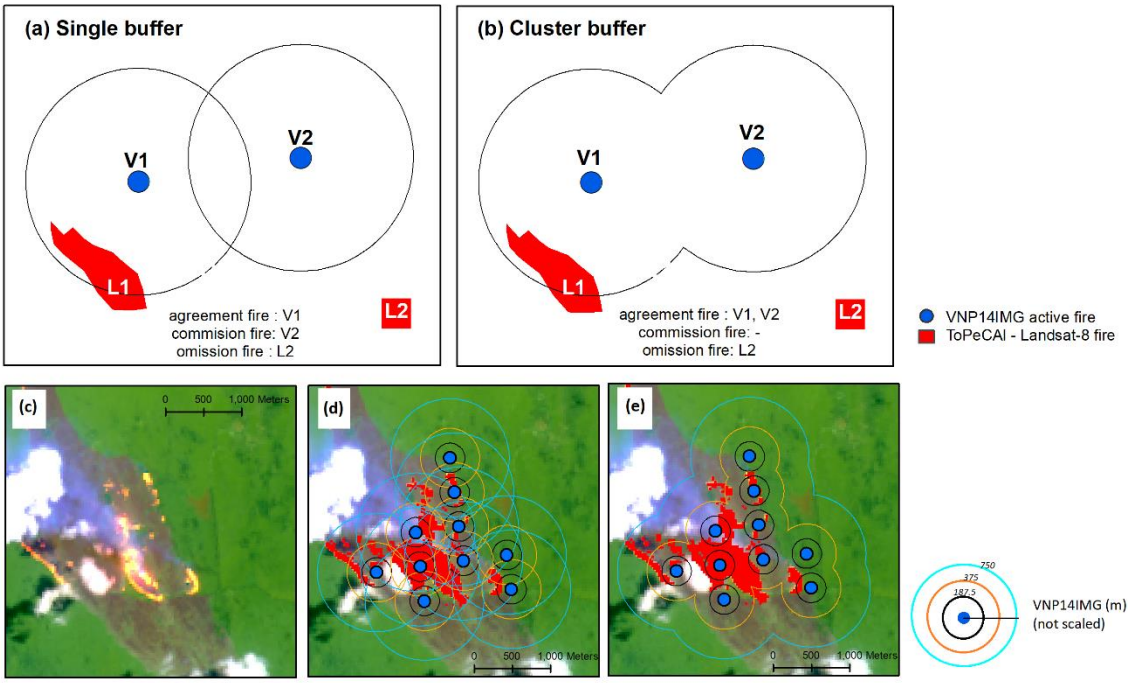


Figure 4.2. The illustration of the assessment of (**a**) single buffer and (**b**) cluster buffer of VNP14IMG with ToPeCAl-L8; (**c**) A sample fire area in the 764-RGB image of Landsat-8 on 30 August 2019 path/row 118/062; (**d**) the daytime VNP14IMG data on 30 August 2019 (blue dots) with the single buffers of VNP14IMG of 187.5 m, 375 m and 750 m (black, orange and aqua circles respectively); (**e**) the daytime VNP14IMG data on 30 August 2019 with the cluster buffer of VNP14IMG of 187.5 m, 375 m and 750 m (black, orange and aqua polygons respectively).

Instead of analysis at a single time of acquisition, there is an opportunity to explore the detection rates by combining multiple times of acquisition of VIIRS at night and daytime i.e. $night_{-1}$ + day_0; day_0 + $night_0$; $night_{-1}$ + day_0 + $night_0$, and both of the nighttime data i.e. $night_{-1}$ + $night_0$. The multi-time combination analysis was considered possible due to the result of the low propagation speed of peatland fires, as were found by Atwood et al. (2016) at an average propagation speed at 14 m/hour.

The sources of false positive at 375 m buffer distance were further examined through visual inspection of RGB images of Landsat-8 OLI/Sentinel-2 MSI before and after the fires to check if there were any active fire or burnt area features as the effect of fires around the buffer area. Additional inspection of high spatial resolution images sourced from ESRI and Google Earth occurred to check for potential thermal anomalies. The VIIRS global flaring data which records the location of flare sites from VIIIRS nighttime (Elvidge et al. 2016) were utilised to confirm the temperatures anomaly (gas flaring) sites for commission error calculation. The VIIRS global flaring data were obtained from https://ngdc.noaa.gov/eog/viirs/download_global_flare.html. Additionally, the omission errors were examined from the fire mask classes of VNP14IMG. The percentage of VNP14IMG points and ToPeCAl-L8 obstructed by clouds in both of Landsat and VIIRS were also counted.

4.3. Results

4.3.1. Probability of Detection of VNP14IMG at Single Time of Acquisition

From a total of 27 VIIRS acquisitions and nine scenes of Landsat-8 data, there were 749 (at night$_{-1}$), 700 (at day$_0$), and 1,270 (at night$_0$) VNP14IMG active fires and between 726 and 1,238 ToPeCAl fires polygons from Landsat-8 analysed at buffer distances of 187.5 m, 375 m and 750 m from VNP14IMG points. However, about 37% of the ToPeCAl-L8 fire polygons occurred under cloud cover during daytime VNP14IMG, 3%–4% existed under cloud cover at nighttime of the VNP14IMG fire mask data, and about 38% of VNP14IMG data was under cloud cover on Landsat-8 images.

The selected cloud free fire data of VNP14IMG and ToPeCAl-L8 presented in Table 4.4 shows the number of matches of active fires of VNP14IMG with ToPeCAl-L8 fire polygons for all fire sizes at each buffer distance of VNP14IMG. The number of fires in both data sources shown in Table 4.4 were less at daytime than nighttime, due to higher cloud cover during daytime. Single buffer analysis resulted in a lower POD than the cluster buffer analysis at the same time of acquisition of VNP14IMG. The POD also tended to increase with larger buffer distances. The night$_{-1}$ time POD (nine hours before daytime Landsat-8) for the single buffer analysis reached 67% while higher POD values, up to 76%, were observed from the cluster buffer analysis. A slight increase of POD occurred at day$_0$ (three hours after daytime Landsat-8) up to 74% for single buffer analysis and 84% in the cluster buffer analysis. At night$_0$ (15 hours after daytime Landsat-8), the

POD increased to 76% for the single buffer analysis and 85% in the cluster buffer analysis.

Table 4.4. Number of VNP14IMG at night$_{-1}$, day$_0$, and night$_0$, and number of ToPeCAl-L8 fire polygons as the fire reference after cloud masking on both of VIIRS and Landsat-8 data. The fire data were counted at buffer distances from VNP14IMG point of 187.5 m, 375 m, and 750 m. The detected fires were analysed with single buffer and cluster buffer techniques. POD equals the number of detected fires divided by the number of ToPeCAl-L8 fires was without classifying the fire sizes.

Time	Buffer (m)	Single Buffer analysis				Cluster Buffer Analysis			
		# VNP14IMG	# ToPeCAl-L8	# Detected fires	POD (%)	# VNP14IMG	# ToPeCAl-L8	# Detected fires	POD (%)
night$_{-1}$	187.5	639	773	416	54	653	751	534	71
	375	655	878	555	63	668	796	609	77
	750	667	916	616	67	647	812	618	76
day$_0$	187.5	614	572	284	50	571	605	438	72
	375	609	628	393	63	602	632	505	80
	750	610	688	510	74	622	673	564	84
nigth$_0$	187.5	1103	852	490	58	1095	1109	878	79
	375	1123	1068	747	70	1129	1170	982	84
	750	1128	1224	924	76	1144	1206	1022	85

Figure 4.3 shows the number of agreement fires according to fire size within buffers of VNP14IMG from single buffer and cluster buffer analysis. The number of agreement fires increased with the buffer size. Small fires at 0.09 ha as a fraction of larger fires were found in a low number at less than 50 fires, or about less than 10% of the agreement fires from single buffer or cluster buffer analysis. Meanwhile small fires at ≤ 14 ha were found in a greater portion at about 500 fires or 80% of agreement fires at nighttime from single buffer analysis (Figure 4.3a). Fire areas larger than one pixel of VNP14IMG (> 14 ha) were mostly presented from cluster buffer analysis up to 85% of agreement fires at nighttime (Figure 4.3b).

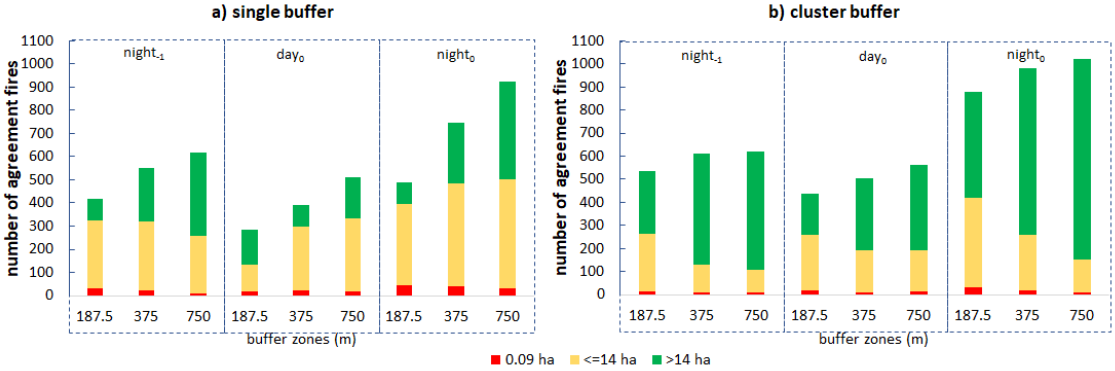


Figure 4.3. Number of agreement fires at 0.09 ha, ≤ 14 ha, and >14 ha from (**a**) single buffer analysis and (**b**) cluster buffer analysis at buffer distances of 187.5 m, 375 m, and 750 m for each VNP14IMG acquisition ($night_{-1}$, day_0, and $night_0$).

All the agreements of active fires from VNP14IMG with ToPeCAl-L8 within 750 m of VNP14IMG from cluster buffer analysis were spatially mapped and presented in Figure 4.4 according to the time acquisition at $night_{-1}$, day_0, and $night_0$. Some locations of agreement of fires were detected only at $night_{-1}$ (black circle) and $night_0$ (red circle), with no detection of active fire by VNP14IMG at day_0 (Figure 4.4a). However, some of the active fires at $night_{-1}$ (black circle) corresponded to the active fires at day_0 (yellow circle) and $night_0$ (red circle) which suggests that the fires existed from $night_{-1}$ to $night_0$ (Figure 4.4a and 4.4b). Others only existed on day_0 (yellow circle) to $night_0$ (red circle), which implies the fires did not exist at $night_{-1}$ (Figure 4.4c). There were also agreement fires that only occurred at daytime (yellow circle) in Figure 4.4c.

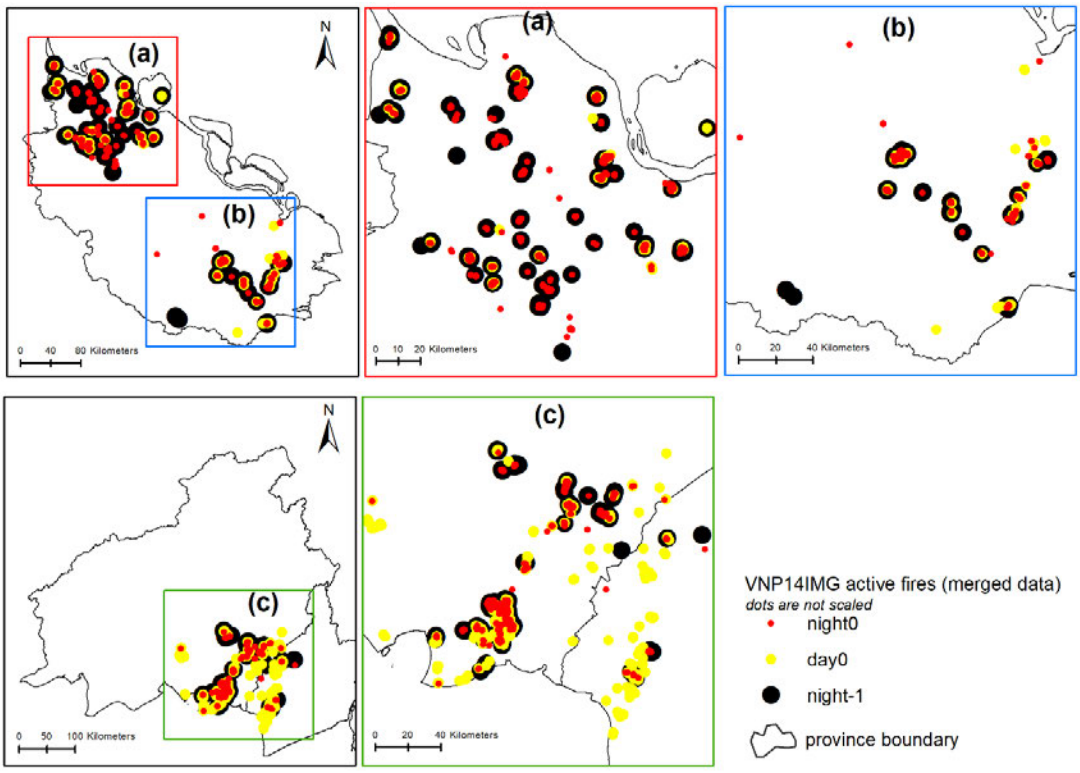


Figure 4.4. Plots of VNP14IMG active fires which agreed with ToPeCAl-L8 fires within 750 m of VNP14IMG from cluster buffer analysis in Riau (top) and part of Central Kalimantan and South Kalimantan Provinces (bottom); (**a**) and (**b**) are enlargements of the north east part (**a**) and south east part (**b**) of Riau Province; (**c**) presents fire data located in the border of Central Kalimantan and South Kalimantan. The data period is the same listed in Table 4.3. The black, yellow, and red circles represent VNP14IMG at night$_{-1}$, day$_0$, and night$_0$, respectively. The relative size of the dot is not associated with the fire size.

4.3.2. Probability of Detection of VNP14IMG at Multi-Times Combinations of Acquisition

The multi-times combinations, which were analysed without considering fire sizes are shown in Figure 4.5a and 4.5b. The night$_{-1}$+day$_0$ combination and the day$_0$+night$_0$ combination performed with similar POD to single time acquisition in single buffer analysis. In cluster buffer analysis the POD of night$_{-1}$+day$_0$ increased to 90% within 375 m buffer and 93% within 750 m buffer, while the POD of day$_0$+night$_0$ reached 88% within 375 m and 91% within 750 m buffer. The dual nighttime combination (night$_{-1}$+night$_0$) performed with the highest POD (81% to 85%) in single buffer analysis within 375 m to 750 m buffer. However, the highest POD from cluster buffer analysis was not achieved from the dual nighttime combination, which had POD up to 89% to 90% from cluster buffer analysis within 375 m to 750 m buffer. A 100% of POD was achieved at the multi-time combination of night$_{-1}$+day$_0$+night$_0$ from cluster buffer analysis for all the buffer sizes, which in this case was for large fires. The results show that POD tends to increase

by increasing buffer size and aggregating all of VNP14IMG data (night$_{-1}$+day$_0$+night$_0$); however, referring to the peatland fires spread rates referenced from Atwood et al (2016), some of peatland fires with maximum propagation speeds of 79 m/hours from unburnt secondary swamp forest might spread more than 750 m over nine hours. The fires with a lower propagation speeds e.g. 14 m/hours (average value) under different vegetation types might still exist within 750 m over 15 hours.

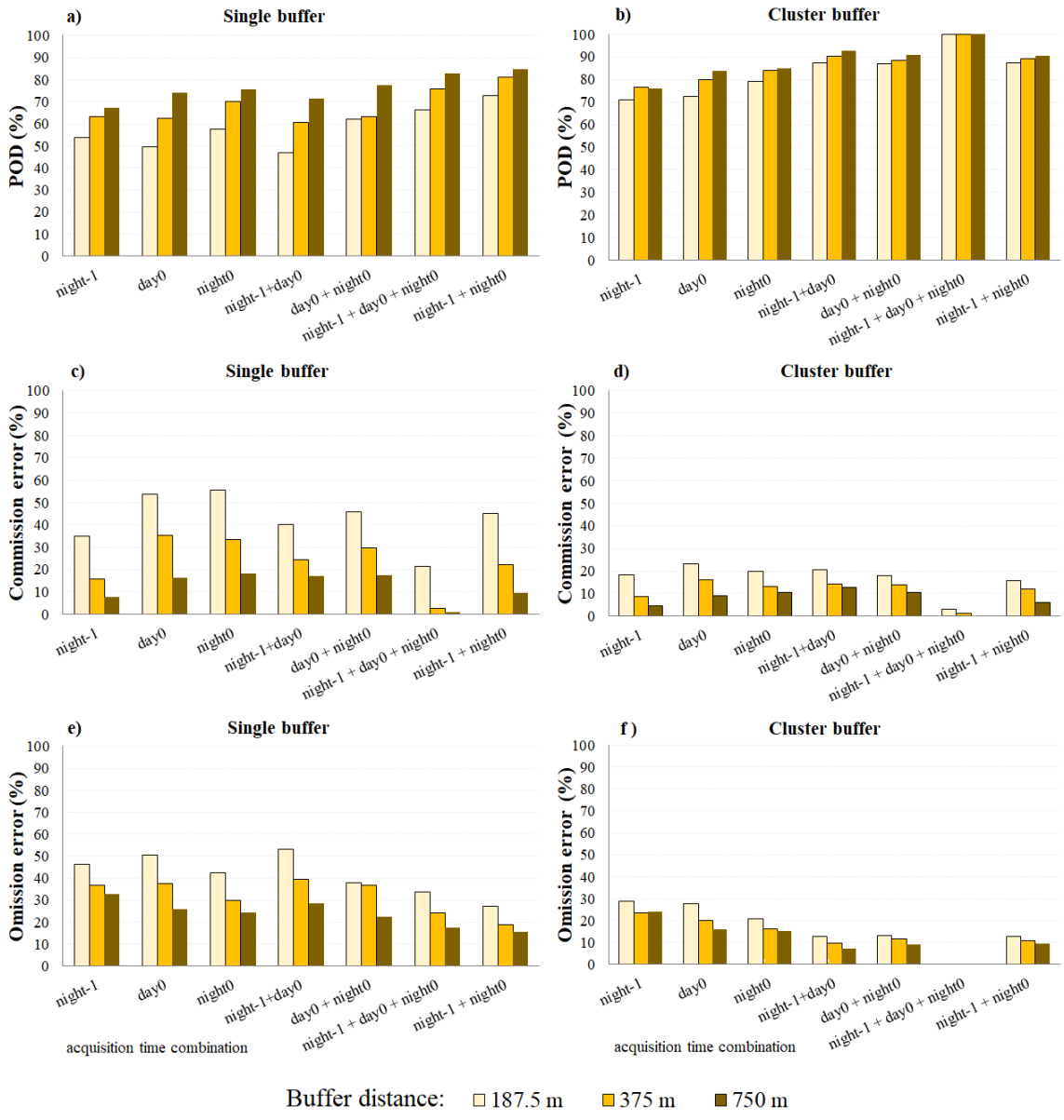


Figure 4.5. (**a**, **b**) POD (%), (**c**, **d**) commission error (%), and (**e**, **f**) omission error (%) of VNP14IMG assessment based on ToPeCAl-L8 fires using single buffer analysis and cluster buffer analysis for three buffer distances (187.5 m, 375 m, 750 m) and single time acquisition (night$_{-1}$; day$_0$; night$_0$) and multi-time acquisition of VNP14IMG (night$_{-1}$ + day$_0$; day$_0$ + night$_0$; night$_{-1}$ + day$_0$ + night$_0$, and nighttime data i.e. night$_{-1}$ + night$_0$). [numerical data corresponding to this figure is available in Appendix - Table A4.1]

4.3.3. Commission and Omission Errors

The increase of POD with larger buffer distances for all fires without considering fire size, correlates with the decrease of commission and omission errors (Figure 4.5). At daytime, the commission error within 375 m buffer was about 35% from single buffer analysis but decreased to 16% when using cluster buffer analysis. At night$_{-1}$, the commission errors within 375 m buffer were about 16% from single buffer analysis and this decreased to 9% from cluster buffer analysis. Meanwhile at night$_0$ the commission errors within 375 m buffer was about 33% from single buffer analysis and 13% from cluster buffer analysis.

There were two main categories of false positive found in this study i.e. spatially related-false positive and independent false positive. The spatially related-false positive error still has a correspondence to the agreement of fires due to its close proximity, while the independent false positive referred to the potential false positive which is caused from other thermal anomalies, such as open land/bare-land, building rooftops, and mining areas. The source of false positives rates (FPR) were classified into six types as shown in Table 4.5.

Table 4.5. The classes and sources of FPR in this study.

FPR classes	Sources of FPR	Types of false positive
FPR-1	ToPeCAl fires outside 375 m buffer, but still within the 750 m buffer	Spatially related-false positive
FPR-2	Omission fire in ToPeCAl which means there was fire feature in Landsat-8 image but missed in ToPeCAl	Spatially related-false positive
FPR-3	Fire features or burnt areas on Landsat-8/Sentinel-2 images (one to two days) before/after VNP14IMG data	Spatially related-false positive
FPR-4	Open land/bare land	Independent/potential false positive
FPR-5	Industrial area with gas flare which were confirmed by high spatial resolution images and the VIIRS global flaring data	Independent/potential false positive
FPR-6	Bright objects e.g. mining area, rooftops building, or river sandbanks	Independent/potential false positive

The percentage of these FPR to the total of commission error are presented in Figure 4.6 which shows the FPR with their sources within 375 m buffers from cluster buffer analysis. The high percentage of false positive sources were found in the spatially related-false positives i.e. FPR-1, FPR-2 and FPR-3 at about 14%, 29%, and 44% on average,

respectively. FPR-1 could be the result of geolocation errors of VIIRS and Landsat-8; something that practically could not be avoided. The FPR-2 and FPR-3 indicated uncertainty in ToPeCAl-L8 and the temporal changes of fires in one or two days before/after VNP14IMG data shown in Landsat-8 or Sentinel-2 images, respectively and may not be appropriate to be included in commission error calculations. False positives relating to other thermal anomalies were from FPR-4 (open land/bare-land) which were lower than 5%, FPR-5 (industrial area with gas flares) were 9% on average, and bright objects (e.g. mining areas, building rooftops) were lower than 5%. However, gas flaring activity – by definition – could not be described as commission error. The VIIRS active fire product is designed to detect fires and thermal anomalies; burning of gas falls well in that category (Oliva and Schroeder 2015). An illustration using satellite images for FPR-3 is shown in Figure 4.7**,** while examples for FPR-5 and FPR-6 are shown in Figure 4.8.

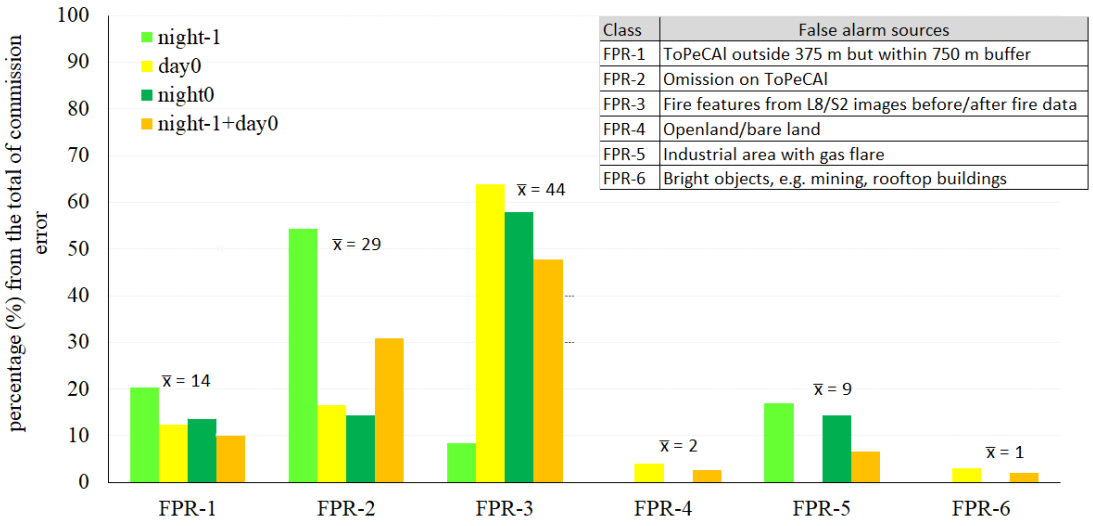


Figure 4.6. The percentage of false positive rates (FPR) sources from the total of commission error at single time ($night_{-1}$, day_0, and $night_0$) and multi-time combination ($night_{-1}$+day_0) within 375 m from cluster buffer analysis. $\bar{x}$ is the average value.

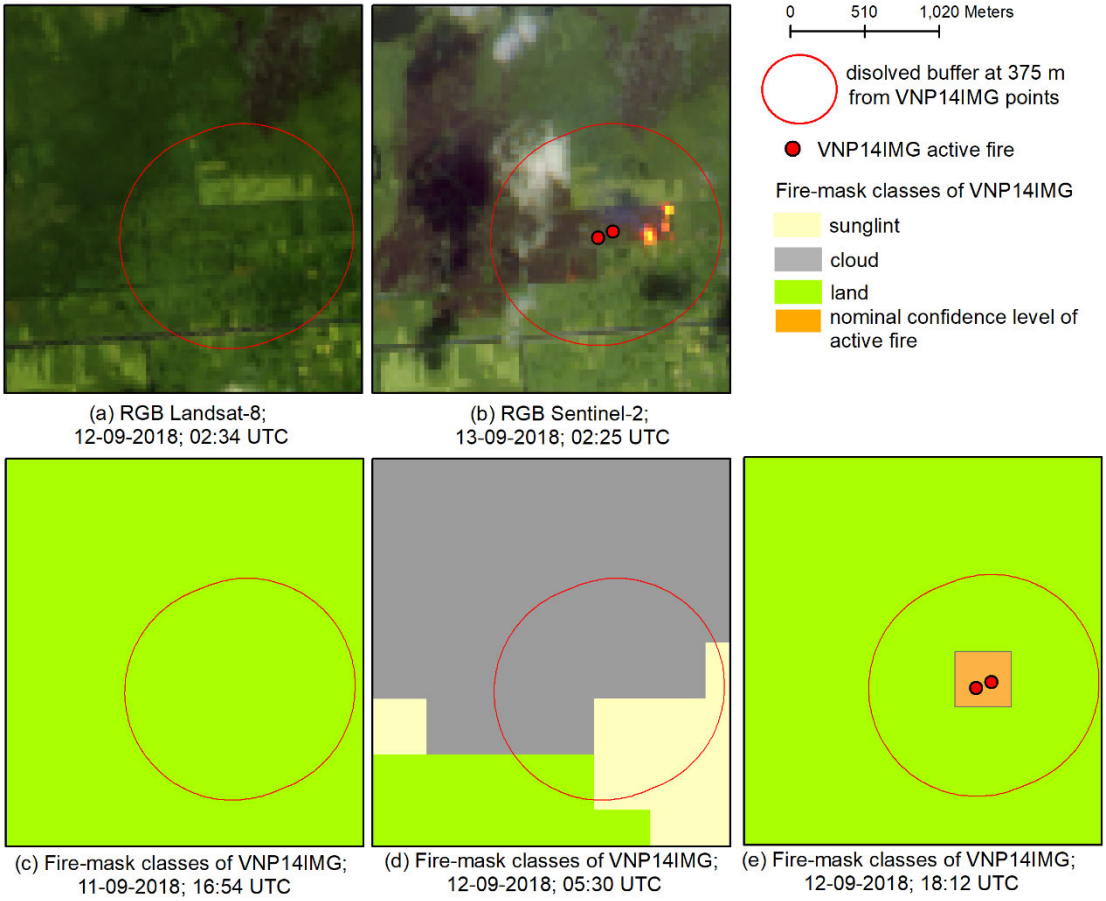


Figure 4.7. An example of FPR-3. (a) There were no fires in Landsat-8 daytime on 12 September 2018; (b) Sentinel-2 image showed fire features on 13 September 2018; (c) no fire detection from VNP14IMG at night$_{-1}$ (11 September 2018); (d) no fire detection from VNP14IMG at day$_0$ (12 September 2018) due to cloud and sun glint; (e) active fires detected from VNP14IMG at night$_0$ (12 September 2018) with nominal confidence level. This caused commission error on night$_0$ data when compared to ToPeCAl-L8 daytime. However, there were fire features from Sentinel-2 image one day after Landsat-8 data.

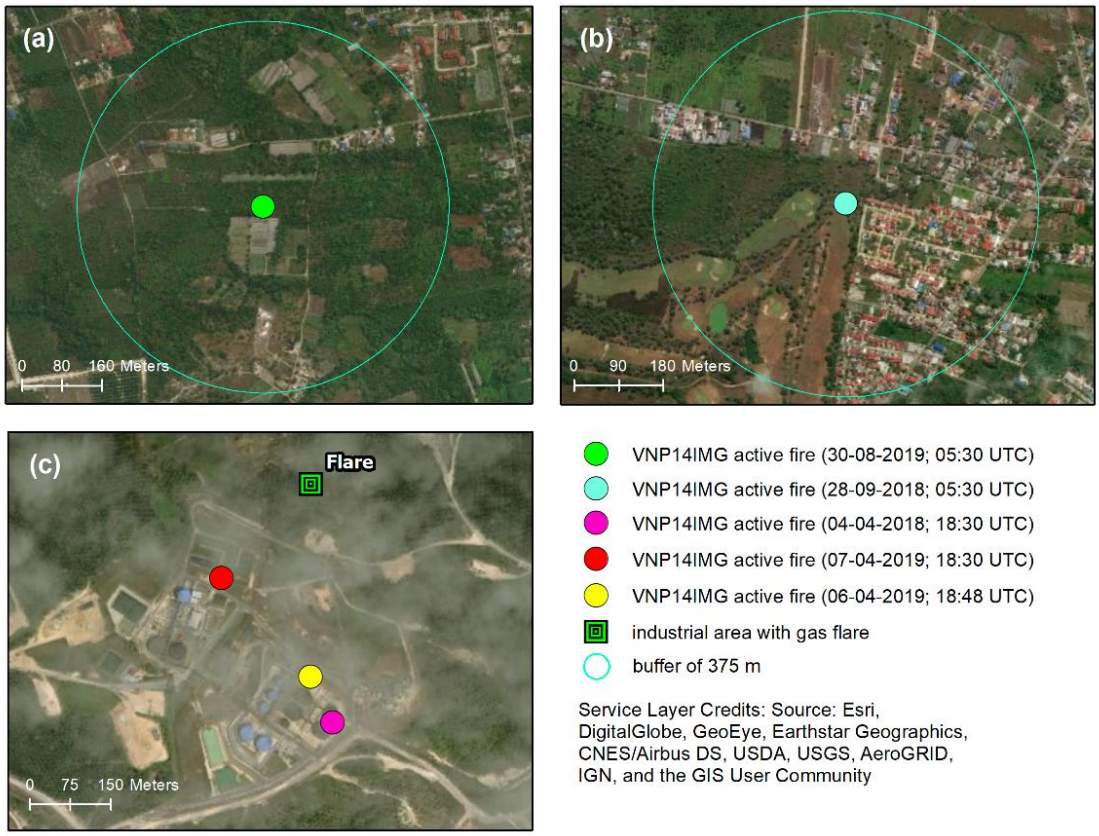


Figure 4.8. Examples of commission errors of VNP14IMG: (a) bright object in intensive agricultural area using plastic membranes observed at daytime (30 August 2019; 05:30 UTC); (b) over open land and bright object in settlement area at daytime (28 September 2018; 05:30 UTC); (c) over industrial area with gas flare at nighttime (04 April 2018; 06 April 2019; 07 April 2019). VNP14IMG active fires were overlaid on high spatial resolution image data sourced from ESRI.

Table 4.6 shows the assessment of VNP14IMG with ToPeCAl-L8 reference fires before and after reducing the false positive data. The scenarios for removing the false positive sources from the total FPR were treated in 2 ways i.e. (1) removing FPR-2 and FPR-3 and (2) removing FPR-2, FPR-3 and FPR-5. A significant decrease in commission error to about 3%–4% resulted by removing FPR-2 and FPR-3. However, nighttime data still had a slightly higher commission error than daytime data, with sources from industrial areas with gas flares (FPR-5). After removing FPR-2, FPR-3 and FPR-5, the commission error decreased to 2% at nighttime, with most other sources of the remaining false positives categories of FPR-1 due to geolocation errors of VIIRS and Landsat-8, and FPR-5 and FPR-6 on open land/bare-land and bright objects in settlement areas at daytime.

Table 4.6. The result of VNP14IMG and ToPeCAl-L8 comparison at night$_{-1}$, day$_0$, night$_0$, and night$_{-1}$+day$_0$ within 375 m buffer from cluster buffer analysis; com-0 = commission errors before reducing false positives; com-1 = commission error after removing FPR-2 and FPR-3; com-2=commission error after removing FPR-2, FPR3 and FPR-5.

Time	# Agreement fire	#Miss fire	Total # false positive	POD (%)	Omission (%)	com-0 (%)	com-1 (%)	com-2 (%)
night-1	609	187	59	77	23	9	3	2
day0	505	127	97	80	20	16	3	3
night0	982	188	147	84	16	13	4	2
night-1+day0	1072	115	154	90	10	13	3	2

Although generally the omission error was lowest at nighttime (night$_0$) compared to daytime, it was also found that the omission errors at night$_{-1}$ were higher than at night$_0$ and day$_0$. Figure 4.9 shows examples of omission errors at night$_{-1}$. In Figure 4.9a, there were three fires areas symbolised by red polygons shown with bluish smoke emanating from fire areas on the RGB image of Landsat colour composite of SWIR-2, SWIR-1, and red bands on 12 September 2018. One of fire areas was detected by VNP14IMG at night$_{-1}$ (Figure 4.9e) at nominal confidence level, however two fires missed detection by VNP14IMG at night$_{-1}$. Other than that, about three hours after the Landsat-8 daytime image of the area, VIIRS daytime (day$_0$) imaged the area; however, fires were not detected potentially because of sun-glint, cloud cover, and some areas being classified in the land class by VNP14IMG fire-mask (Figure 4.9f). Meanwhile, Sentinel-2 observed the same area one day after Landsat-8 (Figure 4.9b) and shows a recent dark burnt areas underneath smoke and cloud on the RGB colour composite. Visually from this RGB image, the burnt areas in dark tones still can be seen through smoke and thin cloud but the origins of smoke were not clearly identified. However, there was an indication that the burnt areas has spread into a larger area than the day before. These indications were also shown in Figure 4.9c and 4.9d with the orange tones on the ShortWave InfraRed Combustion Index (SICI) images generated from the ratio of TOA reflectance of SWIR-2 and SWIR-1, which constitute part of the ToPeCAl calculation to classify combustion and non-combustion areas (Sofan et al. 2019). According to Sofan et al. (2019), SICI values of Landsat-8 which were greater than 1.0 were classified as potential combustion area. The fires areas (red polygons) in Figure 4.9a resulted from ToPeCAl applied to Landsat-8 and corresponded to dark orange colour in SICI image (Figure 4.9c). An adjustment of SICI threshold for classifying combustion and non-combustion area on Sentinel-2 needs further research. In Figure 4.9e, the omitted fires were located in land

class based on the fire-mask classes of VNP14IMG at night$_{-1}$. Continuing with the next VNP14IMG observation at night$_0$ (about 15 hours after Landsat-8), all the fires missed detection by VNP14IMG even though the classification of fire-mask indicated clear sky and land class (Figure 4.9g).

The source of omission errors was observed based on the background fire-mask classes of VNP14IMG data. At daytime, the omission errors within 375 m buffer from cluster buffer analysis were found over land class (41%), sun-glint class (14%) and water class (7%), while the remaining 38% of omission were due to cloud cover. At nighttime data most of the omission errors within 375 m buffer from cluster buffer analysis occurred over land class (86%) and water class (12%), with 2% under cloud cover.

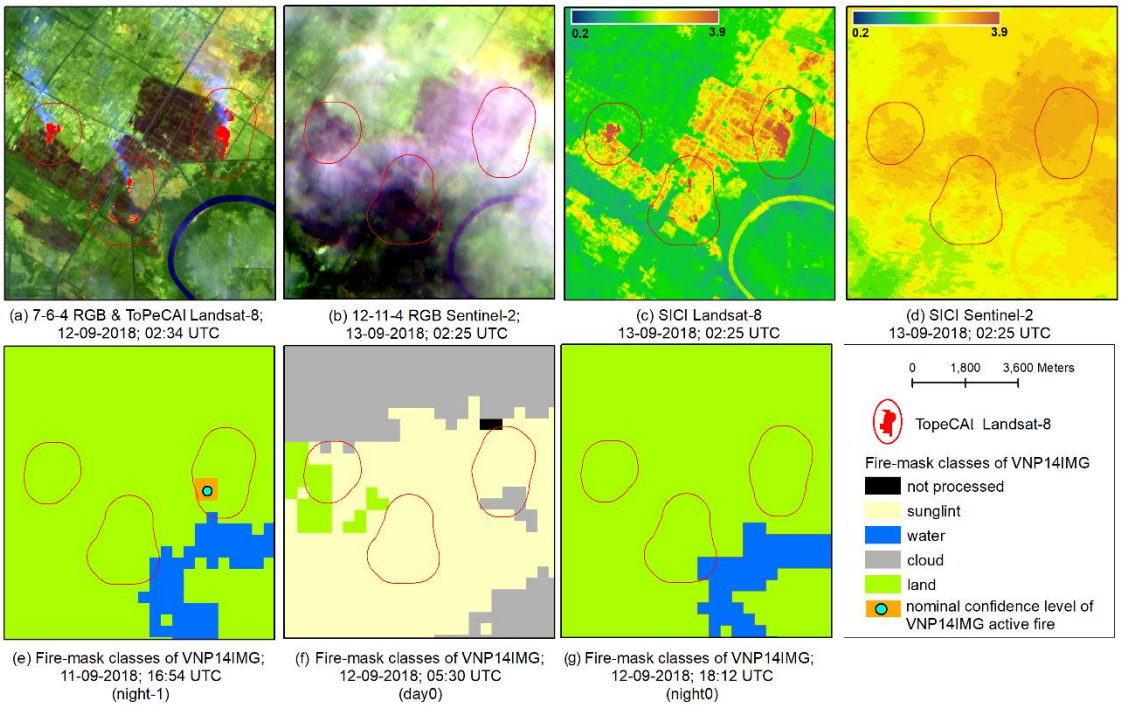


Figure 4.9. An example of omission fires of VNP14IMG data at night$_{-1}$, day$_0$, and night$_0$. (a) Landsat-8 image showed fires from ToPeCAl result (red polygon) and recent burnt area in dark brown on RGB image on 12 September 2018; (b) Sentinel-2 image showed larger recent burnt area in dark brown underneath smoke and cloud in white tones on RGB image on 13 September 2018; (c, d) ShortWave InfraRed Combustion Index (SICI) pseudo colour images of Landsat-8 and Sentinel-2; the higher SICI values in darker orange tones ( ) referred to combustion as shown in Figure c, while in lower tones ( ) associate with recent burnt area. A larger SICI with similar orange tones ( ) shown in Sentinel-2 (Figure d) which indicated a larger burnt area, however, thin cloud is affecting the imagery; (e) one fire area detected by VNP14IMG at night$_{-1}$ of 12 September 2018, but other two fires not detected; (f, g) no fire detection from VNP14IMG at day$_0$ and night$_0$ of 12 September 2018.

4.4. Discussion

Tropical peatland fires in Indonesia mostly occur in July to October with an exception in Riau which also occur in February to March and can extend to April due to low precipitation (Yulianti, Hayasaka & Sepriando 2013; Sofan et al. 2019). The fires mostly occurs as a result of a drier fuel state, land clearance, and farming preparation by smallholder farmers and, for larger areas, by plantation companies who often use regular clearance (Bowen et al. 2000; Cochrane 2003; Dennis et al. 2005; Field, Van Der Werf & Shen 2009; Miettinen et al. 2012; Miettinen, Shi & Liew 2011; Rieley & Page 2016; Siegert et al. 2001). In this study, VNP14IMG, the highest spatial resolution of fire space-based products among the low spatial and high temporal resolution data were assessed over tropical peatland fires of Indonesia using ToPeCAl applied to Landsat-8 daytime data. The use of ToPeCAl-L8 as the fire reference was adopted as an alternative tool to verifying/validating the fire occurrence, rather than using ground truth data.

Although there was a potential for fire behaviour over time to not permit comparison of satellite data acquired at different times, Atwood et al. (2016) found that the maximum peatland fire propagation speeds were about 79 m/hour. These fires burnt about 23,367 ha of secondary swamp forest of Central Kalimantan in a peat depth of greater than 2 m. They might spread horizontally across the surface to about 711 m over nine hours, but within the 750 m buffer of VNP14IMG, while over 15 hours the fire spreads could be more than the highest buffer size used in this study (750 m). Between nine hours to 15 hours, there were possibilities for peatland fires existing within 750 m in the secondary swamp forest, or over different vegetation types under different peat depths and peat moisture content, which had lower spread rates than the maximum spread rates of fires found in the secondary swamp forest. For example, Atwood et al (2016) also found peatland fires in secondary swamp forest, planted plantation, and swamp scrubland with a maximum propagation speed of 443 m/day (~18.5 m/hour), 415 m/day (~17 m/hour), and 828.5 m/day (~34.5 m/hour), respectively; these fires might spread to 277 m, 255 m, and 518 m within 15 hours under uniform conditions. They resulted in smaller burnt areas, less than 5,000 ha (Atwood et al. 2016). In slashed vegetation areas, the fire propagation speeds can be faster and over a short duration due to less fuel availability (Usup et al. 2004), while in vegetated areas with more fuel the fires can propagate slowly and longer depending on wind speeds. However, when the fire fronts meet areas with lower fuel, or recently/frequently burnt areas, then propagation speeds might reduce and even stop

(Usup et al. 2004; Atwood et al. 2016). In addition, the peatland fires in Indonesia may derive from several fire points at the same time or slightly different times, as in the practice of land clearance (Osaki et al. 2016b), and low wind patterns and fuel availability might influence the propagation speed of fires (Atwood et al. 2016; Usup et al. 2004). The propagation speed of fires resulting from 160 m spatial resolution imagery from TET-1 might not represent the peatland fires behaviour at a detailed scale. Other higher spatial resolution data such as Landsat-8 (30 m) and Sentinel-2 (10–20 m) can provide more detail on peatland fire behaviour, cloud permitting, and are worthy of further investigation. Nevertheless, in general the peatland fire propagation speeds from TET-1 permit the comparison of Landsat-8 derived ToPeCAl fire assessment with the VNP14IMG product, within the determined buffer distance up to 15 hours under uniform conditions of landcover types, fuel availability, and weather. The exception is for large fires burning in secondary unburnt swamp forest with a maximum of speed propagation of 79 m/hour.

In the validation of VNP14IMG with ToPeCAl-L8, buffer analysis on VNP14IMG points was utilised to overcome the uncertainty in knowing actual fire location, which could be anywhere inside one pixel of VNP14IMG (Giglio, Schroeder & Justice 2016), includes off-nadir pixel distortion and potential fire spread through time (Koltunov et al. 2016; Koltunov, Ustin & Prins 2012). The buffering processing also accounted for geolocation errors of the two different datasets. The results of VNP14IMG validation show that VNP14IMG provided a higher POD at larger buffer distances using cluster buffer analysis, than from single buffer analysis. These results were associated with large fires of more than 14 ha. The cluster buffer analysis for large fires may have resulted in a larger POD at higher distances (up to 750 m), because all active fires in a cluster buffer were classified as agreement fires, while in single buffer analysis fires were only counted when the buffer which was intersected with the ToPeCAl-L8 fires indicated agreement.

The highest POD from nighttime data for small fires at 0.09 ha (area of one pixel of Landsat-8) and fires at ≤ 14 ha (less than one pixel area of VNP14IMG) were about 9% and 80%, respectively. These were generally found within less or equal to one pixel area of VNP14IMG from single buffer analysis, while fires larger than one pixel area of VNP14IMG they were mostly found (about 85%) from cluster buffer analysis. These results bring a practical technique to the use of VNP14IMG data through the application

of cluster buffer analysis, when more than one VNP14IMG active fire is detected in the localised fire areas.

In general, nighttime data performed better than daytime data. However, there was a possibility that new fires commenced after the night$_{-1}$ acquisition which were not observed by VNP14IMG night$_{-1}$ data, but then commenced in the following morning and subsequently identified on the Landsat-8 daytime image. Such a situation may lead to a decrease in omission error percentage from night$_{-1}$ (23%) to day$_0$ time (20%). This hypothesis can only be proven by continuous field observations. 69% of the VNP14IMG active fires within 750 m that were detected on night$_{-1}$ were also found at day$_0$ and night$_0$, while others were detected about 50% from night$_{-1}$ to day$_0$, and 47% from day$_0$ to night$_0$ within 750 m of VNP14IMG. In other words, some active fires persisted through the observation period and possibly existed prior and post the observation period. Thus, the probability of detection of active fire was increased by aggregating the active fires data from different times. For example, the multi-time combination of night$_{-1}$+day$_0$ and day$_0$+night$_0$ resulted in a high POD of 90% and 88%, respectively from cluster buffer analysis within 375 m, while the combination of all data (night$_{-1}$+day$_0$+night$_0$) resulted in a POD of 100%. The multi-time combination of active fire data was implemented in order to improve the agreement of active fires, including the new fires that occurred in between the two observations of VNP14IMG. It was also implemented to partially offset the impact of higher cloud cover (about 38%) at daytime, which reduces the daytime detection of fires. Multi-temporal aggregation of active fire detection was supported from the peatland fire propagation speeds resulting from Atwood et al. 2016, which showed most of the peatland fires existed within 750 m over 15 hours under constant speed and uniform environmental conditions. These results provide a recommendation that the appropriate multi-time combination of VNP14IMG within 15 hours are night$_{-1}$+day$_0$ and day$_0$+night$_0$. In an operational situation a rolling aggregation of VNP14IMG will generally provide more accurate than from single time data.

The spatially related false positive sources and independent/potential false positive sources were assessed in commission error calculation. Removing the spatially related false positives, which referred to the agreement fires, provided a lower commission error. The highest false positive source was from FPR-3, which showed fire features or burnt areas that occurred after fire reference data (ToPeCAl-L8). The high percentage of FPR-3 could be caused by (1) possibilities of new fires that occurred after Landsat-8 daytime

observation and detected by VNP14IMG three hours later at daytime, or 15 hours later at nighttime; (2) difference in algorithms between ToPeCAl and VNP14IMG; and (3) the time difference of Landsat-8 with VNP14IMG, which might influence the errors especially at the longest time difference ($night_0$ about 15 hours) due to the changes of fire behaviour.

The spatially related false positive, FPR-2, represented the uncertainties of ToPeCAl-L8 especially omitted fires in ToPeCAl; in this case there were fire features visible in RGB-764 Landsat-8 image but not detected in ToPeCAl. Most of these fire features, which were not detected by ToPeCAl, were small fires (less than one Landsat-8 pixel) and/or under smoky conditions, both of which can decrease the apparent combustion power and with similar temperature to the background or burnt area. The omission error of ToPeCAl was about 15% compared with ground truth (Sofan et al. 2019). Lowering the ToPeCAl's threshold may capture these fires but will bring false positives on other objects. However, it was possible that the combustion power increased with oxygen supply from increased wind speed after three hours from the Landsat-8 observation and then the fires were detected by VIIRS. Thus, FPR-2 is a spatially related false positive and can be removed from commission error calculations.

The independent/potential false positives especially for industrial areas with gas flares (FPR-5) were mostly found in Riau Province where they contributed about 9% of the total false positive sources. Many gas flares were also detected in Riau at nighttime with a different algorithm using SWIR spectra of VIIRS (Elvidge et al. 2013). FPR-5 errors were mostly detected in single buffers of VNP14IMG, at nighttime and were caused by a significant thermal anomaly where gas flare temperatures were different to the background area temperatures. An automatic screening of VNP14IMG at relatively permanent gas flare locations (e.g. VNP14IMGML) which provides attributes of other thermal anomalies such as active volcanoes and static land sources (Schroeder & Giglio 2018) needs to be included in VNP14IMG product so that FPR-5 can largely be removed. Oliva and Schroeder (2015) have also suggested screening VNP14IMG data from the thermal anomaly like FPR-5 for forest fire detection. In this study if FPR-5 errors were removed, together with FPR-2 and FPR-3, then the commission error decreased to about 2% at nighttime and 3% at daytime. Here, the remaining false positives were from open/bare-land or bright objects in settlement area at daytime and the geolocation error from VIIRS and Landsat-8.

In this study, the omission errors at daytime were found to be lower than at nighttime. This could be caused by the longer time difference between Landsat-8 daytime observation and the nighttime observation of VNP14IMG (15 hours later), while the daytime observation of VNP14IMG is only three hours different. Some fires may not exist over longer time periods due to either extinguishment, or extension into a large area (more than the 750 m buffer), in which case the fire would be classed as a big fire. In addition, a short fire life may occur as the result of firefighting efforts to extinguish the fire; it may also result from the constraints on burning activity implemented by small land holders or local farmers, especially in Kalimantan (Osaki et al. 2016b). In North India and Cambodia, Oliva and Schroeder (2015) found that a short period of fire constrained by agricultural practise may be the cause of undetectable fires by VIIRS.

On the other hand, there was possibility that peatland fires existed over longer time periods, which was confirmed by other images one day after Landsat-8 such as from Sentinel-2 and with no VNP14IMG detection. In this case, the slow propagation of smouldering peat fires was undetected by VIIRS. The spatial resolution of VNP14IMG may also be an issue of omission detection in peatland fires, where one pixel of VNP14IMG consists of non-homogeneous backgrounds e.g. the area that is affected by sun glint, water/river, smoke from smouldering peat fires, and mixture of burnt area and smouldering peat fires.

Instead of individual limitations of ToPeCAl-L8 and VNP14IMG, both fire products can complement each other in the detection and monitoring of peatland fires. The cloud cover over tropical region and smoky conditions during peat fires season may obscure the detection of fire using optical satellite data. ToPeCAl-L8 presents peat fires information which map smouldering and flaming fires with more detailed fire shape and precise location of fire every 16 days. In comparison, VNP14IMG provides a general fire information of peat fires (smouldering and flaming) in 375 m for daily monitoring.

4.5. Conclusions

In this study, the VIIRS 375 m active fire, VNP14IMG, were assessed with ToPeCAl Landsat-8 fires as the reference and by considering the peatland fires propagation speeds from previous study. Most of the peatland fires were still within 750 m buffer of VNP14IMG over 15 hours under uniform conditions of weather and environment.

The assessment of VNP14IMG in tropical peatland fire environment of Indonesia by referring to the ToPeCAl Landsat-8 fires shows that the small fires (< 14 ha) were largely (~80%) found from single buffer analysis at nighttime. Meanwhile, the fire sizes more than one-pixel area of VNP14IMG (> 14 ha) were more likely (~ 85%) to be detected by cluster buffer analysis at nighttime. The cluster buffer analysis with multi-time combination of VNP14IMG active fires provided more accurate detection (~90 %) and minimised the error of commission and omission.

The effectiveness of peatland fires monitoring based on VIIRS 375 m active fire can be improved by implementing additional cluster buffer analysis and multi-time combination analysis to the operational data. In future research, the temporal gaps in high spatial resolution fire information from Landsat-8 as references for VIIRS 375 m active fire data potentially can be bridged by using Sentinel-2 data, which is available every five days, cloud permitting. The combination of VIIRS 375 m active fires, ToPeCAl-L8, and Sentinel-2 can support the establishment of tropical peatland fires information at higher spatio-temporal resolution than is currently available.

References

Andela, N, Morton, DC, Giglio, L, Paugam, R, Chen, Y, Hantson, S, van der Werf, GR & Randerson, JT 2019, 'The Global Fire Atlas of individual fire size, duration, speed and direction', *Earth Syst. Sci. Data,* vol. 11, no. 2, pp. 529–552, doi:10.5194/essd-11-529-2019.

Atwood, E, Englhart, S, Lorenz, E, Halle, W, Wiedemann, W & Siegert, F 2016, 'Detection and characterization of low temperature peat fires during the 2015 fire catastrophe in Indonesia using a new high-sensitivity fire monitoring satellite sensor (FireBird)', *PLoS ONE*, vol. 11, no. 8, pp. 1–24, doi:10.1371/journal.pone.0159410.

Bowen, MR, Bompard, JM, Anderson, IP, Guizol, P & Gouyon, A 2000, 'Anthropogenic fires in Indonesia: a view from Sumatra', in P Eaton, and M. Radojevic (ed), *Forest Fires and Regional Haze in Southeast Asia*, Nova Science, New York, pp. 41–66.

BPS-Statistic Indonesia 2015, "Plantation Area by Province and Crops, Indonesia (000 Ha), 2012–2014", www.bps.go.id.

Cochrane, M 2003, 'Fire science for rainforests', *Nature,* vol. 421, pp. 913–919, doi:10.1038/nature01437.

Crippa, P, Castruccio, S, Archer-Nicholls, S, Lebron, GB, Kuwata, M, Thota, A, Sumin, S, Butt, E, Wiedinmyer, C & Spracklen, DV 2016, 'Population exposure to hazardous air quality due to the 2015 fires in Equatorial Asia', *Scientific Reports*, vol. 6, no. 1, 2016/11/16, p. 37074, doi:10.1038/srep37074.

Csiszar, IA & Schroeder, W 2008, 'Short-Term Observations of the Temporal Development of Active Fires From Consecutive Same-Day ETM+ and ASTER Imagery in the Amazon: Implications for Active Fire Product Validation', *IEEE Journal of Selected Topics in Applied Earth Observations and Remote Sensing*, vol. 1, no. 4, pp. 248–253, doi:10.1109/JSTARS.2008.2011377.

Dennis, RA, Mayer, J, Applegate, G, Chokkalingam, U, Colfer, CJP, Kurniawan, I, Lachowski, H, Maus, P, Permana, RP, Ruchiat, Y, Stolle, F, Suyanto & Tomich, TP 2005, 'Fire, People and Pixels: Linking Social Science and Remote Sensing to Understand Underlying Causes and Impacts of Fires in Indonesia', *Human Ecology*, vol. 33, no. 4, pp. 465–504, doi:10.1007/s10745-005-5156-z.

Drusch, M, Del Bello, U, Carlier, S, Colin, O, Fernandez, V, Gascon, F, Hoersch, B, Isola, C, Laberinti, P, Martimort, P, Meygret, A, Spoto, F, Sy, O, Marchese, F & Bargellini, P 2012, 'Sentinel-2: ESA's Optical High-Resolution Mission for GMES Operational Services', *Remote Sensing of Environment*, vol. 120, 2012/05/15/, pp. 25–36, doi:10.1016/j.rse.2011.11.026.

Elvidge, CD, Nelson, I, Hobson, V, Safren, J & Baugh, K 2001, *Detection of Forest at Night Using DMSP-OLS Data*, Global and Regional Vegetation Fire Monitoring From Space Planning a Coordinated International Effort, SPB Academic Publishing BV, The Hague.

Elvidge, CD, Zhizhin, M, Baugh, K, Hsu, F-C & Ghosh, T 2016, 'Methods for Global Survey of Natural Gas Flaring from Visible Infrared Imaging Radiometer Suite Data', *Energies*, vol. 9, no. 1, p. 14, doi:10.3390/en9010014.

Elvidge, CD, Zhizhin, M, Hsu, F-C & Baugh, K 2013, 'VIIRS Nightfire: Satellite Pyrometry at Night', *Remote Sensing*, vol. 5, no. 9, p. 4423, doi:10.3390/rs5094423.

Elvidge, CD, Zhizhin, M, Hsu, F, Baugh, K, Khomarudin, M, Vetrita, Y, Sofan, P, Suwarsono & Hilman, D 2015, 'Long-wave infrared identification of smoldering peat fires in indonesia with nighttime landsat data', *Environmental Research Letters*, vol. 10, no. 6, p. 065002, doi:10.1088/1748-9326/10/6/065002.

ESA (European Space Agency) 2015. Sentinel-2 User Handbook, Paris: ESA Standard Document.

Field, RD, Van Der Werf, GR & Shen, SSP 2009, 'Human amplification of drought-induced biomass burning in Indonesia since 1960', *Nature Geoscience*, vol. 2, no. 3, pp. 185–188, doi:10.1038/ngeo443.

Foley, M 2020, 'Bushfires spew two-thirds of national carbon emissions in one season', 2 January 2020, viewed 5 May 2020, <https://www.smh.com.au/politics/federal/bushfires-spew-two-thirds-of-national-carbon-emissions-in-one-season-20200102-p53oez.html>.

Freedman, A 2020, 'Australia's greenhouse gas emissions effectively double as a result of unprecedented bush fires', The Washington Post, 25 January 2020, viewed 5 May 2020, <https://www.washingtonpost.com/weather/2020/01/24/australia-bush-fires-have-nearly-doubled-countrys-annual-greenhouse-gas-emissions/>.

Giglio, L, Csiszar, I, Restás, Á, Morisette, JT, Schroeder, W, Morton, D & Justice, CO 2008, 'Active fire detection and characterization with the advanced spaceborne thermal emission and reflection radiometer (ASTER)', *Remote Sensing of Environment*, vol. 112, no. 6, 2008/06/16/, pp. 3055-3063, doi:10.1016/j.rse.2008.03.003.

Giglio, L, Descloitres, J, Justice, CO & Kaufman, YJ 2003, 'An Enhanced Contextual Fire Detection Algorithm for MODIS', *Remote Sensing of Environment*, vol. 87, no. 2, pp. 273–282, doi:10.1016/S0034-4257(03)00184-6.

Giglio, L, Schroeder, W & Justice, C 2016, 'The collection 6 MODIS active fire detection algorithm and fire products', *Remote Sensing of Environment*, vol. 178, pp. 31–41, doi:10.1016/j.rse.2016.02.054.

Hall, JV, Zhang, R, Schroeder, W, Huang, C & Giglio, L 2019, 'Validation of GOES-16 ABI and MSG SEVIRI active fire products', *International Journal of Applied Earth Observation and Geoinformation*, vol. 83, 2019/11/01/, p. 101928, doi:10.1016/j.jag.2019.101928.

Hantson, S, Padilla, M, Corti, D & Chuvieco, E 2013, 'Strengths and weaknesses of MODIS hotspots to characterize global fire occurrence', *Remote Sensing of Environment*, vol. 131, pp. 152–159, doi:10.1016/j.rse.2012.12.004.

Huang, X & Rein, G 2015, 'Computational study of critical moisture and depth of burn in peat fires', *International Journal of Wildland Fire*, vol. 24, no. 6, pp. 798–808, doi:10.1071/wf14178.

Irons, JR, Dwyer, JL & Barsi, JA 2012, 'The next Landsat satellite: The Landsat Data Continuity Mission', *Remote Sensing of Environment*, vol. 122, pp. 11–21, doi:10.1016/j.rse.2011.08.026.

Ishii, Y, Koizumi, K, Fukami, H, Yamamoto, K, Takahashi, H, H, S, Limin, Kusin, K, Usup, A & Susilo, GE 2016, 'Groundwater in Peatland', in M Osaki & N Tsuki (eds), *Tropical Peatland Ecosystem*, Springer, Tokyo, pp. 265–280.

Justice, C & Korontzi, S 2001, 'A Review of The Status of Satellite Fire Monitoring and the Requirements for Global Environmental Change Research', in JA F, G J.G & J C.O (eds), *Global and Regional Vegetation Fire Monitoring from Space Planning a Coordinated International Effort*, SPB Academic Publishing BV, The Hague.

Koltunov, A, Ustin, SL & Prins, EM 2012, 'On timeliness and accuracy of wildfire detection by the GOES WF-ABBA algorithm over California during the 2006 fire season', *Remote Sensing of Environment*, vol. 127, 2012/12/01/, pp. 194–209, doi:10.1016/j.rse.2012.09.001.

Koltunov, A, Ustin, S, Quayle, B, Schwind, B, Ambrosia, V & Li, W 2016, 'The development and first validation of the GOES Early Fire Detection (GOES-EFD) algorithm', *Remote Sensing of Environment*, vol. 184, pp. 436–453, doi:10.1016/j.rse.2016.07.021.

Koplitz, SN, Mickley, LJ, Marlier, ME, Buonocore, JJ, Kim, PS, Liu, T, Sulprizio, MP, DeFries, RS, Jacob, DJ, Schwartz, J, Pongsiri, M & Myers, SS 2016, 'Public health impacts of the severe haze in Equatorial Asia in September–October 2015: demonstration of a new framework for informing fire management strategies to reduce downwind smoke exposure', *Environmental Research Letters*, vol. 11, no. 9, 2016/09/01, p. 094023, doi:10.1088/1748–9326/11/9/094023.

Kumar, V & Dharssi, I 2015, *Sources of Soil Dryness Measures and Forecasts for Fire Danger Rating*, Bureau of Meteorology Australia, Victoria.

Kumar, SS & Roy, DP 2018, 'Global operational land imager Landsat-8 reflectance-based active fire detection algorithm', *International Journal of Digital Earth*, vol. 11, no. 2, pp. 154-178, doi:10.1080/17538947.2017.1391341.

Liu, X, He, B, Quan, X, Yebra, M, Qiu, S, Yin, C, Liao, Z & Zhang, H 2018, 'Near Real-Time Extracting Wildfire Spread Rate from Himawari-8 Satellite Data', vol. 10, no. 10, p. 1654, doi:10.3390/rs10101654.

Loboda, TV & Csiszar, IA 2007, 'Reconstruction of fire spread within wildland fire events in Northern Eurasia from the MODIS active fire product', *Global and Planetary Change*, vol. 56, no. 3, 2007/04/01/, pp. 258–273, doi:10.1016/j.gloplacha.2006.07.015.

Miettinen, J, Hooijer, A, Wang, J, Shi, C & Liew, SC 2012, 'Peatland degradation and conversion sequences and interrelations in Sumatra', *Regional Environmental Change*, vol. 12, no. 4, pp. 729–737, doi:10.1007/s10113-012-0290-9.

Miettinen, J & Liew, S 2009, 'Burn-scar patterns and their effect on regional burnt-area mapping in insular South-East Asia', *International Journal of Wildland Fire*, vol. 18, no. 7, pp. 837–847, doi:10.1071/wf08102.

Miettinen, J, Shi, C & Liew, S 2011, 'Influence of peatland and land cover distribution on fire regimes in insular Southeast Asia', *Regional Environmental Change*, vol. 11, no. 1, pp. 191–201, doi:10.1007/s10113-010-0131-7.

Morfitt, R, Barsi, J, Levy, R, Markham, B, Micijevic, E, Ong, L, Scaramuzza, P & Vanderwerff, K 2015, 'Landsat-8 Operational Land Imager (OLI) Radiometric Performance On-Orbit', *Remote Sens.*, vol. 7, no. 2, pp. 2208–2237, doi:10.3390/rs70202208.

Murphy, SW, de Souza Filho, CR, Wright, R, Sabatino, G & Correa Pabon, R 2016, 'HOTMAP: Global hot target detection at moderate spatial resolution', *Remote Sensing of Environment*, vol. 177, pp. 78–88, doi:10.1016/j.rse.2016.02.027.

Novitasari, N, Sujono, J, Harto, S, Maas, A & Jayadi, R 2019, 'Drought Index for Peatland Wildfire Management in Central Kalimantan, Indonesia During El Niño Phenomenon', *Journal of Disaster Research*, vol. 14, no. 7, pp. 939–948, doi:10.20965/jdr.2019.p0939.

Oliva, P & Schroeder, W 2015, 'Assessment of VIIRS 375m active fire detection product for direct burned area mapping', *Remote Sensing of Environment*, vol. 160, 2015/04/01/, pp. 144–155, doi:10.1016/j.rse.2015.01.010.

Osaki, M, Nursyamsi, D, Noor, M, Wahyunto, W & Segah, H 2016a, 'Peatland in Indonesia', in M Osaki & N Tsuji (eds), *Tropical peatland ecosystems*, Springer, Tokyo, pp. 40–58.

Osaki, M, Setiadi, B, Takahashi, H & Evri, M 2016b, 'Peatland in Kalimantan', in M Osaki & N Tsuji (eds), *Tropical peatland ecosystems*, Springer, Tokyo, pp. 91–112.

Prat-Guitart, N, Rein, G, Hadden, RM, Belcher, CM & Yearsley, JM 2016, 'Propagation probability and spread rates of self-sustained smouldering fires under controlled moisture content and bulk density conditions', *International Journal of Wildland Fire*, vol. 25, no. 4, pp. 456–465, doi:10.1071/WF15103.

Purnomo, H, Shantiko, B, Sitorus, S, Gunawan, H, Achdiawan, R, Kartodihardjo, H & Dewayani, AA 2017, 'Fire economy and actor network of forest and land fires in Indonesia', *Forest Policy and Economics*, vol. 78, pp. 21–31, doi:10.1016/j.forpol.2017.01.001.

Rein, G 2013, 'Smouldering fires and natural fuels', *Fire Phenomena and the Earth System: An Interdisciplinary Guide to Fire Science*, vol. Chapter 2, pp. 13–22, doi:10.1002/9781118529539.ch2.

Rieley, J & Page, S 2016, 'Tropical Peatland of the World', in M Osaki & N Tsuji (eds), *Tropical peatland ecosystems*, Springer, Tokyo, 3–32.

Ritung, S, Wahyunto, W & Nugroho, K 2012, 'Karakteristik dan Sebaran Lahan Gambut di Sumatera, Kalimantan dan Papua', *Pengelolaan Lahan Gambut Berkelanjutan. Balai Besar Litbang SDLP, Bogor*, in Bahasa.

Roberts, GJ & Wooster, MJ 2008, 'Fire Detection and Fire Characterization Over Africa Using Meteosat SEVIRI', *Geoscience and Remote Sensing, IEEE Transactions on*, vol. 46, no. 4, pp. 1200–1218, doi:10.1109/tgrs.2008.915751.

Sá, ACL, Benali, A, Fernandes, P, Pinto, RS, Trigo, R, Salis, M, Russo, A, Jerez, S, Soares, PM, Schroeder, W & Pereira, JMC 2017, 'Evaluating fire growth simulations using satellite active fire data', *Remote Sensing of Environment*, vol. 190, pp. 302–317, doi:10.1016/j.rse.2016.12.023.

Schroeder, W & Giglio, L 2016, *Visible Infrared Imaging Radiometer Suite (VIIRS) 375 m Active Fire Detection and Characterization Algorithm Theoretical Basis Document 1.0*, NASA.

Schroeder, W & Giglio, L 2018, *NASA VIIRS Land Science Investigator Processing System (SIPS) Visible Infrared Imaging Radiometer Suite (VIIRS) 375 m & 750 m Active Fire Products*, In Product User's Guide Version 1.4: NASA.

Schroeder, W, Oliva, P, Giglio, L & Csiszar, I 2014, 'The New VIIRS 375 m active fire detection data product: Algorithm description and initial assessment', *Remote Sensing of Environment*, vol. 143, pp. 85–96, doi:10.1016/j.rse.2013.12.008.

Schroeder, W, Oliva, P, Giglio, L, Quayle, B, Lorenz, E & Morelli, F 2016, 'Active fire detection using Landsat-8/OLI data', *Remote Sensing of Environment*, vol. 185, pp. 210–220, doi:10.1016/j.rse.2015.08.032.

Schroeder, W, Prins, E, Giglio, L, Csiszar, I, Schmidt, C, Morisette, J & Morton, D 2008, 'Validation of GOES and MODIS active fire detection products using ASTER and ETM+ data', *Remote Sensing of Environment*, vol. 112, no. 5, pp. 2711–2726, doi:10.1016/j.rse.2008.01.005.

Siegert, F, Ruecker, G, Hinrichs, A & Hoffmann, AA 2001, 'Increased damage from fires in logged forests during droughts caused by El Niño', *Nature*, vol. 414, pp. 437–440, doi:10.1038/35106547.

Sofan, P, Bruce, D, Jones, E & Marsden, J 2019, 'Detection and Validation of Tropical Peatland Flaming and Smouldering Using Landsat-8 SWIR and TIRS Bands', vol. 11, no. 4, p. 465, doi:10.3390/rs11040465.

Stolle, F, Dennis, RA, Kurniwan, I & Lambin, EF 2004, 'Evaluation of remote sensing-based active fire datasets in Indonesia', *International Journal of Remote Sensing*, vol. 25, no. 2, pp. 471–479, doi:10.1080/01431160310001618022.

Takahashi, H, Ibie, BF, Usup, A, Shimada, S, & Limin SH, 2002, 'Annual changes of water balance and a drought index in a tropical peat swamp forest of Central Kalimantan, Indonesia', *International Symposium on Tropical Peatlands, Jakarta (Indonesia), 22-23 Aug 2002*.

Tanpipat, V, Honda, K & Nuchaiya, P 2009, 'MODIS Hotspot Validation over Thailand', *Remote Sensing*, vol. 1, no. 4, pp. 1043–1054, doi:10.3390/rs1041043.

USGS 2019, *Landsat8 (L8) Data Users Handbook*, LSDS-1574. Version 5.0, U.S. Geological Survey, South Dakota, USA.

Usup, A, Hashimoto, Y, Takashi, H & Hayasaka, H 2004, 'Combustion and thermal characteristics of peat fire in tropical peatland in Central Kalimantan, Indonesia', *Tropics*, vol. 14, no. 1, pp. 1–19, doi:10.3759/tropics.14.1.

van der Werf, GR, Randerson, JT, Giglio, L, Gobron, N & Dolman, AJ 2008, 'Climate controls on the variability of fires in the tropics and subtropics', vol. 22, no. 3, doi:10.1029/2007gb003122.

Wickramasinghe, C, Jones, S, Reinke, K & Wallace, L 2016, 'Development of a Multi-Spatial Resolution Approach to the Surveillance of Active Fire Lines Using Himawari-8', *Remote Sensing*, vol. 8, no. 11, p. 932, doi:10.3390/rs8110932.

Wickramasinghe, C, Wallace, L, Reinke, K & Jones, S 2018, 'Intercomparison of Himawari-8 AHI-FSA with MODIS and VIIRS active fire products', *International Journal of Digital Earth*, doi:10.1080/17538947.2018.1527402.

World-Bank 2016, *The Cost of Fire: An Economic Analysis of Indonesia's 2015 Fire Crisis*, World Bank Group, Jakarta, Indonesia.

World-Bank 2019, *Investing in People*, World Bank Group, Jakarta, Indonesia.

Yulianti, N, Hayasaka, H & Sepriando, A 2013, 'Recent trends of fire occurrence in Sumatra (Analysis using MODIS hotspot data): a comparison with fire occurrence in Kalimantan', Open Journal of Forestry, vol. 3, no. 04, p. 129, doi:10.4236/ojf.2013.34021.

Chapter 5

Applying The Tropical Peatland Combustion Algorithm to Landsat-8 Operational Land Imager (OLI) and Sentinel-2 Multi Spectral Instrument (MSI) Imagery

---

This chapter is published as:

Sofan, P.; Bruce, D.; Jones, E.; Khomarudin, M.R.; Roswintiarti, O. Applying the Tropical Peatland Combustion Algorithm to Landsat-8 Operational Land Imager (OLI) and Sentinel-2 Multi Spectral Instrument (MSI) Imagery. Remote Sens. 2020, 12, 3958.

(https://doi.org/10.3390/rs12233958)

Applying The Tropical Peatland Combustion Algorithm to Landsat-8 Operational Land Imager (OLI) and Sentinel-2 Multi Spectral Instrument (MSI) Imagery

Abstract

This study establishes a new technique for peatland fire detection in tropical environments using Landsat-8 and Sentinel-2. The Tropical Peatland Combustion Algorithm (ToPeCAl) without longwave Thermal InfraRed (TIR) (henceforth known as ToPeCAl-2) was tested on Landsat-8 Operational Land Imager (OLI) data and then applied to Sentinel-2 Multi Spectral Instrument (MSI) data. The research is aimed at establishing peatland fire information at higher spatial resolution and more frequent observation than from Landsat-8 data over Indonesia's peatlands. ToPeCAl-2 applied to Sentinel-2 was assessed by comparing fires detected from the original ToPeCAl applied to Landsat-8 OLI/Thermal InfraRed Sensor (TIRS) verified through comparison with ground truth data. An adjustment of ToPeCAl-2 was applied to minimise false positive errors by implementing pre-process masking for water and permanent bright objects and filtering ToPeCAl-2's resultant detected fires by implementing contextual testing and cloud masking. Both ToPeCAl-2 with contextual test and ToPeCAl with cloud mask applied to Sentinel-2 provided high detection of unambiguous fire pixels (>95%) at 20 m spatial resolution. Smouldering pixels were less likely to be detected by ToPeCAl-2. The detected smouldering pixels from ToPeCAl-2 applied to Sentinel-2 with contextual testing and with cloud masking were only 35% and 56% correct, respectively; this needs further investigation and validation. These results demonstrate that even in the absence of TIR data, an adjusted ToPeCAl algorithm (ToPeCAl-2) can be applied to detect peatland fires at 20 m resolution with high accuracy especially for flaming. Overall, the implementation of ToPeCAl applied to cost-free and available Landsat-8 and Sentinel-2 data enables regular peatland fire monitoring in tropical environments at higher spatial resolution than other satellite-derived fire products.

Keywords: peatland fires detection, Sentinel-2, Landsat-8, SWIR, TIR.

5.1. Introduction

Tropical peatland is a significant source of global carbon (Page & Baird 2016; Page, Rieley & Banks 2011). The state of tropical peatland is mainly disturbed by conversion of peatland forest to other uses, especially for plantations. Peatland drainage (Carlson, Goodman & May-Tobin 2015) and peatland fires (Stockwell et al. 2016) have contributed to accelerating atmospheric carbon increases and consequential climate change (Huijnen et al. 2016; Murdiyarso, Lilleskov & Kolka 2019). Smouldering peatland fires burn organic soil and thick fuels (e.g., decaying leaves, tree branches and trunks), which release more carbon and smoke with greater particulate concentration than flaming fires (Rein 2013, 2016). Drought, unmanaged drainage, and land use change from natural peatland habitat to agricultural/plantation areas have led to high flammability conditions of degraded peatlands (Hooijer et al. 2006; Joosten & Clarke 2002; Kobayashi, Segah & Momota 2016; Miettinen & Liew 2005; Parish et al. 2008; Rieley & Page 2016; Rydin & Jeglum 2006; Suyanto et al. 2004). Peatland fires together with agriculture, forestry, and other land use are the main contributing sources (about 51%) to greenhouse gases emissions in Indonesia (Boer et al. 2018). Figure 5.1 shows the estimated annual emission of peatland fires during 1997–2019 in the Equatorial Asian region including Indonesia and neighbouring countries (Global Fire Data 2000). The peak emissions from peatland fires, which occurred in 1997, 2002, 2006, 2009, 2015, and 2019, corresponded to the warm episodes of El Niño Southern Oscillation (ENSO) and the positive modes of Indian Ocean Dipole, as shown in the Oceanic Niño Index (ONI) and Dipole Mode Index (DMI) recorded by Climate Prediction Center and Physical Sciences Laboratory of National Oceanic and Atmospheric Administration, respectively (CPC-NOAA 2000; NOAA ESRL 2020). In general, positive modes of these climate indices were associated with extreme droughts and contributed to Indonesian fires (Alsepan & Minobe 2020; Pan et al. 2018). Beside the influences of extreme drought, mainly, peatland fires in Indonesia have anthropogenic origins (Bowen et al. 2000; Dennis et al. 2005; Purnomo et al. 2017). Therefore, it is important to develop a comprehensive monitoring of peatland fires for control and minimisation of carbon emission.

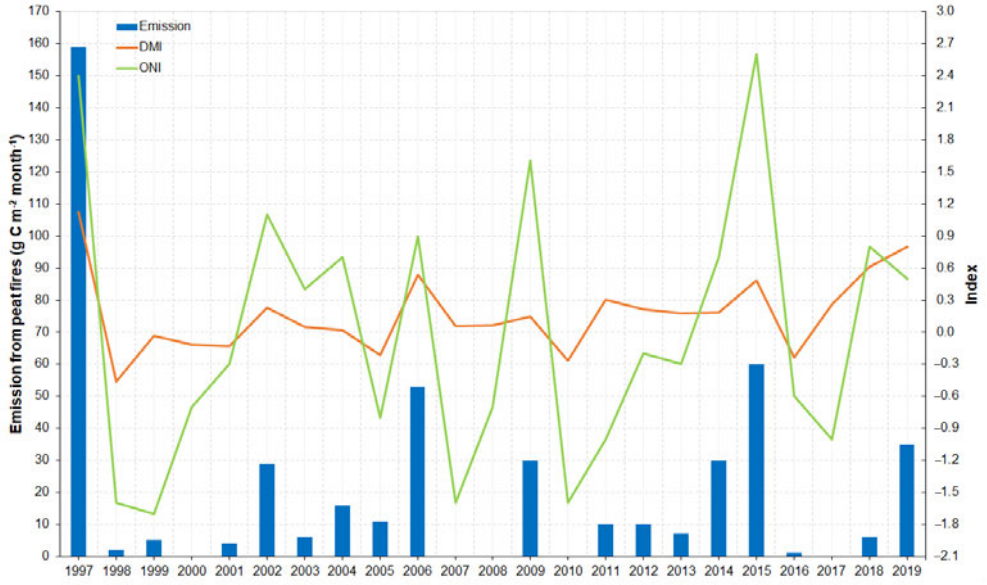


Figure 5.1. Estimated annual emission of peatland fires in Equatorial Asia in 1997–2019 from Global Fire Emissions Database version 4.1 (http://www.globalfiredata.org/data html) and the Oceanic Niño Index (ONI) and Dipole Mode Index (DMI) using 3 month running average of sea surface temperature anomalies during November-December-January period. Climate indices data were accessed at https://origin.cpc.ncep noaa.gov/products/analysis_monitoring/ensostuff/ONI_v5.php and https://psl noaa.gov/gcos_wgsp/Timeseries/Data/dmi.had.long.data.

Remote sensing satellites have been widely used for biomass burning detection. Research on remote sensing satellite applications, particularly for peatland fire detection and its assessment in Indonesia has been conducted from medium spatial resolution to low spatial resolution satellite sensors and from Unpiloted Aerial Vehicle (UAV) as shown in Table 5.1.

Table 5.1. List of peatland fire detection research using medium to low spatial resolution satellite data in Indonesia (OLI is Operational Land Imager; TIRS is Thermal InfraRed Sensor; BIRD is Bi-spectral InfraRed Detection; HSRS is HotSpot Recognition System; TET-1 is Technology Experiment Carrier; Suomi NPP is Suomi National Polar-orbiting Partnership; SWIR is ShortWave InfraRed; TIR is longwave Thermal InfraRed; MWIR is mid-wave infrared; VIIRS is Visible Infrared Imaging Radiometer Suite; UAV is Unpiloted Aerial Vehicle).

Satellite	Sensor	Primary spectra used for fire detection	Revisit time (day)	Spatial resolution (m)	Main objective	Reference
Landsat-8	OLI & TIRS	SWIR, TIR	16	30	Peatland fire detection at nighttime & daytime	(Elvidge et al. 2015; Sofan et al. 2019)
BIRD	HSRS	MWIR, TIR	2–3	370	Peatland fire detection at daytime	(Siegert et al. 2004)
TET-1	TET-1	MWIR	2–5	160	Peatland fire detection at daytime	(Atwood et al. 2016)
Suomi NPP	VIIRS	SWIR	0.5	750	Peatland fire detection at nighttime	(Elvidge et al. 2013)
		MWIR, TIR	0.5	375	Assessment of active fire	(Sofan et al. 2020)
UAV	Tau2 TIR	TIR	as needed	0.185	Peatland fire detection at daytime	(Burke et al. 2019)

Cost-free satellite data with moderately frequent observations have potential to be used in regular peatland fires information collection. The cost-free and available medium spatial resolution (20–30 m) e.g. Sentinel-2 Multi Spectral Instrument (MSI) and Landsat-8 Operational Land Imager (OLI)/ Thermal InfraRed Sensor (TIRS) regularly observe the Earth in the morning at about 10 am every five and 16 days, respectively. At lower spatial resolution (375 m) VIIRS is also available free of cost and provides the highest spatial resolution global active fire product for daytime and night-time among low spatial resolution cost-free active fire products. However, because fire products are not available for Sentinel-2, there exists an opportunity for the development of a detection algorithm for this sensor. A fire detection algorithm, particularly for peatland fires in tropical environments, e.g. Indonesia, called Tropical Peatland Combustion Algorithm (ToPeCAl), has been established using aerosol, ShortWave InfraRed (SWIR) and longwave Thermal InfraRed (TIR) spectra and applied to Landsat-8 OLI/TIRS daytime (Sofan et al. 2019).

The possibility of merging fire information from medium spatial resolution data with low spatial and high temporal resolution data, Visible Infrared Imaging Radiometer Suite (VIIRS) 375 m, was undertaken via a comparison with ToPeCAl fire information from Landsat-8 OLI/TIRS and resulted in accuracies up to 90% for fires in Indonesia's peatland (Sofan et al. 2020). Meanwhile, many of the combined fire products from moderate spatial resolution sensor satellites are specifically designed for burnt area mapping (Fiona et al. 2020; García-Llamas et al. 2019; Quintano, Fernández-Manso & Fernández-Manso 2018; Roy et al. 2019). A global active fire algorithm from moderate spatial resolution data has been developed by (Giglio et al. 2008; Kumar & Roy 2018; Murphy et al. 2016; Schroeder et al. 2016) but is still limited for specific tropical peatland fires environments (Elvidge et al. 2015; Sofan et al. 2019). Moreover, research on spectral comparison between moderate spatial resolution data, e.g., Landsat-8 and Sentinel-2, in many regions, e.g., conterminous United States, Australia, Southern Africa, Europe, and China showed good relationships (Chastain et al. 2019; Flood 2017; Mandanici & Bitelli 2016; Shang & Zhu 2019; Zhang et al. 2018) However, this relationship needs to be explored over equatorial tropical environments.

Higher spatial and temporal information of peatland fires is potentially possible by applying ToPeCAl to Sentinel-2 MSI data. However, Sentinel-2 MSI only has SWIR for fire detection, while ToPeCAl originally used SWIR and TIR in Landsat-8 OLI/TIRS. An approach of using SWIR from medium spatial resolution data for fire detection has been explored by (Giglio et al. 2008; Kumar & Roy 2018; Murphy et al. 2016; Schroeder et al. 2016). It may be possible to apply ToPeCAl without TIR to Sentinel-2 MSI for peatland fires detection in tropical environments.

Thus this study aimed to explore the potential of detecting tropical peatland fires particularly through the use of ToPeCAl at medium spatial resolution without the use of longwave Thermal InfraRed imagery in order to provide peatland fire information at higher spatial resolution (20 m) and at a higher temporal frequency (five days) than Landsat 8; this would complement information from the medium spatial resolution of peatland fires from Landsat-8 (30 m) which is only available every 16 days. A combination of Sentinel-2 and Landsat-8 fire products, together with a lower spatial but higher temporal resolution active fire product, e.g., VIIRS 375 m at daily observation, could potentially ensure high spatial and medium to higher temporal information on peatland fires.

The objectives of this study are: (1) implementation and comparison of Tropical Peatland Combustion Algorithm without TIR (ToPeCAl-2) applied to Landsat-8 OLI, and (2) implementation and comparison of ToPeCAl-2 applied to Sentinel-2 MSI.

5.2. Data

5.2.1. Landsat-8 and Sentinel-2A/B

The National Aeronautics and Space Administration (NASA) and the Department of Interior United States Geological Survey (USGS) developed and launched the Landsat 8 satellite on 11 February 2013 with two science instruments, OLI and TIRS. Nine spectral bands, which span from the visible (VIS), the Near InfraRed (NIR), the SWIR and the cirrus band at 30 m spatial resolution and 15 m for the panchromatic band, are collected in OLI. TIRS collects two bands of TIR spectra at 100 m spatial resolution. Landsat-8 with its near-polar and Sun-synchronous orbit provides a repeat earth observation every 16-days at an equatorial crossing time of 10.00 ±15 min in a 185 km swath (Irons, Dwyer & Barsi 2012; Loveland & Irons 2016). In this study, Landsat-8 data were accessed from https://earthexplorer.usgs.gov/.

Sentinel-2 satellites were developed by the European Commission and the European Space Agency (ESA). Sentinel-2A and 2B were launched on 23 June 2015 and 7 March 2017, respectively. The on-board MSI has 13 spectral bands ranging from the VIS, the NIR, and the SWIR at different spatial resolutions (10, 20 and 60 m). The orbit of Sentinel-2 satellites is Sun-synchronous with observation times close to Landsat local overpass time at 10.30 (descending orbit). The swath width of Sentinel-2 MSI is 290 km with a frequent revisit of five days at the equator from Sentinel-2A and Sentinel-2B. The Sentinel-2 MSI product is provided in tiles which cover 10,000 km2. In a single day of acquisition, the Sentinel-2 MSI product may consist of one or more tiles in a certain area (Drusch et al. 2012). Sentinel-2 data were accessed from https://scihub.copernicus.eu/dhus/#/home.

The bands used for applying ToPeCAl to Landsat-8 OLI/TIR and Sentinel-2 MSI and background mapping, e.g., water, cloud, and bright object are listed in Table 5.2.

Table 5.2. Landsat-8 OLI and Sentinel-2 Multi Spectral Instrument (MSI) spectral band information used in Tropical Peatland Combustion Algorithm (ToPeCAl) and background mapping (Barsi et al. 2018; Du et al. 2016; Irons, Dwyer & Barsi 2012; Schroeder et al. 2016; Sofan et al. 2019; Sun et al. 2017).

Landsat-8 OLI/TIR			**Sentinel-2 MSI**			**Type of information and purpose**
Band	**Centre wavelength (µm)**	**Spatial resolution (m)**	**Band**	**Centre wavelength (µm)**	**Spatial resolution (m)**	
1 (coastal aerosol)	0.443	30	1 (coastal aerosol)	0.433	20 (resampled from 60)	TOA reflectance for classifying clear and smoky atmosphere
3 (Green)	0.561	30	3 (Green)	0.560	20 (resampled from 10)	TOA reflectance for water masking
4 (Red)	0.665	30	-	-	-	TOA reflectance for cloud masking
5 (NIR)	0.865	30	8a (NIR)	0.865	20	TOA reflectance for water masking
6 (SWIR-1)	1.609	30	11 (SWIR-1)	1.610	20	TOA reflectance for fire mapping & water masking
7 (SWIR-2)	2.201	30	12 (SWIR-2)	2.190	20	TOA reflectance for fire mapping & bright object mapping
10 (TIR)	10.9	30 (resampled from 100)	-	-	-	TOA brightness temperature for fire mapping

5.2.2. Study Area and Data Acquisition Period

Kalimantan and Sumatera are the dominant peatland fires prone areas in Indonesia and the focus areas for this research. The study areas were observed in seven scene coverage areas of Landsat-8 which span from South Kalimantan, Central Kalimantan, West Kalimantan, Riau, Jambi, and South Sumatera Provinces of Indonesia (Figure 5.2). Fifteen Landsat-8 images with fire features were selected from July 2015 to October 2019 over the study areas (Table 5.3). These data were used to explore the first objective which was executed in step 1 of data processing: applying and assessing ToPeCAl-2 to Landsat-8 OLI.

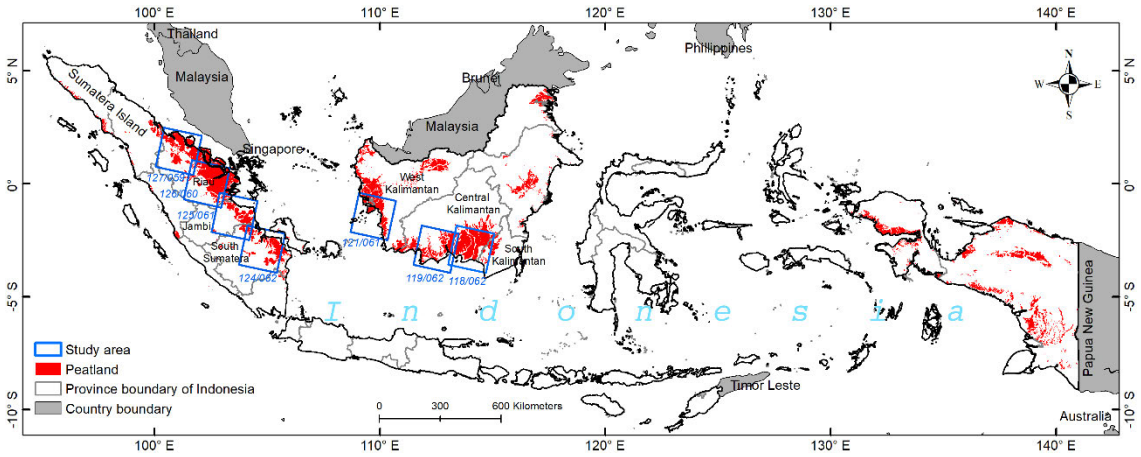


Figure 5.2. Study areas (blue trapezoid) coverage of Landsat-8 scene areas (path/row of 118/062, 119/06, 121/061, 124/062, 125/061, 126/060, 127/059) over Kalimantan and Sumatera's peatland (in red). Peatland data sources from the Indonesian Ministry of Agriculture (2011). Administration boundaries are from Geospatial Information Agency of Indonesia.

Table 5.3. List of Landsat-8 data for applying and assessing Tropical Peatland Combustion Algorithm (ToPeCAl) without TIR (ToPeCAl-2) in Central Kalimantan, South Kalimantan, West Kalimantan, Riau, Jambi, and South Sumatera.

Study area	Acquisition date	Landsat-8's path/row
Central Kalimantan and South Kalimantan	11 August 2018	118/062
	12 September 2018	118/062
	28 September 2018	118/062
	29 July 2019	118/062
	14 August 2019	118/062
	6 September 2019	119/062
West Kalimantan	9 September 2015	121/061
Jambi and South Sumatera	11 October 2019	124/062
	27 October 2019	124/062
	20 August 2015	125/061
	15 August 2019	125/061
	31 August 2019	125/061
Riau	7 September 2019	126/060
	20 August 2016	127/059
	29 August 2019	127/059

Nine pairs of Landsat-8 and Sentinel-2 acquired on the same day were used in this study (Table 5.4) to explore the second objective. The pairs of Landsat-8 and Sentinel-2

were used to undertake a spectral reflectance comparison prior to applying and assessing the application of ToPeCAl-2 to Sentinel-2 MSI; this constituted step 2 in the analysis. Data pairs with fire features analysed from the RGB image composites of SWIR-2, SWIR-1, and Red bands were selected for the implementation of ToPeCAl-2 applied to Sentinel-2 MSI.

Table 5.4. List of Landsat-8 and Sentinel-2 data for applying and assessing application of ToPeCAl-2 to images over Central Kalimantan, South Kalimantan, West Kalimantan, Riau, Jambi, and South Sumatera. There are four pairs of Landsat-8 and Sentinel-2 images contained fires in the same areas on the day of acquisition. Descending orbit Landsat-8 images were acquired at 2–12 min after Sentinel-2 image acquisition. The state of fire features was identified from the Red-Green-Blue (RGB) image composites of SWIR-2, SWIR-1, and Red bands of Sentinel-2 and Landsat-8 images.

Study area	Acquisition date	Landsat-8's path/row	Sentinel-2's tile	Difference time (minutes)	Fire features
Central Kalimantan and South Kalimantan	28 September 2018	118/062	S-2A (T49MHS, T49MHT, T50MKB, T50MKC)	9	Yes
	14 August 2019	118/062	S-2A (T49MHT, T50MKC)	9	Yes
Central Kalimantan	6 September 2019	119/062	S-2A (T49MGS, T49MGT, T49MHT)	5	Yes
Jambi and South Sumatera	21 August 2018	124/061 124/062	S-2A (T48MVC, T48MVD, T48MWC)	5	No
	31 August 2019	125/061	S-2B (T48MUD)	12	Yes
	13 September 2018	125/061	S-2A (T48MUD)	2	No
Riau	16 April 2019	126/059	S-2B (T47NRA, T47NRB, T48NTF, T48NTG)	7	No
	9 May 2019	127/059	S-2B (T47NPB, T47NQC, T47NRB)	3	No
	28 July 2019	127/059	S-2B (T47NQB)	4	No

5.3. Methods

5.3.1. Tropical Peatland Combustion Algorithm with ShortWave InfraRed (SWIR) and Thermal InfraRed (TIR)

Figure 5.3 illustrates the principle of Planck's Law which describes spectral radiance simulation using the MODerate resolution atmospheric TRANSmission (MODTRAN-5) for peatland with limited vegetation under assumption of ground albedo of 0.1 (Caiazzo

et al. 2014) and emissivity of 0.9 (Hayasaka et al. 2016) at given temperatures of 300 K, 360K, 450 K, 500 K, 600 K, 700 K, and 1000 K under a tropical atmosphere and using a rural model with visibility of 3 km and hazy conditions. Previous studies observed that peatlands combustion temperature occurred at 360–500 K for smouldering, 500–700 K for smouldering but close to flaming, and at 700–1000 K for flaming (Elvidge et al. 2015; Hayasaka et al. 2016; Usup et al. 2004). The atmospheric windows where remote sensing of the biosphere best operates (light blue shading in Figure 5.3) shows the radiant energy of flaming peatlands (>700 K) clearly rising in SWIR region (1.6–2.2 μm) and reaching its peak in MWIR region (3–4 μm). Smouldering peatland spectral radiance falls in 360–500 K area, showing less energy in SWIR than MWIR. The presence of cool fires can also be observed in the LongWave InfraRed (LWIR) which shows higher radiance than in SWIR. However, smouldering fires close to flaming (500–700 K) have less energy at LWIR compared with MWIR. The background temperature (~300 K) has a more significant emission in LWIR region. Thus, the wavelengths with high potential to observe peatland combustion using satellite remote sensing are in the 1.6–2.2 μm, 3–4 μm and 8–12 μm zones. However, reflected solar energy in SWIR may interfere with the detection of flaming at daytime, while the background temperature may affect the detection of cool fire in LWIR (Wooster et al. 2013).

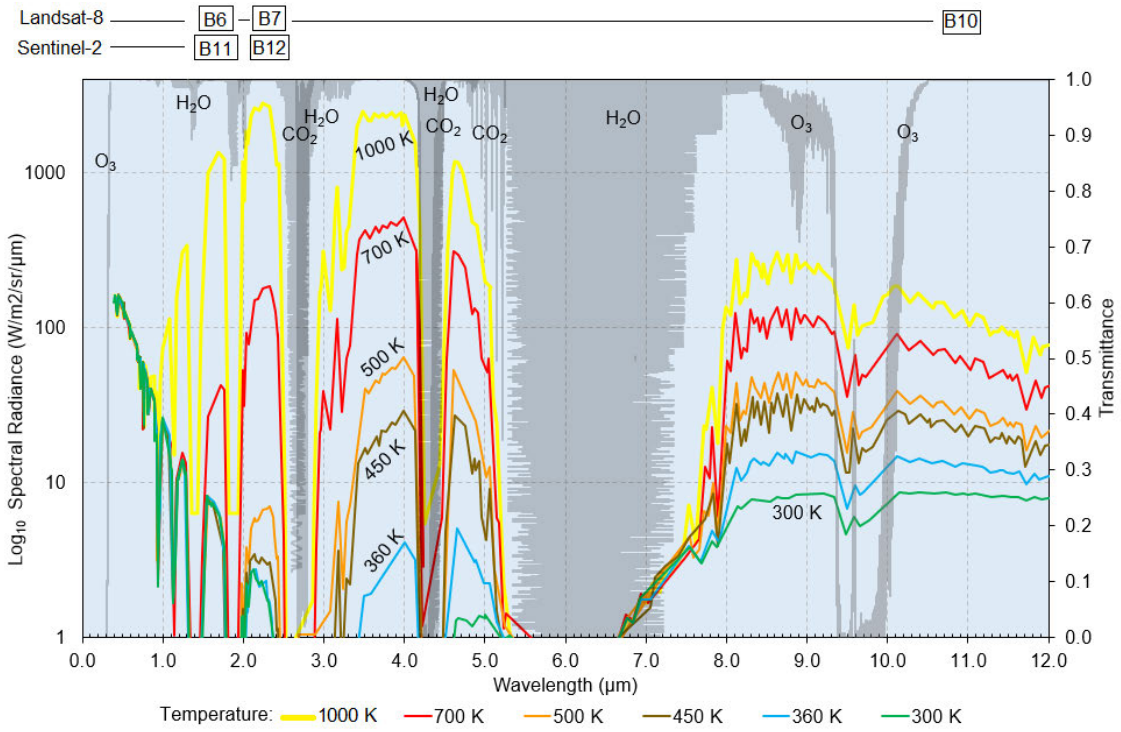


Figure 5.3. Spectral radiance simulated using MODerate resolution atmospheric TRANSmission (MODTRAN) for peatland with limited vegetation. The simulation was made based on albedo of 0.1 with an assumption of emissivity of 0.9 over burning peatland at 300 K, 360 K, 450 K, 500 K, 700 K and 1000 K under a tropical atmosphere and using a rural model. The atmospheric transmittance is presented in light blue background, while water vapour and gas absorption is portrayed in grey. This graph assumes 100% of the pixels corresponding to objects are at the nominated temperature and that might be unrealistic for some flaming at 30 × 30 m pixels, but it may be realistic for smouldering pixels. The graph is not definitive—it gives suggestions as to where to observe peatland fires using remote sensing.

To examine the radiance profile of peatland fire from Landsat-8 OLI/TIRS, (Sofan et al. 2019) analysed the top of atmosphere (TOA) radiance for peatland fires locations based on ground truth. The ground truth data were collected on the same day and up to two days after Landsat-8 observation over Central Kalimantan peatlands on 28 September 2018 at path/row of 118/062. The ground truth data were collected by helicopter from Disaster Management Agency, drone imaging for inaccessible locations, and by direct measurement for accessible peatland fires (Sofan et al. 2019).

Figure 5.4 presents examples of areas of interest in burnt zones and smouldering peatland for extracting TOA radiances from Landsat-8 based on drone imagery in Central Kalimantan. Drone imagery in Figure 5.4a observed burnt areas on the same day with Landsat-8 observation on 28 September 2018. The burnt area is shown in bright brown tones from the drone image and also from surface pictures which were taken by using digital camera (Figure 5.4b). There was no smoke emanating from burnt areas and no

smoky atmosphere in the area at the time these images were taken. Meanwhile, Figure 5.4c shows smouldering peatland which is shown in dark areas mixed with white tones, indicating ash as the product of smouldering (Rein 2013; 2016; Santoso et al. 2019). The drone imagery of smouldering peatlands was taken two days after Landsat-8 observed the area on 28 September 2018. The surface picture of a part of smouldering peatlands (Figure 5.4d) was taken at the same time as drone imagery (Figure 5.4c). Smoky atmosphere existed in the areas when the field measurements were taken and some smoke was still emanating from the smouldering peatlands (Figure 5.4d). The accessible smouldering peatland areas were measured for surface temperature resulting in an average of 452 K by using a handheld IRtek IR150 dual-beam laser infrared thermometer (Figure 5.4e) while the average surface temperature of burnt area was about 315 K.

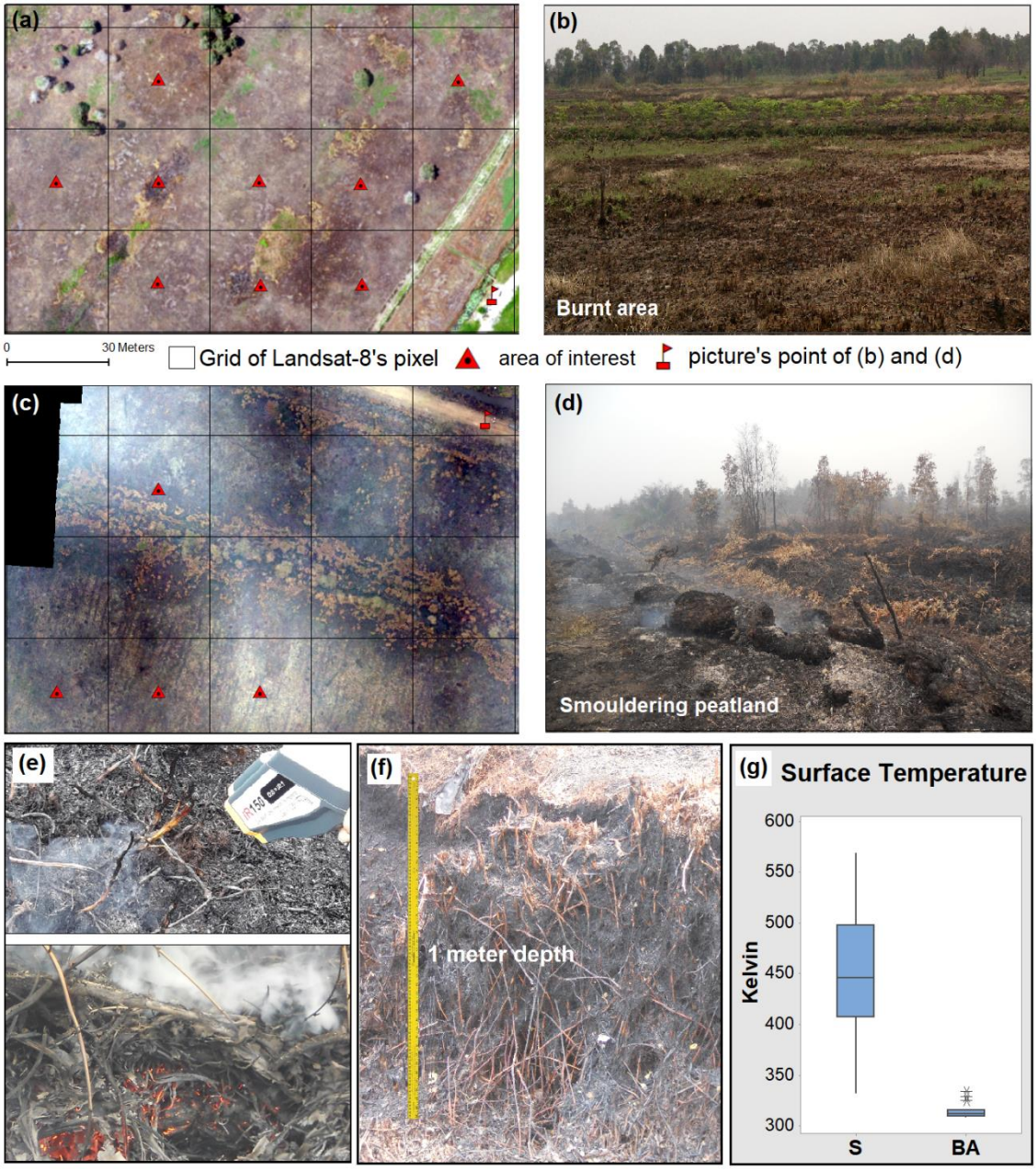


Figure 5.4. (**a**) Example of field picture taken from drone over burnt areas. The areas of interest were selected at homogenous pixels (>80–90% of pixel area of Landsat-8 was burnt area and smouldering peatland). Drone imaging was taken using Da-Jiang Innovations (DJI) Phantom Pro-4 on the same day with Landsat-8 acquisition (28 September 2018); (b) Picture of burnt area taken from the surface by digital camera in the burnt areas shown in Figure (a) at different orientation; (c) Example of smouldering peatlands taken by drone on 30 September 2018, two days after Landsat-8 acquisition time; (d) Picture of smouldering peatlands taken from surface in area of the smouldering peatlands in Figure (c) at different orientation; smoke shown from smouldering logs and surface peatlands; (e) Measurement of surface temperature on smouldering peatland using handheld IRtek IR150 dual-beam laser infrared thermometer; smouldering features below the peatland surface (to −20 cm) with smoke at the surface; (f) An example of peatland depth (1 m) consists of decaying roots and organic soil as the fuels for smouldering peatland; (g) Boxplots of smouldering (S) peatland and burnt area temperatures at the surface from 44 smouldering locations and 16 burnt area (BA) locations.

The graph in Figure 5.5 shows the profile of TOA radiances of Landsat-8 that were extracted from multiple pixels at a total of 1.62 ha of flaming, 2.43 ha of smouldering and 1.62 ha of burnt areas. Each of flaming, smouldering, and burnt area covered at least >80–90% of the pixel areas. The area of interest of smouldering and burnt areas were imaged by drone, while for flaming based features on large fire areas from 7-6-4 RGB image composites of Landsat-8 on 28 September 2018 in Central Kalimantan. The profile for flaming shows high spectral radiance in all bands of Landsat-8 (band 1–7, band-10) compared with smouldering and burnt area radiance. Smouldering showed a higher radiance at NIR (band-5) than burnt areas due to higher scattering from smoky surfaces and also some un-burnt vegetation still existing in the ongoing smouldering peatland which reflected more NIR than in the burnt area. In SWIR bands, burnt area reflectance was higher than smouldering area in band-6, but shown a similar value at band-7. The burnt area with less vegetation than in smouldering peatland may have lower surface moisture which leads to a higher reflection of SWIR in burnt areas. In TIR, smouldering peatland shows a slightly higher radiance than burnt area. Observation of the spectral plots suggests that for separating flaming, smouldering, and burnt area, taking a ratio of band-7 and band-6 may be productive. The spectral signatures in Figure 5.5 were acquired for guiding peatland fire validation from Landsat-8 images for some of locations which were not accessible. These profiles supported the development of ToPeCAl (Sofan et al. 2019).

In addition, previous tropical peatland fire studies using field experiments and using remote sensing data were reviewed when selecting samples of peatland fires. In respect to acquisition times the low speed of peatland fire propagation permits sampling of smouldering areas on different days; in our case the time difference was up to 2 days after Landsat-8 acquisition. Low surface peatland fire propagation speed was reported at 3.8 cm/h (0.9 m/day) on average, or 6.5 cm/h (1.6 m/day) on maximum through field experiments in Central Kalimantan (Usup et al. 2004). Meanwhile, the authors of Atwood et al. 2016 showed active fire propagation using TET-1 data, lasting for about 30 days, at 4 m/day (minimum) to 1,903 m/day (maximum) in Central Kalimantan. From personal communication with local staff of the Indonesian Disaster Management Agency, who accompanied ground truth work on 28 September–1 October 2018, peatland fires can last more than one week if no attempt to extinguish is made. Smouldering is a very persistent type of combustion, which is relatively easy to commence and difficult to suppress (Rein

2013; 2016). Once ignition has occurred, smouldering can exist for long periods (days, months or years). When peatland is ignited, the smouldering combustion dominates the flaming combustion (Rein 2013; 2016) and its propagation develops both laterally and vertically (Santoso et al. 2019; Usup et al. 2004). Smouldering and flaming combustion can lead to one other; however, when the oxygen supply increases, as occurs with an increase in wind velocity, combustion becomes faster, temperature increases and a flaming state may eventuate (Rein 2013; 2016).

ToPeCAl was first developed using SWIR and TIR spectral bands for peatland fire detection with a classification of clear and smoky/hazy tropical atmospheric conditions from the aerosol band (0.433–0.453 µm) of Landsat-8 over Indonesia (Sofan et al. 2019). The TOA reflectance of aerosol band, the TOA reflectance of SWIR bands (1.566–1.651 µm and 2.107–2.294 µm), and the TOA brightness temperature of TIR band (10.61–11.19 µm) were used in ToPeCAl. TOA reflectance for fire detection was introduced in previous studies using Advanced Spaceborne Thermal Emission and Reflection Radiometer (ASTER) and Landsat-8 by (Giglio et al. 2008; Kumar & Roy 2018; Murphy et al. 2016; Schroeder et al. 2016). ToPeCAl uses TIR and SWIR to enhance the detection of smouldering and flaming combustion of tropical peatland fires (Sofan et al. 2019). ToPeCAl applied to Landsat-8 OLI/TIRS provided 82% accuracy compared with ground truth data with omission errors in small smouldering areas of non-homogeneous pixels less than one pixel of Landsat-8 and commission errors corresponding to bright building rooftops. Elimination of the urban area (building rooftops) from the analysis using a landuse map generated from Landsat-8 increased the accuracy to 93% for ToPeCAl fire mappin (Sofan et al. 2019). However, false detection may also occur for smouldering detection resulting from ToPeCAl, as the brightness temperature of smouldering peatlands showed slight differences with burnt areas (Figure 5.5).

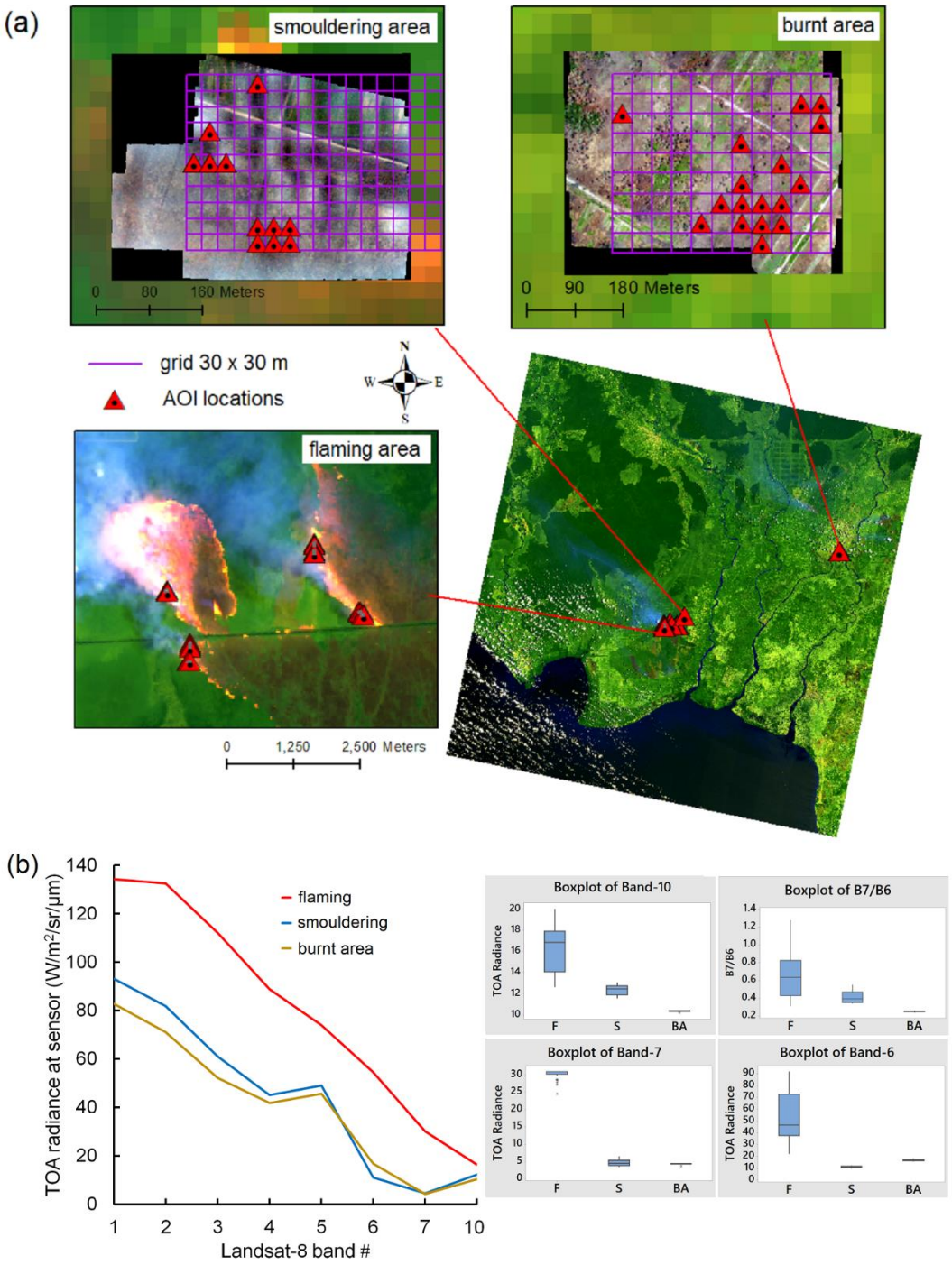


Figure 5.5. (**a**) Inset map of burnt area, smouldering and flaming area with area of interest (AOI) over Landsat-8 image; the AOI of burnt area and smouldering were selected based on drone image while flaming area based on obvious fire features on RGB Landsat-8 image (**b**) Profile of Top of Atmospheric (TOA) radiance of Landsat-8 bands for flaming, smouldering peatland, and burnt areas locations collected from ground truth data on 28 September 2018 to 1 October 2018. Smouldering locations were observed two days after Landsat-8 acquisition due to the longer proses of burning in smouldering peatlands. The Landsat-8 imagery was acquired on 28 September 2018 in Central Kalimantan (path/row of 118/62). Boxplots of band 10, band-7, band-6 and ratio of band-7 to band-6 of Landsat-8 are presented. The ratio of band-7 to band-6 shows a potential index for separating combustion and non-combustion areas. F, S, and BA represent flaming, smouldering and burnt areas respectively.

In ToPeCAl (Sofan et al. 2019), the potential combustion areas are first identified by use of the ShortWave InfraRed Combustion Index ($SICI_\rho$), the ratio of TOA reflectance of SWIR-2 at the central wavelength of 2.2 µm ($\rho_{2.2}$) to SWIR-1 at the central wavelength of 1.6 µm ($\rho_{1.6}$). $SICI_\rho$ values greater than 1 are classified as potential combustion areas, while the non-combustion areas, e.g., vegetation, water, urban area, and cloud, were masked using $SICI_\rho < 1$. Then, flaming and smouldering pixels are identified within the potential combustion areas using TOA reflectance of SWIR-2 ($\rho_{2.2}$) and TOA brightness temperature of TIR ($BT_{10.9}$) on relatively clear or smoky/hazy atmospheric conditions based on TOA reflectance of the aerosol band ($\rho_{0.44}$). The ToPeCAl formulation is given by Equations 5.1–5.12 (Sofan et al. 2019):

Peatland combustion types in relatively-clear atmospheric conditions:

$$SICI_\rho = \frac{\rho_{2.2}}{\rho_{1.6}};\ SICI_\rho > 1 \quad \textbf{(5.1)}$$

AND

$$\rho_{0.44} < 0.27 \quad \textbf{(5.2)}$$

AND

$$\{0.09 \leq \rho_{2.2} \leq 0.31 \text{ AND } BT_{10.9} \geq 297 \quad \text{(smouldering)} \quad \textbf{(5.3)}$$

$$0.31 < \rho_{2.2} < 0.68 \text{ AND } BT_{10.9} \geq 300 \quad \text{(mix of flaming and smouldering)} \quad \textbf{(5.4)}$$

$$\rho_{2.2} \geq 0.68 \text{ AND } BT_{10.9} \geq 307 \quad \text{(flaming)}\} \quad \textbf{(5.5)}$$

AND

$$SICI_\rho \leq 1 \text{ AND } \rho_{2.2} \geq 0.68 \text{ AND } BT_{10.9} \geq 307 \quad \text{(flaming for close to saturated pixel of SWIR radiance)} \quad \textbf{(5.6)}$$

Peatland combustion types in smoky/hazy atmosphere condition:

$$SICI_\rho = \frac{\rho_{2.2}}{\rho_{1.6}};\ SICI_\rho > 1 \quad \textbf{(5.7)}$$

AND

$$\rho_{0.44} \geq 0.27 \quad \textbf{(5.8)}$$

AND

$$\{0.11 \geq \rho_{2.2} \leq 0.32 \text{ AND } BT_{10.9} \geq 297 \quad \text{(smouldering)} \quad \textbf{(5.9)}$$

$$0.32 < \rho_{2.2} < 0.47 \text{ AND } BT_{10.9} \geq 297 \quad \text{(mix of flaming and smouldering)} \quad \textbf{(5.10)}$$

$$\rho_{2.2} \geq 0.47 \text{ AND } BT_{10.9} \geq 303 \quad \text{(flaming)}\} \quad \textbf{(5.11)}$$

AND

$$SICI_{\rho} \leq 1 \text{ AND } \rho_{2.2} \geq 0.47 \text{ AND } BT_{10.9} \geq 303 \quad \text{(flaming for close to saturated pixel of SWIR radiance)} \tag{5.12}$$

In this study, the ToPeCAl algorithm with SWIR and TIR is termed ToPeCAl-1, while ToPeCAl without TIR band is termed ToPeCAl-2. An initial comparison of ToPeCAl-1 and ToPeCAl-2 was conducted through visual analysis on the ToPeCAl fires product compared with 6-5-4 (SWIR-1, NIR, Red) RGB images of Landsat-8. In this visual analysis, the attention was to check what fire objects resulting from ToPeCAl-2 were not detected by ToPeCAl-1; that is, the false positives of ToPeCAl-2. From the 6-5-4 RGB images of Landsat-8, most of the false positive of ToPeCAl-2 fires occurred in the edge of cloud, permanent bright objects such as urban features or factory rooftops and mining areas (Table 5.5). This is indicative of false positive fire detection using ToPeCAl-2 for sensors with no TIR, e.g., Landsat-8 OLI and Sentinel-2 MSI.

Table 5.5. Visual comparison on false positive fire pixels of ToPeCAl with SWIR and TIR (ToPeCAl-1) and ToPeCAl without TIR (ToPeCAl-2) applied to Landsat-8 images.

Object	ToPeCAl-1	ToPeCAl-2	Recommendation for eliminating the false positive pixels on ToPeCAl-2
Edge of cloud	no	yes	Contextual test or cloud masking
Permanent bright objects	less	more	permanent bright object masking

5.3.2. Tropical Peatland Combustion Algorithm without TIR (ToPeCAl-2)

ToPeCAl-1 formulation was adjusted to perform ToPeCAl-2. The general flowchart is shown in Figure 5.6. The adjustment of ToPeCAl-2 included:

- Pre-processing for water body and permanent bright objects masking,
- A variation of ToPeCAl-2 with contextual test for comparing candidate fire pixels with background pixels (Giglio et al. 2008; Schroeder et al. 2016),
- An alternative variation to ToPeCAl-2 using cloud masking.

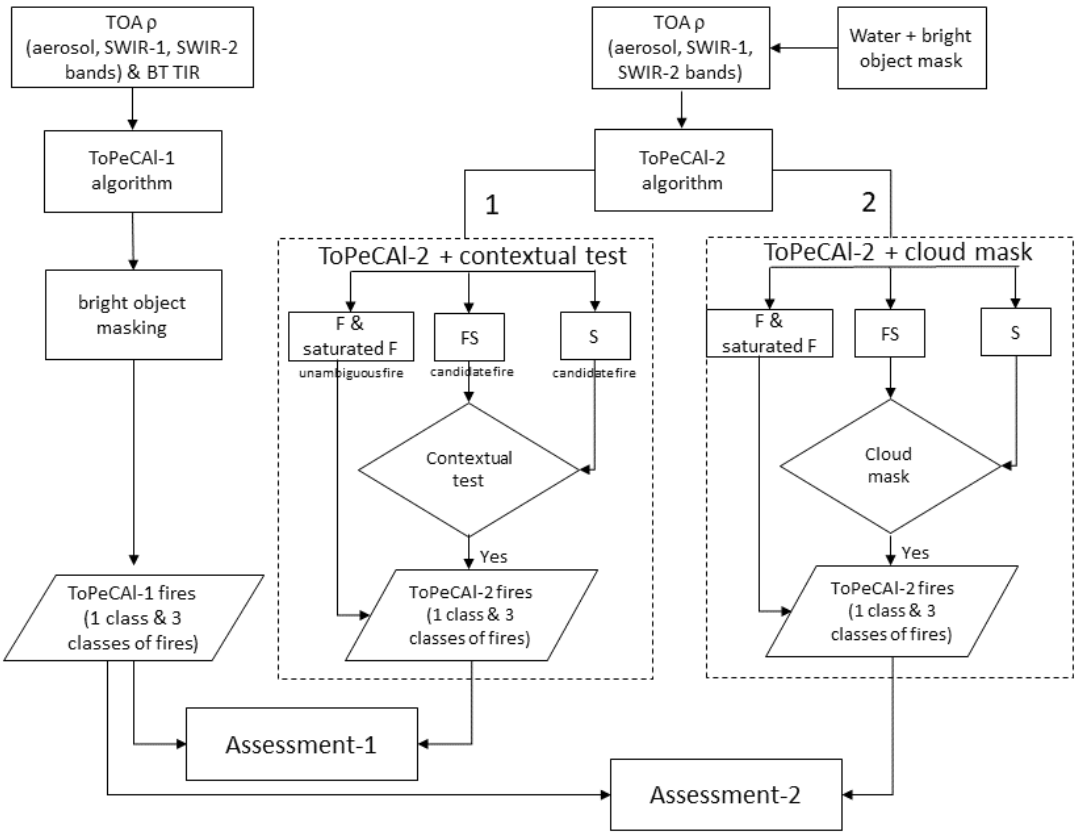


Figure 5.6. Flowchart of general methods used for ToPeCAl-2 compared with ToPeCAl-1. Two methods were assessed, i.e., ToPeCAl-2 with contextual test and ToPeCAl-2 with cloud masking. F is flaming; FS is mix of flaming and smouldering; S is smouldering. TOA is top of atmosphere; ρ is reflectance; BT is brightness temperature; SWIR is ShortWave InfraRed; TIR is Thermal InfraRed.

5.3.2.1. Water Masking

Water and permanent bright objects are outliers or potential outliers in the analysis for fire detection; thus, they were masked, firstly before applying ToPeCAl-2. Normalised Difference Water Index (NDWI) and Modified Normalised Difference Water Index (MNDWI) are widely used for water body mapping from moderate spatial resolution data, e.g., Landsat-8 and Sentinel-2 (Du et al. 2016; Mandanici & Bitelli 2016; Xi, Thinh & Li 2019). NDWI uses green ($\rho_{0.56}$) and NIR ($\rho_{0.865}$) reflectance while MNDWI uses green and SWIR ($\rho_{1.61}$) reflectance in their formulation (Equation (5.13)). We found that NDWI can map water bodies well in clear atmospheric conditions, but for some images with many fires and smoky conditions, NIR does not perform well due to smoke aerosol scattering; thus, MNDWI with SWIR wavelengths which are able to be better detected through smoke was used to map the water bodies. Both NDWI and MNDWI were applied in this study to overcome the variety of smoke conditions over multiple fire images.

According to (Du et al. 2016), NDWI values within 0 to 0.1 and MNDWI values within 0.2 to 0.35 can map water bodies well. In this study, NDWI > 0.1 and MNDWI > 0.35 was used to map water bodies. Some cloud shadows which have the same spectral character with water also were mapped using these thresholds (Equation (5.13)).

$$(\text{NDWI} > 0.1)\ \text{OR}\ (\text{MNDWI} > 0.35) \tag{5.13}$$

$$\text{NDWI} = \frac{\rho_{0.560}-\rho_{0.865}}{\rho_{0.560}+\rho_{0.865}};\ \text{MNDWI} = \frac{\rho_{0.560}-\rho_{1.61}}{\rho_{0.560}+\rho_{1.61}}$$

5.3.2.2. Permanent Bright Object Masking

Previously, in the application of ToPeCAl-1 an urban GIS map was used for masking potential false positive pixels in urban areas (Sofan et al. 2019). However, multi-temporal high spatial resolution images from Google Earth confirmed that the false positive pixels were still found on building or factory rooftops outside the urban area and these objects are relatively permanent, e.g., building/factory and mining areas which existed through several years.

These permanent bright reflective objects can be more effectively eliminated to minimise the false positive pixels through the use of TOA reflectance of SWIR-2 ($\rho_{2.2}$). The mean value of $\rho_{2.2} > 0.2$ was applied by (Schroeder et al. 2016) on multi-temporal data of Landsat-8 OLI in co-located cloud free pixels in the previous 6 months (176 days) to eliminate false positives over permanent bright objects. However, it is rare to obtain cloud free pixels from multi-temporal data of Landsat-8 for every 16-days in tropical environments. Thus, some adjustments were applied in this study to map the permanent bright objects with the following procedure:

- Use of multi-temporal Sentinel-2 MSI images instead of Landsat-8 OLI images to acquire more images containing cloud free pixels. This is a result of the higher temporal resolution of Sentinel-2 acquisition compared with Landsat-8. The cloud free pixels of the multi-temporal images from Level-1C Sentinel-2 MSI for permanent bright object mapping were obtained via the Google Earth Engine platform (Gorelick et al. 2017). According to (Drusch et al. 2012), geometric image quality performance for multi-temporal Sentinel-2 20 m bands was 6 m (2σ). To match with the fire product of ToPeCAl-2 applied to Landsat-8, the product of permanent bright objects from SWIR-2 band of Sentinel-2 was resampled to 30 m.

- The median values of $\rho_{2.2}$ as applied by (Kumar & Roy 2018) instead of the mean values as used by (Schroeder et al. 2016); thus, in this study, the median values of $\rho_{2.2} > 0.18$ were used. This condition needs to exist in the first half-year (January–June) and in the second half-year (July–December) either in the year of data acquisition, or in the previous year. This seasonal period was selected to gain increased possibilities of obtaining cloud free images which were not based on the period of seasons in Indonesia. Otherwise, cloud free images were usually found in dry season (April–September) and barely any cloud free data in wet season (October–March). Permanent bright objects should also have relatively stable and high SWIR reflectance in any period. Thus, these conditions can be expressed as:

$$\text{If } ((\rho_{2.2} \text{ at } t_{(\text{jan-june, y})}) \text{ OR } (\rho_{2.2} \text{ at } t_{(\text{jan-jun, y-1})})) > 0.18 \quad \textbf{(5.14)}$$

AND

$$((\rho_{2.2} \text{ at } t_{(\text{jul-dec, y})}) \text{ OR } (\rho_{2.2} \text{ at } t_{(\text{jul-dec, y-1})})) > 0.18 \quad \textbf{(5.15)}$$

then TRUE as bright permanent objects

where $t_{(\text{jan-june, y})}$ and $t_{(\text{jan-june, y-1})}$ are time period in January–June in on-going year and in previous year; $t_{(\text{jul-dec, y})}$ and $t_{(\text{jul-dec, y-1})}$ are time period in July–December in on-going year and in previous year.

5.3.2.3. ToPeCAl-2 with Contextual Test

The form of ToPeCAl-2 for relatively clear sky and smoky/hazy atmospheres is similar to ToPeCAl-1 but without $BT_{10.9}$. Unambiguous detection is for flaming fires (Equation (5.16)). For detection of flaming close to saturated pixel, $SICI_\rho$ values in ToPeCAl-1 (Equation (5.6) and (5.12)) were expressed as ≤ 1 with conditions for $\rho_{2.2}$ and $BT_{10.9}$. This $SICI_\rho \leq 1$ resulted from $\rho_{1.6}$ or $\rho_{2.2} \geq 1$ and with a condition of $\rho_{1.6} \geq \rho_{2.2}$. The actual values of $SICI_\rho$ for close to saturated pixel were not explicitly stated in ToPeCAl-1 (Equation (5.6) and (5.12)), but because TIR does not exist in ToPeCAl-2 then it should be rewritten as ≥ 0.9 (Equation (5.17)). Meanwhile additional candidate fire pixels are from a mix of flaming and smouldering (FS) and smouldering pixels (Equation (5.18) and (5.19)).

Unambiguous fire pixels on clear sky or smoky/hazy atmosphere:

$$SICI_\rho > 1 \text{ AND } \rho_{0.44} < 0.27 \text{ AND } \rho_{2.2} \geq 0.68 \quad \textbf{(5.16)}$$

OR

$$\mathrm{SICI}_{\rho} > 1 \text{ AND } \rho_{0.44} \geq 0.27 \text{ AND } \rho_{2.2} \geq 0.47$$

Fire pixels at close to saturation for flaming pixel on clear sky or smoky/hazy atmosphere:

$$\mathrm{SICI}_{\rho} \geq 0.9 \text{ AND } \rho_{0.44} < 0.27 \text{ AND } \rho_{2.2} \geq 0.68 \text{ AND } (\rho_{2.2} \geq 1 \text{ AND } \rho_{1.6} \geq 1) \text{ AND } (\rho_{1.6} \geq \rho_{2.2}) \quad \textbf{(5.17)}$$

OR

$$\mathrm{SICI}_{\rho} \geq 0.9 \text{ AND } \rho_{0.44} \geq 0.27 \text{ AND } \rho_{2.2} \geq 0.47 \text{ AND } (\rho_{2.2} \geq 1 \text{ AND } \rho_{1.6} \geq 1) \text{ AND } (\rho_{1.6} \geq \rho_{2.2})$$

Candidate fire pixels for FS pixels on clear sky or smoky/hazy atmosphere:

$$\mathrm{SICI}_{\rho} > 1 \text{ AND } \rho_{0.44} < 0.27 \text{ AND } \rho_{2.2} > 0.31 \quad \textbf{(5.18)}$$

OR

$$\mathrm{SICI}_{\rho} > 1 \text{ AND } \rho_{0.44} \geq 0.27 \text{ AND } \rho_{2.2} > 0.32$$

Candidate fire pixels for smouldering pixels on clear sky or smoky/hazy atmosphere:

$$\mathrm{SICI}_{\rho} > 1 \text{ AND } \rho_{0.44} < 0.27 \text{ AND } 0.09 \leq \rho_{2.2} \leq 0.31 \quad \textbf{(5.19)}$$

OR

$$\mathrm{SICI}_{\rho} > 1 \text{ AND } \rho_{0.44} \geq 0.27 \text{ AND } 0.11 \leq \rho_{2.2} \leq 0.32$$

A contextual algorithm was implemented to compare the candidate fire pixels from Equations (5.18) and (5.19) with background pixels. However, the unambiguous fire pixel (flaming) from Equation (5.16) and the close to saturated flaming pixels from Equation (5.17) were retained as peatland fire pixels. The contextual algorithm was sourced from (Schroeder et al. 2016) with a modification particularly on using the mean and standard deviation of the ratio of $\rho_{2.2}$and $\rho_{1.6}$ rather than the ratio of $\rho_{2.2}$and $\rho_{0.865}$ as used in (Schroeder et al. 2016). The peatland fire pixels from ToPeCAl-2 were derived from the ratio of $\rho_{2.2}$ to $\rho_{1.6}$ and the reflectance of SWIR-2 ($\rho_{2.2}$), thus the statistical calculations of the background pixels were also analysed based on these spectra.

The contextual search was set to a 61 × 61 pixel window similar to (Giglio et al. 2008; Schroeder et al. 2016). Valid background pixels ideally should not be contaminated with outlier pixels. However, in tropical peatland environments the background is mostly

heterogeneous, potentially resulting in a non-normal distribution statistic of the background values. Dense cloud might also exist and also the fire pixels including candidate fire pixels in 61 × 61 pixel windows. These features can also influence the background statistics. In this study, the cloud mask product from Landsat-8 was not chosen as it mapped slightly larger cloud areas which misclassified some clear area as clouds. This result also was reported by (Sun et al. 2017) who suggested to use the Cloud Detection Algorithm Generation (CDAG) to perform better cloud masking. Thus, CDAG with single band of Red reflectance ($\rho_{0.65}$) was applied to map clouds in this study. The formulation of cloud mask is given in Equation (5.20) (Sun et al. 2017).

$$\rho_{0.65} > 0.21 \tag{5.20}$$

Previous studies (Giglio et al. 2008; Kumar & Roy 2018; Schroeder et al. 2016) only masked water/cloud shadow and unambiguous fire pixels from background analyses. In this study, permanent bright objects, dense cloud pixels and all of fire pixels, including candidate pixels from the population of the background were also masked. An example is shown in Figure 5.7c, but with no bright permanent object pixels existing in this sample. The histogram and population statistics of the ratio of reflectance of band-7 to band-6 and the reflectance of band-7 resulting from the image data corresponding to Figure 5.7b are shown in Figure 5.7d. Whilst the background statistics resulting from Figure 5.7c are shown in Figure 5.7e. Based on the histogram, Figure 5.7e exhibits less skewness than Figure 5.7d with improved data distribution for representing the mean and standard deviation values with 1σ to 3σ for the population.

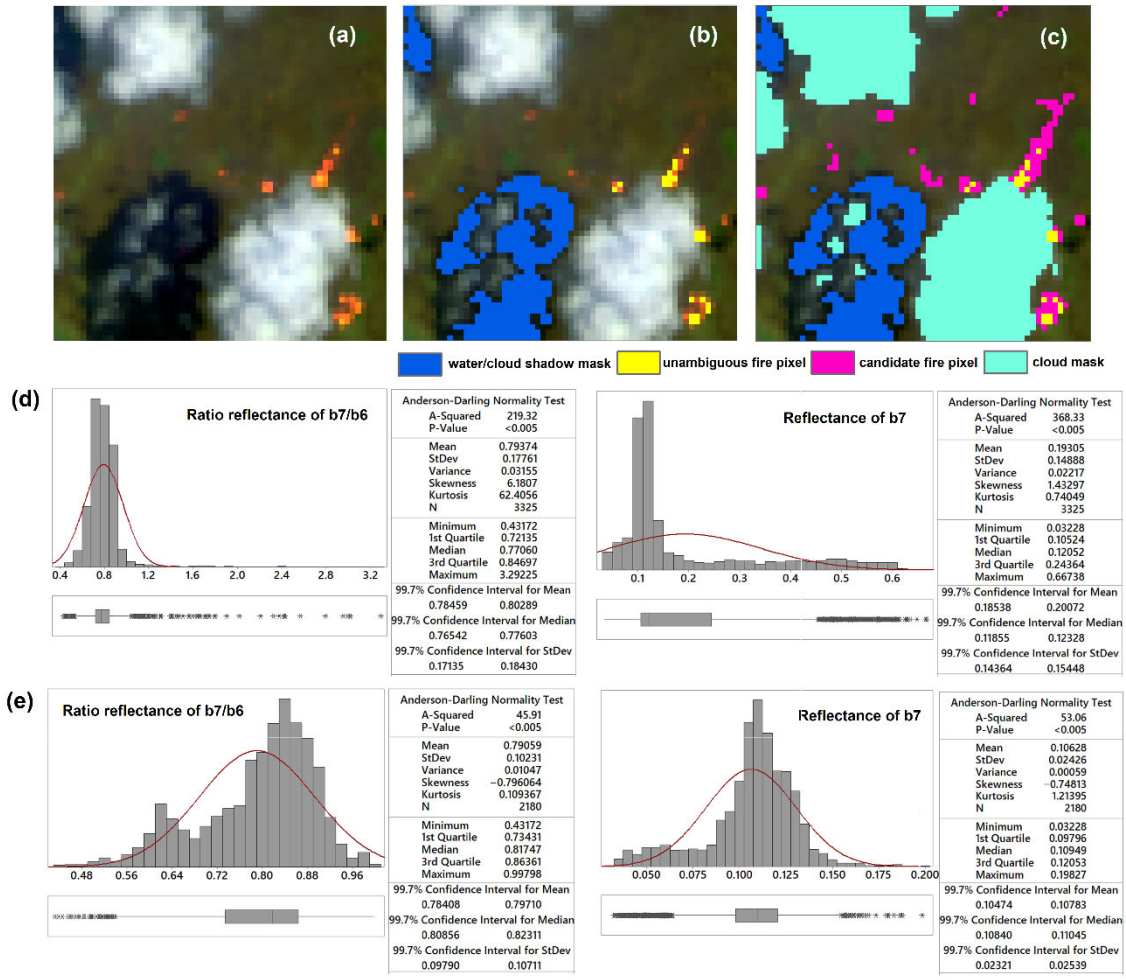


Figure 5.7. (**a**) Example of 764 Red-Green-Blue (RGB) image of Landsat-8 on 28 September 2018 and a 61 × 61 pixel window size with some fire features (in yellow to oranges tones) and background pixels with dominant objects, e.g., cloud (white), cloud shadow (black), soil/open land (brown), and vegetation (green); (**b**) The same RGB image as (**a**) overlaid with water/cloud shadow mask (blue) and obvious fire pixels (yellow) as per-previous studies (Giglio et al. 2008; Kumar & Roy 2018; Schroeder et al. 2016); saturated flaming pixels and permanent bright objects did not exist in this sample; (**c**) The same with (**b**) but with additional masks for cloud (light green) and candidate fire pixels (pink); (**d**) The histogram and population statistics of the ratio reflectance band-7 ($\rho_{2.2}$) to band-6 ($\rho_{1.6}$) and reflectance of band-7 of background pixels which excluded water/cloud shadow and unambiguous fire pixels as shown spatially in (**b**); (**e**) The histogram and population statistics of the same variable with (**d**) but with additional masks of cloud and candidate fire pixels. The ratio of band-7/band-6 and reflectance of band-7 data (**d**,**e**) do not follow a normal distribution according the Anderson-Darling goodness of fit statistic at confidence level of 99.7% (3σ), corresponding to a heterogeneous background, but data in (**e**) is more normal then (**d**).

After selecting valid background pixels, the candidate fire pixels from Equations (5.18) and (5.19) were tested by using a contextual algorithm (Equation (5.21)). The fire pixels that passed this test were merged with fire pixels resulting from Equations (5.16) and (5.17) as the peatland fires pixels.

Contextual test for candidate fire pixels:

$$\frac{\rho_{2.2}}{\rho_{1.6}} > \left(\frac{\overline{\rho_{2.2}}}{\rho_{1.6}}\right) + \max\left[3\sigma\left(\frac{\rho_{2.2}}{\rho_{1.6}}\right), 0.8\right] \quad \textbf{(5.21)}$$

AND

$$\rho_{2.2} > \overline{\rho_{2.2}} + \max[3\sigma\rho_{2.2}, 0.08]$$

Where $\left(\frac{\overline{\rho_{2.2}}}{\rho_{1.6}}\right)$ and $\sigma\left(\frac{\rho_{2.2}}{\rho_{1.6}}\right)$ are the mean and standard deviation of the ratio $\rho_{2.2}$ to $\rho_{1.6}$ respectively, while $\overline{\rho_{2.2}}$ and $\sigma\rho_{2.2}$ are the mean and standard deviation of $\rho_{2.2}$ respectively from 61 × 61 pixel window centred on each potential fire pixel. The values of 0.8 and 0.08 in Equation (5.21) were sourced from (Schroeder et al. 2016) to avoid false alarms in unusually homogeneous regions (Giglio et al. 2008).

5.3.2.4. ToPeCAl-2 with Cloud Masking

ToPeCAl-2 with cloud masking was another approach to eliminate false positives in cloud, dense cloud and the edge of cloud, instead of the contextual test approach. In this second approach, ToPeCAl-2 fires resulted from Equation (5.16) to Equation (5.20) were filtered with cloud masking, particularly for FS and smouldering pixels, to remove false positives. However, the cloud mask data was not produced from Equation (5.21), rather it was obtained from cloud mask product of Level-2 pixel-qa of Landsat-8. The cloud mask from pixel-qa provided a larger cloud area which assisted in removing the false positive pixels in the edge of cloud.

5.3.2.5. Pixel-Based Comparison of ToPeCAl-2 Applied to Landsat-8 Operational Land Imager (OLI) with ToPeCAl-1 Applied to Landsat-8 OLI/Thermal InfraRed Sensor (TIRS)

A pixel-based comparison of 15 Landsat-8 images was conducted between the fire products of ToPeCAl-2 with the fire products of ToPeCAl-1. The reference fire data was ToPeCAl-1 fires. The comparison of peatland fires was calculated for three classes of peatland combustions and one combined class of fire. The three classes of peatland combustions from ToPeCAl are flaming (F), smouldering (S), and mix of flaming and smouldering (FS). The one fire class (Fire) was created by integrating the three peatland combustion classes into one class. Statistical analyses generated the probability of detection (POD), false positive (commission error) and false negative (omission error). POD was calculated by the ratio of true positive fires between ToPeCAl-2 and ToPeCAl-

1 to the total fires produced in the reference data (ToPeCAl-1). Commission error was counted from the ratio of the ToPeCAl-2 fires which were not detected in ToPeCAl-1 to the total ToPeCAl-2 fires, while omission error can be computed as 1-POD.

In addition to ToPeCAl-1 Landsat-8 fires as the reference, others image data, e.g., Google Earth and PlanetScope were used to confirm any indication of fires or false detections. The PlanetScope data were accessed from Planet explorer at www.planet.com.

5.3.3. Implementation and Comparison of ToPeCAl-2 on Sentinel-2 Multi Spectral Instrument (MSI)

5.3.3.1. Sentinel-2 MSI Data Pre-processing

The TOA reflectance of Sentinel-2 MSI data were obtained from Level-1C. Some of the Sentinel-2 listed in Table 5.4 consisted of more than one tile for the corresponding Landsat-8 scene, thus the data of the Sentinel-2 tiles were mosaicked with nearest neighbor resampling method to preserve the original values of data. In the overlap zones, the images with less cloud cover were selected as the primary data. The tiles were mosaicked for each band of aerosol ($\rho_{0.443}$), green ($\rho_{0.560}$), NIR ($\rho_{0.865}$), SWIR-1($\rho_{1.610}$) and SWIR-2 ($\rho_{2.190}$). The spatial resolution of aerosol and green bands was resampled to 20 m to match with spatial resolution of the SWIR bands to produce fire pixels. Pre-processing to mask out water and permanent bright objects was conducted by using Equation (5.13) to Equation (5.15). A general flowchart, which is presented in Figure 5.6, was also applied to Sentinel-2 to produce fire pixels with an initial investigation of sensor comparison for both Landsat-8 OLI and Sentinel-2 MSI and is described in Section 5.3.3.2.

5.3.3.2. Sentinel-2A MSI and Landsat-8 OLI Spectral Reflectance Sensor Comparison

In order to apply ToPeCAl-2 developed from Landsat-8 OLI data, an initial comparison of the difference between spectral reflectance from Landsat-8 OLI and Sentinel-MSI at band-1, SWIR-1 and SWIR-2 was conducted. Figure 5.8 shows that the spectral response function of Sentinel-2A/2B MSI slightly varied compared with Landsat-8 OLI at aerosol band, SWIR-1 and SWIR-2 bands. The spectral response data was sourced from ESA (ESA 2017) and (Barsi, J et al. 2014).

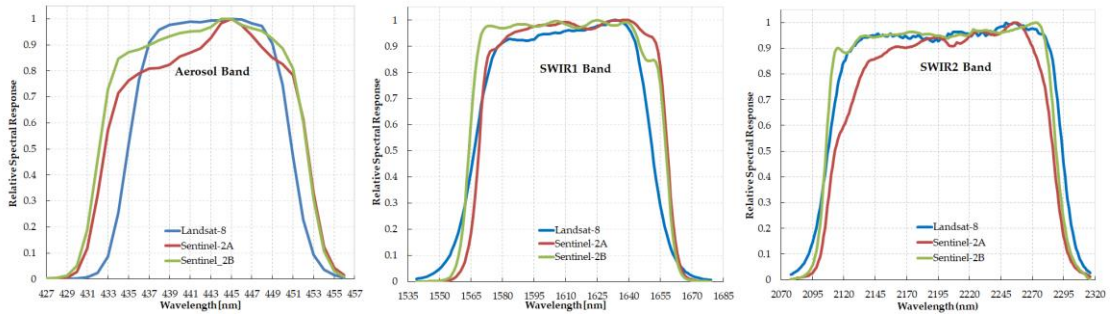


Figure 5.8. Relative spectral response curve at aerosol-band, SWIR-1 and SWIR-2 bands of Sentinel-2A/2B and Landsat-8 Operational Land Imager (OLI). The data was accessed from https://landsat.gsfc.nasa.gov/preliminary-spectral-response-of-the-operational-land-imager-in-band-band-average-relative-spectral-response/ and https://earth.esa.int/documents/247904/685211/S2-SRF_COPE-GSEG-EOPG-TN-15-0007_3.0.xlsx.

Pairs of Sentinel-2A/2B MSI pixels and Landsat-8 OLI pixels on the same day of acquisition also exhibiting fire features in the same area in both data were compared at aerosol, SWIR-1 and SWIR-2 bands. All bands used in ToPeCAl were set at the same spatial resolution of 20 m using the nearest neighbor resampling method in projection of UTM/WGS84. In this study, a valid pixel selection for comparing TOA reflectance of Sentinel-2 and Landsat-8 was built from the same data acquisition utilising criteria which were provided in Scene Classification (SC) of Sentinel-2 from Level-2A through Sen2Cor and pixel-qa of Landsat-8 from Level-2. The valid pixels were from vegetation and non-vegetation class based on the SC data.

In addition to the cloud masking, the physical environment close to cloud generates cloud adjacency effects or 3-D radiative effects. The cloud adjacency effects cause a brighter pixels around the edge of clouds and an increased high-biased aerosol optical depth thus contributing to an increase in observed reflectance (Baetens, Desjardins & Hagolle 2019; Spencer et al. 2019; Várnai & Marshak 2014; Wen et al. 2007). The parallax error due to a difference of earth viewing angles observed from Sentinel-2 spectral bands also was mentioned as a possible displacement of cloud mask (Baetens, Desjardins & Hagolle 2019). In this study, an additional 40 m (2 pixels) buffer from the cloud mask was generated and applied to masking the cloud adjacency effects in the remaining imagery. The cloud mask was merged from medium and high confidence cloud from Sentinel-2 data.

Meanwhile, the mask data from pixel-qa of Landsat-8 were cloud, cloud shadow, water, and high confidence cirrus. All of the mask data selected from SC data and pixel-

qa data were merged as one mask and then applied to Sentinel-2A/2B MSI and Landsat-8 OLI images.

The valid pixels of TOA reflectance data of Sentinel-2A/2B and Landsat-8 OLI in aerosol, SWIR-1 and SWIR-2 bands were then statistically compared and analysed using *t*-tests to determine if there was a significant difference between the means of Sentinel-2 and Landsat-8 TOA reflectance. Ordinary least squares (OLS) regression analysis was also conducted to explore the relationships using the slope and intercept coefficient values between the TOA reflectance of the two sensors. The goodness of fit and significance of the OLS regressions were defined by the coefficient of determination and statistic *p*-value.

5.3.3.3. Implementation of ToPeCAl-2 Applied to Sentinel-2 MSI

ToPeCAl-2 was applied to original values of TOA reflectance of Sentinel-2 MSI and to the transformed values of TOA reflectance of Sentinel-2 MSI resulting from the OLS regression equations between Landsat-8 and Sentinel-2 at band aerosol, SWIR-1 and SWIR-2. As tested in Landsat-8 OLI, ToPeCAl-2 applied to Sentinel-2 was also adjusted by implementing two approaches, i.e., ToPeCAl-2 with contextual test and ToPeCAl-2 with cloud masking.

The formulation of ToPeCAl-2 with contextual test was based on to Equation (5.16) to Equation (5.21). However, the cloud mask was not generated from Equation (5.20). The cloud product from SC map of Sentinel-2 was used for background analysis in the contextual test and for removing false positive pixels from FS and smouldering pixels in the second approach of ToPeCAl-2 adjustment, ToPeCAl-2 with cloud masking.

The masking data used for calculating ToPeCAl-2 was different from the masks data for analysing the spectral relationship between Sentinel-2 and Landsat-8 in the Section 5.3.3.2. The mask data used in ToPeCAl-2 application was high confidence cloud from SC map with additional buffer zone of five pixels (100 m) from outside high confidence cloud polygon. According to Richter, Louis & Muller-Wilm (2012), the high and medium confidence cloud has above 65% and 35% of cloud probability, respectively. The buffer created around dense cloud was also aimed to mask the cloud adjacency effects close to dense cloud. The medium confidence cloud, which was not adjacent to high confidence cloud, was not masked out from the calculation of ToPeCAl-2 in order to detect possible fire pixels under the thin cloud.

5.3.3.4. Pixel-Based Comparison of ToPeCAl-2 Applied to Sentinel-2 MSI with ToPeCAl-1 Applied to Landsat-8 OLI/TIRS

The comparison of fire products of ToPeCAl-2 applied to Sentinel-2 MSI were conducted on a pixel-basis with the fire products of ToPeCAl-1 applied to Landsat-8 OLI/TIRS as reference. The statistical comparisons conducted were POD, false positive (commission error), and false negative (omission error). Potential geometric error existing between both Sentinel-2 and Landsat-8, which is about 38 m (2σ) (Storey et al. 2016) and peatland fires propagation zone during the difference in time of observation between Landsat-8 and Sentinel-2 were considered for analysing the zones of true positive fires. According to (Atwood et al. 2016), the peatland fires propagation can be approximated at 1.3 m/min. This value was then multiplied by the time difference between acquisition of Landsat-8 and Sentinel-2 to estimate the potential spread of peatland fires between the observations. Thus, fire pixels located in the zone of geometric error plus the zone of peat fire propagation from the true positive fires were counted as spatially related true positive fire pixels. Others fire features from higher spatial resolution images, e.g., Google Earth and PlanetScope were also used to confirm any indication of fires or false detections.

5.4. Results

5.4.1. Statistical Comparison of ToPeCAl-2 Applied to Landsat-8 OLI and ToPeCAl-1 Applied to Landsat-8 OLI/TIRS

ToPeCAl-1 and ToPeCAl-2 was applied to about 609 million pixels from fifteen Landsat-8 OLI/TIRS images. Figure 9a shows POD of ToPeCAl-2 with contextual test and cloud masking provided 55% and 98%, respectively. The percentage of independent commission errors (ICE) from ToPeCAl-2 with contextual test and ToPeCAl-2 with cloud masking were low (≤3%). Meanwhile, a high independent omission error (IOE) resulted from ToPeCAl-2 with contextual test (45%). Low of IOE resulted from ToPeCAl-2 with cloud masking (2%). Detail statistical values can be found in Appendix-Table A5.1.

Figure 5.9b shows the comparison of ToPeCAl-1 and ToPeCAl-2 from two approaches in three classes of peatland fires. Both of F and FS pixels resulting from ToPeCAl-2 with either contextual test or cloud masking provided high POD (93–99%). Meanwhile, the accuracy of detection of smouldering pixels from ToPeCAl-2 with contextual test was less than from ToPeCAl-2 with cloud masking. The POD of

smouldering pixels from ToPeCAl-2 with contextual test was only 35% with IOE of 65%. Referring to the result shown in Figure 5.9a, the low POD of ToPeCAl-2 with contextual test was related to the poorer detection of smouldering pixels, as shown in Figure 5.9b. Detailed statistical values of this comparison can be found in Appendix-Table A5.2.

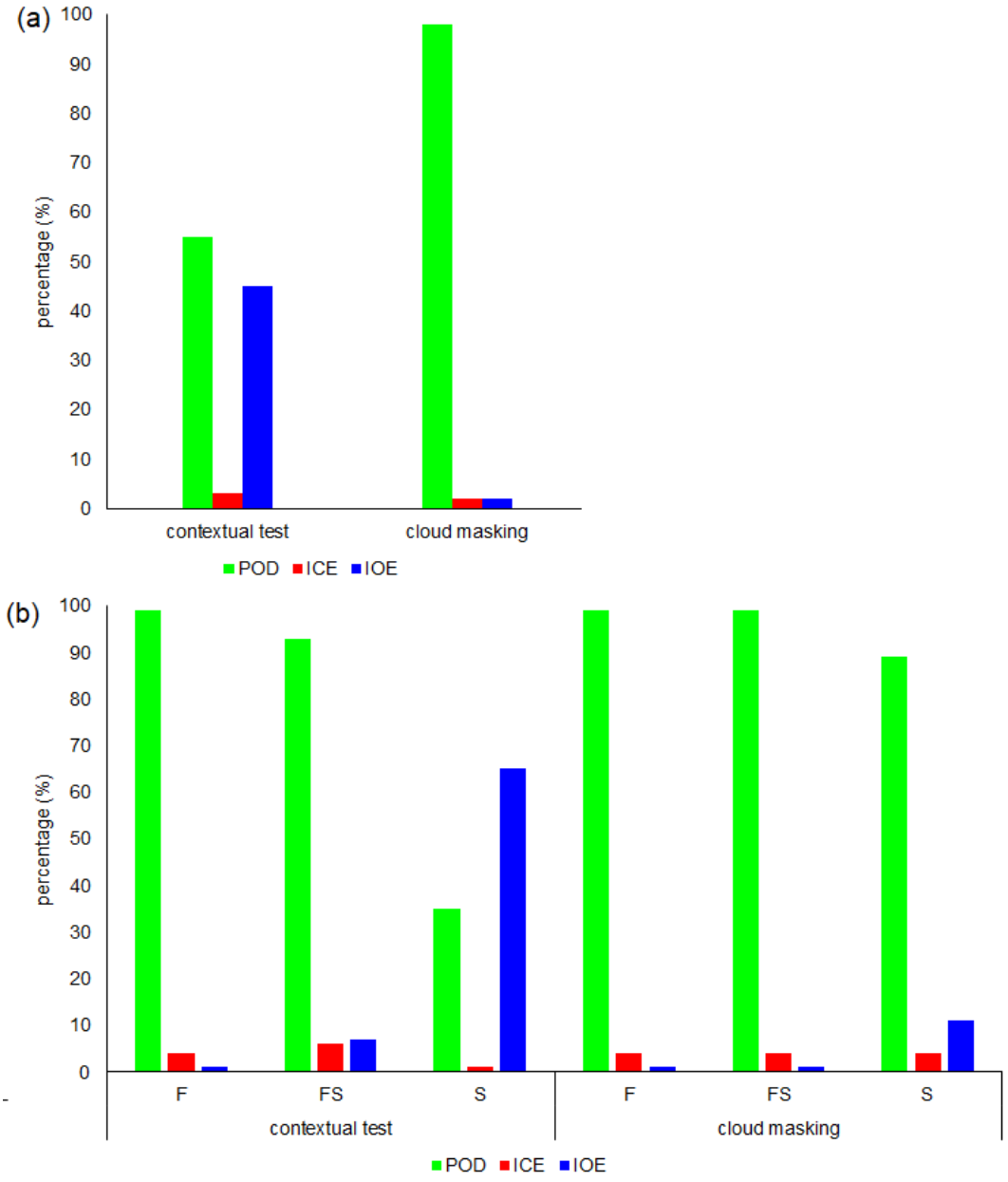


Figure 5.9. (**a**) Percentage of probability of detection (POD), independent commission errors (ICE) and independent omission errors (IOE) of ToPeCAl-2 with contextual test and ToPeCAl-2 with cloud masking applied to Landsat-8 OLI compared with fires resultant from ToPeCAl-1 applied to Landsat-8 OLI/TIRS images; (**b**) As per Figure (**a**) but showing the comparison of fire classes, i.e., flaming (F), smouldering (S), and mix of flaming and smouldering (FS).

Figure 5.10 shows an example comparing the results of ToPeCAl-2 from the two approaches compared to ToPeCAl-1 in Riau's peatland. There are obvious fires features

visually shown in orange to yellow tones in the false composite of RGB Landsat-8 image (Figure 5.10a) and Figure 5.10b shows the fire areas resultant from ToPeCAl-1 as the fire reference. ToPeCAl-2 with contextual test (Figure 5.10c) resulted in less true positive (TP) pixels than from ToPeCAl-2 with cloud masking (Figure 5.10d). The TP from ToPeCAl-2 with contextual test which are shown in red colour were general spatially correlated with flaming pixels from ToPeCAl-1 (Figure 5.10b), while the TP from ToPeCAl-2 with cloud masking (Figure 5.10d) corresponds to all the fires in ToPeCAl-1. Figure 5.10e is the natural RGB composite of PlanetScope data with spatial resolution of 3.7 m about 11 min before Landsat-8 observation on 29 August 2019. Fire features cannot be displayed from the natural RGB image of PlanetScope, but smoke as an indication of fires, shown from this RGB image, confirmed peatland fires detected by ToPeCAl-1 and ToPeCAl-2. An enlarged area (red square) of burning peatlands on PlanetScope image was made and overlaid with fires resulting from ToPeCAl-2 with contextual test (Figure 5.10f) and ToPeCAl-2 with cloud masking (Figure 5.10g). Most of FN pixels from ToPeCAl-2 with contextual test (Figure 5.10f) were in the area of burning peatlands with smoke features in Figure 5.10h. Meanwhile, Figure 5.10i shows PlanetScope image at the same area with Figure 10h after three days on 1 September 2019. Some of the burnt areas in dark tones were covered by smoke which could be sourced from smouldering peatlands or surrounding areas. However, based on the experience observed during ground truth and drone mapping in Central Kalimantan, the burnt peatlands were still emitting smoke after 2–3 day (Sofan et al. 2019).

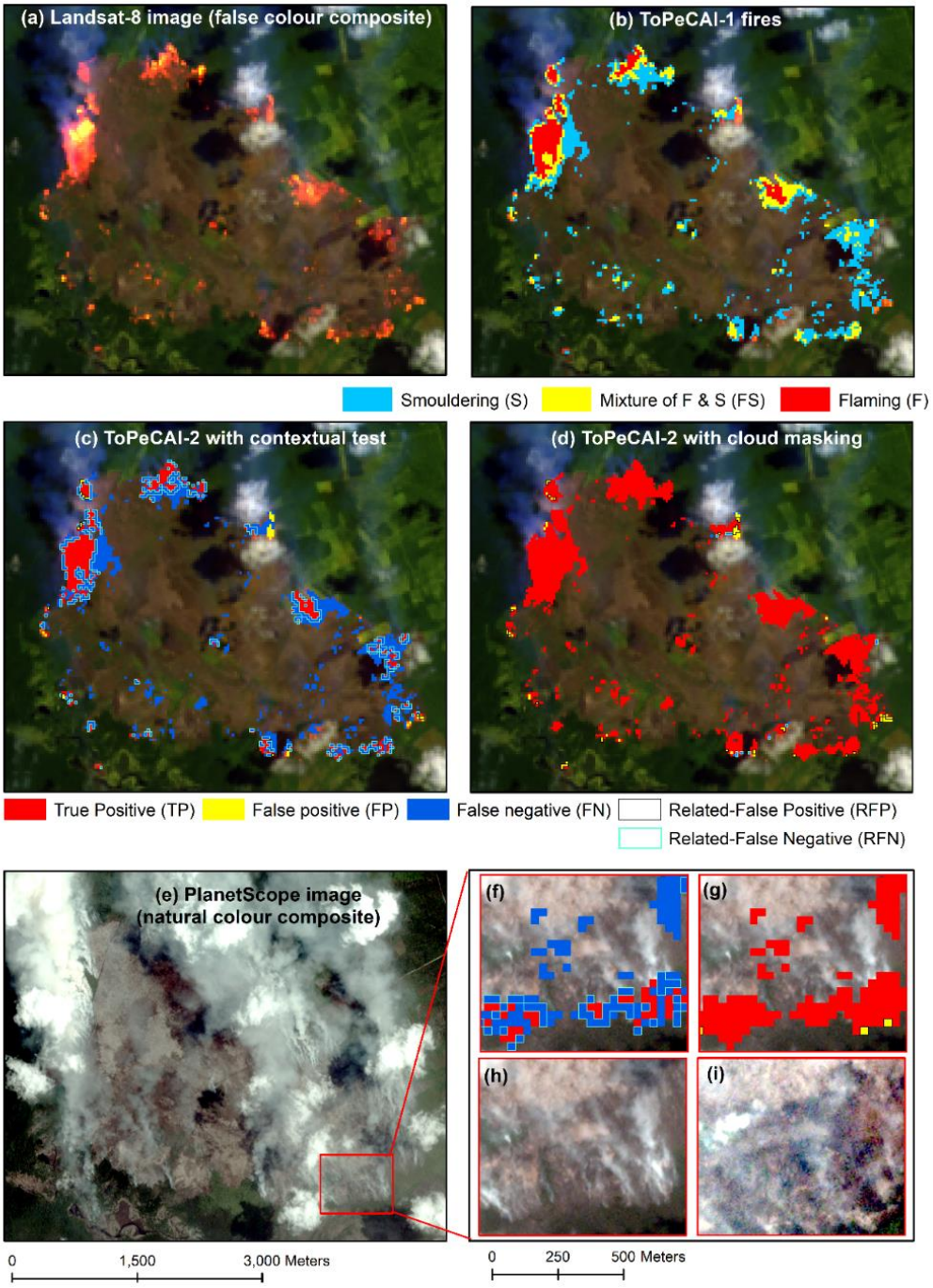


Figure 5.10. (**a**) RGB image of Landsat-8 OLI with SWIR-2 band as Red layer, SWIR-1 band as Green layer, and Red band as Blue layer. Landsat-8 image was acquired on 29 August 2019 over Riau's peatland; (**b**) ToPeCAl-1 fires overlaid on the same RGB image of Landsat-8 in Figure (**a**); (**c**) Result of ToPeCAl-2 fires with contextual test compared with ToPeCAl-1 fires from the same Landsat-8 image of Figure (**a**); (**d**) Comparison result of ToPeCAl-2 with cloud masking. TP is the true positive fire pixel; FP is the false positive fire pixel; FN is the false negative fire pixel. The RFP or RFN is the spatially related of false positive/false negative pixels which adjacent to TP pixel and existed within one pixel buffer from the TP pixel; (**e**) Natural RGB image of PlanetScope in the same area of Landsat-8 image and the same day about 11 min before Landsat-8 acquisition on 29 August 2019; (**f**,**g**) An enlargement of peatland fires in the area of red squares line on Figure (**e**) with fires from ToPeCAl-2 with contextual test and ToPeCAl-2 with cloud masking, respectively; (**h**,**i**) the same enlargement area with Figure (**f**,**g**), but showing smoke features from PlanetScope images on 29 August 2019 and 1 September 2019, respectively.

5.4.2. Relationship between Top of Atmosphere (TOA) Reflectance of Landsat-8 and Sentinel-2 for Aerosol and SWIR Bands

The number of pixel pairs for TOA reflectance values comparison between Landsat-8 and Sentinel-2 ranged between two million and 27.7 million. The aerosol band showed high variability in regression slope values with the lowest value at 0.14 in Jambi and South Sumatera sites and the highest value at 1.07 in a Central Kalimantan site. The data pairs with weak relationships for the aerosol bands also experienced lower R^2 values in the SWIR-1 and SWIR-2 bands compared with the higher R^2 data for other regressions. Each data pair with higher R^2 values (greater than 0.70 at SWIR-2) were merged into one data set with 58.7 million pairs of pixels and analysed with OLS regression. The merged data provided 0.66, 0.78, and 0.83 for R^2 at aerosol, SWIR-1, and SWIR-2 bands, respectively. The results of OLS these regression analyses were significant at *p*-values < 0.001. The statistical values can be found in Appendix-Table A5.3.

Table 5.6 summaries the *t*-test statistic resulting from the mean differences between TOA reflectance of Landsat-8 OLI and TOA reflectance of Sentinel-2 MSI with transformation and no transformation at aerosol, SWIR-1 and SWIR-2 bands. In general, the Sentinel-2 TOA reflectance values with transformation and no transformation were slightly greater than Landsat-8 OLI. The mean difference of TOA reflectance from the two sensors with no transformation at aerosol, SWIR-1, and SWIR-2 bands were 0.0045, 0.0171, and 0.0086, respectively with *p*-values < 0.001 indicating statistical significance. Meanwhile, the mean differences of the transformed TOA reflectance values of Sentinel-2 MSI sourced from the merged OLS model and the local OLS model with the TOA reflectance of OLI were lower than the mean difference resulting from Sentinel-2 TOA reflectance with no transformation.

Table 5.6. The mean differences of TOA reflectance of Sentinel-2 MSI and Landsat-8 OLI at aerosol, SWIR-1, and SWIR-2 bands. Total data (n) were compiled from three data sets representing study sites in Central Kalimantan and South Kalimantan (CK-SK), Jambi and South Sumatera (JSS), and Riau. *Resulted from T-test with significant different at p-values <0.001.

OLS Model	Site	Acquisition Date	n (pixel)	Mean of the differences of MSI – OLI		
				Aerosol Band	SWIR-1 Band	SWIR-2 Band
No-transformation	CK-SK JSS Riau	28 September 2018 21 August 2018 16 April 2019	58,716,843	0.004497*	0.017121*	0.008576*
Merged OLS model	CK-SK JSS Riau	28 September 2018 21 August 2018 16 April 2019	58,716,843	0.000047*	0.000015*	0.000027*
Local OLS model	CK-SK JSS Riau	28 September 2018 21 August 2018 16 April 2019	58,716,843	-0.006369*	0.000024*	0.000193*

5.4.3. Implementation and Comparison of ToPeCAl-2 Applied to Sentinel-2 MSI

As mentioned in Table 5.4 only four of the nine pairs of data sets were found with fire features on both Sentinel-2 and Landsat-8 images. ToPeCAl-2 with contextual test and ToPeCAl-2 with cloud masking were applied to more than 128 million pixels of Sentinel-2 MSI at 20 m spatial resolution. Figure 5.11a shows the performance of ToPeCAl-2 fires resultant from Sentinel-2 MSI compared with the ToPeCAl-1 fires of Landsat-8 OLI/TIRS. Based on the three OLS transformation models, the highest POD resulted from no transformation value for both ToPeCAl-2 with contextual test and ToPeCAl-2 with cloud mask. Overall, the POD of ToPeCAl-2 with cloud mask (88%) was higher than ToPeCAl-2 with contextual test (62%). However, ToPeCAl-2 with cloud mask showed a higher independent commission error (ICE) and a lower independent omission error (IOE) than ToPeCAl-2 with contextual test. The ICE of ToPeCAl-2 with cloud masking and contextual test from the no transformation model were 21% and 10%, while the IOE were 12% and 38%, respectively. Detailed statistical values can be found in Appendix-Table A5.4.

To distinguish the origin of classes of fire in ICE and IOE pixels, Figure 5.11b presents the ToPeCAl fires comparison shown in Figure 5.11a in the three peatland fires classes, i.e., flaming, mix of flaming and smouldering (FS) and smouldering. Flaming pixels were well detected (≥95%) in ToPeCAl-2 from either ToPeCAl-2 with contextual test or ToPeCAl-2 with cloud masking. About 76–78% of FS pixels from ToPeCAl-2 with contextual test agreed with ToPeCAl-1, while 86–97% of FS pixels were found from

ToPeCAl-2 with cloud masking. Smouldering pixels were less well-detected (32–56%) from both ToPeCAl-2 with highest detection from ToPeCAl-2 with cloud masking (56%). The ICE shows the highest error percentage in flaming or FS pixel, while IOE was high in smouldering pixel. Detail statistical values can be found in Appendix-Table A5.5.

In general, Figure 5.11 shows a lower smouldering pixel detection and a higher FS or flaming detection from ToPeCAl-2. ToPeCAl-2 with cloud masking showed a higher peatland fire detection for overall fires, but with higher false positive pixels in FS or flaming fire and lower false negative pixels in smouldering fire. Whilst ToPeCAl-2 with contextual test was likely to have lower false positive pixels in FS fire but, higher false negative in smouldering fire.

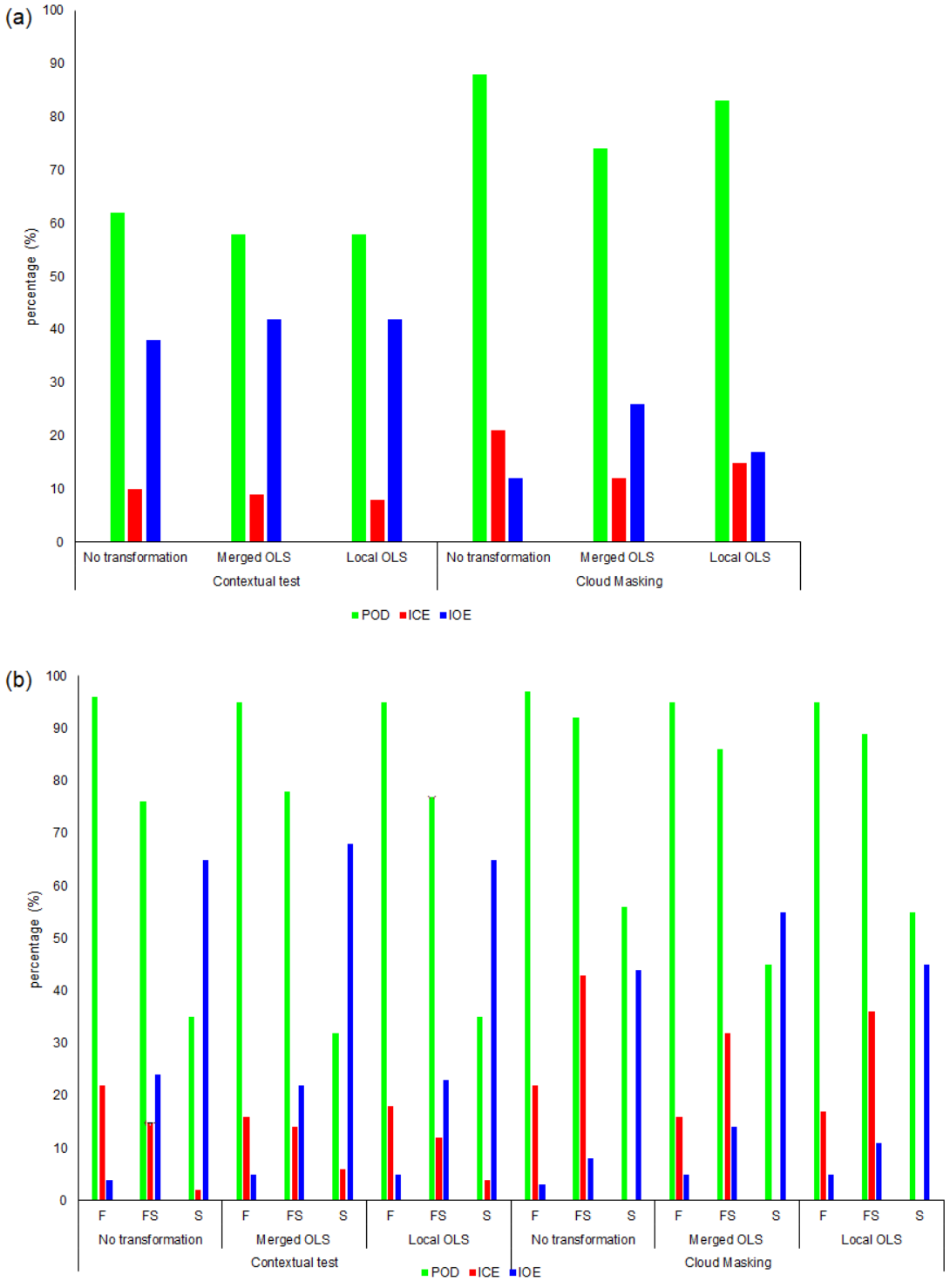


Figure 5.11. (**a**) Percentage of probability of detection (POD), independent commission errors (ICE) and independent omission errors (IOE) of ToPeCAl-2 with contextual test and ToPeCAl-2 with cloud masking applied to Sentinel-2 images compared with fires resultant from ToPeCAl-1 applied to Landsat-8 images; (**b**) As per Figure (**a**) but showing the comparison of fire classes, i.e., flaming (F), smouldering (S), and mix of flaming and smouldering (FS). The Top of Atmosphere (TOA) reflectance used in ToPeCAl-2 were with no transformation values and with transformation values from the merged Ordinary least squares (OLS) model and local OLS model.

Figure 5.12 shows an example of the comparison of ToPeCAl-2 fires resulted from Sentinel-2 image with ToPeCAl-1 fires resulted from Landsat-8 image in Central Kalimantan. The Sentinel-2 image was acquired nine minutes before the Landsat-8 image. The RGB composite of SWIR-2, SWIR-1 and Red bands was applied to Landsat-8 image (Figure 5.12a) and to the Sentinel-2 image (Figure 5.12b) to enhance the fire features under heavy smoke conditions; fires cannot be seen in the natural RGB composite as shown in Figure 5.12c. Figure 5.12d,e show fires resultant from ToPeCAl-2 with contextual test and ToPeCAl-2 with could masking applied to Sentinel-2 image, respectively. True positive (TP) fire pixels are shown in red colour in most of the fire areas. A boundary of spatially related-false positive fires (RFP) is shown in black bordered squares and spatially related-false negative fires (RFN) in cyan bordered squares shown adjacent to the true positive fires. Some of these RFP/RFN were within the distance of the geometric error from both Sentinel-2 and Landsat-8 and within the boundary of peatland fires propagation which was based on estimates from the previous research (Atwood et al. 2016) at 1.3 m/min horizontally. These RFP and RFN pixels were counted as the true positive pixels. In Figure 5.12d, some ToPeCAl-2 fires with contextual test remained as false negative (FN) pixels in blue colour while from ToPeCAl-2 with cloud masking some of these FN pixels were classified as true positive pixels (red colour) in Figure 5.12e. An enlargement of fires area which classified as FN from ToPeCAl-2 with contextual test and TP from ToPeCAl-2 with cloud masking is presented in the PlanetScope image with natural colour composite (Figure 5.12f) on the same day with Sentinel-2 and Landsat-8. PlanetScope images have a higher spatial resolution (3.7 m) than Sentinel-2 but SWIR is not available in PlanetScope. However, it can show smoke as an indication of fires, as illustrated in Figure 5.12f.

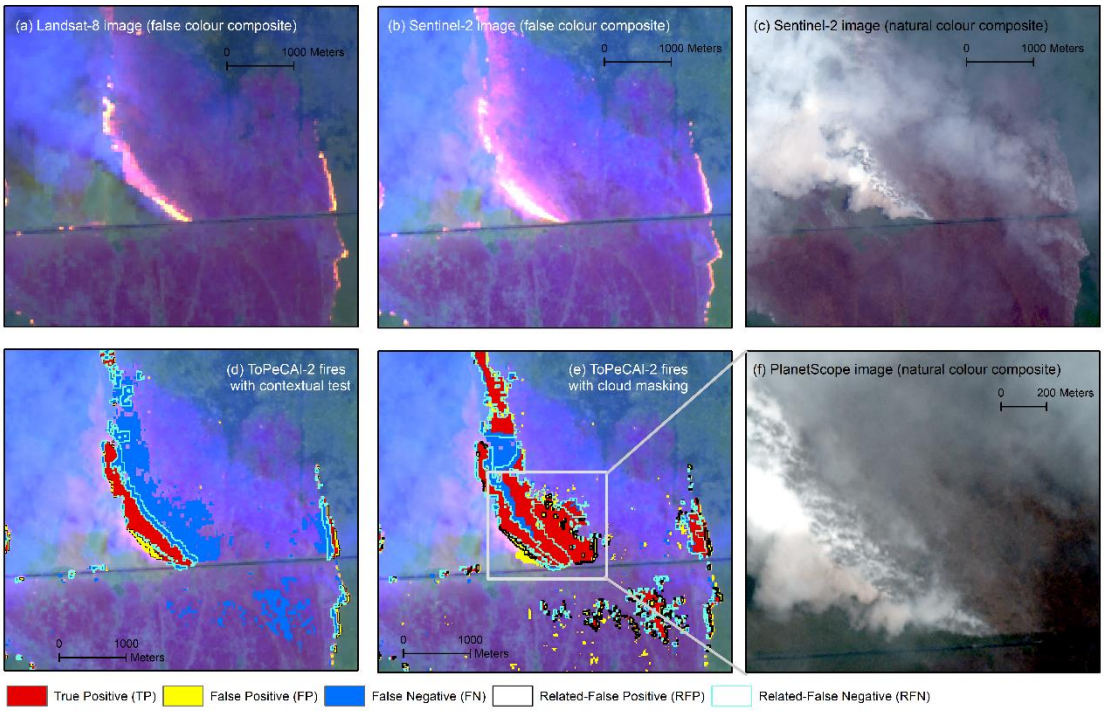


Figure 5.12. (**a**) RGB image of Landsat-8 with SWIR-2 band as Red layer, SWIR-1 band as Green layer, and Red band as Blue layer. Landsat-8 was acquired on 28 September 2018 at 2:34 Universal Time Coordinated (UTC) over Central Kalimantan's peatland; the dark straight line below the fires features (light yellow) is a river canal; green is vegetation and reddish purple is burnt area; (**b**) The same RGB composite image with Figure (**a**), but for Sentinel-2, which was acquired nine minutes before Landsat-8; (**c**) Natural RGB composite of Sentinel-2 on the same data with Figure (**b**); (**d**) Peatland fires from ToPeCAl-2 with contextual test applied to Sentinel-2 image compared with ToPeCAl-1 fires from Landsat-8 overlaid on RGB image of Sentinel-2; (**e**) the same with Figure (**d**) but from ToPeCAl-2 with cloud mask; (**f**) Natural composite of PlanetScope image on 28 September 2018 at 2:47 UTC showing smoke emanating from fire areas (white square) in Figure (**e**).

Another example in smaller peatland fires (about 104 ha) is presented in Figure 5.13. Peatland fires started with bluish smoke emanating from ground in the false colour composite of Sentinel-2 image (Figure 5.13a) and pixels detected as fire from ToPeCAl-2 with contextual test and ToPeCAl-2 with cloud masking in Figure 5.13b,c, respectively. The FN areas (blue colour) in Figure 5.13b,c correspond to the dark area with smoke shown by PlanetScope image on Figure 5.13d. The PlanetScope image was acquired three minutes after Sentinel-2 acquisition. Some smoke emanates from dark burning peatland and is one of the characteristics of smouldering peatlands which were observed in the field. The RFP and RFN fire pixels showed adjacent to TP areas resultant from ToPeCAl-2 corresponded to smoke features from the ground in PlanetScope image (Figure 5.13d). The RFN/RFP pixels adjacent to TP fires were classified as FS and smouldering pixels from ToPeCAl-1 of Landsat-8. The FS and smouldering pixels surrounding unambiguous

fire pixels were found by (Usup et al. 2004) in their field experiment in Central Kalimantan's peatland. Peatland fires (smouldering or FS fires) were found at 20–30 m distance surrounding the front line of the burning area due to lateral propagation of smouldering fires at <20 cm depth as described in Figure 5.13e. This scheme for peatland fires propagation supports the results of ToPeCAl fires detection.

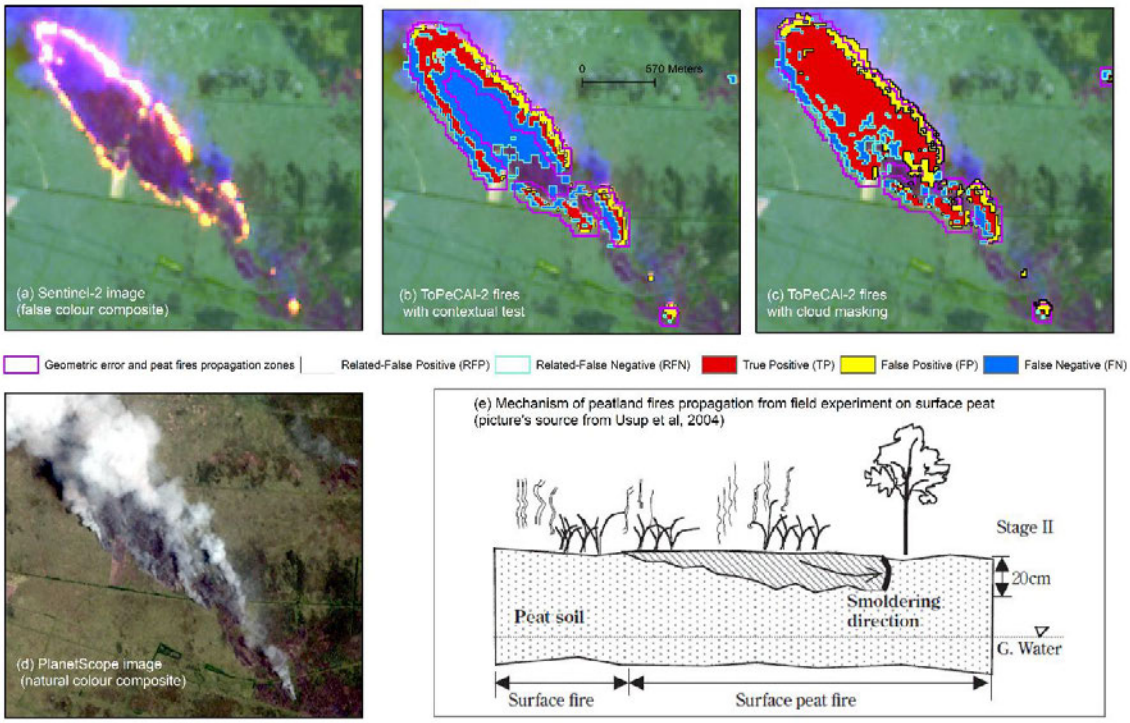


Figure 5.93. **(a)** Peatland fire areas (±104 ha) presented in false colour composite for Sentinel-2 image on 28 September 2018 in Central Kalimantan. Light pink to yellow represented fire areas with bluish smoke emanating from fire areas; **(b)** ToPeCAl-2 fires with contextual test overlaid on RGB image of Sentinel-2 in the same area with Figure (a). The RFP and RFN pixels are adjacent to TP fires (red colour). In this data pairs of Sentinel-2 and Landsat-8, the RFP and RFN pixels were within geometric error (38 m) and propagation zones (12 m) which about 50 m from TP pixels (magenta square line); **(c)** As per Figure (b) but from ToPeCAl-2 with cloud mask; **(d)** PlanetScope image in natural colour composite showed smoke emanating from fires areas from in the same area and in three minutes after Sentinel-2's acquisition; **(e)** Surface peatland fires propagation in lateral (horizontal) direction according to (Usup et al. 2004) from field experiment in Central Kalimantan's peatland after ignition and during surface burning in the first stage; the propagation were also in depth spread in the next stage.

5.5. Discussion

5.5.1. Comparison and Adjustment of ToPeCAl-2 to Landsat-8 OLI

The comparison and adjustment of ToPeCAl without TIR (ToPeCAl-2) was conducted in order to explore the potential of this algorithm for the detection of tropical peatland fires using Sentinel-2 MSI data. An initial test was accomplished by

implementing ToPeCAl-2 compared with ToPeCAl-1 on the same source of Landsat-8 data. In this study, ground truth to validate the ToPeCAl-2 fires performance were not conducted; however, ToPeCAl-1 was validated by ground truth data and provided 82% accuracy which can be improved by removing permanent bright objects (Sofan et al. 2019). Although ToPeCAl-1 has SWIR and TIR to support peatland fire mapping, the spatial resolution of TIR in Landsat-8 is quite low to observe small peatland fires, often in mixed pixels which contain heterogeneous objects. However, smouldering pixels resultant from ToPeCAl-1, which are located adjacent to or surrounding unambiguous fire, may be considered as the true smouldering peatland. Smouldering is a very persistent type of combustion, which is relatively easy to commence and difficult to suppress [7] and its residual can last for days after flaming fires pass over (Santoso et al. 2019). Smouldering and flaming peatland fires can lead to one other, however, when the oxygen supply increases, as occurs with an increase in wind velocity, combustion becomes faster, temperature increases and a flaming state may eventuate (Rein 2013; 2016). Other than that, from field experiment, (Usup et al. 2004) found that smouldering peatlands were found in surrounding or adjacent un-slashed areas to the burning peatland. The information gained from laboratory and field experiments (Barsi et al. 2018; Caiazzo et al. 2014; Rein 2013; 2016) for peatland fire characteristics support the interpretation of peatland fires resultant from satellite.

In addition, for confirming of ToPeCAl-2 fire detections, some verification occurred by observing the state of smoke emanating from fire areas which are shown in natural RGB images from PlanetScope on the same day with Landsat-8/Sentinel-2 as shown in Figure 5.10, 5.12 and 5.13. However, some of the smouldering or FS pixels detected by ToPeCAL-2 were difficult to be verified using specific smoke features in a generally smoky atmosphere, which can influence the quality of radiometry of PlanetScope RGB images. Further investigation on the radiometry of smoke features can potentially support the validation of ToPeCAl-2 for mapping peatland fires.

In this study, the adjustments of ToPeCAl were performed by adding a pre-processing for water masking, permanent bright object masking and performing some filtering methods on ToPeCAl-2 results, i.e., contextual test and cloud masking. ToPeCAl-2 with contextual test examining FS and smouldering fire pixels was compared to their background statistics using mean and standard deviation in 61×61 pixel window. In this contextual test, high confidence fire pixels were adopted from previous literature

(Giglio et al. 2008; Kumar & Roy 2018; Schroeder et al. 2016) by using statistical values of mean+3σ or 99.7% of confidence level for active fire detection. The fire pixels that passed this contextual test were highly likely to be active fire or flaming fire. Peatland fires particularly smouldering fire has lower combustion power and low temperature which is significantly different with flaming fires. A lower confidence level, e.g., 95% (mean+2σ) or 68% (mean+σ) for the background statistic can be tested to cover low confidence fires such as smouldering peatland fires. However, ToPeCAl-2 depends only on SWIR for detecting peatland fires, thus it may be possible to generate more false positive smouldering pixels by lowering the confidence level, for example, in burnt areas. Additional analysis such as smoke detection and analysis for smouldering peatland can be added to confirm smouldering fire pixels. In this study, ToPeCAl-2 with contextual test applied to Landsat-8 OLI provided low detection (55%) of fires compared with ToPeCAl-1 fires. From the results comparison using peatland fires types derived from ToPeCAl-1, the missed detection of ToPeCAl-2 with contextual test was for smouldering fire at about 45%. Flaming and FS fire pixels were well detected by ToPeCAl-2 with contextual test (≥93%).

A second approach was conducted by implementing cloud mask to ToPeCAl-2 fires. Initial assessment of ToPeCAl-2 fires compared with RGB image of Landsat-8 using visual analysis showed that false positive pixels occurred in cloud and at the edge of cloud. These false positive pixels were from FS and smouldering fire pixels detected by ToPeCAl-2. Thus, the cloud mask was only applied to FS and smouldering pixels, while unambiguous fire pixels (flaming and close to saturated flaming) were classified as true fire pixels. Dense cloud with highly reflective aerosols tends to brighten the cloud (NASA 2010) which might be classified as false detection in ToPeCAl-2. The uncertainty in observation on the edge of cloud is commonly termed “cloud adjacency effects” or “3-D radiative effects”. These can increase the reflectance around the edge of cloud with an increase of aerosol properties (Spencer et al. 2019; Várnai & Marshak 2014; Wen et al. 2007). The cloud adjacency effect has also exhibited as a problem in other optical remote sensing applications, e.g., ocean monitoring (Feng & Hu 2016) and atmospheric monitoring (Spencer et al. 2019; Wen et al. 2007). The results of ToPeCAl-2 with cloud mask provided higher percentage of peatland fire detection (98%) because only FS and smouldering pixels occurring in cloud areas were removed as fire pixels. Lower counts of false positive and false negative pixel resulted from this model. Most of FS and

smouldering pixels that passed cloud masking were located in areas surrounding true positive fire pixels. However, the smouldering pixels resultant from ToPeCAl-2 may include false positive pixels in burnt areas as they have similar SWIR reflectance as shown in Figure 5.5.

Although most permanent bright objects pixels were excluded in ToPeCAl-2 by implementing bright object masking, it is still possible to have some of them generate false positive pixels in ToPeCAl-2′s results. Undetected bright objects were potentially due to the mixture of reflectance with other dominant objects (e.g., soil and vegetation in one-pixel area) and some of the rooftops had lower SWIR reflectance than the threshold used (<0.18). Most of the mining areas identified as false positive pixels also exhibited mixed reflectance with some dark soils, thus resulting in lower reflectance than the threshold for bright object masking. Some miss-detection of mining areas was possible due to their typical landscape which often consists of open-cut quarries which generate deep shadows leading to a decrease in reflectance. However, the state of the particular mining landscapes in this research requires further checking with very high spatial resolution data (for example Geo-eye, World-View 4 or SkySat). The removal of false positives related to mining areas and industrial gas flares can also be assisted via the use of other data sources, such as the record of location of registered mining areas and industrial gas flares from government agencies.

5.5.2. Relationships between TOA Reflectance of Sentinel-2 and Landsat-8 at Aerosol and SWIR bands

There was a significant difference of the mean values between TOA reflectance of Sentinel-2 and Landsat-8 at aerosol, SWIR-1, and SWIR-2 bands in the study areas. The mean differences of TOA reflectance from the two sensors at SWIR bands found in this study were slightly higher than the mean difference resulting from previous research in the Conterminous United States and southern Africa (Chastain et al. 2019; Zhang et al. 2018). There was a lack of consistent relationship found in aerosol band which was also reflected at SWIR-1 and SWIR-2 bands. Conversely, good relationships of TOA reflectance at SWIR-1 and SWIR-2 bands were associated with a good relationship at aerosol band at other locations and times. The data resampling from lower to higher spatial resolution applied to aerosol band of Sentinel-2 and Landsat-8 could possibly influence the poorer relationship between both sensors at the aerosol band. Moreover, in

this study sensor to sensor relationship analysis was conducted based on a linear empirical model, whereas the pre-launch relative spectral response of Landsat-8 and Sentinel-2, at mid spatial resolution, particularly in the aerosol band (Figure 5.8), shows obvious sensitivity differences of signal across the wavelength range. The atmospheric conditions, e.g., moist or dry, also influence the spectral response of SWIR (Barsi et al. 2014). The variability in coefficients from OLS modelling, suggests that corrections from TOA reflectance of Sentinel-2 to Landsat-8 should not be applied in ToPeCAl, as the modelling exhibits too much uncertainty. However, the subtle differences in band sensitivities between Sentinel-2 and Landsat-8 might be significant for other applications.

The atmospheric conditions in the tropics can be an important factor which influences the relationship of TOA reflectance between Sentinel-2 and Landsat-8, although the environments, season, and geographic location may also affect the relationships. Another aspect to consider is the cloud product of Sentinel-2 data which is generated from Sen2COR (Richter, Louis & Muller-Wilm 2012). This might generate uncertainty in providing a clear image due to a lack of thermal data that can impact the approach and efficacy of cloud masking (Baetens, Desjardins & Hagolle 2019; Zhu, Wang & Woodcock 2015), particularly in tropical atmospheres. The influence of terrestrial environments, such as vegetation types, seasons, and an improvement of cloud masking product in tropical environments can be investigated further for relating the TOA reflectance of Sentinel-2 and Landsat-8.

5.5.3. The Application of ToPeCAl-2 to Sentinel-2 Data

The results of ToPeCAl-2 were not sensitive to the effects of TOA reflectance correction from Sentinel-2 to Landsat-8. Thus, ToPeCAl-2 with no transformation value can be applied to Sentinel-2 MSI. General results for peatland fires pattern resultant from ToPeCAl-2 applied to Landsat-8 were also found in ToPeCAl-2 applied to Sentinel-2. ToPeCAl-2 applied to Sentinel-2 with cloud masking provided higher detection for overall peatland fires with POD of 88%, ICE of 21% and IOE of 12%. Meanwhile, ToPeCAl-2 with a contextual test provided lower POD (62%), but with lower ICE (10%) and higher IOE (38%). The results also showed that smouldering fires were less likely to be detected from ToPeCAl-2 applied to Sentinel-2 data, but flaming pixels were well detected. Although ToPeCAl-2 with cloud masking resulted lower IOE than ToPeCAl-2 with contextual test, especially for smouldering pixels, validation still needs to be

investigated for those smouldering pixels which may contain false detection in burnt areas. Meanwhile, the false positive pixels from ToPeCAL-2 might be the result from another fire at a different time of observation or un-detected bright object pixels. The POD values from the comparison of two fires produced from Sentinel-2 and Landsat-8 were presented in order to illustrate the strong similarity of fire pattern and the existence of fire for a certain time difference. Thus, they can be utilised together to fill temporal gaps in detailed fire spatial information.

The choice of using ToPeCAl-2 with contextual test or ToPeCAl-2 with cloud masking is dependent on the purpose for obtaining the peatland fires information. Users who are dealing with fire extinguishment may utilise ToPeCAl-2 fires from contextual test which provided high confidence of flaming detection. For users who work in peatland rehabilitation or carbon loss inventory from peatland fires, then the fire product from ToPeCAl-2 with cloud masking can be considered. However, smouldering resulting from ToPeCAl-2 especially from cloud-masked approach still needs further validation. One should also consider the advantages and the limitation of both ToPeCAl-2 models.

The application of ToPeCAl without TIR to Sentinel-2 MSI and relying on SWIR to detect fires in tropical peatland environments is possible, but may present with false positives related to bright objects and warm soil due to the contamination of sun radiation on SWIR reflectance during daytime. Smouldering peatlands can also be confirmed by observation of smoke over smouldering surfaces; a process which can be explored in further research. Overall, without MIR or TIR, ToPeCAl has a weaker detectability of smouldering peatland which is important for carbon emission estimations. This constraint introduces a future challenge to provide a sensor, or constellation of sensors incorporating MIR/TIR with similar, or better, temporal and spatial resolution specifications to Sentinel-2 to improve peatland fire monitoring; for example the Copernicus High Spatio-Temporal Resolution Land Surface Temperature Mission – LSTM mission which is planned by European Space Agency for future earth observation in 2025 (Koetz et al. 2019).

5.6. Conclusion

A new technique for peatland fires detection in tropical peatland environments has been established using Landsat-8 OLI and Sentinel-2 MSI data in this study. ToPeCAl-2 (ToPeCAl without TIR) applied to Sentinel-2 MSI generates reliable results for fire

detection at 20 m resolution especially for flaming and mix of flaming and smouldering with less smouldering detection. Furthermore, it can be combined with the use of ToPeCAl-1 to fill in the peatland fires information gaps at Landsat-8 spatial resolution (30 m) for tropical environment conditions, e.g., Indonesia. ToPeCAl-2 and ToPeCAl-1 has similar capability on detecting flaming fires (>95%) in tropical peatland environments. Smouldering peatlands detected by ToPeCAl-2 were only 35–56% correct, which still may include false detection in warm soil or burnt areas. ToPeCAl-2 with contextual test provides less detection of smouldering pixel than ToPeCAl-2 with cloud-masked approach. To further extend these smouldering results, especially from ToPeCAl with cloud-masked, requires further investigation and ground validation.

Adjustments to eliminate the false positive fires pixels were applied to ToPeCAl-2 to enhance its performance. It is important for tropical peatland fires management, with limited resources, to support a priority to extinguish actual biomass fires, which extend over large areas, rather than send resources to incorrectly identified fires.

In relating peatland fires products from Sentinel-2 and Landsat-8 at different times certain aspects were also examined, including the geometric errors between the two sensors, spectral response, and the propagation of fires between images captured at different times. The subtle differences in the spectral response of Landsat-8 and Sentinel-2 were less significant for fire detection, possibly due to specific local atmospheric conditions which can interfere with TOA reflectance in tropical environments.

There is a high potential to apply ToPeCAl-2 to Sentinel-2 MSI for operational peatland fires monitoring especially for flaming conditions, together with ToPeCAl-1 applied to Landsat-8 OLI/TIRS, leading to a higher temporal monitoring frequency than currently available from a single sensor alone. An integration with lower spatial resolution fire products from VIIRS 375 m data will also complement peatland fires monitoring on daily basis.

References

Alsepan, G & Minobe, S 2020, 'Relations between Interannual Variability of Regional-Scale Indonesian Precipitation and Large-Scale Climate Modes during 1960–2007', *Journal of Climate,* vol. 33, no. 12, pp. 5271–5291.

Atwood, E, Englhart, S, Lorenz, E, Halle, W, Wiedemann, W & Siegert, F 2016, 'Detection and characterization of low temperature peat fires during the 2015 fire catastrophe in Indonesia using a new high-sensitivity fire monitoring satellite sensor (FireBird)', *PLoS ONE*, vol. 11, no. 8, pp. 1-24, doi:10.1371/journal.pone.0159410.

Baetens, L, Desjardins, C & Hagolle, O 2019, 'Validation of Copernicus Sentinel-2 Cloud Masks Obtained from MAJA, Sen2Cor, and FMask Processors Using Reference Cloud Masks Generated with a Supervised Active Learning Procedure', *Remote Sensing*, vol. 11, no. 433, doi:10.3390/rs11040433.

Barsi, J, Lee, K, Kvaran, G, Markham, B & Pedelty, J 2014, 'The Spectral Response of the Landsat-8 Operational Land Imager', *Remote Sensing*, vol. 6, no. 10, pp. 10232–10251, doi:10.3390/rs61010232.

Barsi, JA, Alhammoud, B, Czapla-Myers, J, Gascon, F, Haque, MO, Kaewmanee, M, Leigh, L & Markham, BL 2018, 'Sentinel-2A MSI and Landsat-8 OLI radiometric cross comparison over desert sites', *European Journal of Remote Sensing*, vol. 51, no. 1, pp. 822–837.

Boer, R, Dewi, RG, Ardiansyah, M & Siagian, UW 2018, *Indonesia Second Biennial Update Report, Under the United Nations Framework Convention on Climate Change*, Directorate General of Climate Change, Ministry of Environment and Forestry, Jakarta, Indonesia.
<http://ditjenppi.menlhk.go.id/reddplus/images/adminppi/dokumen/Indonesia-2nd_BUR_web.pdf>.

Bowen, MR, Bompard, JM, Anderson, IP, Guizol, P & Gouyon, A 2000, 'Anthropogenic fires in Indonesia: a view from Sumatra', in P Eaton, and M. Radojevic (ed), *Forest Fires and Regional Haze in Southeast Asia*, Nova Science, New York, pp. 41–66.

Burke, C, Wich, S, Kusin, K, McAree, O, Harrison, ME, Ripoll, B, Ermiasi, Y, Mulero-Pázmány, M & Longmore, S 2019, 'Thermal-Drones as a Safe and Reliable Method for Detecting Subterranean Peat Fires', *Drones*, vol. 3, no. 1, p. 23.

Caiazzo, F, Malina, R, Staples, MD, Wolfe, PJ, Yim, SHL & Barrett, SRH 2014, 'Quantifying the climate impacts of albedo changes due to biofuel production: a comparison with biogeochemical effects', *Environmental Research Letters*, vol. 9, no. 2, p. 024015.

Carlson, KM, Goodman, LK & May-Tobin, CC 2015, 'Modeling relationships between water table depth and peat soil carbon loss in Southeast Asian plantations', *Environmental Research Letters*, vol. 10, no. 7, p. 074006.

Chastain, R, Housman, I, Goldstein, J, Finco, M & Tenneson, K 2019, 'Empirical cross sensor comparison of Sentinel-2A and 2B MSI, Landsat-8 OLI, and Landsat-7 ETM+ top of atmosphere spectral characteristics over the conterminous United States', *Remote Sensing of Environment*, vol. 221, pp. 274–285, doi: 10.1016/j.rse.2018.11.012.

Climate Prediction Center-National Oceanic Atmosphere Administration (CPC-NOAA) 2000, *Cold & Warm Episodes by Season*, viewed 1 July 2020, <https://origin.cpc.ncep.noaa.gov/products/analysis_monitoring/ensostuff/ONI_v5.php>

Dennis, RA, Mayer, J, Applegate, G, Chokkalingam, U, Colfer, CJP, Kurniawan, I, Lachowski, H, Maus, P, Permana, RP, Ruchiat, Y, Stolle, F, Suyanto & Tomich, TP 2005, 'Fire, People and Pixels: Linking Social Science and Remote Sensing to Understand Underlying Causes and Impacts of Fires in Indonesia', *Human Ecology*, vol. 33, no. 4, pp. 465–504, doi: 10.1007/s10745-005-5156-z.

Drusch, M, Del Bello, U, Carlier, S, Colin, O, Fernandez, V, Gascon, F, Hoersch, B, Isola, C, Laberinti, P, Martimort, P, Meygret, A, Spoto, F, Sy, O, Marchese, F & Bargellini, P 2012, 'Sentinel-2: ESA's Optical High-Resolution Mission for GMES Operational Services', *Remote Sensing of Environment*, vol. 120, pp. 25–36, doi: 10.1016/j.rse.2011.11.026.

Du, Y, Zhang, Y, Ling, F, Wang, Q, Li, W & Li, X 2016, 'Water Bodies' Mapping from Sentinel-2 Imagery with Modified Normalized Difference Water Index at 10-m Spatial Resolution Produced by Sharpening the SWIR Band', *Remote Sensing*, vol. 8, no. 4, p. 354.

Elvidge, CD, Zhizhin, M, Hsu, F-C & Baugh, K 2013, 'VIIRS Nightfire: Satellite Pyrometry at Night', *Remote Sensing*, vol. 5, no. 9, p. 4423, doi:10.3390/rs5094423.

Elvidge, CD, Zhizhin, M, Hsu, F, Baugh, K, Khomarudin, M, Vetrita, Y, Sofan, P, Suwarsono & Hilman, D 2015, 'Long-wave infrared identification of smoldering peat fires in indonesia with nighttime landsat data', *Environmental Research Letters*, vol. 10, no. 6, p. 065002, doi:10.1088/1748-9326/10/6/065002.

ESA 2017, *Sentinel-2 Spectral Response Functions (S2-SRF) COPE-GSEG-EOPG-TN-15-0007*, European Space Agency, viewed 5 May 2020, <https://earth.esa.int/web/sentinel/user-guides/sentinel-2-msi/document-library/-/asset_publisher/Wk0TKajiISaR/content/sentinel-2a-spectral-responses>.

Feng, L & Hu, C 2016, 'Cloud adjacency effects on top-of-atmosphere radiance and ocean color data products: A statistical assessment', *Remote Sensing of Environment*, vol. 174, pp. 301–313, doi: 10.1016/j.rse.2015.12.020.

Fiona, N, Kudzai Shaun, M, Blessing, K, Henry, N & Monalisa Shingirayi, M 2020, 'Exploring the utility of Sentinel-2 MSI and Landsat 8 OLI in burned area mapping for a heterogenous savannah landscape', *PLoS ONE*, vol. 15, no. 5, p. e0232962.

Flood, N 2017, 'Comparing Sentinel-2A and Landsat 7 and 8 Using Surface Reflectance over Australia', vol. 9, no. 7, p. 659, doi:10.3390/rs9070659.

García-Llamas, P, Suárez-Seoane, S, Fernández-Guisuraga, JM, Fernández-García, V, Fernández-Manso, A, Quintano, C, Taboada, A, Marcos, E & Calvo, L 2019, 'Evaluation and comparison of Landsat 8, Sentinel-2 and Deimos-1 remote sensing indices for assessing burn severity in Mediterranean fire-prone ecosystems', *International Journal of Applied Earth Observation and Geoinformation*, vol. 80, pp. 137–144.

Giglio, L, Csiszar, I, Restás, Á, Morisette, JT, Schroeder, W, Morton, D & Justice, CO 2008, 'Active fire detection and characterization with the advanced spaceborne thermal emission and reflection radiometer (ASTER)', *Remote Sensing of Environment*, vol. 112, no. 6, pp. 3055–3063, doi:10.1016/j.rse.2008.03.003.

Global Fire Data 2000, *Global Fire Emissions Database*, viewed 1 July 2020, <http://globalfiredata.org/pages/data/>.

Gorelick, N, Hancher, M, Dixon, M, Ilyushchenko, S, Thau, D & Moore, R 2017, 'Google Earth Engine: Planetary-scale geospatial analysis for everyone', *Remote Sensing of Environment*, vol. 202, pp. 18–27, doi: 10.1016/j.rse.2017.06.031.

Hayasaka, H, Takahashi, H, Limin, SH, Yulianti, N & Usup, A 2016, 'Peat Fire Occurrence', in M Osaki & N Tsuji (eds), *Tropical Peatland Ecosystems*, Springer Japan, Tokyo, pp. 377–395.

Hooijer, A, Silvius, M, Wosten, H & Page, S 2006, *PEAT-CO2, Assessment of CO2 emissions from drained peatlands in SE Asia*, Delft Hydraulics report Q3943: Netherlands, p. 41.

Huijnen, V, Wooster, MJ, Kaiser, JW, Gaveau, DLA, Flemming, J, Parrington, M, Inness, A, Murdiyarso, D, Main, B & van Weele, M 2016, 'Fire carbon emissions over maritime southeast Asia in 2015 largest since 1997', *Scientific Reports*, vol. 6, no. 1, p. 26886.

Irons, JR, Dwyer, JL & Barsi, JA 2012, 'The next Landsat satellite: The Landsat Data Continuity Mission', *Remote Sensing of Environment*, vol. 122, pp. 11–21, doi: 10.1016/j.rse.2011.08.02.

Joosten, H & Clarke, D 2002, *Wise use of mires and peatlands*, International Mire Conservation Group and International Peat Society, Finland.

Kobayashi, S, Segah, H & Momota, E 2016, *Local Community Safeguard by REDDC and Payment for Ecosystem Services (PES) in Peatland*, Springer, Tokyo.

Koetz, B, Berger, M, Blommaert, J, Bello, UD, Drusch, M, Duca, R, Gascon, F, Ghent, D, Hoogeveen, J, Hook, S, Kerr, Y, Lagouarde, J-P, Manolos, I, Marini, A, Menenti, M, Martimort, P, Masek, J, Massart, M, Notarnicola, C, Sallusti, M, Sandholt, I, Schuettemeyer, D, Sobrino, J, Strobl, P, Volden, E & Udelhofen, T 2019, *Copernicus High SPatio-Temporal Resolution Land Surface Temperature Mission: Mission Requirements Document*, ESA, Noorwijk, The Netherlands.

Kumar, SS & Roy, DP 2018, 'Global operational land imager Landsat-8 reflectance-based active fire detection algorithm', *International Journal of Digital Earth*, vol. 11, no. 2, pp. 154–178, doi: 10.1080/17538947.2017.1391341.

Loveland, TR & Irons, JR 2016, 'Landsat 8: The plans, the reality, and the legacy', *Remote Sensing of Environment*, vol. 185, pp. 1–6, doi: 10.1016/j.rse.2016.07.033.

Mandanici, E & Bitelli, G 2016, 'Preliminary Comparison of Sentinel-2 and Landsat 8 Imagery for a Combined Use', vol. 8, no. 12, p. 1014.

Miettinen, J & Liew, SC 2005, 'Connection between fire and land cover change in Southeast Asia: a remote sensing case study in Riau, Sumatra', *International Journal of Remote Sensing*, vol. 26, no. 6, pp. 1109–1126, doi: 10.1080/01431160512331326756.

Murdiyarso, D, Lilleskov, E & Kolka, R 2019, 'Tropical peatlands under siege: the need for evidence-based policies and strategies', *Mitigation and Adaptation Strategies for Global Change*, vol. 24, no. 4, pp. 493–505.

Murphy, SW, de Souza Filho, CR, Wright, R, Sabatino, G & Correa Pabon, R 2016, 'HOTMAP: Global hot target detection at moderate spatial resolution', *Remote Sensing of Environment*, vol. 177, pp. 78–88, doi:10.1016/j.rse.2016.02.027.

NASA 2010, *Aerosols and Clouds (Indirect Effects)*, Earth Observatory, NASA, viewed 4 September 2020, <https://earthobservatory.nasa.gov/features/Aerosols/page4.php>.

Page, SE, Rieley, J & Banks, C 2011, 'Global and regional importance of the tropical peatland carbon pool', *Global Change Biology*, vol. 17, no. 2, pp. 798–818.

Page, SE & Baird, AJ 2016, 'Peatlands and Global Change: Response and Resilience', *Annual Review of Environment and Resources*, vol. 41, pp. 35–57.

Pan, X, Chin, M, Ichoku, CM & Field, RD 2018, 'Connecting Indonesian Fires and Drought With the Type of El Niño and Phase of the Indian Ocean Dipole During 1979–2016', vol. 123, no. 15, pp. 7974–7988.

Parish, F, Sirin, A, Charman, D, Joosten, H, Minayeva, T & Silvius, M 2008, 'Assessment of Peatlands, Biodiversity, and Climate Change', *National Wetlands Newsletter*, vol. 30, no. 1, pp. 13–17.

Physical Sciences Laboratory, National Oceanic and Atmospheric Administration 2000, *Dipole Mode Index*, viewed 14 September 2020 <https://psl.noaa.gov/gcos_wgsp/Timeseries/DMI/>.

Purnomo, H, Shantiko, B, Sitorus, S, Gunawan, H, Achdiawan, R, Kartodihardjo, H & Dewayani, AA 2017, 'Fire economy and actor network of forest and land fires in Indonesia', *Forest Policy and Economics*, vol. 78, pp. 21–31, doi: 10.1016/j.forpol.2017.01.001.

Quintano, C, Fernández-Manso, A & Fernández-Manso, O 2018, 'Combination of Landsat and Sentinel-2 MSI data for initial assessing of burn severity', *International Journal of Applied Earth Observation and Geoinformation*, vol. 64, pp. 221–225.

Rein, G 2013, 'Smouldering fires and natural fuels', *Fire Phenomena and the Earth System: An Interdisciplinary Guide to Fire Science*, vol. Chapter 2, pp. 13–22.

Rein, G 2016, 'Smoldering Combustion', in MJ Hurley et al (eds), *SFPE Handbook of Fire Protection Engineering*, Springer New York, New York, NY, pp. 581–603.

Richter, R, Louis, J & Muller-Wilm, U 2012, *Sentinel-2 MSI – Level 2A Products Algorithm Theoretical Basis Document*, Telespazio VEGA Deutschland GmbH, Darmstadt, Germany.

Rieley, J & Page, S 2016, 'Tropical Peatland of the World', in M Osaki & N Tsuji (eds), *Tropical peatland ecosystems*, Springer, Tokyo, pp. 3–32.

Roy, DP, Huang, H, Boschetti, L, Giglio, L, Yan, L, Zhang, HH & Li, Z 2019, 'Landsat-8 and Sentinel-2 burned area mapping - A combined sensor multi-temporal change detection approach', *Remote Sensing of Environment*, vol. 231, p. 111254, doi: 10.1016/j.rse.2019.111254.

Rydin, H & Jeglum, JK 2006, *The Biology of Peatlands*, Oxford University Press, UK, Oxford.

Santoso, MA, Huang, X, Prat-Guitart, N, Christensen, E, Hu, Y & Rein, G 2019, 'Smouldering fires and soils', in P Pereira et al (eds), *Fire Effects on Soil Properties*, CSIRO Publishing, Victoria, Australia, p. 382.

Schroeder, W, Oliva, P, Giglio, L, Quayle, B, Lorenz, E & Morelli, F 2016, 'Active fire detection using Landsat-8/OLI data', *Remote Sensing of Environment*, vol. 185, pp. 210–220, doi:10.1016/j.rse.2015.08.032.

Shang, R & Zhu, Z 2019, 'Harmonizing Landsat 8 and Sentinel-2: A time-series-based reflectance adjustment approach', *Remote Sensing of Environment*, vol. 235, p. 111439.

Siegert, F, Zhukov, B, Oertel, D, Limin, S, Page, SE & Rieley, JO 2004, 'Peat fires detected by the BIRD satellite', *International Journal of Remote Sensing*, vol. 25, no. 16, pp. 3221-3230, doi: 10.1080/01431160310001642377.

Sofan, P, Bruce, D, Jones, E & Marsden, J 2019, 'Detection and Validation of Tropical Peatland Flaming and Smouldering Using Landsat-8 SWIR and TIRS Bands', *Remote Sensing*, vol. 11, no. 4, p. 465, doi:10.3390/rs11040465.

Sofan, P, Bruce, D, Schroeder, W, Jones, E & Marsden, J 2020, 'Assessment of VIIRS 375 m active fire using tropical peatland combustion algorithm applied to Landsat-8 over Indonesia's peatland', *International Journal of Digital Earth*, doi: 10.1080/17538947.2020.1791268.

Spencer, RS, Levy, RC, Remer, LA, Mattoo, S, Arnold, GT, Hlavka, DL, Meyer, KG, Marshak, A, Wilcox, EM & Platnick, SE 2019, 'Exploring Aerosols Near Clouds With High-Spatial-Resolution Aircraft Remote Sensing During SEAC4RS', *Journal of Geophysical Research: Atmospheres*, vol. 124, no. 4, pp. 2148–2173, doi: 10.1029/2018JD028989.

Stockwell, CE, Jayarathne, T, Cochrane, MA, Ryan, KC, Putra, EI, Saharjo, BH, Nurhayati, AD, Albar, I, Blake, DR, Simpson, IJ, Stone, EA & Yokelson, RJ 2016, 'Field measurements of trace gases and aerosols emitted by peat fires in Central Kalimantan, Indonesia, during the 2015 El Niño', *Atmos. Chem. Phys.*, vol. 16, no. 18, pp. 11711–11732.

Storey, J, Roy, DP, Masek, J, Gascon, F, Dwyer, J & Choate, M 2016, 'A note on the temporary misregistration of Landsat-8 Operational Land Imager (OLI) and Sentinel-2 Multi Spectral Instrument (MSI) imagery', *Remote Sensing of Environment*, vol. 186, pp. 121–122, doi: 10.1016/j.rse.2016.08.025.

Sun, L, Mi, X, Wei, J, Wang, J, Tian, X, Yu, H & Gan, P 2017, 'A cloud detection algorithm-generating method for remote sensing data at visible to short-wave infrared wavelengths', *ISPRS Journal of Photogrammetry and Remote Sensing*, vol. 124, pp. 70–88.

Suyanto, S, Applegate, G, Permana, R, Khususiyah, N & Kurniawan, I 2004, 'The Role of Fire in Changing Land Use and Livelihoods in Riau-Sumatra', *Ecology and Society*, vol. 9, no. 1, pp. 15–15.

Usup, A, Hashimoto, Y, Takashi, H & Hayasaka, H 2004, 'Combustion and thermal characteristics of peat fire in tropical peatland in Central Kalimantan, Indonesia', *Tropics*, vol. 14, no. 1, pp. 1–19.

Várnai, T & Marshak, A 2014, 'Near-cloud aerosol properties from the 1 km resolution MODIS ocean product', *Journal of Geophysical Research: Atmospheres*, vol. 119, no. 3, pp. 1546–1554, doi:10.1002/2013JD020633.

Wen, G, Marshak, A, Cahalan, RF, Remer, LA & Kleidman, RG 2007, '3-D aerosol-cloud radiative interaction observed in collocated MODIS and ASTER images of cumulus cloud fields', *Journal of Geophysical Research: Atmospheres*, vol. 112, no. D13204, doi:10.1029/2006JD008267.

Wooster, MJ, Roberts, G, Smith, AMS, Johnston, J, Freeborn, P, Amici, S & Hudak, AT 2013, 'Thermal Remote Sensing of Active Vegetation Fires and Biomass Burning Events', in C Kuenzer & S Dech (eds), *Thermal Infrared Remote Sensing: Sensors, Methods, Applications*, Springer Netherlands, Dordrecht, pp. 347–390.

Xi, Y, Thinh, NX & Li, C 2019, 'Preliminary comparative assessment of various spectral indices for built-up land derived from Landsat-8 OLI and Sentinel-2A MSI imageries', *European Journal of Remote Sensing*, vol. 52, no. 1, pp. 240–252.

Zhang, HK, Roy, DP, Yan, L, Li, Z, Huang, H, Vermote, E, Skakun, S & Roger, J-C 2018, 'Characterization of Sentinel-2A and Landsat-8 top of atmosphere, surface, and nadir BRDF adjusted reflectance and NDVI differences', *Remote Sensing of Environment*, vol. 215, pp. 482–494, doi: 10.1016/j.rse.2018.04.031.

Zhu, Z, Wang, S & Woodcock, CE 2015, 'Improvement and expansion of the Fmask algorithm: cloud, cloud shadow, and snow detection for Landsats 4–7, 8, and Sentinel 2 images', *Remote Sensing of Environment*, vol. 159, pp. 269–277, doi: 10.1016/j.rse.2014.12.014.

Chapter 6

Key Outcomes, Discussions and Future Research

Key Outcomes, Discussions and Future Research

6.1. Summary of Key Outcomes

The studies presented within this thesis were undertaken to investigate Indonesian peatland fires detection from satellite remote sensing data. The addition of new techniques to map Indonesian peatland fires provided new contribution particularly on mapping peatland fires (flaming and smouldering fires) with more detail scale and information from medium spatial resolution (20–30 m) data at temporal resolution of five day and 16 day. The daily global active fire information from low spatial resolution (375 m) has been assessed to be utilised together with the peatland fires information resulting from medium spatial resolution; thus ensure to establish peatland fires information in tropical environments in a higher spatial resolution than existing fire products.

Chapter 1 introduced the fundamental concepts and characteristic of peatland fires (smouldering and flaming) from previous laboratory and field experiments and peatland fires in significant environmental locations. The remote sensing principles for fire detection were also introduced by the implementation of Planck law on radiance curves simulated by MODTRAN on peatland rainforest associated with flaming, smouldering peatland, and background temperatures under tropical atmospheric conditions. SWIR, MIR, and TIR showed significant radiance signatures for peatland fires detection. A review of global fire detections and local applications to tropical peatland fires was presented with the link to sensor availability with spectral, temporal and spatial characteristics. A research gap was found in small and smouldering peatland fires detection, which is still absent in research, especially from moderate spatial resolution data which only rely on SWIR and TIR or only SWIR alone.

Chapter 2 presented initial work on spectral radiance analysis of combustion areas and non-combustion areas (urban, burnt area and forest) over peatlands in Central Kalimantan from medium spatial resolution data (Landsat-8 OLI/TIRS daytime). The combustion areas were sampled based on the RGB image composites of 7-6-4 of Landsat-8 which had fire features and smoke emanating from the combustion areas. The SWIR radiance in combustion areas were close to saturation values at 24–29 $Wm^{-2}sr^{-1}\mu m^{-1}$ which agreed with a previous study using field experiments for flaming fires. The research in chapter 2 used the ratio of the SWIR band radiances of Landsat-8 as the

ShortWave InfraRed Combustion Index (SICI). This index related to a previous study for potassium emission index from hyperspectral data. Moreover, TIR radiance in the combustion areas showed significant difference with background areas, but there was a potential to have a similar value with burnt area from the statistical values. Flaming and smouldering peatland were associated with the high and low values from SWIR and TIR radiance under the SICI threshold for the combustion area. The estimated fire temperatures from the implementation of Planck's equation and Radiative Transfer Modelling for SWIR and TIR were in the range of flaming and smouldering peatland temperatures measured from previous studies in Central Kalimantan. This chapter addressed research question-1 to show that there was a possibility to map flaming and smouldering peatland fires from Landsat-8 data but requited further exploration over larger data period together with field verification.

Chapter 3 extended the findings from chapter 2 using more Landsat-8 data and ground validation. The first research question was answered in this chapter. A new algorithm for peatland fires detection under clear and smoky atmospheres termed the Tropical Peatland Combustion Algorithm (ToPeCAl) was established based on SICIρ, TOA reflectance ShortWave InfraRed band-7 (SWIR), TOA brightness temperature of Thermal InfraRed band-10 (TIR), and TOA reflectance of the aerosol band of Landsat-8. ToPeCAl was developed in Central Kalimantan's peatland fires and applied to Riau's peatlands. The ground truth was conducted by direct observation, drone imaging, and pictures taken from helicopter by Indonesian Disaster Management Agency. An accuracy of 82% resulted from a verification of 103 ground data in Central Kalimantan and Riau with omission errors related to small smouldering areas which occurred in mixed Landsat pixels and commission errors related to bright objects. An initial comparison between VIIRS active fire product and results of ToPeCAl applied to Landsat-8 resulted in 71% accuracy of VIIRS.

Chapter 4 presented a new finding on how to utilise global active fires data from VIIRS 375 m to monitor peatland fires in Indonesia by using ToPeCAl Landsat-8 fires results as reference. This chapter fulfilled the second research question. The multi-time combination of VIIRS active fire with additional cluster buffer analysis improved peatland fires detection up to more than 90% compared with a single time of active fire data, which could only provide a probability of fire detection up to 70%. Small fires (< 0.09 ha) could only be detected at about 10% from VIIRS, while larger fires up to 14 ha

were detected about 80%. The day-time and nigh-time products of VIIRS active fires data with different times within a 15 hour time interval were allowed to be combined together due to the low propagation speed of peatland fires. False positive alarms were also found from VIIRS active fires data on bareland (5 %), industrial area of gas flares (9%) and bright rooftops (5%).

Chapter 5 showed the performance of peatland fires detection by only relying on SWIR without TIR from medium spatial resolution data. ToPeCAl without TIR, termed ToPeCAl-2, was adjusted and tested on to Landsat-8 OLI images and then implemented to Sentinel-2 MSI imagery as a complement of peatland fires information at higher spatial and higher temporal resolution than Landsat-8. An improved bright object masking was presented to minimise false detection on permanent bright objects. ToPeCAl-2 was also presented with an improved contextual test and cloud masking for selecting candidate fire pixels. Peatland fires information resulted from these methods can be used for fire suppression and peatlands rehabilitation input with more detail scale than available. The third research question was answered in this chapter.

6.2. Discussions

6.2.1. Flaming and Smouldering Peatland Fires Detection

Flaming occurs when oxidation takes place in the gas phase, resulting in gaseous and particulate matter at significant radiance power and high temperatures with radiation at all wavelengths; flaming is certainly visible to the naked eye (Rein 2013; 2016). The strong radiance and high temperatures of flaming are generally easier to interpret and analyse from satellite data than the radiance from smouldering fire. Smouldering chemistry involves a two-step process as biomass pyrolysis with the chemical decomposition of solid organic material through heating, which produces char and then in-situ oxidisation. Low power and low temperature result from the oxidation process of char with gas and ash, as other products of smouldering (Rein 2013; 2016; Santoso et al. 2019). The moisture content of the peatland also influences the peat combustion, especially for smouldering (Huang & Rein 2015; Prat-Guitart et al. 2016a; 2016b; Rein 2013; Usup et al. 2004). Peat surface critical ignition moisture content was recorded at 100% gravimetric moisture measurement (gms) (Usup et al. 2004), 115% gms (Prat-Guitart et al. 2016b) and 117 % gms (Huang & Rein 2015). Thus, instead of temperature, smouldering can also be identified from smoke, ash and moisture content.

Referring to the principle of fires detection represented by the Planck curve with MODTRAN simulation in Figure 5.3, the medium spatial resolution data (e.g. Landsat-8 OLI/TIRS) can use SWIR and TIR, while Sentinel-2 MSI can only use SWIR for detecting peatland fires. Based on the capabilities of SWIR and TIR in Landsat-8, flaming in the range of temperatures between 700 and 1,000 K has a more significant radiance at SWIR than TIR, while smouldering at 360–500 K and smouldering close to flaming at 500–700 K are more clearly detected at TIR than SWIR. The detection of smouldering with SWIR alone showed a significant difference with background temperatures starting from 450 K to temperatures of smouldering close to flaming (500–700 K) (Figure 5.3). There is a possibility of a mixture of smouldering with background objects at temperatures below 450 K at SWIR (Figure 5.3). Surface temperatures taken from field measurement of smouldering peatlands were about 452 K on average (Figure 5.4). These results were in the range of smouldering temperatures simulated by MODTRAN for grey body over peatland with limited vegetation (Figure 5.3).

In Chapter 3, the detection of peatland fires using ToPeCAl was not only based on SWIR and TIR, but also on the ratio of SWIR-2 (2.2 μm) to SWIR-1 (1.6 μm), termed the ShortWave InfraRed combustion index (SICI), and the aerosol band to represent atmospheric scattering from particulates generated from combustion. The SICI was used to separate potential combustion areas from non-combustion areas. As presented by the boxplots of radiance on the SWIR bands and the TIR band of Landsat-8 in Figure 5.5, the burnt area and smouldering peatlands were in similar ranges and were hard to separate using SWIR and TIR alone. However, SICI presented a way to separate burnt areas from smouldering ones. Thus, at first, SICI was applied to separate potential combustion areas from non-combustion areas and then the SWIR-2 and TIR thresholds were applied. The aerosol band was used to assess atmospheric conditions, which may result in different values of SWIR and TIR under relatively clear or smoky atmospheres during peatland fires.

In this thesis, most smouldering pixels detected by ToPeCAl were associated with the flaming signatures surrounding combustion areas, which were visually easier to recognise in the 764-RGB image of Landsat-8. As explained in Rein (2013; 2016), smouldering and flaming each lead to the other; this pattern was reflected in the fires detected by ToPeCAl with SWIR and TIR (ToPeCAl-1), where the presence of

smouldering pixels was adjacent to flaming pixels or a mix of flaming and smouldering pixels. In addition, it was mentioned in previous literature that the initial stage of smouldering fire is difficult to observe because of low thermal radiance and slow propagation (Rein 2009), and the pixel reflectance is dominated by either green vegetation or recently slashed vegetation; thus, it is less separable from the background (Elvidge et al. 2015). Hence, ToPeCAl-1 applied to Landsat-8 OLI/TIRS failed to detect small smouldering fires during the initial stages.

When the temperature increases and sufficient oxidation takes place, smouldering transforms to flaming and the radiant power from pixels increases; hence, ToPeCAl-1 may detect the fire as a mix of flaming and smouldering or simply as flaming. To detect the smallest sized fires in a mix of flaming and smouldering, sub-pixel analysis could be conducted. However, in this thesis, sub-pixel analysis was not undertaken because the original spatial resolution of TIR from Landsat-8 was 100 m, which is still quite coarse for detecting small smouldering fires in real peatland fires. Thus, the smallest cool fire detected by ToPeCAl-1 applied to Landsat-8 was assumed to be at 30 × 30 m or 0.09 ha. VIIRS active fire (375 m) data found that only 10% of peatland fires were small fires (0.09 ha), while 80% of the fires were related to large fires (> 0.09 ha to 14 ha) based on the ToPeCAl-1 results. In Indonesia, most of the small smouldering fires were related to burning activity implemented by local farmers. Oliva and Schroeder (2015) also discovered that the VIIRS (375 m) active fire product failed to detect small fires related to agricultural practices in North India and Cambodia. The issue of inadequate spatial and spectral resolution in sensors may influence the detection of small peatland fires. However, the smallest fires (0.09 ha) detected from ToPeCal-1 may still support the Indonesian disaster management agency to conduct early suppression before a fire extends to larger areas.

Some smouldering pixels in relatively homogenous and large areas were detected by ToPeCAl-1 in the rear of the fire front and in areas with a mix of flaming and smouldering pixels. These smouldering pixels can be associated with residual smouldering combustion (Rein 2013; Rabelo et al. 2004; Bertschi et al. 2003; Urbanski 2014), which reflects the transition from flaming to smouldering peatlands. In these smouldering pixels, the radiant heat from char still exists and produces ash, with other gases and particulate matter, as smoke from smouldering peatlands (Rein 2013; 2016; Santoso et al. 2019). Higher spatial resolutions, for example, drone imagery, can show the presence of ash in smouldering peatlands and, in this study, smouldering peatlands were confirmed by the presence of ash from drone images. Meanwhile, in the medium spatial resolution (20–30 m) satellite imagery, instead of radiant temperature, some smouldering areas were shown in a brighter pixels where ash dominated the area or in a darker pixels where the pixel contained mixed objects—for example, ash, smouldering logs and burnt areas. These smouldering areas were adjacent to flaming features and were confirmed by visual analysis in the satellite imagery by identifying the smoke features that emanated from smouldering fires. In this thesis, smoke features were visually identified from higher spatial resolutions—that is, using PlanetScope imagery on the same day with Landsat-8/Sentinel-2's acquisition. According to Hu et al. (2018), smouldering peatland produces whitish/yellowish smoke accumulating near ground level, which contains abundant organic carbon as haze aerosols. The smoke plume from smouldering is slowly distributed by wind to the atmosphere, causing regional haze for long periods of time (Hu et al. 2018; Rein 2013). Meanwhile, flaming releases black or dark-grey smoke with strong fire plumes, which contain more soot and less organic carbon than smouldering peatlands. The schemes of smouldering and flaming smoke are presented in Figure 6.1 (Hu et al. 2018). Further analysis of remote sensing observations is needed to explore smoke properties, as described in Figure 6.1.

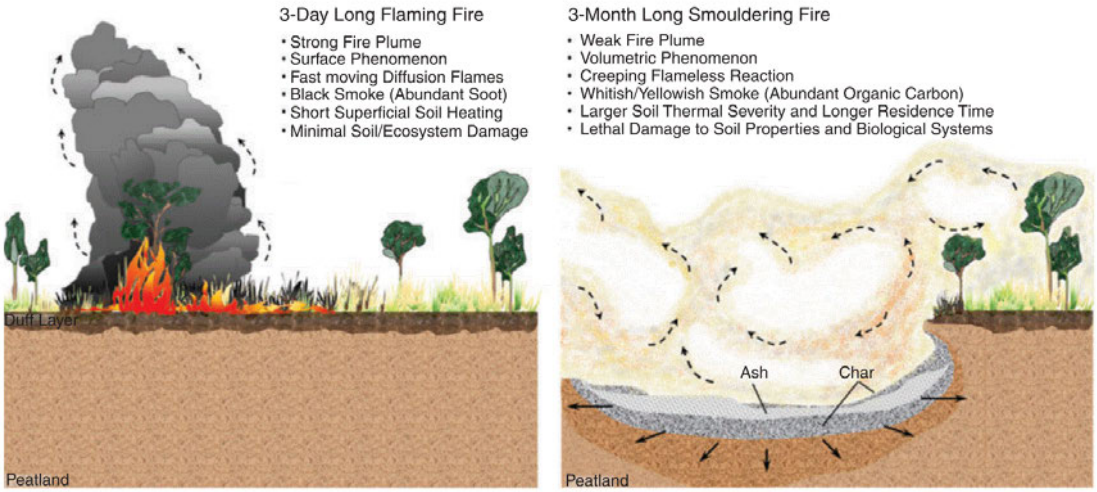


Figure 6.1. Schemes of flaming and smouldering peatland fires (Hu et al. 2018) CC-BY-NC-ND.

Meanwhile, for measuring peatland moisture content, airborne (Hashim et al. 2001; 2002) and spaceborne-SAR (Novresiandi and Nagasawa 2016; Watanabe et al. 2011) at L-band showed a strong relationship between the backscatter and the soil moisture in the tropical peatlands. The water table on the degraded peatland in Central Kalimantan was confirmed using the SAR interferometry approach, the differential interferometric InSAR/DInSAR and the backscattering of ALOS-2/PALSAR-2 (Widodo et al. 2019a; 2019b). These approaches could be applied to support the results of peatland fires detection from ToPeCAl, with a reduction in peatland moisture occurring during and after fire events. The pending launch of the NASA-ISRO Synthetic Aperture Radar (NISAR) mission in 2022 will provide free S- and L-band SAR (NASA 2020).

6.2.2. Accuracy of ToPeCAl Fires

ToPeCAl-1 fires detected from Landsat-8 OLI/TIRS, which were verified by ground data in Central Kalimantan and Riau Province by direct observation, drone imaging and helicopter images, demonstrated 82% accuracy with omission errors for small smouldering fires in mixed pixels and commission errors on bright objects. Applying an urban GIS map to mask out false positives, ToPeCAl-1 resulted in 93% accuracy. Based on the peatland fire stages, ToPeCAl-1 mapped 100% of flaming, 96% of the mix of flaming and smouldering and 73% of the smouldering peatlands observed in the field. This finding shows it is possible to map flaming and smouldering peatland fires from a moderate spatial resolution (Landsat-8 data) with SWIR and TIR using daytime data.

Applying ToPeCAl without TIR (ToPeCAl-2) to Landsat-8 OLI and Sentinel-2 MSI resulted in viable detection of flaming fires (> 95% accuracy), with poorer detection of smouldering fires at only 35%–56%, in contrast to the ToPeCAl-1 smouldering fires. Referring to the simulation of Planck curves for peatland rainforest (grey body) at smouldering temperatures in the SWIR region, the potential smouldering peatland temperatures ranged from 450 K to smouldering close to flaming at temperatures of 500–700 K. Without MIR or TIR, the detection of smouldering relying on SWIR alone may result in a confusion between smouldering events with warm soil. A false detection may potentially occur for smouldering pixels with no flaming or without a mix of flaming and smouldering pixels. Aside from this, ToPeCAl-2 provided higher false detections for bright objects than ToPeCAl-1—for example, over bright, dense cloud, which has strong reflectance in SWIR, but a low brightness temperature in TIR. Permanent bright objects generated other false positive errors. These objects—normally, building rooftops and gas flares in oil-industrial areas—were masked out by applying an improved bright object detection algorithm, which considered the seasonal changes in bright object reflectance using multi-temporal Sentinel-2 imagery. About 90% of permanent bright objects can be eliminated using this approach (Appendix-Table A6.1). This masking, if applied systematically and regularly (e.g. annually) across the whole of Indonesia, will make ground-fire management by disaster management agencies more efficient.

Fixed threshold and contextual methods have mostly been applied for fire detection from low spatial resolution satellite imagery (Justice et al. 2002; Robert & Wooster 2008; Xu et al. 2010; Wooster, Xu & Nightingale 2012; Schroeder et al. 2014; Wickramasinghe et al. 2016; Giglio, Schroeder & Justice 2016) to medium spatial resolution satellite imagery (Giglio et al. 2008; Schroeder et al. 2016; Kumar and Roy 2018). In this thesis, contextual testing was also applied to ToPeCAl-2 with the modification of selecting background pixels. The previous contextual tests for medium spatial resolution satellite imagery (Giglio et al. 2008; Schroeder et al. 2016; Kumar and Roy 2018) only masked water and unambiguous fire pixels from the background analysis, whereas, in this thesis, permanent bright objects, dense cloud and fire pixels were also masked from the background analysis; thus, an appropriate background statistic was provided. A high confidence threshold was applied when selecting potential fire pixels from ToPeCAL-2; it was chosen because ToPeCAl-2, using only SWIR, may only be useful for detecting fires at high temperatures and may be less suitable for cool fires. Previous contextual tests

that applied fire algorithms by relying on SWIR reflectance from ASTER and Landsat-8 also used high confidence levels (Giglio et al. 2008; Schroeder et al. 2016; Kumar and Roy 2018). A lower confidence level for selecting potential fire pixels could be applied to ToPeCAl-1, which uses SWIR and TIR for detecting peatland fires. In this thesis, ToPeCAl-2 as applied to Sentinel-2 using a high confidence level for the contextual test provided a POD of 96% for flaming, a POD of 76% for the mix of flaming and smouldering and a POD of 35% for smouldering. This finding shows it is possible to detect and map peatland fires from higher spatial resolution satellite data, such as that of Sentinel-2 MSI without TIR information.

6.2.3. Opportunity for Integration of Multi Fire Information from Different Observations

The limited temporal resolution of the medium spatial resolution satellite sensors for monitoring peatland fires can be complemented with fire information produced from low spatial resolution sensors (e.g. MODIS, SLSTR, VIIRS or AHI). Fire behaviour across a certain period is an important factor for allowing the integration of multi-fire data from different satellite image acquisition times. Data merging is possible for peatland fires, which have a slow propagation speed, provided that the difference between acquisition times does not exceed a threshold based on the fire propagation speed. One of the methods presented in this thesis for merging active fire information was buffer distance and clustering from one sensor (VIIRS) using different times of acquisition. These methods could also be applied to the merging of active fire data from different sensors and time acquisitions. However, the merged active fires information from low spatial resolution imagery may only be suitable for representing flaming and may be limited for smouldering peatlands because of its coarse spatial resolution. Wind speed and direction could also be integrated into this merging scheme to support the trajectory of fire behaviour information. Moreover, the smouldering fire which mostly occurs on a small area may not be able to emit enough radiant energy or Fire Radiative Power particularly in a coarse spatial resolution of pixel.

In this thesis, the spreading rates of the peatland fires were adopted from previous studies using TET-1 at 160 m spatial resolution in the range of 4.0 m/day to 1,903 m/day (Atwood et al. 2016). These estimated fire spread rates illustrated that most peatland fires remained within a 750 m buffer over 15 h under uniform conditions of weather and

environment; this may not be true for very large fires, which, in Indonesia, often have multiple ignition sources. However, there is a possibility of enhancing the fire spread rate estimation by using higher spatial resolution imagery data from Landsat-8 at 30 m and from Sentinel-2 at 20 m. An improvement of peatland fire spread rates may update the threshold for the duration between two different acquisitions when integrating fire products.

An investigation of the global active fire product from VIIRS (375 m) was assessed based on the ToPeCAL-1 fires that resulted from Landsat-8 OLI/TIRS in this thesis. The VIIRS (375 m) nighttime data performed with better detection (85%) than the daytime data. The importance of having nighttime data arises not only because of its strong capacity to detect fires without the influence of solar radiation, but also because of its potential to address the time gaps between daytime acquisitions. A merging of VIIRS (375 m) active fires at daytime and nightime using a 375 m cluster buffer analysis increases the detection of peatland fires by up to 90% for fires larger than 14 ha. False positive alarms were also found from the VIIRS active fire data over bare land (5%), industrial areas of gas flares (9%) and bright rooftops (5%). The bright object mapping implemented in the pre-processing step of ToPeCAl could also be applied to the VIIRS (375 m) active fire data to minimise false detections from gas flares and bright rooftop objects. These findings answered Research Question 2 through the merging and buffering analysis applied to daytime and nighttime active fires data in low spatial resolutions (VIIRS) to guide disaster management agencies to efficiently conduct ground validation and subsequent suppression.

The integration of multi fire data resultant from different acquisition times and sensors is also aimed at overcoming cloud problems, which limit satellite observations over tropical regions. In this thesis, cloud cover reduced fire detections during daytime by about 38%. Frequent observations from geostationary and constellations of satellites may overcome the cloud issue by detecting fires at different times. Moreover, microwave sensors can complement optical remote sensing data, which are often affected by cloud obscuration problems in tropical regions (Ahmad, Zhang & Nichols 2011; Awange & Kyalo Kiema 2013; Wang & Qu 2009). However, the radiant energy emitted from fire, particularly small fires, is weak for passive microwave sensors as a result of a low signal-to-noise ratio. Most SAR applications for pre-fire mapping are related to peat soil moisture as an early warning tool for mapping the fire-prone area (Widodo et al. 2019a;

2019b). The peatland moisture observation based on SAR could be combined with active fires information from optical sensors to support fire prevention and monitoring under cloud conditions. SAR observations will show both land clearance and reduced peatland moisture during fire situations.

6.3. Future Research Directions

Methodological aspects that could be explored in the future given the current set of available imagery are:

- Increased ground validation for smouldering peatland
- Applying the contextual test with low confidence level for selecting smouldering pixels from fires detected by ToPeCAl-1.
- Improving the peatland fires spread rates estimation by using Sentinel-2 data or Landsat-8 data which have higher spatial resolution (20-30 m) than used previously from TET-1 (167 m). The spread rate information will update the application of cluster buffer zones, which allow the integration of multi time combination of VIIRS active fire data.
- Preprocessing of imagery, especially for cloud mapping can be improved by establishing new algorithm for cloud mapping. The quality of cloud product of Sentinel-2 derived from Sen2cor is poor for mapping various cloud types in tropical atmospheres. This will potentially improve the selection of candidate smouldering pixels in the background.
- Automatic screening for masking gas flares should be applied on any biomass fire monitoring system.

Further investigations for smouldering peatlands resulting from ToPeCAl can be explored, particularly in relation to smoke properties, ash and soil moisture. Smoke from smouldering has different chemical properties and bigger particle sizes than flaming (Koppmann et al. 2005; Rein et al. 2009; Wiggins et al. 2018; Reid et al. 2005). Ash is the product of smouldering in ongoing or recently smouldering peatland (Rein 2013; 2016; Santoso et al. 2019). Meanwhile, soil moisture will decrease during the initial smouldering process and then decline further during the fire situation (Huang & Rein 2015; Prat-Guitart et al. 2016a; 2016b; Rein 2013; Usup et al. 2004). High spatial

resolution data, for example, PlanetScope images, as used in this thesis, or WorldView-3 imagery, can only confirm the existence of smoke features over peatland fires. However, the spectral resolution of high spatial resolution sensors may not be sufficient to differentiate the smoke features sourced from smouldering or flaming combustion, based on particle chemical properties and/or particle size. To date, the most specific satellite built for atmospheric monitoring is the Sentinel-5P with a TROPOspheric Monitoring Instrument (TROPOMI). The information provided by TROPOMI includes the atmospheric ozone, methane, formaldehyde, aerosol, carbon monoxide, NO_2 and SO_2 levels. TROPOMI provides an observation at 7 x 3.5 km with revisiting times of less than one day available from 2017. TROPOMI, with its coarse spatial resolution, can only be useful for monitoring atmospheric conditions related to large fires.

Table 6.1 shows some future sensors that may have the potential to support peatland fire monitoring using higher spatial, spectral and temporal resolutions. For example, Hyperspectral X Imagery (HypXIM) could be explored for investigating smoke and ash characteristics through spectral analysis, although most of the reported hyperspectral applications are mainly for land and water, while for atmospheric or smoke properties, application is still limited (Transon et al. 2018). Moreover, HypXIM with SWIR and TIR could also be explored to provide peatland fires monitoring at higher spatial resolutions of up to 8 m. The Copernicus High Spatio–Temporal Resolution Land Surface Temperature Mission (LSTM) with VNIR, SWIR and TIR has the potential for future peatland fire monitoring. The LSTM is planned by the European Space Agency for future Earth observation in 2025 at a spatial resolution of 30–50 m, every 1–3 days (Koetz et al. 2019). Meanwhile, SAR applications for peatland moisture monitoring can be strengthened by the NASA–ISRO SAR Mission (NISAR) with L- and S-bands, which will be launched in 2022. Moisture content for peatland fires from SAR, together with smoke and ash properties from hyperspectral sensors, can support the detection and validation of smouldering peatlands.

Table 6.1. Potential future sensors for supporting peatland fires monitoring (ESA 2020; Michel et al. 2011; Briottet et al. 2011; Transon et al. 2018; Futureearth 2020; Koetz 2019; NASA 2020).

Instrument	HypXIM	LSTM	NISAR
Launch	2021	2025	2022
Sensor type	Hyperspectral	Multispectral	SAR
Swath width (km)	15	700	240
Spectral	VNIR, SWIR, TIR	VNIR, SWIR, TIR	L-band, S-band
Spatial resolution (m)	8 (VNIR-SWIR) 100 (TIR)	30–50	3–10
Temporal resolution (day)	3 (60° S/N) 19 (nadir)	1–3	12
Mission	geosciences, urban, vegetation, coastal, atmospheric science, security and defence	food and water security, soil, urban, high temperature events (volcanic, biomass fires), permafrost, coastal	solid Earth, cryosphere and ecosystems
Country/ Organisation	France/CNES	European Union/ ESA	USA and India/ NASA &ISRO

The spatial resolution constraint of SWIR, MIR or TIR for improving smouldering peatlands detection offers a future challenge in providing a sensor or a constellation of sensors incorporating these spectra with similar, or better, temporal and spatial resolution specifications to Landsat-8/Sentinel-2, to improve peatland fires monitoring. Space observation over tropical peatlands is not only a mandate for a single country, such as Indonesia, it also includes the international community, who are experiencing similar issues. Thus, multi-lateral or international cooperation may establish a specific satellite sensor, or a constellation of sensors, with sufficient spectral, spatial and temporal resolutions to monitor tropical peatland fires in an effort to reduce global greenhouse emissions and environmental degradation.

References

Ahmad, A, Zhang, Y & Nichols, S 2011, 'Review and evaluation of remote sensing methods for soil-moisture estimation', *Journal of Photonics for Energy*, pp. 028001–028017.

Atwood, E, Englhart, S, Lorenz, E, Halle, W, Wiedemann, W & Siegert, F 2016, 'Detection and characterization of low temperature peat fires during the 2015 fire catastrophe in Indonesia using a new high-sensitivity fire monitoring satellite sensor (FireBird)', *PLoS ONE*, vol. 11, no. 8, pp. 1–24.

Awange, JL & Kyalo Kiema, JB 2013, *Environmental Geoinformatics Monitoring and Management*, Springer, Verlag Berlin Heidelberg.

Bertschi, I, Yokelson, RJ, Ward, DE, Babbitt, RE, Susott, RA, Goode, JG & Hao, WM 2003, 'Trace gas and particle emissions from fires in large diameter and belowground biomass fuels', *J. Geophys. Res,* vol. 108, no. D13.

Briottet, X, Marion R, Carrere, V, Jacquemoud, S, Chevrel, S, Prastault, P, D'oria, M, Gilouppe 2011, "HYPXIM: A new hyperspectral sensor combining science/defence applications," *3rd Workshop on Hyperspectral Image and Signal Processing: Evolution in Remote Sensing* (WHISPERS), Lisbon, pp. 1–4, doi: 10.1109/WHISPERS.2011.6080957.

Elvidge, CD, Zhizhin, M, Hsu, F, Baugh, K, Khomarudin, M, Vetrita, Y, Sofan, P, Suwarsono & Hilman, D 2015, 'Long-wave infrared identification of smoldering peat fires in Indonesia with nighttime landsat data', *Environmental Research Letters,* vol. 10, no. 6, p. 065002.

ESA 2020, *Sentinel-5P*, viewed in 22 October 2020, <https://sentinel.esa.int/web/sentinel/missions/sentinel-5p>.

Futureearth 2020, *Plans for a New Wave of European Sentinel Satellites*, viewed on 4 July 2020, <https://futureearth.org/publications/explainers/plans-for-a-new-wave-of-european-sentinel-satellites/#:~:text=LSTM%3A%20Copernicus%20Land%20Surface%20Temperature,than%20currently%20measured%20from%20space>.

Giglio, L, Csiszar, I, Restás, Á, Morisette, JT, Schroeder, W, Morton, D & Justice, CO 2008, 'Active fire detection and characterization with the advanced spaceborne thermal emission and reflection radiometer (ASTER)', *Remote Sensing of Environment*, vol. 112, no. 6, pp. 3055–3063.

Giglio, L, Schroeder, W & Justice, C 2016, 'The collection 6 MODIS active fire detection algorithm and fire products', *Remote Sensing of Environment*, vol. 178, pp. 31–41, doi:10.1016/j.rse.2016.02.054.

Hashim, M, Busu, I, Sim, SH, Jong, TK, Wan Kadir, WH & Salam, ND 2002, 'Soil moisture, depth of water table, and peat decomposition in Sadong Simunjan River Basin, Sarawak using AIRSAR/TOPSAR data', *3rd Malaysian Remote Sensing and GIS Conference and Exhibition "Spatial Information Technology in the New Millenium"*.

Hashim, M, Sim Hock Seng, P, Wan Kadir, WH & Salam, ND 2001, 'Soil moisture estimation of drained peat area using TOPSAR data', *Malaysian Journal of Remote Sensing & GIS*, vol. 2, no. July.

Hu, Y, Fernandez-Anez, N, Smith, TEL & Rein, G 2018, 'Review of emissions from smouldering peat fires and their contribution to regional haze episodes ', *Int. J. of Wildland Fire*, vol. 27, no. 5, pp. 293–312.

Huang, X & Rein, G 2015, 'Computational study of critical moisture and depth of burn in peat fires', *International Journal of Wildland Fire,* vol. 24, no. 6, pp. 798–808.

Justice, C, Giglio, L, Korontzi, S, Owens, J, Morisette, J, Roy, D, Descloitres, J, Alleaume, S, Petitcolin, F & Kaufman, Y 2002, 'The MODIS fire products', Remote Sensing of Environment, vol. 83, no. 1, pp. 244–262.

Koetz, B, Berger, M, Blommaert, J, Bello, UD, Drusch, M, Duca, R, Gascon, F, Ghent, D, Hoogeveen, J, Hook, S, Kerr, Y, Lagouarde, J-P, Manolos, I, Marini, A, Menenti, M, Martimort, P, Masek, J, Massart, M, Notarnicola, C, Sallusti, M, Sandholt, I, Schuettemeyer, D, Sobrino, J, Strobl, P, Volden, E & Udelhofen, T 2019, *Copernicus High SPatio-Temporal Resolution Land Surface Temperature Mission: Mission Requirements Document*, ESA, Noorwijk, The Netherlands, viewed 8 March 2019.

Koppmann, R, von Czapiewski, K & Reid, JS 2005, 'A review of biomass burning emissions, part I: gaseous emissions of carbon monoxide, methane, volatile organic compounds, and nitrogen containing compounds', *Atmos. Chem. Phys. Discuss.*, vol. 2005, pp. 10455–10516.

Kumar, SS & Roy, DP 2018, 'Global operational land imager Landsat-8 reflectance-based active fire detection algorithm', *International Journal of Digital Earth*, vol. 11, no. 2, pp. 154–178.

Michel, S, Gamet, P and Lefevre-Fonollosa, M 2011, "HYPXIM — A hyperspectral satellite defined for science, security and defence users," *3rd Workshop on Hyperspectral Image and Signal Processing: Evolution in Remote Sensing* (WHISPERS), Lisbon, pp. 1-4, doi: 10.1109/WHISPERS.2011.6080864.

NASA 2020, *NASA-ISRO SAR Mission*, viewed on 22/10/2020, <https://nisar.jpl.nasa.gov/>.

Novresiandi, DA & Nagasawa, R 2016, 'Tropical peatland identification using ALOS PALSAR imageries - A case study in Kahayan River catchment area, Central Kalimantan, Indonesia', *Journal of the Japanese Agricultural Systems Society*, vol. 32, no. 1, pp. 1–9.

Oliva, P & Schroeder, W 2015, 'Assessment of VIIRS 375m active fire detection product for direct burned area mapping', *Remote Sensing of Environment*, vol. 160, 2015/04/01/, pp. 144–155.

Prat-Guitart, N, Rein, G, Hadden, R, Belcher, C & Yearsley, J 2016a, 'Effects of spatial heterogeneity in moisture content on the horizontal spread of peat fires', *Science of the Total Environment*, vol. 572, pp. 1422–1430.

Prat-Guitart, N, Rein, G, Hadden, RM, Belcher, CM & Yearsley, JM 2016b, 'Propagation probability and spread rates of self-sustained smouldering fires under controlled moisture content and bulk density conditions', *International Journal of Wildland Fire*, vol. 25, no. 4, pp. 456–465.

Rabelo, ERC, Veras, CAG, Carvalho, JA, Alvarado, EC, Sandberg, DV & Santos, JC 2004, 'Log smoldering after an amazonian deforestation fire', *Atmospheric Environment*, vol. 38, no. 2, 2004/01/01/, pp. 203–211.

Reid, JS, Koppmann, R, Eck, TF & Eleuterio, DP 2005, 'A review of biomass burning emissions part II: intensive physical properties of biomass burning particles', *Atmos. Chem. Phys.*, vol. 5, no. 3, pp. 799–825.

Rein, G 2009, *Smouldering Combustion Phenomena in Science and Technology*, 1, International Review of Chemical Engineering IRECHE - Praise Worthy Prize, pp. 3–18.

Rein, G 2013, 'Smouldering fires and natural fuels', *Fire Phenomena and the Earth System: An Interdisciplinary Guide to Fire Science*, vol. Chapter 2, pp. 13–22.

Rein, G 2016, 'Smouldering Combustion', in MJ Hurley et al (eds), *SFPE Handbook of Fire Protection Engineering*, Springer New York, New York, NY, pp. 581–603.

Roberts, GJ & Wooster, MJ 2008, 'Fire Detection and Fire Characterization Over Africa Using Meteosat SEVIRI', *Geoscience and Remote Sensing, IEEE Transactions on*, vol. 46, no. 4, pp. 1200–1218.

Santoso, MA, Huang, X, Prat-Guitart, N, Christensen, E, Hu, Y & Rein, G 2019, 'Smouldering fires and soils', in P Pereira et al (eds), *Fire Effects on Soil Properties*, CSIRO Publishing, Victoria, Australia, p. 382.

Schroeder, W, Oliva, P, Giglio, L & Csiszar, I 2014, 'The New VIIRS 375 m active fire detection data product: Algorithm description and initial assessment', *Remote Sensing of Environment*, vol. 143, pp. 85–96, doi:10.1016/j.rse.2013.12.008.

Schroeder, W, Oliva, P, Giglio, L, Quayle, B, Lorenz, E & Morelli, F 2016, 'Active fire detection using Landsat-8/OLI data', *Remote Sensing of Environment*, vol. 185, pp. 210–220.

Transon, J, D'Andrimont, R, Maugnard, A & Defourny, P 2018, 'Survey of Hyperspectral Earth Observation Applications from Space in the Sentinel-2 Context', *Remote Sens.*, vol. 10, no. 2, p. 157.

Urbanski, S 2014, 'Wildland fire emissions, carbon, and climate: Emission factors', *Forest Ecology and Management*, vol. 317, pp. 51–60.

Usup, A, Hashimoto, Y, Takashi, H & Hayasaka, H 2004, 'Combustion and thermal characteristics of peat fire in tropical peatland in Central Kalimantan, Indonesia', *Tropics*, vol. 14, no. 1, pp. 1–19.

Wang, L & Qu, J 2009, 'Satellite remote sensing applications for surface soil moisture monitoring: A review', *Frontiers of Earth Science in China*, vol. 3, no. 2, pp. 237-247.

Watanabe, M, Kushida, K, Yonezawa, C, Sato, M & Fukuda, M 2011, 'PALSAR full-polarimetric observation for peatland', *Asian Journal of Geoinformatics*, vol. 11, no. 3.

Wickramasinghe, C, Jones, S, Reinke, K & Wallace, L 2016, 'Development of a Multi-Spatial Resolution Approach to the Surveillance of Active Fire Lines Using Himawari-8', *Remote Sensing*, vol. 8, no. 11, p. 932.

Widodo, J, Izumi, Y, Takahashi, A, Kausarian, H, Perissin, D & Sumantyo, JTS 2019a, 'Detection of Peat Fire Risk Area Based on Impedance Model and DInSAR Approaches Using ALOS-2 PALSAR-2 Data', *IEEE Access*, vol. 7, pp. 22395–22407.

Widodo, J, Sulaiman, A, Awaluddin, A, Riyadi, A, Nasucha, M, Perissin, D & Sri Sumantyo, JT 2019, 'Application of SAR Interferometry Using ALOS-2 PALSAR-2 Data as Precise Method to Identify Degraded Peatland Areas Related to Forest Fire', *Geosciences*, vol. 9, no. 11, p. 484.

Wiggins, EB, Czimczik, CI, Santos, GM, Chen, Y, Xu, X, Holden, SR, Randerson, JT, Harvey, CF, Kai, FM & Yu, LE 2018, 'Smoke radiocarbon measurements from Indonesian fires provide evidence for burning of millennia-aged peat', *Proceedings of the National Academy of Sciences*, vol. 115, no. 49, p. 12419.

Wooster, MJ, Xu, W & Nightingale, T 2012, 'Sentinel-3 SLSTR active fire detection and FRP product: Pre-launch algorithm development and performance evaluation using MODIS and ASTER datasets', *Remote Sensing of Environment*, vol. 120, 5/15/, pp. 236–254.

Xu, W, Wooster, MJ, Roberts, G & Freeborn, P 2010, 'New GOES imager algorithms for cloud and active fire detection and fire radiative power assessment across North, South and Central America', *Remote Sensing of Environment*, vol. 114, no. 9, 9/15/, pp. 1876–1895.

Appendices

Statement of Authorship: Chapter 2

Title of Paper: Detecting Peatland Combustion using Shortwave and Thermal Infrared Landsat-8 Data

Publication Status: Published

Publication details: Sofan, P.; Bruce, D.; Jones, E.; Marsden, J. Detecting peatland combustion using shortwave and thermal infrared Landsat-8 data. In Advance Forest Fire Research; Imprensa da Universidade de Coimbra: Coimbra,Portugal, 2018; pp. 969–979. https://doi.org/10.14195/978-989-26-16-506_106.

Submitted: 15 March 2018 / Reviewed: 2 May 2018 / Revised: 29 May 2018 / Published: 28 November 2018

Principle Author

Name	Parwati Sofan		
Contribution to paper	Designing, conceptual, data processing and analysing, graphics drawing and writing of manuscript		
Signature		Date	21/10/2020

Co-Author Contributions

Name	David Bruce		
Contribution to paper	Designing, Conceptual, principal supervising, and reviewing of manuscript		
Signature		Date	22/10/2020

Name	Eriita Jones		
Contribution to paper	Designing, Conceptual, reviewing of manuscript		
Signature		Date	21/10/2020

Name	Jackie Marsden		
Contribution to paper	reviewing of manuscript		
Signature		Date	21/10/2020

Statement of Authorship: Chapter 3

Title of Paper: Detection and Validation of Tropical Peatland Flaming and Smouldering using Landsat-8 SWIR and TIRS Bands

Publication Status: Published

Publication details: Sofan, P.; Bruce, D.; Jones, E.; Marsden, J. Detection and Validation of Tropical Peatland Flaming and Smouldering using Landsat-8 SWIR and TIRS Bands. *Remote Sens.* 2019, *11*, 465. https://doi.org/10.3390/rs11040465.

Received: 24 January 2019 / Revised: 18 February 2019 / Accepted: 19 February 2019 / Published: 24 February 2019

Principle Author

Name	Parwati Sofan		
Contribution to paper	Designing, conceptual, data processing and analysing, ground truth validation, graphic drawing, and writing of manuscript		
Signature	[redacted]	Date	21/10/2020

Co-Author Contributions

Name	David Bruce		
Contribution to paper	Designing, conceptual, analysing, principal supervising, and reviewing of manuscript		
Signature	[redacted]	Date	22/10/2020

Name	Eriita Jones		
Contribution to paper	Designing, conceptual, analysing, and reviewing of manuscript		
Signature	[redacted]	Date	21/10/2020

Name	Jackie Marsden		
Contribution to paper	Designing, conceptual and reviewing of manuscript		
Signature	[redacted]	Date	21/10/2020

Statement of Authorship: Chapter 4

Title of Paper:	Assessment of VIIRS 375 m Active Fire using Tropical Peatland Combustion Algorithm Applied To Landsat-8 over Indonesia's Peatlands
Publication Status:	Published
Publication details:	Sofan, P.; Bruce, D.; Schroeder, W.; Jones, E.; Marsden, J. Assessment of VIIRS 375 m Active Fire using Tropical Peatland Combustion Algorithm Applied to Landsat-8 over Indonesia's Peatlands. *Int J Digit Earth*. 2020. https://doi.org/10.1080/17538947.2020.1791268. Received: 04 March 2020 / Revised: 11 June 2020 / Accepted: 29 June 2020 / Published online: 09 July 2020

Principle Author

Name	Parwati Sofan		
Contribution to paper	Designing, conceptual, data processing and analysing, graphics drawing, and writing of manuscript		
Signature	[redacted]	Date	21/10/2020

Co-Author Contributions

Name	David Bruce		
Contribution to paper	Designing, conceptual, analysing, principal supervising, and reviewing of manuscript		
Signature	[redacted]	Date	22/10/2020

Name	Wilfrid Schroeder		
Contribution to paper	Analysing and reviewing of manuscript		
Signature	[redacted]	Date	26/10/2020

Name	Eriita Jones		
Contribution to paper	Analysing and reviewing of manuscript		
Signature	[redacted]	Date	21/10/2020

Name	Jackie Marsden		
Contribution to paper	Analysing and reviewing of manuscript		
Signature	[redacted]	Date	21/10/2020

Statement of Authorship: Chapter 5

Title of Paper:	Applying the Tropical Peatland Combustion Algorithm to Landsat-8 Operational Land Imager (OLI) and Sentinel-2 Multi Spectral Instrument (MSI) Imagery
Publication Status:	Published
Publication details:	Sofan, P.; Bruce, D.; Jones, E.; Khomarudin, M.R.; Roswintiarti, O. Applying the Tropical Peatland Combustion Algorithm to Landsat-8 Operational Land Imager (OLI) and Sentinel-2 Multi Spectral Instrument (MSI) Imagery. Remote Sens. 2020, 12, 3958. https://doi.org/10.3390/rs12233958. Received: 14 September 2020 / Revised: 19 November 2020 / Accepted: 27 November 2020 / Published: 3 December 2020

Principle Author

Name	Parwati Sofan		
Contribution to paper	Designing, conceptual, data processing and analysing, graphics drawing, and writing of manuscript		
Signature	[redacted]	Date	04/12/2020

Co-Author Contributions

Name	David Bruce		
Contribution to paper	Designing, conceptual, analysing, principal supervising, and reviewing of manuscript		
Signature	[redacted]	Date	04/12/2020

Name	Eriita Jones		
Contribution to paper	Designing, conceptual, analysing, and reviewing of manuscript		
Signature	[redacted]	Date	04/12/2020

Name	M. Rokhis Khomarudin		
Contribution to paper	Reviewing of manuscript		
Signature	[redacted]	Date	04/12/2020
Name	Orbita Roswintiarti		
Contribution to paper	Reviewing of manuscript		
Signature	[redacted]	Date	04/12/2020

Chapter 2 Appendix

Table A2.1. Statistical values for sample of combustion areas, burnt areas, urban and forest from Landsat-8 on August 3rd and August 19th, 2015. B6, B7, B10 represent TOA radiance ($Wm^{-2}sr^{-1}\mu m^{-1}$) of band-6, band-7 and band-10 of Landsat-8, respectively. SICI is ShortWave InfraRed Combustion Index or the ratio of band-6 to band-7.

Object	Band/ index	N (pixel)	Mean	StDev	Min	Q1	Median	Q3	Max
Combustion area	B6	563	20.44	16.22	2.78	10.11	13.78	24.55	89.84
	B7		15.43	7.96	2.70	6.93	16.04	23.52	28.46
	B10		12.05	2.51	9.63	10.43	11.05	12.56	20.89
	SICI		1.75	0.73	0.63	1.21	1.59	2.19	4.81
Burnt area	B6	1,594	6.15	1.40	3.26	5.29	5.79	6.63	12.11
	B7		1.86	0.36	1.14	1.73	1.82	1.90	6.58
	B10		10.93	0.38	9.83	10.55	11.10	11.27	11.52
	SICI		3.29	0.40	1.53	2.98	3.21	3.52	4.78
Urban	B6	8,424	13.78	2.29	7.88	12.13	13.59	15.23	45.54
	B7		3.73	0.71	1.77	3.24	3.67	4.15	15.72
	B10		10.36	0.27	9.63	10.16	10.41	10.58	10.89
	SICI		3.72	0.24	2.64	3.56	3.69	3.84	5.63
Forest	B6	84,049	0.17	0.03	0.12	0.16	0.17	0.19	0.26
	B7		0.02	0.00	0.02	0.02	0.02	0.02	0.03
	B10		0.01	0.01	0.01	0.01	0.01	0.02	0.05
	SICI		8.95	0.33	8.27	8.69	9.05	9.18	9.56

Chapter 3 Appendix

Table A3.1. Spectral properties of Landsat-8 OLI and TIRS (Morfitt et al. 2015; USGS 2018; Irons et al. 2012). The radiance and temperature values are at sensor at the Top of Atmosphere (TOA). The TOA temperature is only measured in TIR bands.

Band Name	Band width (µm)	Center wavelength (µm)	Saturation	
			Radiance ($Wm^{-2}sr^{-1}µm^{-1}$)	Temperature (K)
Band-1: coastal/aerosol	0.435–0.451	0.443	950	-
Band-2: blue	0.452–0.512	0.482	800	-
Band-3: green	0.533–0.590	0.561	760	-
Band-4: red	0.636–0.673	0.655	740	-
Band-5: NIR	0.851–0.879	0.865	500	-
Band-6: SWIR-1	1.566–1.651	1.609	96	-
Band-7: SWIR-2	2.107–2.294	2.201	29	-
Band-10: TIR-1	10.61–11.19	10.9	20.5	360
Band-11: TIR-2	11.50–-12.51	12.0	17.8	360

Table A3.2. Statistic median values of Top of Atmosphere (TOA) planetary reflectance of Landsat-8 bands (band 1–7), TOA brightness temperature of TIR-1 (band-10) and the ratio of ShortWave InfraRed band-7 (SWIR-2) and band-6 (SWIR-1) reflectance or ShortWave InfraRed Combustion Index ($SICI_{\rho}$). Samples of combustion areas and non-combustion areas were extracted from Landsat-8 path/row 118/062 over Central Kalimantan in the period of August–October 2015. The sample areas were categorized based on atmosphere conditions, i.e. clear and smoky based on aerosol band (band-1).

Median	Total N (pixel)	Coastal Aerosol	Blue	Green	Red	NIR	SWIR-1	SWIR-2	TIR-1	$SICI_{\rho}$
Clear atmosphere										
Flaming	584	0.20	0.18	0.15	0.12	0.27	0.37	1.00	311.38	2.69
Smouldering	515	0.22	0.20	0.16	0.14	0.26	0.19	0.31	307.65	1.65
Burnt area	9068	0.14	0.11	0.08	0.07	0.09	0.09	0.08	309.10	0.90
Forest	211501	0.14	0.11	0.08	0.05	0.28	0.09	0.03	298.67	0.34
Plantation	6076	0.12	0.10	0.09	0.07	0.32	0.19	0.08	299.90	0.43
Urban	4212	0.15	0.13	0.11	0.11	0.19	0.22	0.17	306.03	0.80
Building	1640	0.27	0.26	0.27	0.27	0.33	0.42	0.36	301.14	0.84
Cloud	5176	0.52	0.53	0.53	0.55	0.70	0.58	0.45	290.23	0.77
Smoky atmosphere										
Flaming	1143	0.43	0.43	0.40	0.39	0.41	0.28	0.47	307.31	1.70
Smouldering	1347	0.42	0.40	0.37	0.34	0.38	0.21	0.24	306.15	1.14
Burnt area	5107	0.21	0.18	0.14	0.12	0.20	0.10	0.07	304.51	0.68
Forest	9160	0.27	0.24	0.19	0.15	0.31	0.12	0.05	297.11	0.43
Plantation	3779	0.43	0.43	0.41	0.40	0.45	0.24	0.12	297.32	0.48
Urban	5303	0.26	0.24	0.20	0.18	0.28	0.25	0.19	302.16	0.75
Building	398	0.45	0.45	0.30	0.39	0.42	0.35	0.28	296.38	0.79

Chapter 4 Appendix

Table A4.1. POD (%), commission error (%), and omission error (%) of VNP14IMG assessment based on ToPeCAl-L8 fires using single buffer analysis and cluster buffer analysis for three buffer distances (187.5 m, 375 m, 750 m) and single time acquisition ($night_{-1}$; day_0; $night_0$) and multi-time acquisition of VNP14IMG ($night_{-1}$ + day_0; day_0 + $night_0$; $night_{-1}$ + day_0 + $night_0$, and nighttime data i.e. $night_{-1}$ + $night_0$).

POD	buffer (m)	$night_{-1}$	day_0	$night_0$	$night_{-1}$+day_0	day_0 + $night_0$	$night_{-1}$ + day_0 +$night_0$	$night_{-1}$ + $night_0$
single-buffer	187.5	54	50	58	47	62	66	73
	375	63	63	70	61	63	76	81
	750	67	74	75	71	77	83	85
cluster-buffer	187.5	71	72	79	87	87	100	87
	375	77	80	84	90	88	100	89
	750	76	84	85	93	91	100	90

Commission Error	buffer (m)	$night_{-1}$	day_0	$night_0$	$night_{-1}$+day_0	day_0 + $night_0$	$night_{-1}$ + day_0 + $night_0$	$night_{-1}$ + $night_0$
single-buffer	187.5	35	54	56	40	46	22	45
	375	16	35	33	25	30	3	22
	750	8	16	18	17	17	1	10
cluster-buffer	187.5	18	23	20	21	18	3	16
	375	9	16	13	14	14	1	12
	750	4	9	11	13	11	0	6

Omission Error	buffer (m)	$night_{-1}$	day_0	$night_0$	$night_{-1}$+day_0	day_0 + $night_0$	$night_{-1}$ + day_0 + $night_0$	$night_{-1}$ + $night_0$
single-buffer	187.5	46	50	42	53	38	34	27
	375	37	37	30	39	37	24	19
	750	33	26	25	29	23	17	15
cluster-buffer	187.5	29	28	21	13	13	0	13
	375	23	20	16	10	12	0	11
	750	24	16	15	7	9	0	10

Chapter 5 Appendix

Table A5.1. Statistical comparison of ToPeCAl-2 to ToPeCAl-1 applied to Landsat-8 image data based on contextual test and cloud masking approach. The comparison was for one class of fire and ToPeCAl-1 was the reference fire data. Columns a to h are the summation values from 15 datasets of Landsat-8. False positive and false negative pixels consisted of fires spatially related to true positive fires – called related false positive/negative (RFP/RFN) and independent false positive/negative (IFP/IFN) pixels. The RFP pixels were the fire pixels that were adjacent to the true positive fire pixels within a one pixel outer buffer; they were considered not to be counted as commission errors and were classified as true positive pixels. Likewise, the RFN pixels for omission error. (TN=True Negative; TP=True Positive; FP=False Positive; RFP=Related False Positive; IFP=Independent False Positive; FN=False Negative; RFN=Related False Negative; IFN=Independent False Negative; POD=Probability of Detection, ICE=Independent Commission Error, IOE=Independent Omission Error).

Method	**TN (pixel)** (a)	**TP (pixel)** (b)	**FP (pixel)** (c)	**RFP (pixel)*** (d)	**IFP (pixel)** (e)	**FN (pixel)** (f)	**RFN (pixel)*** (g)	**IFN (pixel)** (h)	**POD (%)**	**ICE (%)**	**IOE (%)**
Contextual	609,216,243	37,041	2,551	606	1,945	63,124	17,915	45,209	55	3	45
Cloud masking	609,216,383	96,847	2,413	831	1,582	3,312	1,477	1,835	98	2	2

*) spatially adjacent to the true positive fire pixels; IFP=c-d; IFN=f-g; POD= $(\frac{b+d+g}{b+d+g+h})$; ICE = $(\frac{e}{b+d+g+e})$; IOE= (100 - POD)

Table A5.2. As per Table A5.1 but showing the comparison of fire classes i.e., flaming (F), smouldering (S), and mix of flaming and smouldering (FS).

Method	**TN (pixel)** (a)	**Fire classes**	**TP (pixel)** (b)	**FP (pixel)** (c)	**RFP (pixel)*** (d)	**IFP (pixel)** (e)	**FN (pixel)** (f)	**RFN (pixel)*** (g)	**IFN (pixel)** (h)	**POD (%)**	**ICE (%)**	**IOE (%)**
Contextual	609,216,245	F	11,971	871	301	570	252	167	85	99	4	1
		FS	13,842	1,374	291	1,083	2,945	1,823	1,122	93	6	7
		S	7,842	306	14	292	59,925	15,925	44,000	35	1	65
Cloud mask	609,216,383	F	11,971	871	322	549	252	138	114	99	4	1
		FS	17,187	1,129	457	672	618	489	129	99	4	1
		S	65,481	413	41	372	2,286	1,142	1,144	89	4	11

*) spatially adjacent to the true positive fire pixels; IFP=c-d; IFN=f-g; POD= $(\frac{b+d+g}{b+d+g+h})$; ICE = $(\frac{e}{b+d+g+e})$; IOE= (100 - POD)

Table A5.3. Landsat-8 OLI TOA reflectance as a function of Sentinel-2 MSI TOA reflectance at aerosol, SWIR-1, and SWIR-2 bands. Intercept and slope values were derived from the ordinary least squares (OLS) regression of total data (n). The coefficients of determination (R^2) were significant at p-values < 0.001. The data sites were Central Kalimantan and South Kalimantan (CK-SK), Jambi and South Sumatera (JSS), and Riau.

Band	Site	Acquisition Date	Intercept	Slope	n	R^2
Aerosol	CK-SK	28 September 2018 [a]	0.0022	0.9297	27,701,821	0.8585
		14 August 2019	0.0350	0.7769	4,012,759	0.5439
		6 September 2019	-0.0071	1.0763	7,656,763	0.5784
	JSS	21 August 2018 [b]	0.0295	0.7853	27,540,936	0.5553
		31 August 2019	0.0928	0.1427	2,705,635	0.1242
		13 September 2018	0.0457	0.3497	12,913,944	0.1642
	Riau	16 April 2019 [c]	0.0050	0.6378	4,785,880	0.4004
		9 May 2019	0.0792	0.3652	11,602,209	0.1379
		28 July 2019	0.0850	0.2951	2,689,892	0.0642
	CK-SK, JSS and Riau (merged data[a,b,c])	28 September 2018 [a], 21 August 2018 [b], 16 April 2019 [c]	0.0169	0.8509	58,716,843	0.6619
SWIR-1	CK-SK	28 September 2018 [a]	-0.0043	0.8878	27,701,821	0.8669
		14 August 2019	-0.0041	0.9299	4,012,759	0.8856
		6 September 2019	0.0164	0.8552	7,656,763	0.7647
	JSS	21 August 2018 [b]	0.0193	0.8516	27,540,936	0.7769
		31 August 2019	0.0654	0.2717	2,705,635	0.4016
		13 September 2018	0.0295	0.4261	12,913,944	0.6305
	Riau	16 April 2019 [c]	0.0305	0.7213	4,785,880	0.6091
		9 May 2019	0.0681	0.5808	11,602,209	0.4267
		28 July 2019	0.0638	0.3316	2,689,892	0.4026
	CK-SK, JSS and Riau (merged data[a,b,c])	28 September 2018 [a], 21 August 2018 [b], 16 April 2019 [c]	0.0131	0.8404	58,716,843	0.7856
SWIR-2	CK-SK	28 September 2018 [a]	0.0004	0.8553	27,701,821	0.8649
		14 August 2019	-0.0002	0.8968	4,012,759	0.8846
		6 September 2019	0.0059	0.8710	7,656,763	0.8099
	JSS	21 August 2018 [b]	0.0064	0.8776	27,540,936	0.8261
		31 August 2019	0.0170	0.3298	2,705,635	0.5879
		13 September 2018	0.0108	0.4459	12,913,944	0.7337
	Riau	16 April 2019 [c]	0.0089	0.7771	4,785,880	0.7094
		9 May 2019	0.0222	0.6619	11,602,209	0.5070
		28 July 2019	0.0246	0.3680	2,689,892	0.4148
	CK-SK, JSS and Riau (merged data[a,b,c])	28 September 2018 [a], 21 August 2018 [b], 16 April 2019 [c]	0.0041	0.8549	58,716,843	0.8318

Table A5.4. Statistical comparison of fires resultant from ToPeCAl-2 with contextual test and ToPeCAl-2 with cloud masking applied to Sentinel-2 MSI compared with fires resultant from ToPeCAl-1 applied to Landsat-8 OLI/TIRS images. The comparison was for one class of fire. The TOA reflectance used in ToPeCAl-2 were with no transformation values and with transformation values from the merged OLS model and local OLS model. (TN=True Negative; TP=True Positive; FP=False Positive; RFP=Related False Positive; IFP=Independent False Positive; FN=False Negative; RFN=Related False Negative; IFN=Independent False Negative; POD=Probability of Detection, ICE=Independent Commission Error, IOE=Independent Omission Error).

Method	TN (pixel) (a)	TP (pixel) (b)	FP (pixel) (c)	RFP (pixel)* (d)	IFP (pixel) (e)	FN (pixel) (f)	RFN (pixel)* (g)	IFN (pixel) (h)	POD (%)	ICE (%)	IOE (%)
ToPeCAl-2 with Contextual test											
No transformation	128,855,177	22,664	9,422	4,578	4,844	46,923	18,434	28,489	62	10	38
Merged OLS	128,541,534	19,002	8,279	4,202	4,077	50,985	19,457	31,528	58	9	42
Local OLS	128,552,020	19,632	7,435	3,675	3,760	50,460	19,648	30,812	58	8	42
ToPeCAl-2 with Cloud Masking											
No transformation	128,909,378	38,169	29,013	10,505	18,508	31,937	22,366	9,571	88	21	12
Merged OLS	128,921,723	29,547	15,634	7,878	7,756	40,530	20,443	20,087	74	12	26
Local OLS	128,913,901	36,118	23,456	11,827	11,629	33,959	19,882	14,077	83	15	17

*) spatially adjacent to the true positive fire pixels; IFP=c-d; IFN=f-g; POD= $(\frac{b+d+g}{b+d+g+h})$; ICE = $(\frac{e}{b+d+g+e})$; IOE= (100 - POD)

Table A5.5. As per Table A5.4 but showing the comparison of fire classes i.e., flaming (F), smouldering (S), and mix of flaming and smouldering (FS).

Method	TN (pixel) (a)	Fire classes	TP (pixel) (b)	FP (pixel) (c)	RFP (pixel)* (d)	IFP (pixel) (e)	FN (pixel) (f)	RFN (pixel)* (g)	IFN (pixel) (h)	POD (%)	ICE (%)	IOE (%)
ToPeCAl-2 with Contextual test												
No transformation	128,825,338	F	7,102	5,910	2,572	3,338	2,336	1,900	436	96	22	4
		FS	2,000	3,002	1,762	1,240	5,168	3,069	2,099	76	15	24
		S	1,327	774	411	363	39,795	12,881	26,914	35	2	65
Merged OLS	128,541,534	F	6,215	3,720	1,769	1,951	3,092	2,497	595	95	16	5
		FS	1,891	2,768	1,528	1,240	5,920	3,908	2,012	78	14	22
		S	1,053	1,742	838	904	41,874	12,151	29,723	32	6	68
Local OLS	128,538,496	F	6,242	4,157	1,850	2,307	3,229	2,631	598	95	18	5
		FS	1,771	2,357	1,388	969	5,931	3,881	2,050	77	12	23
		S	1,369	1,177	568	609	37,970	12,116	25,854	35	4	65
ToPeCAl-2 with Cloud Masking												
No transformation	128,905,237	F	7,293	5,763	2,525	3,238	2,075	1,726	349	97	22	3
		FS	2,939	22,986	10,438	12,548	4,764	3,225	1,539	92	43	8
		S	-	-	-	-	24,757	13,801	10,956	56	0	44
Merged OLS	128,917,292	F	6,198	3,756	1,836	1,920	2,954	2,385	569	95	16	5
		FS	3,129	11,904	6,080	5,824	5,353	3,263	2,090	86	32	14
		S	-	-	-	-	31,751	14,409	17,342	45	0	55
Local OLS	128,909,701	F	6,301	4,101	1,892	2,209	2,817	2,319	498	95	17	5
		FS	3,195	19,150	9,852	9,298	5,234	3,299	1,935	89	36	11
		S	-	-	-	-	25,625	13,970	11,655	55	0	45

*) spatially adjacent to the true positive fire pixels; IFP=c-d; IFN=f-g; POD= $(\frac{b+d+g}{b+d+g+h})$; ICE = $(\frac{e}{b+d+g+e})$; IOE= (100 - POD)

Chapter 6 Appendix

Table A6.1.Permanent bright object (BO) before and after masking on the independent false positive pixels applied to fifteen scenes of Landsat-8 OLI data.

Landsat-8 image number	False positive before BO masking (pixel)	False positive after BO masking (pixel)
1	31	3
2	31	1
3	13	0
4	105	4
5	65	1
6	0	0
7	0	0
8	7	1
9	8	2
10	29	2
11	42	8
12	19	2
13	26	15
14	52	2
15	29	3
Total	457	44